ABSTRACT

Title of Dissertation: EXPLORING THE RELATIONSHIPS BETWEEN FUEL AND OXIDIZER REACTION OF BIOCIDAL ENERGETIC MATERIALS

Tao Wu, Doctor of Philosophy, 2019

Dissertation directed by: Professor Michael R. Zachariah, Department of Chemistry and Biochemistry and Department of Chemical and Biomolecular Engineering

Energetic materials are defined as a class of material with extremely high amount of stored chemical energy that can be released when ignited, along with intensive light emission and shock generation. Developing new energetic materials with high efficiency neutralization of biological warfare agents has gained increased attention due to the increased threat of bioterrorism. The objective of this dissertation is to develop new energetic materials with biocidal capabilities and apply them in various nanothermite systems to explore the relationships between fuel and oxidizer reactions.

Aerosol techniques offer a convenient route and potentially direct route for preparation of small particles with high purity, and is a method proven to be amenable and economical to scale-up. Here I demonstrate the synthesis of various iodine oxides/iodic acids microparticles by a direct one-step aerosol method from iodic acid.

A previously misidentified phase of I_4O_9 hydrate is in fact a new polymorph of HIO_3 which crystalizes in the orthorhombic space group $P2_12_12_1$.

Various iodine oxides/iodic acids, including I_2O_5, HI_3O_8 and HIO_3, were employed as oxidizers in thermite systems. Their decomposition behaviors were studied using a home-made time resolved temperature-jump/time-of-flight mass spectrometer (T-Jump/TOFMS). In addition, nano-aluminum (nAl), nano-tantalum and carbon black were adopted as the fuel or additive in order to fully understand how iodine containing oxidizers react with the fuel during ignition. The ignition and reaction process of those thermites were characterized with T-Jump/TOFMS. Carbon black was found to be able to lower both initiation and iodine release temperatures compared to those of Al/iodine oxides and Ta/iodine oxides thermites.

Their combustion properties were evaluated in a constant-volume combustion cell and results show that nAl/*a*-HI_3O_8 has the highest pressurization rate and peak pressure and shortest burn time. However, an ignition delay was always present in their pressure profiles while combusting. To shorten or eliminate this ignition delay, a secondary oxidizer CuO is incorporated into Al/I_2O_5 system and four different Al/I_2O_5/CuO thermites by varying the mass ratio between two oxidizers are prepared and studied in a constant volume combustion cell. Significant enhancement is observed for all four thermites and their peak pressures and pressurization rates are much higher than that of Al/I_2O_5 or Al/CuO. Two other oxidizers also demonstrate similar effects as to CuO on promoting the combustion performance of Al/I_2O_5.

A novel oxidizer $AgFeO_2$ particles was prepared via a wet-chemistry method and evaluated as an oxidizer in aluminum-based thermite system. Its structure,

morphologies and thermal behavior were investigated using X-ray diffraction, scanning electron microscopy, TGA/DSC, and T-Jump/TOFMS. The results indicate the decomposition pathways of $AgFeO_2$ vary with heating rates from a two-step at low heating rate to a single step at high heating rate. Ignition of Al/$AgFeO_2$ at a temperature just above the oxygen release temperature and is very similar to Al/CuO. However, with a pressurization rate three times of Al/CuO, Al/$AgFeO_2$ yields a comparable result to Al/hollow-CuO or Al/$KClO_4$/CuO, with a simpler preparation method.

T-Jump/TOFMS was used to study the ignition and decomposition of boron-based thermites. The ignition behaviors of bare boron nanopowders and boron-based nanothermites at various gaseous oxygen pressure were investigated using the T-Jump method. High-heating rate transmission electron microscopy studies were performed on both B/CuO and B/Bi_2O_3 nanothermites to evaluate the ignition process. I propose a co-sintering effect between B_2O_3 and the oxidizer play an important role in the ignition process of boron-based nanothermites.

EXPLORING THE RELATIONSHIPS BETWEEN FUEL AND OXIDIZER REACTION OF BIOCIDAL ENERGETIC MATERIALS

by

Tao Wu

Dissertation submitted to the Faculty of the Graduate School of the
University of Maryland, College Park, in partial fulfillment
of the requirements for the degree of
Doctor of Philosophy
2019

Advisory Committee:
Professor Michael R. Zachariah, Chair
Professor Efrain E. Rodriguez
Professor Bryan W. Eichhorn
Professor Dongxia Liu
Professor John Cumings, Dean's Representative

Dedication

To

My Parents

Jinping Wang and Xiangdong Wu

And My Sister: Fei Wu

And My Niece: Jiayi Zhou.

谨以此论文献给我的母亲王金平，父亲武向东，姐姐武菲和外甥女周珈熠。

Thank you for your unconditional love and support.

感谢你们对我无条件的爱和支持。

Acknowledgements

I am grateful for all the people who helped make this dissertation possible over the past 5 years.

First and foremost, I would like to thank my advisor, Dr. Michael Zachariah for his continuous guidance, encouragement and support throughout my PhD study. I felt extremely lucky to be able to work in such an environment where everyone in the group is completely open to share and help each other in their research. I am grateful for everything Dr. Zachariah has done for me and everything I have learned from him has been very valuable and it is information that I will use throughout my life.

I would like to thank Dr. Peter Y. Zavalij for his valuable help on determining the crystal structures of materials prepared in Chapter 3-5. I learned a lot about XRD from him and am thankful for everything he has done for me.

I would also like to thank all the group members from Dr. Zachariah's group for both contributing the work in this dissertation and making my graduate study at the University of Maryland enjoyable. Special thanks to Dr. Xizheng Wang, Scott Holdren, Dr. Jeffery DeLisio and Dr. Haiyang Wang for their invaluable suggestions and continuous support throughout my PhD studies especially the toughest first two years. Scott Holdren also helped edit Chapter 1 in my dissertation and I am very grateful for that. I would like to thank Dr. Lu Liu, Miles Rehwoldt, Dylan Kline, Dr. Yi Wang, Yong Yang, Dr. Phillip Guerieri, Dr. Wenbo Zhou, Michelangelo Romano, Dr. Luning Wang, Dr. Garth Egan, Dr. Rohit Jacob, Dr. Haihan Chen, Feiyu Xu, Wanjun Zhao, Xiuli Hu, Chenbo Ru and Xiangyu Li for their support in our collaborative work.

Thanks to Dr. Sz-Chian Liou and Dr. Wen-An Chiou of the UMD Nanocenter's AIMLab.

Finally, I'd like to acknowledge my advisory committee for their time and advice. I'd also like to thank the Army Research Office and the Defense Threat Reduction Agency for financial support of my projects.

Tao Wu

武 涛

Table of Contents

List of Tables

List of Figures

List of Abbreviations

ASP	Aerosol Spray Pyrolysis
SEM	Scanning Electron Microscopy/Microscope
TEM	Transmission Electron Microscopy/Microscope
SAED	Selected Area Electron Diffraction
EDS/EDX	Energy Dispersive X-ray Spectroscopy
BSE	Backscattered Electrons
EELS	Electron Energy Loss Spectroscopy
XRD	X-ray Diffraction
T-Jump	Temperature Jump
TOFMS	Time-of-Flight Mass Spectrometer
FWHM	Full Width at Half Maximum
TGA	Thermogravimetric Analysis
DSC	Differential Scanning Calorimetry
MEMS	Microelectromechanical Systems
NIST	National Institute of Standards and Technology
LLNL	Lawrence Livermore National Laboratory
nAl	Nanoaluminum
nTa	Nanotantalum
nTi	Nanotitanium
nB	Nanoboron
CB	Carbon Black

CNT	Carbon Nanotube
FGS	Functionalized Graphene Sheet
a-I_2O_5	Aerosol route synthesized I_2O_5
Al-NPs	Aluminum Nanoparticles
RDX	Cyclotrimethylenetrinitramine
TNT	2, 4, 6-trinitrotoluene
NC	Nitrocellulose
MIC	Metastable Intermolecular Composites
ESD	Electrostatic Discharge
MDM	Melt Dispersion Mechanism
ARM	Arrested Reactive Milling

Chapter 1: Introduction

1.1 Energetic materials

Energetic materials are defined as a class of material with an extremely high stored chemical energy that can be released when ignited, along with intensive light emission and shock generation.[1, 2] Once one part of the material ignites, the heat released from the combustion can be further conducted to adjacent regions leading to continuous propagation.

Using different categorization methodologies, energetic materials can be classified into various types. Based on their function, energetic materials comprise explosives, propellants, pyrotechnics, batteries, etc. The disadvantage with this classification method is these categories are vaguely defined that the same energetic material can be classified as either an explosive, propellant, or pyrotechnic. A typical example is gunpowder that consists of a mixture of sulfur, charcoal and potassium nitrate, which has been employed in the fields of explosives, propellants and pyrotechnics.[3, 4]

A better way to categorize energetic materials is based on their formulations; they can be divided into heterogeneous energetic composite materials where the fuel and oxidizer are in different molecules and homogeneous energetic materials where both the fuel and oxidizer exist as one molecule. Take gunpower again for xample, it contains fuels (sulfur and carbon) and oxidizer (potassium nitrate) in separate formulations; thus, it is classified as a heterogeneous energetic material. However, homogeneous energetic materials have both fuel and oxidizer components within one formulation. In other words, a single molecule functionalizes as the fuel and the

oxidizer.. Thus, homogeneous energetic materials usually can achieve a very rapid energy release due to the lack of the diffusion length between the fuel and oxidizer. Materials like dynamite, 2, 4, 6-trinitrotoluene (TNT), cyclotrimethylenetrinitramine (RDX), etc, have been widely studied in energetic fields and used in military applications. However, homogeneous energetic materials suffer from low energy density owing to the limitation of their physical density and extremely high sensitivity that obstructed their development in energetic studies.[5] As indicated in Figure 1.1, the energy densities of homogeneous energetic materials are significantly lower than those of heterogenous energetic composites materials. Due to these reasons, researchers have devoted their attention to heterogeneous energetic materials in recent times.

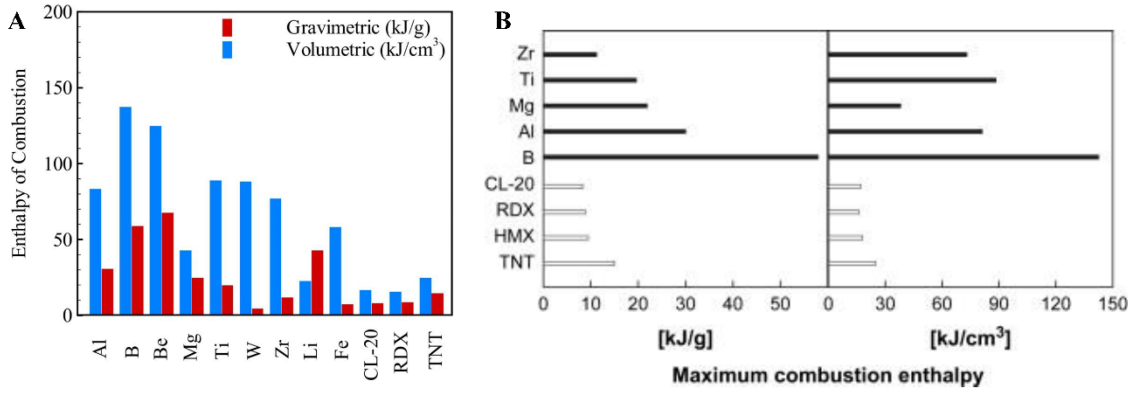

Figure 1.1. (A) Gravimetric and volumetric energy densities of some metals and homogeneous energetic materials in pure oxygen at stoichiometric conditions.[5] (B) Maximum combustion enthalpies for some reactive metals and homogeneous energetic materials.[1]

Thermite reactions refer to a redox reaction between a physically mixed metal fuel and solid metal oxides and have been substantially studied due to their high energy densities and greater stabilities. The thermite reaction was first employed in welding especially for joining rail tracks starting in 1899. This thermite welding process employs an exothermic reaction of aluminum powder and a metal oxide. Researchers

expanded to other reactive metals as a replacement of aluminum, which defines a thermite reaction in a broad sense. As shown in Figure 1.1, most metal-based energetic materials feature high energy densities that make them a potential fuel in thermite reactions. Typically, a thermite reaction undergoes as follows:

$$A + BO \rightarrow B + AO + \Delta H$$

where A represents a reactive metal, B refers to a less reactive metal, ΔH represents the heat of reaction. The overall reaction is exothermic because the metal oxide on the product side has a much lower enthalpy of formation than the metal oxide on the reactant side. As indicated in Figure 1.2, aluminum-based thermite reactions have much higher volumetric energy densities compared to those of homogeneous energetic materials (e.g. TNT, RDX).

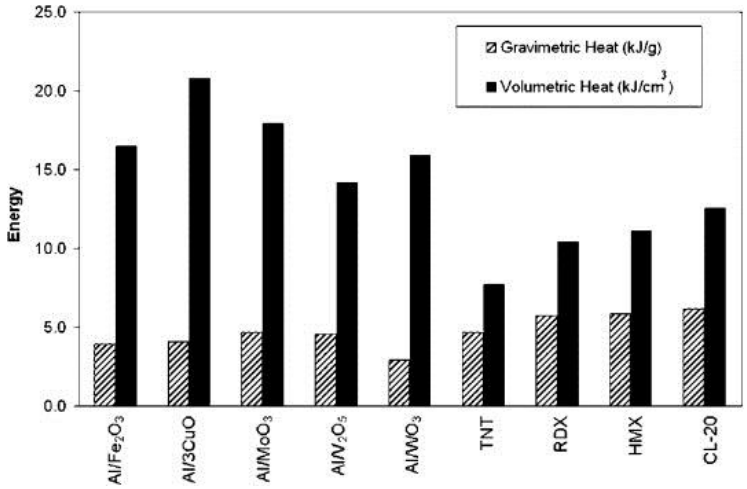

Figure 1.2. Volumetric and gravimetric densities of energy for some thermites and conventional high explosives.[6]

1.2. Nanothermites

Even though thermites usually feature a high energy density, the slow rates of energy release caused by the low mass transfer rate between reactants limits their applications. To increase the mass transfer rate, one obvious method is to reduce the size of the

reactants and therefore shortening the diffusion length between fuel and oxidizer due to the increased surface to volume ratio of the nano-sized materials. The length scales of the nanoparticles are normally distributed in between 1 to 100 nanometers. By decreasing the particle size (assuming spherical particles), the ratio of surface atoms to bulk atoms increases dramatically as indicated in Figure 1.3. As a result, the energy release rate of the energetic materials is enhanced. Aumann et al first reported the benefits by employing nano-sized aluminum in thermite systems.[7] Since then, employing nanoparticles in energetic materials has drawn great attention.[1, 2, 7-11] Yetter et al reported that nano-sized aluminum-based thermites show more than 10^3 increase in reaction rates compared to micron-sized thermites.[2] Later, researchers named those energetic materials employing nano-size fuels or oxidizers, nanothermites. By increasing the interfacial contact area between fuels and oxidizers, the performance of nanothermites is significantly improved. By employing nanostructure in thermite studies, the reactivity of the nanothermites can be tuned easily by just varying the particle sizes, morphology, composition or packing. In addition, it has been reported that the ignition temperature of aluminum-based thermite decreases when the aluminum particle sizes decreases. On the other hand, ignition with high heating rate by its nature is essentially the point where the self-heating by an exothermic reaction exceeds heat loss and a non-linear reaction event occurs; therefore, the initial heat release from thermite reaction should not be affected by oxidizers particles size.[12]

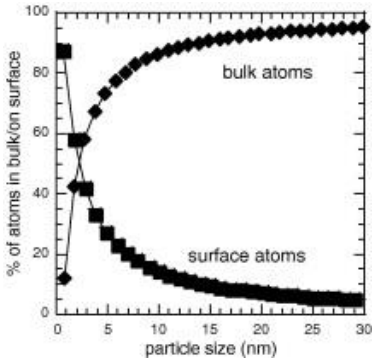

Figure 1.3. Surface to bulk atom ratio for spherical iron crystals.[2]

Nanothermite reactions occur over extremely short time periods (several micro seconds).[13] To be able to probe these fast reactions, ultrafast heating rate diagnostic tools are needed. By utilizing rapid heating techniques and in-situ measurements, the initiation mechanisms and reaction kinetics of nanothermites have been studied throughout this dissertation. An overview of these tools is provided in Chapter 2.

1.3. Fuels and thermite reaction mechanisms

In nanothermites, the most commonly studied metal is aluminum because of its abundance and relatively high reactivity compare with other metals (Figure 1.1). Moreover, aluminum is often coated with a layer of aluminum oxide due to its high reactivity in air and this passivated oxide layer serves as a barrier between the metal core and the outside oxygen to prevent the aluminum core from further oxidizing in air. However, once the aluminum core reaches near the melting temperature, it can diffuse through the oxide shell and interact with any available oxidizer which leads to ignition.[13] Those unique properties inspired researchers to adopt aluminum into numerous types of explosives and rocket propellants for improving the reaction heat; however, the very existence of a passivated oxide layer outside of aluminum leads to

long ignition delays and a slow combustion rate, which limits the performance of aluminum additives. To solve those problems, considerable effort has been devoted to studying the initiation mechanism of aluminum-based nanothermites.

As reported, the initiation/reaction of aluminum-based nanothermites differ significantly upon different heating rates. At low heating rate, Trunov et al discovered that the oxide shell undergoes phase transitions when heating to above 550 ^{o}C, in which the aluminum core and oxygen can transfer through the shell and therefore enables continuous combustion/reaction.[14] The scenarios are much more complicated at high heating rates, but it is believed that the molten aluminum is essential for ignition. Rai et al and Nakamura et al reported, about the same time, a hollow alumina particle after oxidization, which was ascribed to the outward leaking of the aluminum core due to the concentration/pressure gradient across the shell.[15, 16] Later, Sullivan et al used a high heating rate microscopy measurement to examine Al/WO_3 nanothermite and reported a reactive sintering mechanism is dominating the initiation/reaction of Al/WO_3 nanothermite, in which initiation occurred at a fuel/oxidizer interface. The generated heat further melts/sinters adjacent particles as heat is conducted away from the interface and more unreacted materials transfer to the reactive sites to react until no more material is left.[17] On the other hand, Stamatis et al reported Al/MoO_3 ignited at a temperature lower than the melting point of aluminum due to an alumina phase transition at 500 ^{o}C.[18] It seems the ignition mechanism of aluminum-based nanothermites is somehow related to the metal oxides. Later, Sullivan et al reported that a reactive sintering mechanism is occurring early during the combustion of most aluminum-based nanothermites.[19]

Jian et al investigated the role of gas phase oxygen generation from different oxygen carriers in the ignition of aluminum-based nanothermites, where ignition temperature is used as the criterion for the onset of the thermite reaction.[20] In general, ignition temperature is defined as the temperature where the self-heating by the exothermic reaction exceeds heat loss and a self-sustained reaction occurs. As shown in Figure 1.4, it turns out the ignition temperature has no clear correlation with the gas phase oxygen generation. For example, the ignition temperatures of Al/CuO and Al/Fe_2O_3 nanothermites are slightly higher than the oxygen release temperature from the pure oxidizers indicating gas-phase oxygen generated from the oxygen carrier may be the key for their ignitions. However, the ignition temperature of Al/Bi_2O_3 and Al/SnO_2 is lower than the oxygen release temperature of the corresponding oxidizers; in other words, it can be ignited without any available gaseous oxygen, suggesting a condensed phase reaction mechanism might be dominant here. Along with the fact that the ignition of Al/Bi_2O_3 and Al/SnO_2 happens slightly below the melting point of aluminum implies the oxygen and molten aluminum transports in condensed phase may be driving the ignition/reaction. It is also noted that Al/WO_3, Al/MoO_3 and Al/Sb_2O_3 can be ignited even though no gaseous oxygen can be released from the corresponding oxidizers upon heating. Therefore, the gas phase oxygen is only essential for the ignition of certain aluminum-based nanothermites and a condensed-phase mechanism seems to dominate the ignition of other nanothermites. In general, the ignition mechanism of aluminum-based nanothermites can be divided into two categories: gas-condensed heterogeneous reaction and condensed-phase interfacial reaction.

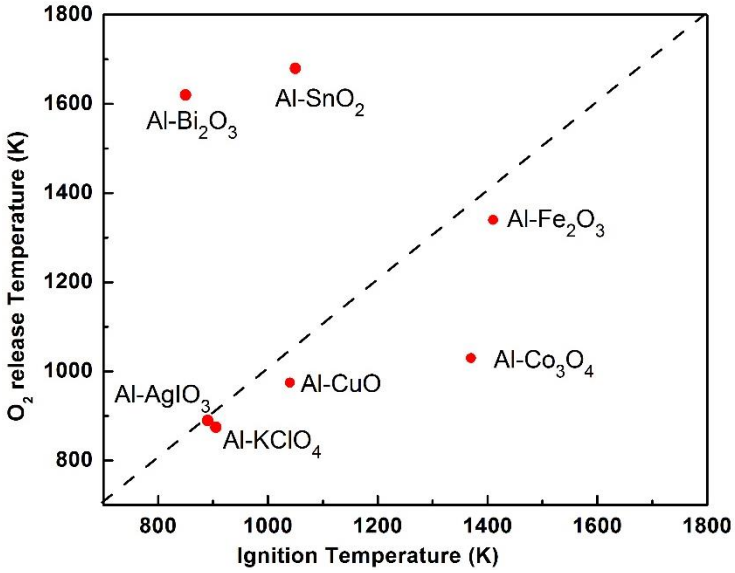

Figure 1.4. Ignition temperature of Al/oxidizer vs O2 release temperature from bare oxidizer.[20]

For the gas-condensed heterogeneous reaction mechanism, the gaseous oxygen released from the oxidizer dominates the ignition: either by the release rate of oxygen gas from the oxidizer or the reaction kinetics between gaseous oxygen and the aluminum. Zhou et al evaluated free vs bound oxygen on ignition of bare aluminum nanoparticles by examining them in various oxygen pressures and found a critical temperature existed for the ignition of aluminum in a gaseous oxygen environment where increasing oxygen pressure cannot further decrease the ignition temperature simply because the mobility of aluminum migrating towards the surface has become the new limiting factor. Thus, the release rate of oxygen gas from the oxidizer (earlier stage) and the reaction kinetics between gaseous oxygen and the aluminum (later stage) are both important for understanding the gas-condensed heterogeneous reaction mechanism. Zhou et al also investigated the ignition of Al/Fe_2O_3, Al/Bi_2O_3 and Al/$K_2S_2O_8$ under different oxygen pressure.[21] It is found that the ignition temperature

of Al/Fe_2O_3 is higher than that of aluminum in a gaseous oxygen environment when the same oxygen pressures are applied, indicating the reaction rate between aluminum and bound oxygen from Fe_2O_3 is slower than that between aluminum and free oxygen. Even though the ignition of Al/Fe_2O_3 is clearly controlled by the gas-condensed heterogeneous reaction mechanism based on the result shown in Figure 1.4; the high ignition temperature and extremely low reactivity of Al/Fe_2O_3 is due to the relatively low decomposition rate of Fe_2O_3, which limits the amount of released gaseous oxygen that comes in contact with the aluminum. [22, 23] Sullivan et al also examined Fe_2O_3 using high heating rate in-situ microscopy and discovered oxygen is being trapped and bubbles out over a time-scale three times longer than that of CuO, suggesting the insufficient decomposition is limiting the performance of Fe_2O_3 as an oxidizer.[19] By increasing the oxygen pressure from vacuum to 1 atm, the ignition temperature of $Al/K_2S_2O_8$ deceases from 755 ^oC to 610 ^oC suggesting the gaseous oxygen is important for its ignition. Under the same oxygen pressures, $Al/K_2S_2O_8$ always shows a lower ignition temperature than that of aluminum in gaseous oxygen which implies the rapid release of oxygen from the oxidizer could significantly increase the local oxygen concentration and thus favors a lower ignition temperature.

As for the condensed phase interfacial mechanism, it is proposed the ignition/reaction is controlled by the diffusion of molten aluminum and/or the condensed phase oxygen transport. The direct contact between the fuel and oxidizer is essential for ignition in both cases.[17, 19] Zhou et al reported that the ignition temperature of Al/Bi_2O_3 is not affected by the oxygen pressure and argued that the extremely high oxygen ion conductivity of Bi_2O_3 greatly enhances condensed phase

transport of oxygen and therefore gaseous oxygen would not participate in the oxidization of aluminum.[21] Considering the ignition temperature is very close to the melting temperature of aluminum, it is reasonable to assume that the condensed phase oxygen transport and the diffusion of molten aluminum both affect the ignition of Al/Bi_2O_3. Since the diffusion of molten aluminum has been systematically studied previously, more efforts are needed to discover what properties make a good oxidizer in the nanothermite reaction to better understand the condensed phase interfacial ignition mechanism.

Wang et al systematically studied different Al/Bi_2O_3 systems and reported that a critical oxygen ion conductivity exists for Bi_2O_3 to oxidize aluminum while aluminum is in the molten phase and oxygen ion transport limits the condensed state of Bi_2O_3 oxidizes thermite ignition.[24] They also discovered that a larger oxygen vacancy concentration and smaller metal-oxide bond energy in the oxidizers could give a lower ignition temperature, which suggests the microscopic properties of the oxidizers might be the key to understanding the ignition mechanism of aluminum-based nanothermites. A later time at the same year, Wang et al employed systematic doped perovskites as oxidizers in aluminum-based nanothermites and discovered a linear relationship between average bond energy and electronegativity with ignition temperature.[25] For the very first time, the tuning of the nanothermite ignition can be fulfilled by simply manipulating the properties of oxidizers.

Besides aluminum, boron features the highest gravimetric and volumetric energy densities (Figure 1.1) and the highest maximum combustion enthalpy when reacting with copper oxide shown in Figure 1.5. Thus, boron theoretically could be an attractive

alternative for aluminum. Like aluminum, boron particles also have a passivated oxide shell, B_2O_3. Since B_2O_3 melts at a much lower temperature (450 ^oC) than the core (2100 ^oC), the burning scenario of boron is very different from aluminum. Upon heating, the molten B_2O_3 shell will surround the outside which prevents the outside oxygen from diffusing through. Over the last few decades, the ignition and combustion of boron particles were extensively studied both theoretically and experimentally.

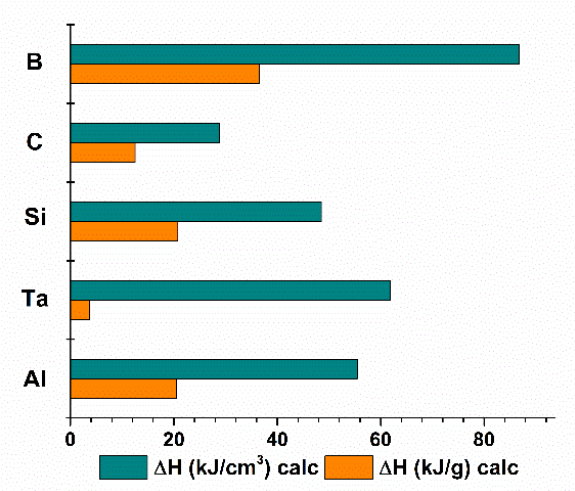

Figure 1.5. Maximum combustion enthalpy for the reaction of various metals with CuO.

Prentice [26] observed a two-stage combustion process for the ignition of boron particles in air and in oxygen-argon mixtures at atmospheric pressures. The low-temperature stage involves a surface burning process followed by a high-temperature stage corresponding to gas-phase combustion. Later, Macek and Semple [27] investigated combustion of boron particles at atmospheric pressure in hot oxidizing gases of different compositions and found that boron combustion always happens in a two-stage process verifying what Prentice claimed previously. The first short stage involves the removal of the oxide layer and can be a kinetic and/or diffusion-controlled

process. The second stage involves the burnout of a bare boron particle and is controlled by gas-phase diffusion of the oxidants. The burn time of each stage is found to be inversely proportional to the oxygen molar ratio and merge as the mole fraction of oxygen decreases. Macek and Semple [28] then studied the combustion of boron particles at elevated pressures and found that the low-temperature stage was nonreproducible at pressures above ~10 atm. There are contradictory theories about the mechanisms that dominate species diffusing into the liquid boron oxide layer during the first stage of boron particles ignition. Glassman et al [29] claimed that boron oxide production during the first ignition stage results from boron diffusion across the oxide layer rather than oxygen diffusion claimed by King [30, 31]. Yeh and Kuo [32] later verifies that the diffusion of dissolved boron into molten boron oxide dominates the diffusion process. They also found the boron oxide layer of boron particles changed from a crystalline to an amorphous structure at elevated temperatures and its chemical composition was identified as a polymeric vitreous $(BO)_n$ complex through the reaction between dissolved boron and molten boron oxide. Theoretical models were also developed by Knipe [33], Mohan and Williams [34] and others to simulate the two-stage combustion of boron particles.

The influence of the initial thickness of the boron oxide layer on ignition and combustion of boron particles was studied by Ao et al [35]. They reported the oxide layer thickness has little effect on the reactivity of the oxidation of boron particles below 775 ^{o}C. With increasing boron oxide layer thickness, the combustion efficiency decreases, and the time required for complete removal of the oxide layer is longer,

while the ignition delay time significantly increases, and the oxide layer removal rate is increased.

In recent years, more efforts have been devoted to the ignition and combustion of boron-based thermite systems. As mentioned previously, thermites involve an exothermic reaction of a metal fuel and a metal oxide. Sullivan et al [36] studied the reaction of nano-B/Al/CuO metastable intermolecular composites and reported the addition of nanoboron to Al/CuO can enhance the reactivity when the boron is less than 50 mol% of the fuel, while no enhancement was observed for micro-sized boron. From both experimental and theoretical results, they speculated that the sensible heating, removal of the oxide shell and the melting of the boron are all critical for fast reaction. Liu et al[37] prepared B/CuO nano-thermite through a chemistry precipitation method. They reported an improved thermochemistry behavior of boron particles with a coating of nano-CuO and a lower onset reaction temperature. Recently, Wang et al[38] reported a clear relationship between molecular properties of the oxidizer and ignition temperature as well as combustion performance of boron-based nano-thermites in which larger oxygen vacancy concentration and smaller metal-oxygen bond energy lead to lower ignition temperatures.

In addition to aluminum and boron, tantalum,[39] titanium[40] and carbon[24, 41] have also been investigated recently for the purpose of expanding the fields of thermite reactions. Similar to aluminum, tantalum also has a passivated oxide layer. However, tantalum has a very high melting point of about 3017 ^{o}C, which rules out the influence of the melting phase transition in the scope of ignition temperature test. In other words, the tantalum core would remain immobile at least at the point of ignition, which

provides us a different scenario to understand the relationship between the fuel and oxidizer. DeLisio et al investigated the oxidation mechanism of tantalum nanoparticles at high heating rates and discovered that a rapid crystallization occurs in the oxide shell of the tantalum nanoparticles upon heating creates cracks for oxygen to diffuse through.[39] They also conducted similar studies on tantalum-based nanothermites and reported their ignition temperatures are independent of metal oxide types because the oxide shell crystallization can induce reactive sintering of metal oxides followed by the ignition of the nanothermites. Rehwoldt et al studied the reaction mechanism and ignition characteristics of titanium nanoparticles and potassium perchlorate thermites and reported the oxide layer of titanium nanoparticles consists not just amorphous TiO_2 but also crystalline TiN and titanium oxynitride.[40] The existence of the latter two compounds make the oxide layer of titanium nanoparticles reactive to some extent. This exact titanium oxide layer can catalyze oxygen release from the oxidizer and facilitate oxygen diffusion and thus lead to a much lower ignition temperature compared to aluminum-based nanothermites.[40] Carbon, as a fuel without a passivated oxide shell, provides a very valuable perspective in understanding the ignition/reaction mechanism of thermites. With a melting point as high as 3550 ^{o}C, carbon remains immobile at least at the point of ignition. The direct contact between carbon and the oxidizer rules out the difficulty for oxygen to go through the oxide layer and therefore the oxygen transport from the oxidizer to carbon surface is controlling the ignition/reaction.[24, 42] All aforementioned fuels are used in a way to aid the understanding of the ignition/reaction mechanisms of nanothermites in this dissertation.

1.4. Biocidal energetic materials

A chemical substance that can destroy or inhibit any harmful organism like spores or bacteria can be considered a biocide. Th commonly used method for spore neutralization is by suspending spores in a high-temperature environment or associated with chemical influence of the halogen gas. Take gunpowder for example, doctors in ancient China used gunpowder to treat bacterial contaminations, plague and skin infection due to biocidal effect of sulfur that is part of the ingredients in gunpowder. Therefore, any energetic materials featuring biocidal functions can be categorized as a biocidal energetic material. Over the last decades, researchers have started utilizing energetic materials in biocidal applications. Developing new energetic materials with high efficiency neutralization of biological warfare agents such as potentially harmful spores and bacteria has gained increased attention due to the increased threat of bioterrorism [43-47]. Preliminary laboratory studies have suggested that an ideal neutralization process should generate not only a high temperature, but also release a long-lasting biocidal agent such as sulfur or halogen elements [48-54]. Those elements are known to be effective biocides.[53] The main limitation of conventional energetic materials is low neutralization efficiency since the thermal neutralization mechanism is dominant in this case, with the lack of effective biocidal agent release [48]. Therefore, it has been proposed that simultaneously delivering a rapid thermal pulse with a remnant biocidal agent would prolong the exposure time and improve the inactivation process [55]. To endue biocidal function in nanothermites, biocidal agents need to be incorporated. Dreizin et al. employed mechanically alloyed aluminum-iodine composites as a fuel in energetic formulations and the initiation and combustion

tests in air indicated that higher iodine concentration lowers initiation temperatures and the combustion temperatures were not substantially diminished [54]. They also found improvements in the pressurization rate and maximum pressure at constant volume with 15 wt.% and 20 wt.% of I_2 [54]. Furthermore, an effective inactivation of aerosolized spores has been achieved using Al/I_2 and $Al/B/I_2$ composites with 15-20 wt.% of iodine [56]. Since the fuel in thermites is limited to its composition, the goal to incorporate biocidal agents into thermites shifts to the oxidizer side. Among all oxides, halogen-containing and silver-containing oxidizers have drawn attention because of their excellent biocidal properties.[56-60]

Among all halogens, iodine stands out owing to its strong neutralization effect. Different methods have been reported for incorporating elemental iodine into energetic materials [56, 61-63]. To incorporate halogens into energetic materials, one can either directly add halogens into the system or assemble halogens into the oxidizers.[56] Wang et al. incorporated solid iodine into Al/CuO thermite systems and found that the $Al/CuO/I_2$ thermite reaction rate was significantly decreased with increasing the iodine content.[62] Guerreo et al also showed that mechanical incorporation of iodine into aluminum severely decreases the reaction rate of Al/metal oxide mixtures and even resulted in failed ignition of $Al•I_2/Fe_2O_3$.[63]

Another approach is to use iodine-containing oxy-compounds that can release HI or I_2 when used as an oxidizer.[64] Iodine-containing oxy-compounds can be broken down into two main categories: metal iodates and iodine oxides/iodic acids. The metal iodates, $AgIO_3$,[48, 65] $Bi(IO_3)_3$,[66] $Cu(IO_3)_2$,[55] $Fe(IO_3)_3$ [55] etc., have been previously investigated. One issue with employing metal iodates in thermites is that

part of the produced I_2 vapor (all for $AgIO_3$) may react with the product metal particles to form corresponding metal iodides, which lowers the effective iodine content in the metal iodate-based thermite systems. Unfortunately, there are only a limited number of iodine oxides/iodic acids which are relatively stable and obtainable. These include I_2O_5, I_4O_9, HI_3O_8, HIO_3, H_5IO_6, etc.[67-69] Among these compounds, I_2O_5 (~76% iodine mass fraction), is the most studied in thermite systems.[10, 70-73] In these studies, aluminum particles with different sizes were chosen as the fuel due to its high reaction enthalpy, thermal conductivity and availability. With reported propagation velocities of up to ~2,000 m/s for loose ball-milled nAl and nano-scaled I_2O_5 (~10 nm), I_2O_5 shows its high potential in aluminum-based thermites as an extremely aggressive oxidizer.[73] Constant volume combustion tests also show nAl/micro-I_2O_5 outperforms traditional aluminum-based thermites such as Al/CuO and Al/Fe_2O_3.[72] A pre-ignition reaction was proposed as the ignition trigger in which ionic I_2O_5 fragments diffused into the alumina passivation shell of aluminum to create some reactive complexes exothermically.[59, 71] However, this mechanism is far from clear as Smith et al reported that a pre-ignition reaction was not found for aluminum/nano crystalline I_2O_5 reaction in contrast to nano amorphous I_2O_5.[74]

Recently, Smith et al reported that a 150% increase in flame speed was found for Al/amorphous I_4O_9 compared with Al/I_2O_5 indicating I_4O_9 has more reactive potential than I_2O_5 as an oxidizer when combined with aluminum.[75] Other iodine-containing oxy-compounds have received comparatively much less attention due to their relatively lower iodine content and availability. Nevertheless, their iodine content is still much higher than metal iodates or per-iodates on a per mass basis. This is particularly so for

HI_3O_8, which has an iodine content of ~75% (similar to I_2O_5 with 76 wt% iodine). Currently, no comparative study examining how the aforementioned iodine oxides/iodic acids perform as oxidizers in thermites system is available. This gives me motive to address this issue in this dissertation.

As for silver, it has been pointed out that silver exhibits biocidal properties in the forms of metallic Ag particles and silver ions in a humid environment.[76] Since most of the products of thermite combustion tend to be primarily in the condensed phase,[44] metallic silver particles are normally the focus. As indicated by Morones et al[77] and Smetana et al[78], small particle sizes are necessary for silver particles to perform well in biocidal activities. To deliver not only a high thermal event but also a large amount of small silver particles as the active biocidal sites could be very useful for biocidal applications.

When it comes to silver-containing oxidizers, Ag_2O was the obvious choice to be considered as an oxidizer in an aluminum-based thermite system. In 2010, Clark et al[79] investigated the combustion performance and biocidal abilities of both Al/I_2O_5 and Al/Ag_2O thermites using a homemade biocidal reaction chamber. They concluded Al/I_2O_5 thermite exhibited significant spore neutralization owing to the generation of large amounts of iodine gas. Al/Ag_2O, on the other hand, underperforms in various aspects due to the poor reactivity of Ag_2O. In 2011, Russell et al[80] further studied the flame propagation behaviors of Al/I_2O_5 and Al/Ag_2O thermites using mechanical impact and thermal initiation. The results show that Al/Ag_2O features a lower average flame propagation by about 2.5 times in thermal ignition tests but produce much more energy than Al/I_2O_5 in impact-driven ignition tests. They also argued that the energy

release of the thermite reactions is significantly enhanced by reducing the sizes of the oxidizer particles. In the same year, Sullivan et al[48] investigated the performance of $AgIO_3$ as an oxidizer in aluminum-based thermite because it decomposed to O_2 and I_2 gases and O and I radicals when heated at an ultra-high heating rate. Silver was not observed in the mass spectra probably because the temperature was not high enough to reach the adiabatic flame temperature and thus could not vaporize silver. However, $Al/AgIO_3$ considerably outperformed Al/CuO in pressurization rate due to many gaseous products released from $AgIO_3$; however, its high combustion performance was mitigated by the fact that the reaction products were found to form AgI instead of elemental silver and iodine, thus obstructing its usage in biocidal applications.

Sullivan et al[44] subsequently synthesized nano-Ag_2O particles and investigated its reactivity as an oxidizer in biocidal energetic systems since it produces high yields of antimicrobial silver as one of the combustion products. They found that Ag_2O alone performs poorly in terms of pressurization rate and burn time, but its performance is significantly improved when combined with one more reactive oxidizer, such as $AgIO_3$ or CuO. The morphology of the final products was also studied and indicated that abundant active sites of silver particles were sacrificed since some silver particles were trapped within the interior of other products, which might affect its biocidal activity to some extent.

In addition to halogens and silver, sulfur has also been considered as biocides for spores. Different sulfur-containing compounds, such as sulfur dioxide[81] and sulfuryl fluoride[82] have been studied and indicates effective bactericidal properties. Various sulfur-containing salts have also been prepared and incorporated into aluminum-based

nanothermites and demonstrated superior combustion performance and release of potential biocidal active agents.[83, 84]

1.5. Scope of the Dissertation

As discussed in the previous sections, nanothermites offers great potential in various energetic applications because they offer high energy densities and high reaction rates. By employing biocidal agents within the system, they can be the potential solution to counterfeit the threat of bioterrorism. The objective of this dissertation is to develop new energetic materials with biocidal capabilities and apply them in various nanothermite systems to explore the relationships between fuel and oxidizer reactions.

The work done in this dissertation will be discussed in eleven chapters. Chapter 1 provides a detailed literature review on nanothermites and biocidal materials. The detailed information about the high-heating rate characterization tools and bulk combustion test are included in Chapter 2. Chapter 3 and 4 present studies on preparations and characterizations of various iodine oxides/iodic acids as well as the scale-up methods. Chapter 5 and 6 investigate the initiation/reaction mechanisms and bulk combustion performance of iodine-containing nanothermites. Chapter 7 focuses on shortening the ignition delay and further improving the combustion performance of Al/I_2O_5 nanothermites. A new silver-containing oxidizer and its performance in nanothermites are discussed in Chapter 8. Chapter 9 investigates the ignition and reaction mechanism of boron-based nanothermites. A summary of my works and recommendations for future work are presented in Chapter 10.

Chapter 2: Experimental Methods

Overview

As discussed in Chapter 1, a thermite ignition/reaction by its nature is essentially the point where self-heating by exothermic reaction exceeds heat loss and product formation occurs. It should be noted that the light emission of metal-based thermites aligns well with the product release profile based on our previous work.[1-3] Considering this process occurs within a few milliseconds requires characterization methods that operate on similar time-scale. For this specific purpose, Temperature-jump Time-of Flight Mass Spectrometry (T-Jump TOFMS) is employed here for studying thermite ignition mechanism since it can provide an ultra-high heating rate (>10^5 °C/s). A brief introduction about this method is included in this chapter. In addition, constant volume combustion cell technique is included here as well since bulk combustion performance is equally important for thermite characterization as to the ignition mechanism.

2.1. Temperature-jump Time-of Flight Mass Spectrometry (T-Jump TOFMS)

Throughout this dissertation, T-Jump TOFMS has been used to study the decomposition behaviors of bare oxidizers and ignition mechanisms of thermites reactions. Typically, a ~1 cm long platinum wire (76 um in width) with a thin coating of oxidizer or thermite sample is rapidly joule-heated to about 1200 °C with a 3 ms pulse at a heating rate of ~10^5 °C/s. Different current pulses varying from 2 to 20 ms

could be applied to the wire. The current and voltage signals were recorded using an oscilloscope by measuring the resistance data of the wire while heating. And the temporal temperature on the wire was calculated according to the Callendar–Van Dusen equation that correlates resistance and temperature of the wire.[4]

When studying the ignition mechanism of thermites reaction, another analytical technique is required in order to acquire the ignition point. To achieve this goal, a high-speed camera (Vision Research Phantom v12.0) was employed to record the combustion on the wire during heating. The camera is triggered at the same time as the T-jump power supply. An external pulse generator is employed here to account for synchronization of optical and wire temperature data. Ignition temperatures of thermite reactions in vacuum were measured from the correlation of optical emission from high speed imaging and temporal temperature of the wire and were further analyzed in combination with the temporal mass spectra. Each experiment was repeated 3 times.

To analyze the gas species released from the thermite reaction, a R. M. Jordan style linear time-of-flight mass spectrometry (TOFMS) is integrated with the T-jump system was employed because it can be pulsed at high rates allowing for sufficient temporal resolution between adjacent spectra. Figure 2.1 is a schematic image of this integrated system. The gas species produced from the thermite combustion are ionized by an electron gun (operating at 70 eV and 1 mA). An electronic gate is pulsed at 10 kHz, which accelerating ions into the electric field-free region of the TOFMS. Ions are detected using a microchannel plate dectector and data is recorded on an oscilloscope operating in sequence mode with a 100 Ms/s sampling rate. MATLAB scripts allowed

for simultaneous data processing on the oscilloscope. The detailed information of the scripts could be found in a dissertation by Jeffery B. DeLisio.[5]

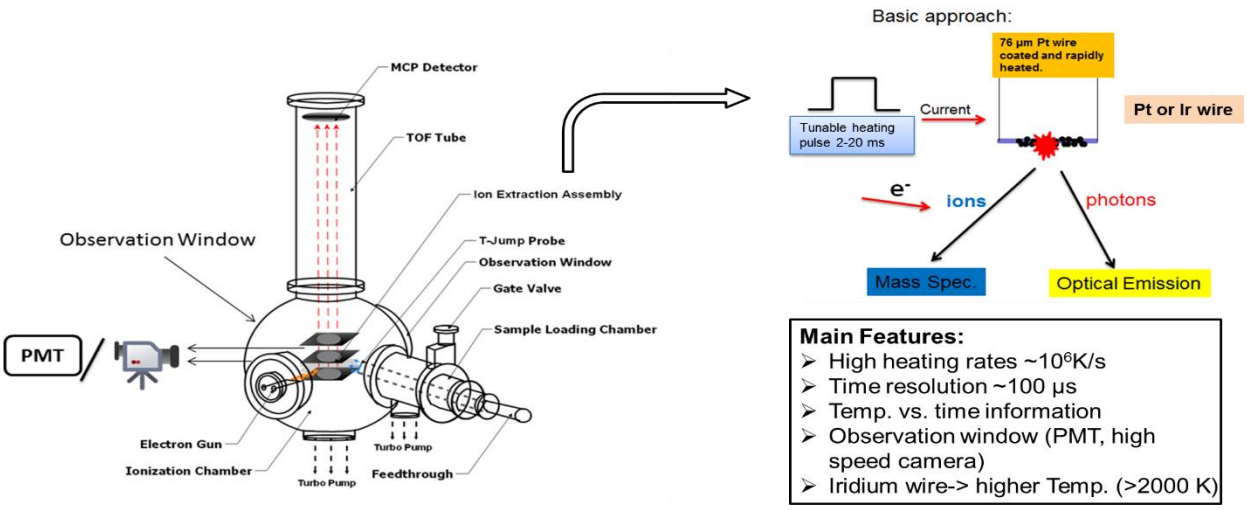

Figure 2.1. Schematic illustration of T-jump/TOFMS system. This figure is a modification to one in reference.

2.2. Constant volume combustion cell

A customized constant volume combustion cell is employed to evaluate the bulk thermite combustion performance. Figure 2.2 shows a schematic illustration of the cell. 25 mg of thermite powders was loaded inside the cell (constant volume, ~13 cm^3) and ignited by a resistively heated nichrome wire. The temporal pressure and optical emission from the thermite reaction were simultaneously measured using a piezoelectric pressure sensor and a photodetector, respectively. The pressure and optical data were collected on an oscilloscope. By plotting the data, pressurization rate, maximum pressure and burn time can be obtained and used for evaluation of the combustion performance. Pressurization rate is calculated by dividing the first peak

pressure by the corresponding time. Burn time is defined as the full width of the half maximum of the optical profile. Since 25 mg of sample are used for each run, combustion product can be collected afterwards for post-combustion characterization. In order to collect freshly condensed combustion product, a double-side carbon tape could be placed inside the cell during combustion cell test and later removed from the cell and examined in SEM for morphology information.

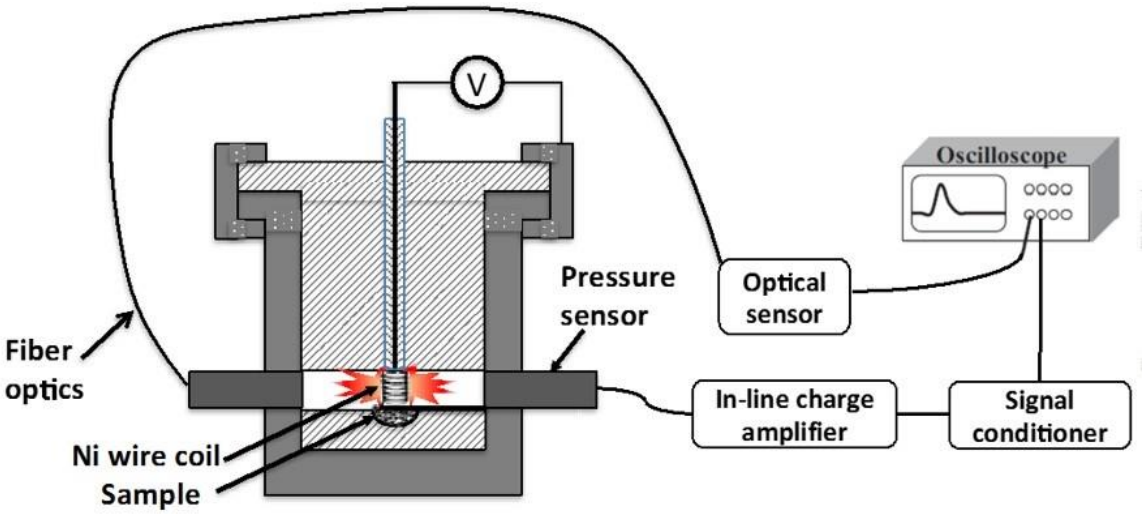

Figure 2.2 A schematic illustration of the combustion cell.

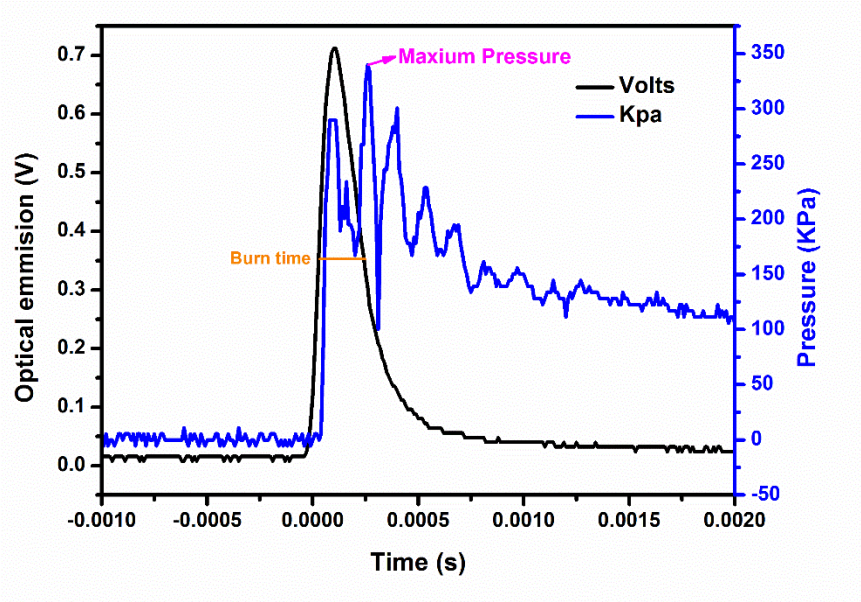

Figure 2.3 Pressure and optical traces obtained from the combustion cell. The sample used is Al/CuO.

Chapter 3: Aerosol Synthesis of Phase Pure Iodine/Iodic Biocide Microparticles [*]

Overview

High iodine containing oxides are of interest as biocidal components in energetic application requiring fast exothermic reactions with metallic fuels. Aerosol techniques offer a convenient route and potentially direct route for preparation of small particles with high purity, and is a method proven to be amenable and economical to scale-up. Here I demonstrate the synthesis of various iodine oxides/iodic acids microparticles by a direct one-step aerosol method from iodic acid. By varying temperature and humidity, I produced near phase pure δ-HIO_3, HI_3O_8 and I_2O_5 as determined by X-ray diffraction. δ-HIO_3, a previously unknown phase, was confirmed in this work. In addition, scanning electron microscopy was employed to examine the morphology and size of those prepared iodine oxides/iodic acids particles and the results show that all particles have an irregularly spherical shape. Thermogravimetric/differential scanning calorimetry measurement results show that HIO_3 dehydrates endothermically to HI_3O_8, and then I_2O_5, and lastly I_2O_5 decompose into I_2 and O_2.

[*] The results presented in this chapter have been published in the following journal article: Wu, T.; SyBing, A.; Wang X.; Zachariah, M. R., Aerosol Synthesis of Phase Pure Iodine/Iodic Biocide Microparticles. J Mater Res 2017, 32 (4), 890-896.

3.1. Introduction

In recent years, the interest in developing new energetic materials with biocidal capabilities [1,2] has drawn increased attention.[3-13] The motivation for this is based on evidence that conventional energetic materials, which employ a thermal neutralization mechanism are not sufficiently efficient[14]. Laboratory studies have demonstrated that the addition of a biocidal component can significant enhance neutralization through a synergistic mechanism.[15-20] Therefore, it has been proposed that simultaneously delivering a rapid thermal pulse with a remnant biocidal agent would prolong the exposure time and improve the inactivation process.[21] Both halogens and silver-containing energetic materials have been explored [22-24] with the halogens offering the most promise due to their excellent biocidal properties.[25] Various methods have been used for incorporating halogens into energetic materials. One approach is through directly introducing halogens into the system, and the other is by incorporating halogens into the oxidizers.[25,26] Thus, iodine-rich compounds that can release HI or I_2 are the ideal candidates for biocidal energetics.[27]

Iodine (V) oxide, as one of the iodine-containing oxides with ~76% iodine mass fraction, has been recently studied as an oxidizer with aluminum fuel.[28] In this case, various metals (primarily aluminum) are mixed with I_2O_5 to form a thermite system whose combustion properties were studied.[29-32] The first paper concerning the reactivity between aluminum and I_2O_5 was published by Ivanov et al in 1980 in which a global reaction mechanism between iodine gas and fuels was proposed [29] and confirmed in a later work.[32] I_2O_5 has received considerable interest because it is an extremely aggressive oxidizer with aluminum with reported propagation velocities up

to ~2,000 m/s for loose ball-milled nano-aluminum and nano-scaled I_2O_5 (~10 nm).[31] In addition, constant volume combustion tests on nano-Al/micro-I_2O_5 thermite exhibits the highest pressurization rate and the shortest burn time relative to other aluminum based traditional thermites such as Al/CuO and Al/Fe_2O_3.[32]

Moreover, oxoacids of iodine, such as HIO_3 and HI_3O_8, have been investigated in the recent decades. Until now, two polymorphs of iodic acid, the stable α-HIO_3 [33,34] and metastable γ-HIO_3,[35] have been reported and well-characterized. However, more evidence is required to verify the existence of β-HIO_3.[35] The thermal behavior of HIO_3 was studied via thermogravimetric/differential scanning calorimetry (TG/DSC) and the result shows three decomposition steps upon heating in air: the dehydration of HIO_3 into HI_3O_8 at 100 ºC, the dehydration of HI_3O_8 into I_2O_5 at 210 ºC and the melting/decomposition of I_2O_5 at 400 ºC[36]. It also reveals that I_2O_5 would be slowly converted to the initial hydrate HI_3O_8 and later to the final hydrate HIO_3 under ambient environment. Furthermore, the crystal structure of HI_3O_8 was determined to be an adduct HIO_3•I_2O_5, which are connected by hydrogen bonds.[37]

Aerosol techniques offer a convenient route and potentially direct route for preparation of nano-sized or micro-sized particles with high purity, and is a method proven to be amenable and economical to scale-up. Along with the fact that decreasing the size of oxidizer particles can improve the burn rate of thermite,[32] in this study I develop a synthesis approach to prepare various iodine oxides/iodic acids microparticles based on aerosol spray pyrolysis (ASP) using commercial iodic acid (HIO_3) as the starting material, because of its water solubility and ready

availability.[38] The decomposition behavior of iodine oxides/iodic acids was also studied using low heating rates with TG/DSC.

3.2. Experimental Details

3.2.1. Materials

Iodic acid (HIO_3) (99.5 wt %) purchased from Sigma-Aldrich were directly used as received. All the other chemicals were of analytical grade and used as purchased without further treatment.

3.2.2. Preparation of various iodine oxide/iodic acid particles via aerosol spray pyrolysis

Small-sized particles of oxides were obtained via aerosol spray pyrolysis (ASP). In general, 100 mL iodic acid aqueous solution (10 mg/mL) were sprayed into small droplets (~1 um in diameter) with a homemade pressure atomizer (~35 pounds per square inch (psi) pressure air) and passed through a silica-gel diffusion drier (silica-gels were regenerated at ~50 ºC or 80 ºC in order to prepare different products) to remove water and are then passed through a tube furnace for chemical conversion. The tube reactor consisted of a ~ 1.9 cm diameter alumina tube with a heated length of ~40 cm. The furnace temperature was set at ~230 and ~375 °C to obtain either δ-HIO_3 or I_2O_5, respectively with a residence time of about 1 second.[39] For both δ-HIO_3 and I_2O_5, silica-gels were regenerated at 50 °C. I find that δ-HIO_3 can be obtained within a large range of temperature from 210 to 250 °C. In addition, HI_3O_8 was obtained with a tube furnace temperature ~250 °C and silica-gels regeneration temperature ~80 °C. The

final product was collected on a Millipore membrane filter (0.4 um pore) and characterized by scanning electron microscopy (SEM, Hitachi, SU-70 FEG-SEM) and powder X-ray diffraction (XRD, Bruker D8 Advance using Cu Kα radiation).

3.2.3. In-situ heating XRD measurement

In-situ heating XRD was performed using a Bruker C2 diffractometer with a Vantec500 2D detector with 2θ ranging from 10º to 50º (λ = 1.5418 Å, step size = 0.05º) and the sample was heated via an Anton Paar DHS 1100 graphite-dome hot stage with a heating rate of 10 ºC/min under air condition. I collected patterns at 26, 100, 200, 300, 400, and 500 ºC and also collected a final pattern at 30 ºC after the sample was cooled. At each temperature, we collected two 10-minute frames at 20 and 40º 2θ. Integrating and merging the two frames together gave us a final powder diffraction pattern from 9.5º to 50º 2θ.

3.2.4. Thermogravimetric/differential scanning calorimetry (TG/DSC) measurement

TGA and Differential Scanning Calorimetry (DSC) were conducted using a SDT Q600 (TA instruments) equipped with a TA Discovery MKS104-S0212004 Micro Vision 2 mass spectrometer. The analysis was performed under a 100 mL min^{-1} argon flow with ~ 1.0 mg samples placed into an alumina pan and heated from room temperature up to 550 °C at a rate of 5 °C min^{-1} in argon atmosphere.

3.3. Result and discussion

Iodic acid (HIO_3) is a white solid at room temperature and is often used as the starting material for preparing iodine-containing materials due to its ready availability, high solubility in water, and that with controlled dehydration yields iodine oxides.

Atomized aqueous HIO_3 droplets in air were passed through a silica-gel diffusion dryer to produce solid HIO_3 particles, which were then directly passed through the tube furnace at a desired temperature to form various iodine oxide/iodic acids (Figure 3.1). In order to determine what temperature should be run for silica gels regeneration, thermal analysis was conducted on a fully hydrated silica gel and the result is shown in Figure 3.2. The black line represents the mass change of the silica gel with increasing temperature. From this I note that silica gel reaches its fully dehydrated state after 15% weight loss (water loss). Assume a fully dehydrated silica gel has a weight of 85 mg, it could absorb 15 mg of water to reach its fully hydrated state (100 mg weight).

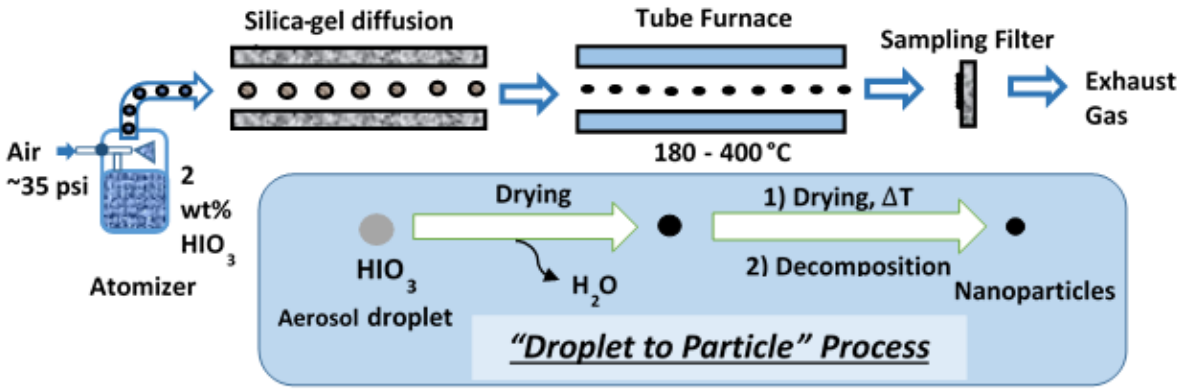

Figure 3.1. Aerosol spray pyrolysis to synthesize various iodine oxides/iodic acids.

For silica gel$_{m=85\ mg}$ regenerated at 50 and 80 ºC, they could absorb 4.4 mg and 8 mg of water, respectively, to reach their fully hydrated state based on the TGA result in Figure 3.2. Since silica-gels obtained from different regeneration temperature have different water-absorbing capabilities, silica-gels regeneration temperature also play an important role in the aerosol route. In this work, regeneration temperatures of ~50 and 80 ºC were used to obtain different products to change the water absorbing properties.

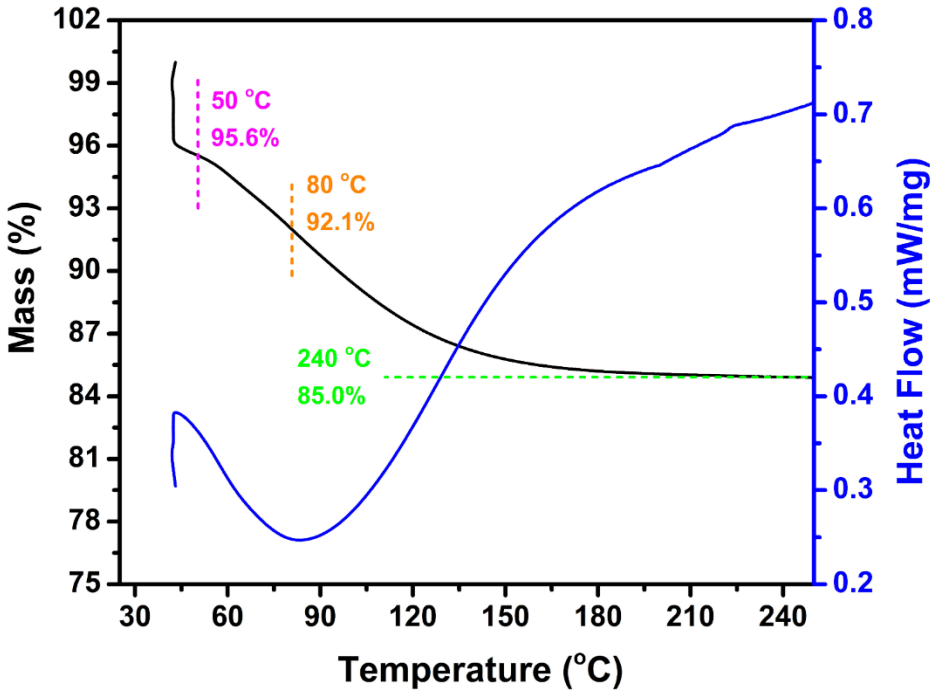

Figure 3.2. The TGA and DSC curves of a fully hydrated silica gel under argon environment at a heating rate of 5 °C/min.

Since iodic acid droplets pass through the tube furnace where the thermal event occurs, I use TGA/DSC results to determine set points for the furnace. Figure 3.3 shows the TGA and DSC curves of iodic acid under air environment with a heating rate of 5 ºC/min, which indicates that there are three decomposition steps: the dehydration of HIO_3 to HI_3O_8 at ~120 ºC, dehydration of HI_3O_8 to I_2O_5 at ~210 ºC and the

decomposition of I_2O_5 at 380 ºC. Thus, I_2O_5 and HI_3O_8 could be obtained via thermal treatment at 210-380 ºC and 120-210 ºC, respectively. The thermal behavior of HIO_3 under argon was very similar to the air case and the detailed information is shown in Figure S3.1.

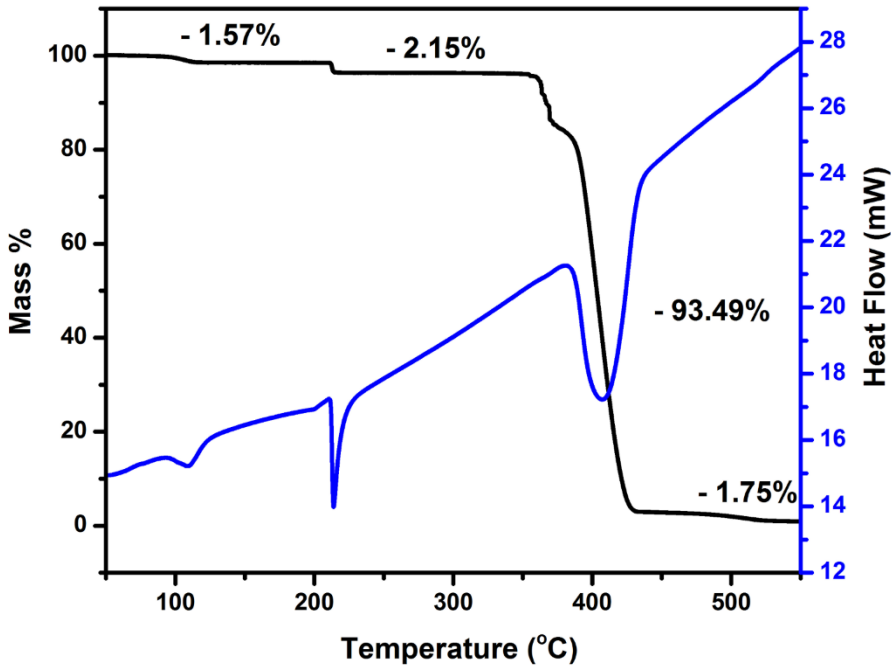

Figure 3.3. TGA and DSC curves of HIO¬3 under air environment at a heating rate of 5 °C/min.

The residence time for a droplet in the aerosol reactor is about 1 second, which is obviously much shorter than that in the TGA ramp time. To obviate this effect, I ran the furnace temperature higher than what the TGA would indicate in order to speed up the kinetics. To validate the phases indicted in the TGA, in-situ hot-stage XRD was ran the HIO_3 powder at a heating rate of 10 ºC/min from room temperature to 500 ºC in air. From Table 3.1, I_2O_5 and HI_3O_8 could be obtained at 300-400 ºC and 200-300 ºC,

respectively. The XRD patterns of HIO_3 at different temperatures are provided in Figure S3.2.

Table 3.1. The chemical composition of HIO3 during in-situ heating XRD test at different temperatures in air.

Temperature (°C)	**26**	**100**	**200**	**300**	**400**	**500**
Product(s)	HIO_3	HIO_3, HI_3O_8	HI_3O_8	I_2O_5	I_2O_5	I_2+ O_2

3.3.1. Preparation of I_2O_5

I_2O_5 [Figure 3.4(c)] was obtained when the tube furnace was set at 350-400 ºC which is consistent with the TGA result in Figure S3.1. TGA and DSC curves of I_2O_5 [Figure 3.4(d)] show the characteristically endothermic decomposition of I_2O_5 into I_2 and O_2 at ~360 ºC which also proves the formation of I_2O_5. The small weight loss at ~210 ºC indicates that small amount of I_2O_5 product is probably rehydrated into HI_3O_8 during the collection process and preparation for TGA/DSC test. The SEM images [Figure 3.4(a)-(b)] show that I_2O_5 particles are irregularly spherical and some large aggregates are also observed in those images indicating that some sintering/coalescence between particles takes place. Crystalline compositions of I_2O_5 determined by Rietveld refinement indicate that 9% of the product rehydrates into δ-HIO_3.

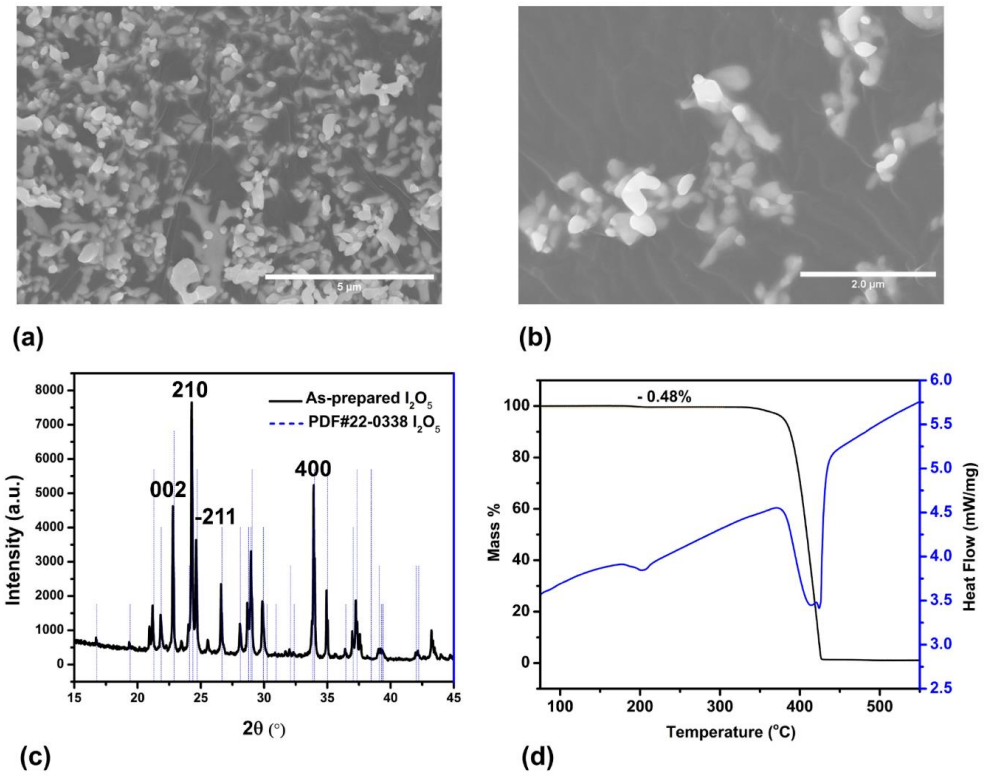

Figure 3.4. SEM image (a and b), XRD pattern (c), TGA and DSC (Ar, 5 °C/min) (d) of as-prepared I_2O_5.

3.3.2. Preparation of δ-HIO_3

Based on the thermal behavior of HIO_3, HI_3O_8 could be obtained when the tube furnace was set at 120-210 ºC. Considering the short residence time within the whole aerosol process and the difference between theoretical and experimental temperatures for preparing I_2O_5, the furnace temperature for synthesis of HI_3O_8 was set higher at 210-250 ºC.

The XRD [Figure 3.5(a)] of as-prepared iodine oxide were consistent with an XRD pattern previously identified as I_4O_9• xH_2O (PDF#45-0872), with no indication of any other iodine oxides/iodic acids. Like I_2O_5 particles, the SEM images [Figure 3.5(c) and

3.5 (d)] shows that "I_4O_9• xH_2O" particles are irregularly spherical due to the sintering/coalescence between particles. This is also confirmed because the resulting particles are larger than expected based on the initial droplet size and concentration used and were nominally ~ 400 nm in diameter.

The proposed structure implies that xH_2O could be removed *via* vacuum drying. However, TGA/DSC and XRD results shown in Figure S3.3 and Figure 3.5(b) indicated surprisingly that there were no changes after vacuum drying. Moreover, the TGA and DSC results of I_4O_9• xH_2O shown in Figure S3.3 are very similar to those of HIO_3 (Figure S3.1), and this similar behavior was further confirmed with in-situ heating XRD (Table 3.2). Given that the previous report proposed the formula I_4O_9• xH_2O without any chemical composition or any crystal structure information [40] lead us to conjecture that the proposed formula may be in error.

Table 3.2. The chemical composition of "I_4O_9• xH_2O" during in-situ heating XRD test at different temperatures in argon environment.

Temperature (°C)	**26**	**100**	**200**	**300-400**	**500**
Product(s)	"I_4O_9• xH_2O"	"I_4O_9• xH_2O", HI_3O_8	HI_3O_8	I_2O_5	$I_2 + O_2$

Based on its powder XRD pattern, I find a distorted octahedral crystal system, space group $P_{2_12_12_1}$ which consists of IO_3 ions with three I-O bonds with distances of 1.78, 1.80 and 1.92 Å, and three I-O contacts with distances of 2.51, 2.76 and 2.76 Å. This reveals that the correct assignment of the phase is actually a previously unreported phase of HIO_3, which I refer to as δ-HIO_3. The detailed crystal information is included in Chapter 4. In addition, the difference between XRD patterns (Figure S3.4) of as-prepared δ-HIO_3 and as-received HIO_3 also suggests a new phase HIO_3.

Thus, instead of obtaining HI_3O_8, as the TGA results would suggest I obtain δ-HIO_3 which indicates that the decomposition pathways of HIO_3 in TGA (slow heating) and ASP (fast heating) are different. This result implies that the δ-HIO_3 is metastable at elevated temperatures and at slow heating converts to I_2O_5. The ASP process enables a rapid thermal ramp and rapid quench to trap the material as δ-HIO_3 which appears to be quite stable at room temperature. In fact, I_2O_5 was obtained when the furnace temperature was raised to above 300 °C.

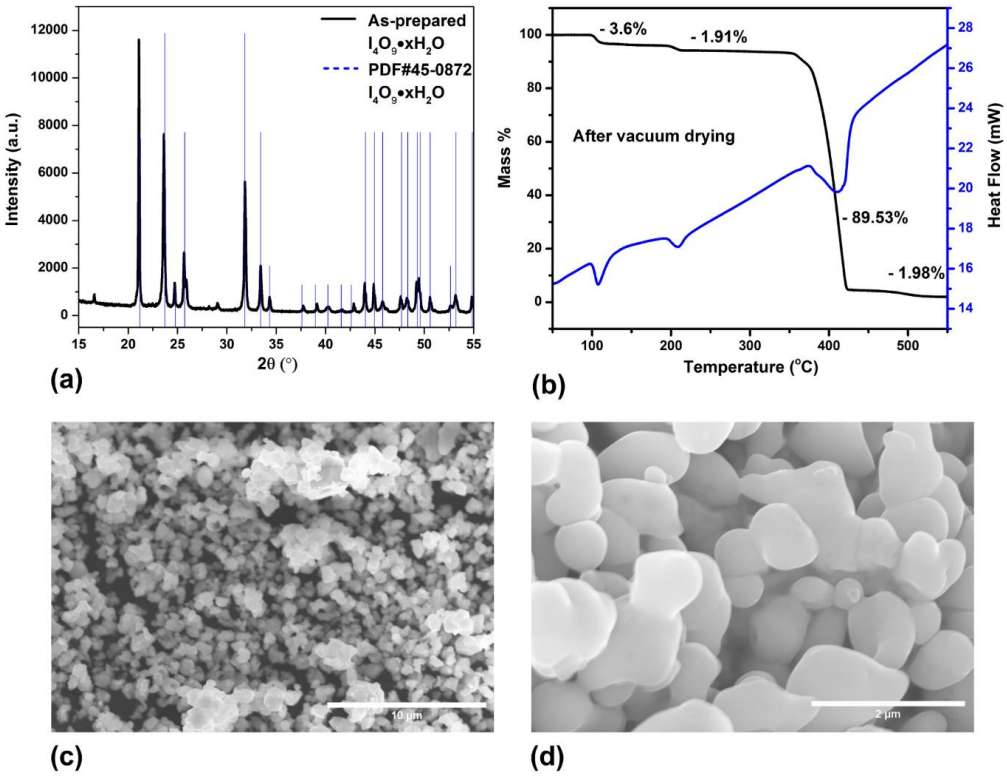

Figure 3.5. XRD pattern (a), TGA/DSC (b) and SEM images (c and d) of as-prepared I_4O_9•xH_2O after vacuum drying treatment.

3.3.3. Preparation of HI_3O_8

Based on the result in Figure 3.3, I am expecting to obtain HI_3O_8 by thermal treatment of HIO_3 at temperature between 120 to 210 °C in air. Therefore, we annealed HIO_3 at different temperatures in air for one hour and it turns out that HIO_3 was fully dehydrated to HI_3O_8 at 150-260 °C (Figure S3.4). Surprisingly, HI_3O_8 was obtained after only two minutes annealing at ~165 °C (Figure S3.4), which indicates that the dehydration of HIO_3 is fast and also suggests ASP is a promising method to prepare HI_3O_8.

Previous results show that δ-HIO_3 rather than HI_3O_8 is the product when the tube furnace was set between 210 to 250 °C with silica-gels regenerated at ~50 ºC. Considering HI_3O_8 is a dehydrated product of HIO_3, the failure to prepare HI_3O_8 might be caused by the relatively weak dehydrating capacity of the original set-up. Again, I_2O_5 was appeared when the tube furnace was increased to 300 ºC or above. This suggested that tuning the tube furnace temperature alone could not obtain HI_3O_8. From the previous discussion, I know that the silica gel regeneration temperature also affects the aerosol synthesis and might be employed to manipulate the hydrating ability of the set-up. I found that regenerating the silica gel at ~80 ºC rather than ~50 ºC would form HI_3O_8 as confirmed by XRD [Figure 3.6(a)] in a single step with a tube furnace temperature of ~250°C. The TGA shown in Figure 3.6(b) indicates two decomposition steps: one is the dehydration of HI_3O_8 to I_2O_5 at ~210 ºC with an experimental weight loss of 1.2% (theoretical weight loss, 1.8%; impurities, ~6%); another is the decomposition of I_2O_5 at ~360 ºC, both of which are endothermic as determined by DSC. Similar to δ-HIO_3, the SEM images of HI_3O_8 in Figure 3.6(c)-(d) show that particles are irregular spheres due to sintering/coalescence between particles during preparation. Crystalline compositions of HI_3O_8 determined by Rietveld refinement indicate that 9% of the product rehydrates into δ-HIO_3.

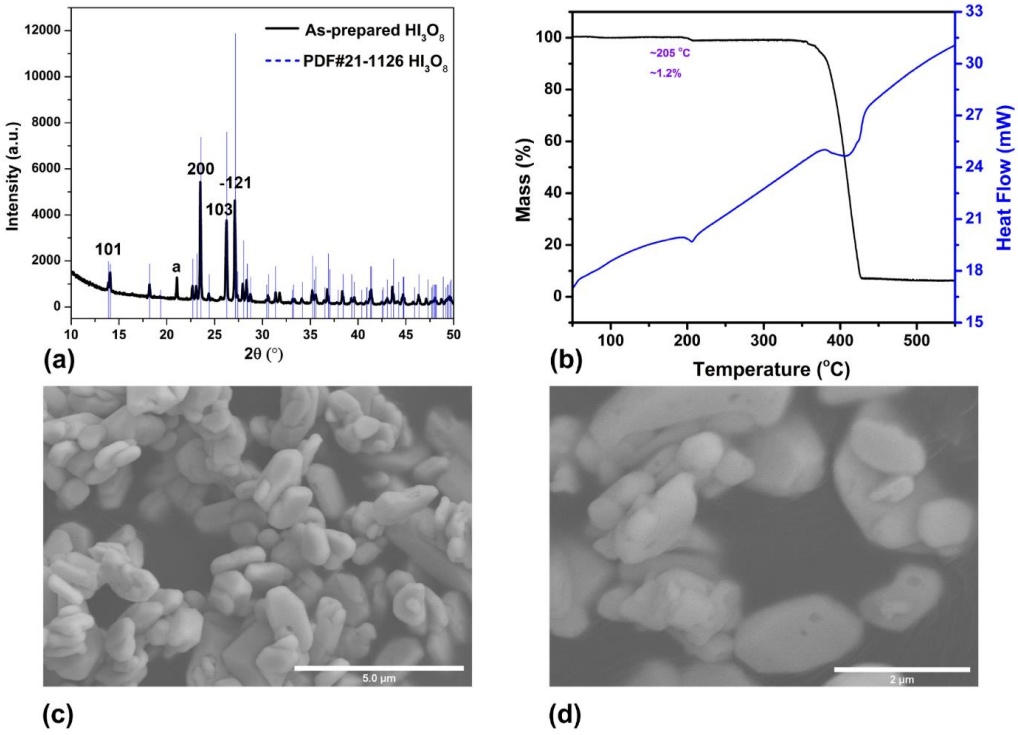

Figure 3.6. XRD pattern (a), TGA/DSC[a] (b) and SEM images (c and d) of as-prepared HI_3O_8.

[a]: Ran under argon environment at a heating rate of 5 ºC/min.

3.4. Conclusions

In summary three different products, δ-HIO_3, HI_3O_8 and I_2O_5, were obtained via ASP as summarized in Table 3.3. Both temperature and humidity control in silica gel preparation were necessary to obtain all three products without post-processing, for temperatures not listed in Table 3.3, either mixtures (HIO_3/HI_3O_8 /I_2O_5) or no product was collected.

Table 3.3. Summarizing the parameters of ASP for preparing different product.

Parameters | Products	I_2O_5	δ-HIO_3	HI_3O_8
Silica Gel Regeneration Temperature (ºC)	*50*	*50*	*80*
Furnace Temperature (ºC)	*350-400*	*210-250*	*~250*

This study demonstrates a facile and environmentally friendly aerosol spray pyrolysis method to prepare various iodine oxides/iodic acids using a single precursor HIO_3. By tuning the furnace temperature and the humidity I was able in a single step to produce near phase pure δ-HIO_3, HI_3O_8 and I_2O_5 as determined by XRD. TGA and DSC results show that HIO_3 dehydrates to HI_3O_8, and then I_2O_5, and lastly I_2O_5 decompose endothermically into I_2 and O_2.

3.5. Supplemental Information

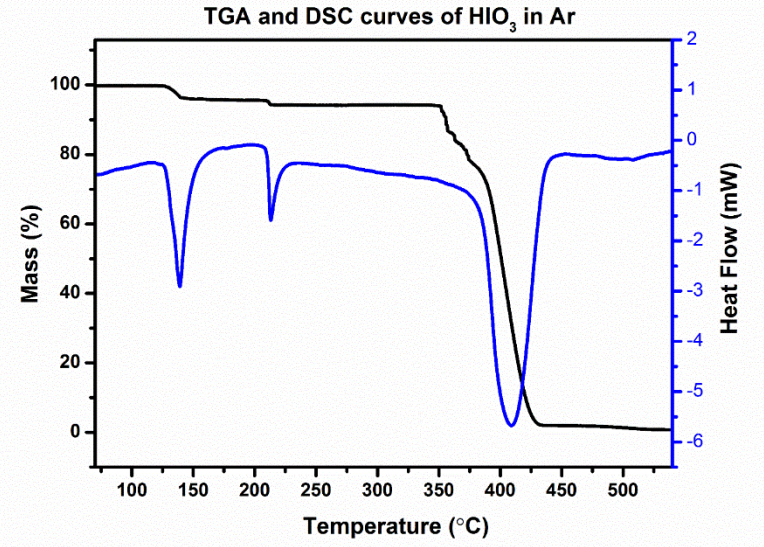

Figure S3.1. TGA and DSC curves of HIO_3 under argon environment at a heating rate of 5 ºC/min.

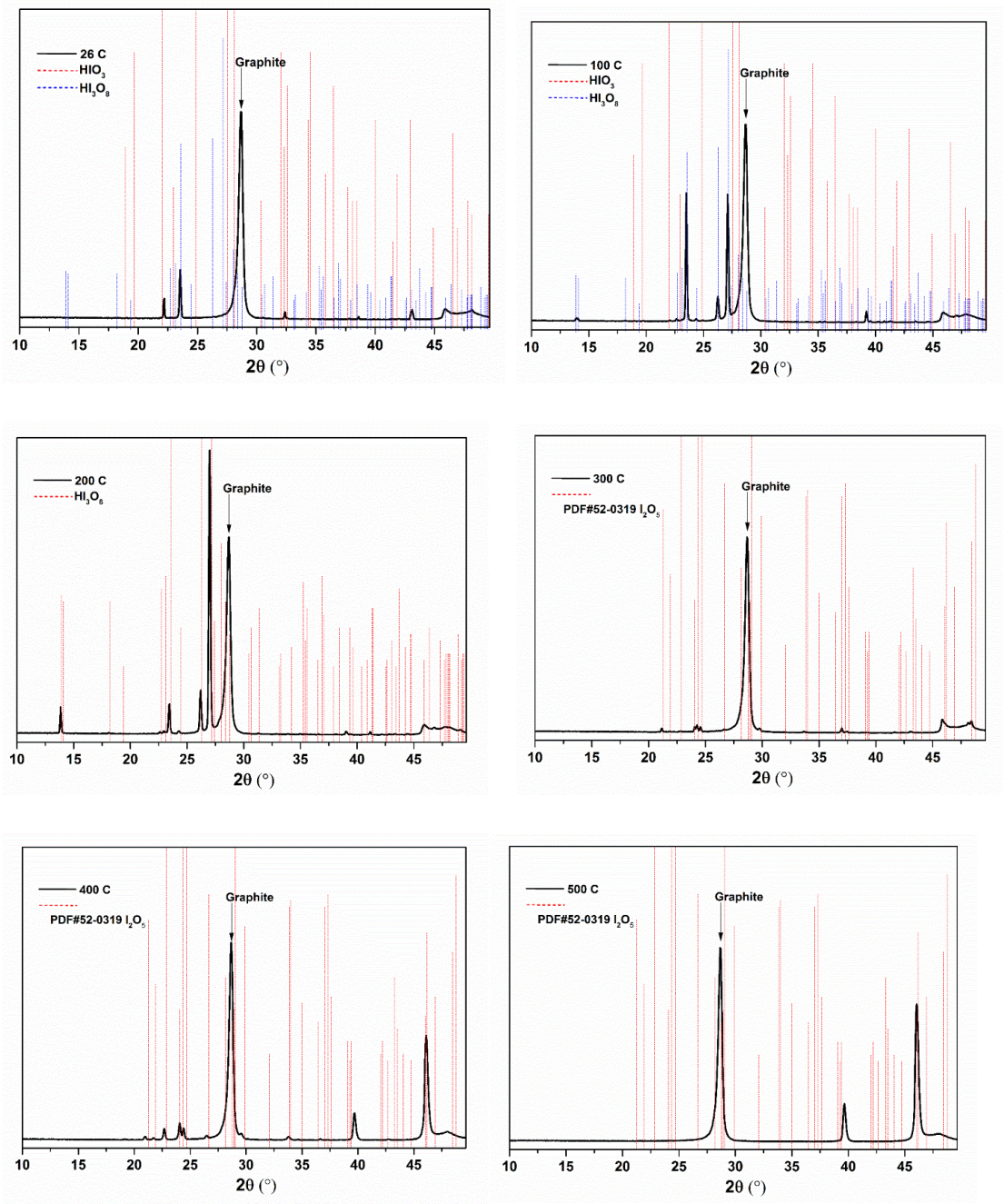

Figure S3.2. The XRD patterns of HIO_3 at different temperatures.

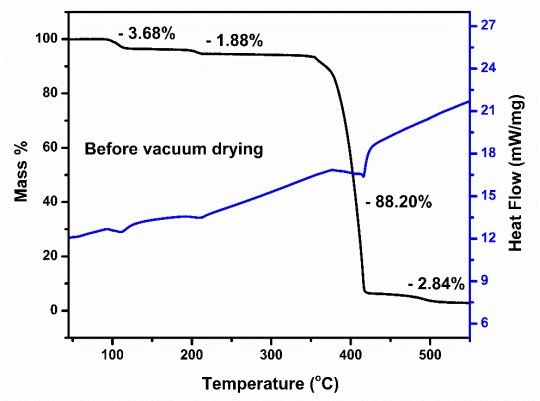

A

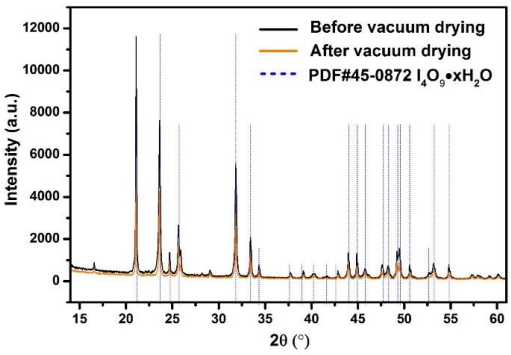

B

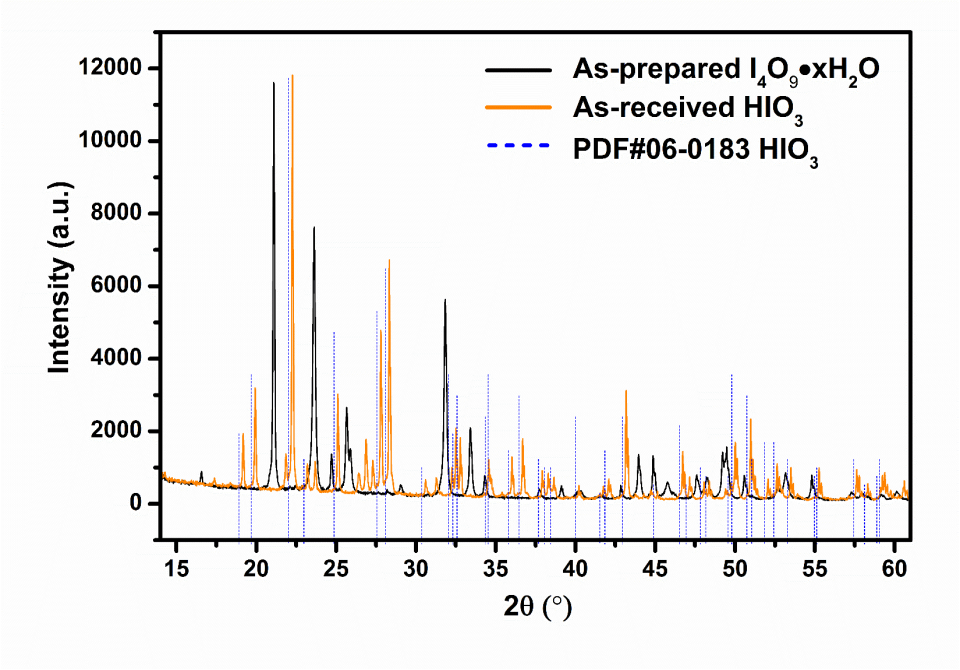

C

Figure S3.3. TGA/DSC (A) and XRD (B) of as-prepared I_4O_9• xH_2O before vacuum drying treatment and XRD (C) of as-prepared I_4O_9• xH_2O and as-received HIO_3.

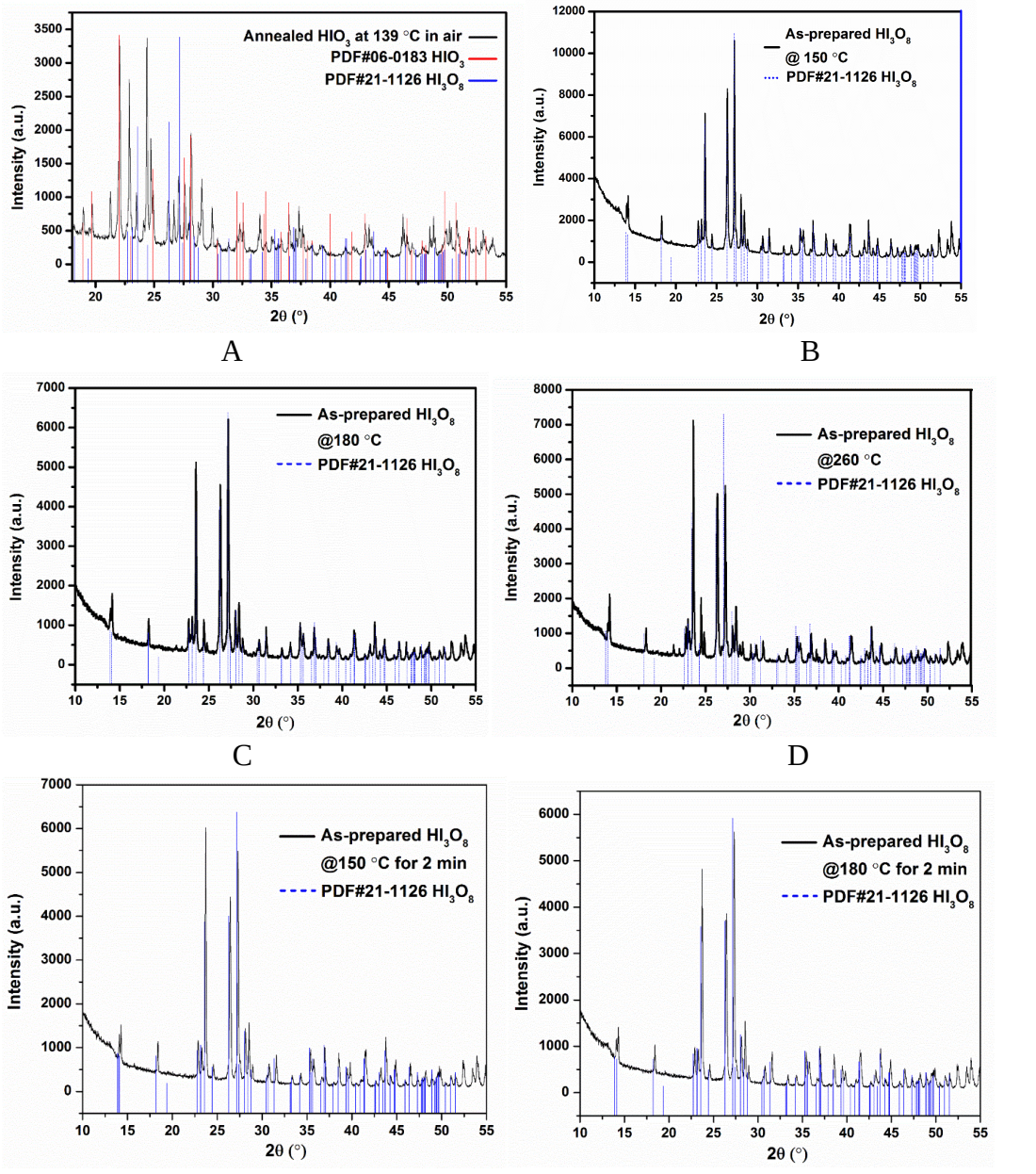

Figure S3.4. XRD patterns of the product by annealing of HIO_3 at 139 (A), 150 (B), 180 (C) and 260 °C (D) for one hour, respectively. XRD patterns of the product by annealing of HIO_3 at 150 (E) and 180 (F) for two minutes, respectively.

Table S3.1. Listed hkl values for each phase in each XRD pattern.

PDF#22-0338 I_2O_5		PDF#21-1126 HI_3O_8	
2θ (°)	**hkl values**	**2θ (°)**	**hkl values**
21.29	-111	22.72	112
1.87	-102	23.14	020
22.9	002	23.58	200
24.4	210	26.27	103
24.71	-211	27.16	-121
26.67	102	28.03	022
28.13	-112	35.26	123
28.77	-302	36.88	-222
28.96	012	43.71	321
29.06	211		
29.94	-212		
33.86	-312		
33.99	400		
35.02	-402		
37.04	212		
37.3	021		
38.5	410		

Chapter 4: Crystal structure of a new polymorph of iodic acid, δ-HIO_3.*

Overview

A new polymorph of iodic acid, δ-HIO_3, synthesized via aerosol spray pyrolysis was characterized with powder X-Ray diffraction and its crystal structure was solved. I find that a previously misidentified phase of I_4O_9 hydrate is in fact a new polymorph of HIO_3 which crystalizes in the orthorhombic space group $P2_12_12_1$.

4.1. Introduction

As one of the iodates (MIO_3, where M = H^+, NH^{4+}, alkali ions, etc), HIO_3 has been of interest due to its potential application as an optically non-linear material. [1-3] The crystal structure of α-phase of iodic acid was first reported in 1941 and crystalizes in the orthorhombic space group D_2^4-$P2_12_12_1$.[4] The structure is held together by hydrogen bonds and relatively weak intermolecular iodine oxygen bonds. More recently, neutron powder diffraction at various temperatures were able to more precisely determine the position of hydrogen atoms in the crystal structure.[1] Decreased inter-molecular distances and O-I-O angles of α-HIO_3 were observed with decreasing temperature. In 2005, a new metastable, centrosymmetric polymorph of iodic acid, γ-HIO_3, was obtained via reaction

* The results presented in this chapter have been published in the following journal article: Wu, T.; Zavalij, P.Y.; Zachariah, M.R., Crystal structure of a new polymorph of iodic acid, δ-HIO_3, from powder diffraction. Powder Diffraction 2017 32(4) 261-264.

between H_5IO_6 and $Cr(ClO_4)_3$ in aqueous solution, which crystalizes in the orthorhombic space group *Pbca*. This phase is stabilized by hydrogen-bonded $(HIO_3)_2$ dimers.[5]

Thermal decomposition of iodic acid in air can lead to I_2O_5 or HI_3O_8 depending on temperature.[6] Gas phase aerosol techniques offer a convenient route and potentially direct route for preparation of small particles with high purity, and is a method proven to be amenable and economical to scale-up.[7-10] In Chapter 3, I found a new polymorph of iodic acid could be obtained with silica-gels regenerated at ~50 ºC and the furnace temperature at ~210 ºC.[11] Here, its crystal structure is reported for the first time.

4.2. Experimental and structure determination

Iodic acid (α-HIO_3) (99.5 wt %) purchased from Sigma-Aldrich was directly used as received. All the other chemicals were of analytical grade and used as purchased without further treatment.

Small-sized particles of δ-HIO_3 were obtained via aerosol spray pyrolysis (ASP). In general, 100 mL iodic acid solution (10 mg/mL) were sprayed into small droplets (~1 um in diameter) with a homemade pressure atomizer (~35 psi pressure air) and pass through a silica-gel diffusion drier (silica-gels were regenerated at ~50 ºC) to remove most of the water, and are then passed through a tube furnace for chemical conversion. The tube reactor consisted of a ~ 1.9 cm diameter alumina tube with a heated length of ~40 cm. The furnace temperature was set at ~ 210 °C to obtain δ–HIO_3 with a residence time of about 1 second. I

find that δ-HIO_3 can be obtained within a large range of temperature from 180 to 250 °C. The final product was collected on a Millipore membrane filter (0.4 um pore) and characterized by powder X-ray diffraction (XRD, Bruker D8 Advance using Cu Kα radiation).

The as-prepared samples were characterized by powder X-ray diffraction. Diffraction pattern was measured using Cu Kα radiation in Bragg-Brentano geometry on Bruker D8 Advance powder diffractometer equipped with incident beam Soller slits, Ni β-filter and LynxEye position sensitive detector. Data were collected from 14º to 130º 2θ with a step size of 0.01578º and counting time of 1 sec per step (total exposure time of 180 sec per step).

The powder pattern was indexed in the orthorhombic crystal system and reflection conditions pointed to a $P2_12_12_1$ space group symmetry. This phase matched a previously reported for I_4O_9• xH_2O (PDF#00-045-0872) (Table 4.1). In this case "I_4O_9• xH_2O" was designated to refer to a crystal hydrate product of amorphous I_4O_9 according to the paper that published its XRD result.[12] However, the I_4O_9• xH_2O reference provides only composition and powder pattern and motivated our consideration of determining rigorously the crystal structure.

The crystal structure was solved from the integrated intensities obtained from a LeBail full pattern decomposition by a charge flipping method using an XT program from ShelX software.[13] The crystal structure (Figure 4.1) was refined by Rietveld method using the Topas software.[14] The refinement revealed a presence of preferred orientation with a March-Dollase parameter of 0.75(1).

Hydrogen atom was positioned from geometric considerations at the longest I-O bond along the shortest oxygen-oxygen contact line as it was observed in other structures of iodic acid. It was refined as riding on the attached O atom. Here I would like to acknowledge the help from Dr. Peter Zavalij on solving, refining and analyzing the crystal structure.

Table 4.1. X-Ray diffraction patterns for δ-HIO_3 and I_4O_9• xH_2O (PDF#00-045-0872).

	δ-HIO_3		I_4O_9• xH_2O	
$2\theta_{calc}$ (º)	d_{calc} (Å)[i]	I_{obs}[ii]	d_{obs} (Å)	I_{obs}[iii]
16.494	5.37	7		
21.022	4.222	100	4.19	m
23.534	3.777	66	3.75	s
24.642	3.61	11	3.59	vw
25.585	3.479	22		
25.818	3.448	13	3.46	m
28.982	3.078	4		
31.760	2.815	49	2.81	s
33.344	2.685	18	2.68	m
34.337	2.609	7	2.61	w
37.667	2.386	3	2.39	vw
39.039	2.305	4	2.31	vw
40.293	2.236	3	2.24	vw
42.797	2.111	4	2.12	vw
43.886	2.061	11	2.055	m
44.826	2.02	11	2.015	m
45.672	1.985	5	1.98	m
47.538	1.911	7	1.905	m
48.143	1.889	6	1.882	m
49.144	1.852	12	1.847	m
49.414	1.843	13	1.837	m
50.527	1.805	6	1.803	m
52.570	1.739	4	1.737	w
53.079	1.724	7	1.72	m
54.760	1.675	7	1.672	m

(i) d_{calc} – *d*-spacing calculated from lattice parameters obtained from Rietveld refinement.

(ii) Normalized observed integrated intensities as obtained from the Rietveld refinement.

(iii) Observed intensity denoted as m = medium, s = strong, vw = very weak, w = weak (Wikjord et al., 1980).

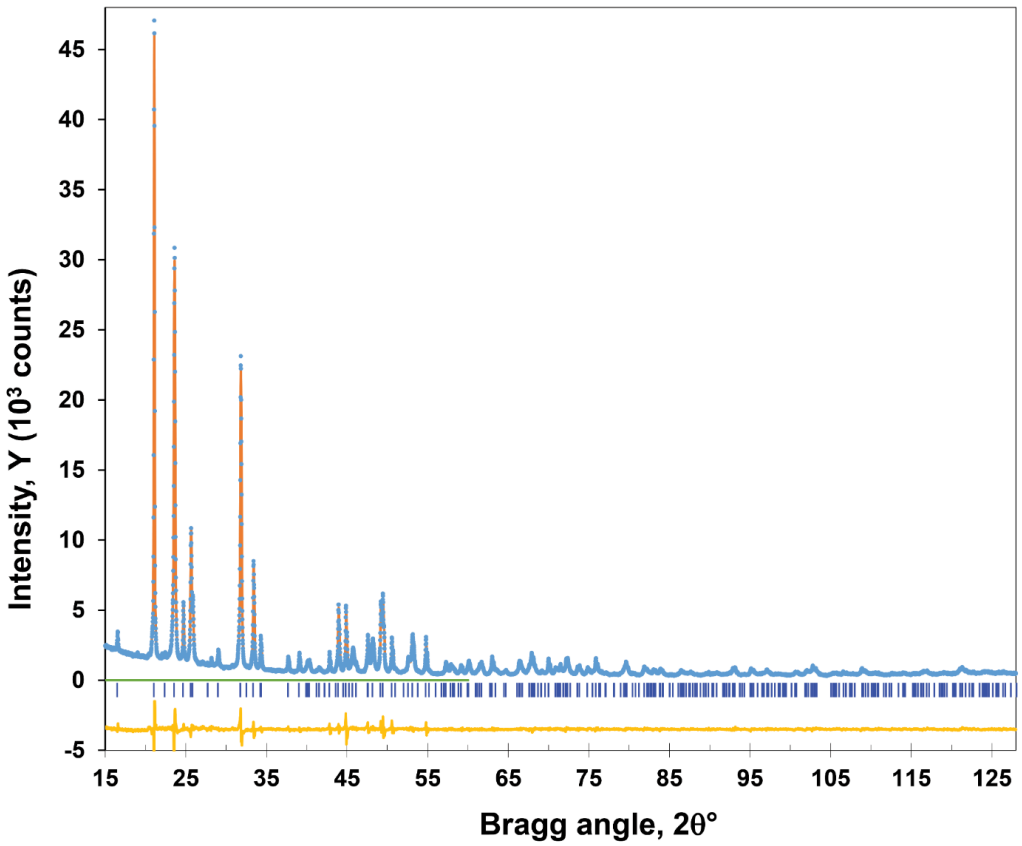

Figure 4.1. The Rietveld plot of δ-HIO_3 (Circles - experimental profile, solid line - calculated, their difference is shown at the bottom, vertical lines show reflection position).

4.3. Discussion

This crystal structure determination shows that the actual chemical composition of I_4O_9• xH_2O is HIO_3 which could also be written as I_4O_{10}•2H_2O. This new polymorphic modification of iodic acid is further referred as δ-HIO_3 (CCDC#1526763).

Details of the crystal structure determination are shown in Table 4.2. The atomic parameters are listed in Table 4.3. Selected interatomic distances and

bond angles of δ-HIO_3, α-HIO_3,[1] γ-HIO_3 [5] and HI_3O_8 [15] are shown in Table IV.

Table 4.2. Details of the crystal structure determination of δ-HIO_3.

Formula	HIO_3
Lattice constants, Å	a = 8.44504(13)
	b = 6.95785(13)
	c = 4.49753(10)
Cell volume, $Å^3$	264.272(9)
Density	4.421
Formula weight	175.91
Number of formula units	4
Crystal system, space group	Orthorhombic, $P2_12_12_1$
Temperature of measurement	Room temperature
Diffractometer	Bruker D8 Advance
Radiation, wavelength	Cu$K\alpha$ radiation, 1.5418 Å
Absorption coefficient, cm^{-1}	93.256
F000, electrons	312
Number of reflections	284
R values, %	R_{exp} = 3.09
	R_{wp} = 6.56
	R_p = 5.10
	R_{Bragg} = 1.22
Goodness of fit	2.122

Table 4.3. Atomic coordinates and isotropic displacement parameters (Å2) of δ-HIO_3.

Atom	Site	x/a	y/b	z/c	B_{iso}
I1	4a	0.27820(7)	0.23062(12)	0.0264(2)	0.79(5)
O1	4a	0.3414(16)	0.4389(14)	0.274(3)	0.62(13)
O2	4a	0.3542(15)	0.0372(16)	0.255(3)	0.62(13)
O3	4a	0.0873(7)	0.254(2)	0.1678(16)	0.62(13)
H1	4a	0.440511	0.444325	0.282977	0.92(19)

Delta-HIO_3 crystalizes in the orthorhombic space group $P2_12_12_1$. Figure 4.2(a-b) show the crystal structure of δ-HIO_3 with each iodine atom 3-coordinated with oxygen atoms (I1-O1 = 1.904, I1-O2 = 1.811, I1-O3 = 1.741), and all four atoms

form trigonal pyramid with iodine atoms in the apex and 3 oxygen atoms in the base. One of the I-O contacts of 2.49 A between molecules make spiral chain along the z direction (Figure 4.2(a)), and two more long I-O contacts of ~2.76 A bind the chains in x and y directions into a three-dimensional framework (Figure 4.2(b)). O1-H1...O2 hydrogen bond links HIO_3 molecules into a zig-zag chain along the y direction, which make it unique as compared with other two polymorphs of HIO_3. Two neighboring molecules are in a mirror position along with xy plane. Three I-O bonds and three I…O contacts together make a distorted octahedra.

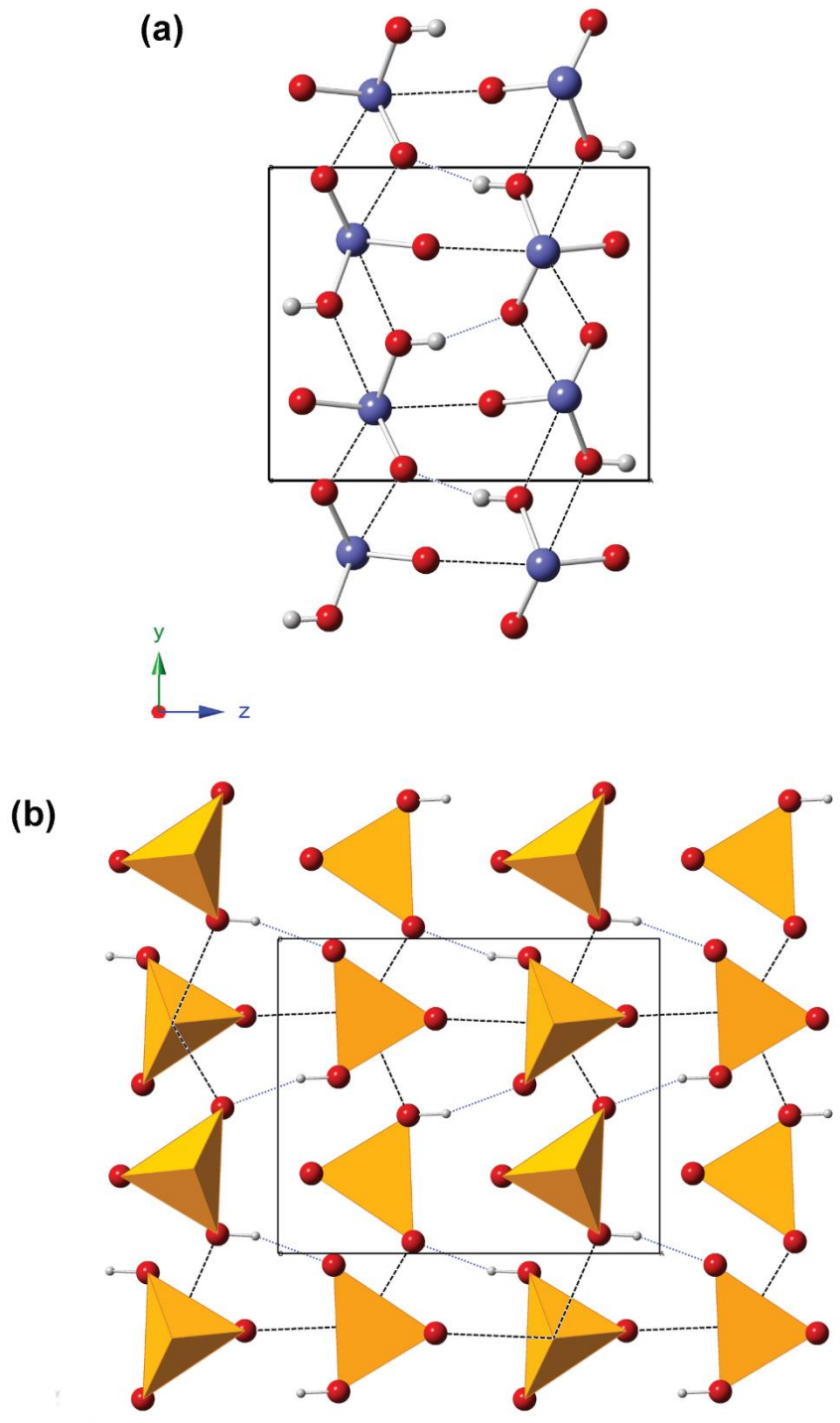

Figure 4.2. The structure of δ-HIO_3 showing: (a) a layer in ab plane with chains H-bonded along b axis and (b) corresponding polyhedral representation. Blue dotted lines show H…O contacts and dashed black lines show I…O contacts. Red, blue and grey balls represent oxygen, iodine and hydrogen atoms, respectively.

All 3 iodic acid structures α, γ, and δ differ by packing of the HIO_3 molecules and therefore by arrangement of their hydrogen bonds. In α-HIO_3, similarly δ-HIO_3 structure, hydrogen bonds link molecules into a zig-zag chains (Fig. 4.3(a). However in γ-HIO_3 hydrogen bonds form $(HIO_3)_2$ pair as shown in Fig. 3(b). Figure 4.3(c) shows that HI_3O_8 molecule is an adduct of both HIO_3 and I_2O_5 moieties that are connected by a hydrogen bond.[15] Interestingly, the hydrogen bond in δ-HIO_3 structure is similar in length to γ-HIO_3 molecule and both are slightly shorter than that of α-HIO_3 and HI_3O_8 structures.

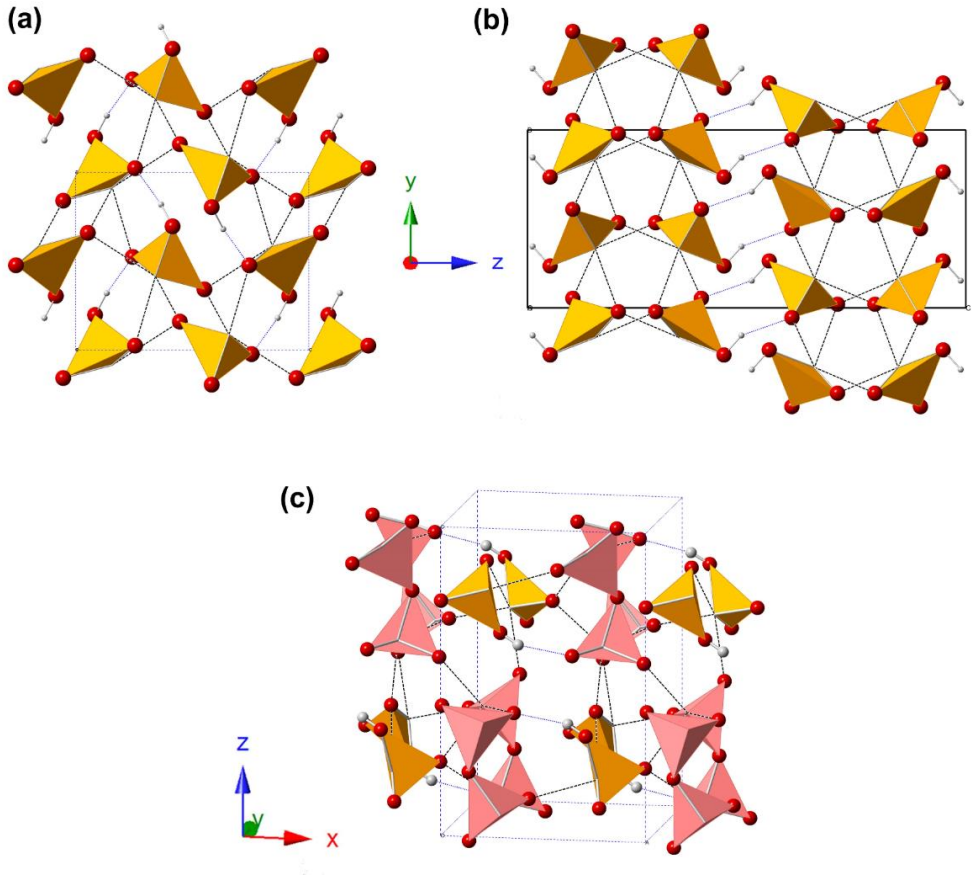

Figure 4.3. The polyhedral representation of (a) α-HIO_3, (b) γ-HIO_3 (both in zy plane) and (c) HI_3O_8 (in xz plane) structures. Blue dotted lines show H…O contacts and dashed black lines show I…O contacts. Red and grey balls represent oxygen and hydrogen atoms respectively. The pink and yellow pyramids in (c) represent I_2O_5 and HIO_3, respectively.

Each IO_3 pyramid forms 3 I…O intermolecular contacts in 2.5 to 3.1 Å range (Table 4.4) which along with 3 I-O bonds form a distorted octahedra. Each I…O contact is positioned across I-O bond so that O-I…O angle deviates from liner for not more than 17°. This is true for all HIO_3 structures as well as HIO_3 and I_2O_5 molecules in HI_3O_8 structure. There is also correlation, at least qualitatively, between length of I-O bonds and opposite I…O contact distances: the shorter bond corresponds to longer contact and vice versa.

Table 4.4. Selected interatomic distances (Å) and angles (º) δ-HIO_3 in comparison to corresponding geometries of similar compounds.

	Atom labels	δ-HIO_3 (this work)	α-HIO_3	γ-HIO_3	HI_3O_8 ($HIO_3 \cdot I_2O_5$)
Distances, Å	I1-O1	1.904(12)	1.896(2)	1.873(2)	1.880(3)
	I1-O2	1.811(12)	1.812(2)	1.791(2)	1.792(2)
	I1-O3	1.741(6)	1.783(1)	1.804(2)	1.790(3)
Valence angles, °	O1-I-O2	97.7(5)	97.63(7)	100.1(1)	93.73(12)
	O1-I-O3	88.6(6)	93.86(6)	96.4(1)	95.07(12)
	O2-I-O3	101.0(6)	100.92(7)	101.3(1)	99.16(13)
Contacts, Å	I1...O2^{i}	2.493(12)	2.504(2)	2.694(2)	2.545(2)
	I1...O1^{ii}	2.757(11)	2.760(2)	2.689(2)	2.593(3)
	I1...O3^{iii}	2.754(6)	2.889(1)	2.753(2)	3.123(3)
Contact angles, °	O1-I...O2^{i}	168.9(5)	174.47(7)	174.26(8)	176.39(11)
	O2-I...O1^{ii}	169.6(5)	166.49(6)	171.49(8)	177.44(11)
	O3-I...O3^{iii}	171.8(5)	163.28(7)	168.17(9)	163.16(9)
H bond length, Å	O1-H1...O2^{iv}	2.663(18)	2.718(2)	2.665(3)	2.744(4)

(i) 1/2-x,-y,-1/2+z; (ii) 1/2-x,1-y,-1/2+z; (iii) 1/2+x,1/2-y,-z; (iv) 1-x,1/2+y,1/2-z

4.4. Conclusion

A new polymorph of iodic acid, δ-HIO_3, which crystallizes in the orthorhombic space group $P2_12_12_1$, was obtained via a reproducible aerosol spray pyrolysis method using iodic acid solution as the precursor. *Ab initio* crystal structure determination of δ-phase reveals that previously known $I_4O_9.xH_2O$ phase is actually HIO_3.

4.5. Supplemental Information

Since the CIF file of δ-HIO_3 and the corresponding data for Figure 4.1 are too large to be included in this thesis, for those who are interested in these data could find them online with the link provided below.

https://www.cambridge.org/core/journals/powder-diffraction/article/crystal-structure-of-a-new-polymorph-of-iodic-acid-hio3-from-powder-diffraction/7E9176F241D23CB1246A9F905FC00930#fndtn-supplementary-materials

Chapter 5: Performance of iodine oxides/iodic acids as oxidizers in thermite system [*]

Overview

Iodine oxides are of interest as biocidal components in energetic application such as thermites due to their high energy release and biocidal agent delivery. In this study, various iodine oxides/iodic acids, including I_2O_5, HI_3O_8 and HIO_3, were employed as oxidizers in thermite systems. Their decomposition behaviors were studied using a home-made time resolved temperature-jump/time-of-flight mass spectrometer (T-Jump/TOFMS), which identified a single step decomposition for all oxides at high heating rates (~10^5 K/s). In addition, both nano-aluminum (nAl, ~80 nm) and nano-tantalum (nTa, <50 nm) were adopted as the fuel in order to fully understand how iodine containing oxidizers react with the fuel during ignition. The ignition and reaction process of nAl-based and nTa-based thermites were characterized with T-Jump/TOFMS, and their combustion properties were evaluated in a constant-volume combustion cell and compared to a traditional thermite system (nAl/CuO). The ignition temperatures of nAl-based thermites using these oxidizers were all very close to the melting point of aluminum (~660 ºC), which suggests that the mobility of the aluminum core dominats the ignition/reaction and the gaseous oxygen released from the decomposition of the oxidizer does not participate in the ignition until the molten aluminum is available. Unlike nAl-based thermites, the ignition temperatures of nTa-

[*] The results presented in this chapter have been published in the following journal article: Wu, T.; Wang, X.; Zavalij, P.Y.; DeLisio, J.B.; Zachariah, M.R., Performance of iodine oxides/iodic acids as oxidizers in thermite systems. Combustion and Flame 2018 191 335-342.

based thermites are lower than the oxygen release temperatures from the corresponding bare oxidizers. All nTa-based thermites ignited prior to the release of gas phase oxygen. In this case, a condensed phase reaction mechanism is proposed to dominate the ignition process. Moreover, combustion cell tests results show that nAl/*a*-HI_3O_8 has the highest pressurization rate and peak pressure and shortest burn time, and since it also has an iodine content of ~75% as high as I_2O_5 on a per mass basis, this material may be a very promising candidate in biocidal application.

5.1 Introduction

High efficiency neutralization of biological warfare agents has become a major research focus within the United States, in addition to many other countries, due to the increased threat of bioterrorism [1-7]. Preliminary laboratory studies have suggested that an ideal neutralization process should contain not only a high thermal but also long-lasting biocidal agent release [8-14]. The main problem with conventional energetic materials is low neutralization efficiency since a thermal neutralization mechanism is dominant in this case [8]. Therefore, it has been proposed that simultaneously delivering a rapid thermal pulse with a remnant biocidal agent would prolong the exposure time and improve the inactivation process [15]. Halogens-based energetic materials show the most promise because of their excellent biocidal properties [16] when compared to silver-containing energetic materials [17-19]. To incorporate halogens in energetic materials, one can either directly add halogens into the system or assemble halogens into the oxidizers [16, 20]. Wang et al. incorporated iodine molecules into Al/CuO thermite systems and found that the Al/CuO/I_2 thermite reaction

rate was significantly decreased with increasing the iodine content [21]. Guerreo et al also showed that mechanical incorporation of iodine into aluminum severely decreases the reaction rate of Al/metal oxides mixtures and even resulted in failed ignition of Al•I_2/Fe_2O_3 [22]. In addition, Dreizin et al employed mechanically alloyed aluminum-iodine composites as a replacement of aluminum as a fuel additive in energetic formulations and the ignition and combustion tests of those fuels in air indicated that higher iodine concentration lowers ignition temperatures but did not affect the combustion temperatures substantially [14]. They also found improvements in terms of pressurization rate and maximum pressure at constant volume with 15 wt.% and 20 wt.% of I_2 [14]. Furthermore, an effective inactivation of aerosolized spores was achieved using Al/I_2 and Al/B/I_2 composites with 15-20 wt.% of iodine [16].

Another approach is to use iodine-containing oxy-compounds that can release HI or I_2 when used as an oxidizer [23]. Iodine-containing oxy-compounds can be broken down into two main categories: metal iodates and iodine oxides/iodic acids. The metal iodates, $AgIO_3$ [8, 24], $Bi(IO_3)_3$ [25], $Cu(IO_3)_2$ [15], $Fe(IO_3)_3$ [15] etc., have been previously investigated. One issue with employing metal iodates in thermites is that part of the produced I_2 vapor (all for $AgIO_3$) may react with the product metal particles to form corresponding metal iodides, which lowers the effective iodine content in the metal iodate-based thermite systems. Unfortunately, there are only a limited number of iodine oxides/iodic acids which are relatively stable and obtainable. These include I_2O_5, I_4O_9, HI_3O_8, HIO_3, H_5IO_6, etc [26-28]. Among these compounds, I_2O_5 (~76% iodine mass fraction), is the most studied in thermite systems [29-33]. In these studies, aluminum particles with different sizes were chosen as the fuel due to its high reaction

enthalpy, thermal conductivity and availability. With reported propagation velocities of up to ~2,000 m/s for loose ball-milled nAl and nano-scaled I_2O_5 (~10 nm) [32], I_2O_5 shows its high potential in aluminum-based thermites as an extremely aggressive oxidizer. Constant volume combustion tests also show nAl/micro-I_2O_5 outperforms traditional aluminum-based thermites such as Al/CuO and Al/Fe_2O_3 [33]. A pre-ignition reaction was proposed as the ignition trigger in which ionic I_2O_5 fragments diffused into the alumina passivation shell of aluminum and to create some reactive complexes exothermically [31,34]. However, this mechanism is far from clear as Smith et al reported that a pre-ignition reaction was not found for aluminum/nano crystalline I_2O_5 reaction in contrast to nano amorphous I_2O_5 case [35].

Recently, Smith et al reported that a minimum of 150% increase in flame speed was found for Al/amorphous I_4O_9 compared with Al/I_2O_5 indicating I_4O_9 has more reactive potential than I_2O_5 as an oxidizer when combined with aluminum [36]. Other iodine-containing oxy-compounds have received comparatively much less attention due to their relatively lower iodine content and availability. Nevertheless, their iodine content is still much higher than metal iodates or per-iodates on a per mass basis. This is particularly so for HI_3O_8, which has an iodine content of ~75% and very close to the 76% for I_2O_5. Currently no comparative study examining how the aforementioned iodine oxides/iodic acids perform as oxidizers in thermites system is available. Moreover, we have recently reported that iodine oxides/iodic acids with different particles' sizes can be prepared via either aerosol spray pyrolysis (ASP) or thermal treatment [37,38], making a variety of these materials readily available.

Most of the focus on reactive studies of oxidizers has focused on Aluminum as the fuel. Aluminum has a passivating alumina shell that stabilized the material at ambient conditions. However once the aluminum core reaches near the melting temperature, it can diffuse through the oxide shell and interact with any available oxidizer leading to ignition [39]. To explore the fuel melting aspect of ignition, we also explore in the paper tantalum as a fuel because it has a melting point of ~3000 ºC, and thus would not be melted at the point of ignition.

In this paper, I examine the performance of various iodine oxides/iodic acids (I_2O_5, HI_3O_8 and HIO_3) as oxidizers in nAl-based and nTa-based thermites system. Iodine-containing oxides/acids were prepared via an ASP method following procedures in our previous work [37]. Time-resolved temperature-jump time-of-flight mass spectrometer (T-Jump/TOFMS) was used to study the ignition and decomposition of nAl-based and nTa-based thermites. A high-speed camera simultaneously captured optical emission from the ignition/reaction of the thermites allowing for the ignition time, and corresponding ignition temperature. In addition, constant volume combustion cell tests were performed on aluminum-based thermites.

5.2. Experimental Details

5.2.1. Materials

The aluminum nanopowders (nAl) (Alex, ~80 nm) were purchased from Novacentrix. The active Al was 81 % by mass, determined by TGA. Nano-tantalum powders (nTa, <50 nm) were purchased from Global Advanced Metals, with 70% of the mass. Iodic acid (*c*-HIO_3) (99.5 wt %), Iodine Pantoxide (*c*-I_2O_5), CuO

nanoparticles (*n*-CuO, <50 nm) and micro-sized CuO powders (m-CuO) purchased from Sigma-Aldrich were directly used as received ("*c*" represents commercial product; "*n*" and "*m*" represents nano-scaled and micro-scaled sizes, respectively). All other chemicals were of analytical grade and were used as purchased without further treatment.

5.2.2. Preparation of iodine oxides/iodic acids particles

Small-sized (<1 μm) particles of oxides includes *δ*-HIO_3, *a*-HI_3O_8 and *a*-I_2O_5 were synthesized via aerosol spray pyrolysis (ASP). Here, "*a*" represents ASP and "*δ*" refers to HIO_3 with a delta phase. Detailed information on the ASP synthesis method has been previously described [37]. Briefly, 100 mL iodic acid solution (10 mg/mL) were aerosolized (~1 um in diameter) with a homemade pressure atomizer (~35 psi pressure air) and passed through a silica-gel diffusion drier to remove water. The dry particles are then passed through a tube furnace for chemical conversion. The furnace temperature was set at ~230 and ~375 °C to obtain either δ-HIO_3 or a-I_2O_5, respectively with a residence time of about 1 second. For both δ-HIO_3 and a-I_2O_5, silica-gels were regenerated at 50 °C. I find that δ-HIO_3 can be obtained within a large range of temperature from 210 to 250 °C. In addition, a-HI_3O_8 was obtained with a tube furnace temperature ~250 °C with a silica-gel regeneration temperature of ~80 °C. The final product was collected on a Millipore membrane filter (0.4 um pore). HI_3O_8 was also prepared via thermal treatment of commercial HIO_3 at ~180 ºC and labeled as *t*-HI_3O_8. The final product was characterized by scanning electron microscopy (SEM, Hitachi, SU-70 FEG-SEM) and powder X-ray diffraction (XRD, Bruker D8 Advance using Cu Kα radiation).

5.2.3. Preparation of thermites

Physically mixed stoichiometric mixtures of nAl and nTa with δ-HIO_3, *c*-HIO_3, *a*-HI_3O_8, *t*-HI_3O_8, *a*-I_2O_5, *c*-I_2O_5, and CuO were based on the following equations. The mixtures were sonicated in dry hexane for 30 minutes and left uncapped at room temperature in a low-pressure desiccator to evaporate the solvent. All of the samples employed in this work were stored in a sealed desiccator for future use. Below we list the stoichiometric relations used to prepare the mixture ratios and the associated enthalpy of reactions.

$4Al + 2HIO_3 \rightarrow I_2 + 2Al_2O_3 + H_2$, $\Delta H_{theoretical}$ = -2413 KJ/mol

$32Al + 6HI_3O_8 \rightarrow 9I_2 + 16Al_2O_3 + 3H_2$, $\Delta H_{theoretical}$ = -20721 KJ/mol

$10Al + 3I_2O_5 \rightarrow 3I_2 + 5Al_2O_3$, $\Delta H_{theoretical}$ = -6740 KJ/mol

$2Al + 3CuO \rightarrow 3Cu + Al_2O_3$, $\Delta H_{theoretical}$ = -1109 KJ/mol

$12Ta + 10HIO_3 \rightarrow 5I_2 + 6Ta_2O_5 + 5H_2$, $\Delta H_{theoretical}$ = -9059 KJ/mol

$32Ta + 10HI_3O_8 \rightarrow 15I_2 + 16Ta_2O_5 + 5H_2$, $\Delta H_{theoretical}$ = -26515 KJ/mol

$2Ta + I_2O_5 \rightarrow I_2 + Ta_2O_5$, $\Delta H_{theoretical}$ = -1745 KJ/mol

5.2.4. X-Ray Diffraction (XRD) measurement and Rietveld refinement

The as-prepared samples were characterized by powder X-ray diffraction. Diffraction pattern was measured using Cu Kα radiation in Bragg-Brentano geometry on Bruker D8 Advance powder diffractometer equipped with incident beam Soller slits, Ni β-filter and LynxEye position sensitive detector. Data were collected from 10º to 90º 2θ with a step size of 0.01578º and counting time of 1 sec per step (total exposure time of 180 sec per step). The crystal structures were refined by Rietveld method using

the Topas software [38]. Here I would like to acknowledge the help from Dr. Peter Zavalij on refining and determining the crystal information of different thermites.

5.2.5. T-Jump/TOFMS measurement and high-speed imaging

The decomposition of each oxide listed above was investigated using T-Jump/TOFMS [8]. Typically, a ~1 cm long platinum wire (76 um in width) with a thin coating of oxidizer sample was rapidly joule-heated to about 1200 °C by a 3 ms pulse at a heating rate of ~10^5 °C/s. The current and voltage signals were recorded, and the temporal temperature of the wire was determined using the Callendar–Van Dusen equation [40]. Spectra were collected at 0.1 ms intervals. The detailed experimental set-up has been previously described [8, 40].

In order to experimentally determine the ignition temperature for each thermite, a high-speed camera (Vision Research Phantom v12.0) was used to record the optical emission from combustion on the wire during heating. Ignition temperatures of thermite reactions in vacuum were measured from the correlation of optical emission from high speed imaging and temporal temperature of the wire and were further analyzed in combination with the temporal mass spectra. Each experiment was repeated 3 times.

5.2.6. Combustion Cell Test

Combustion properties of themites were evaluated in a constant-volume combustion cell, with simultaneous pressure and optical emission measurements. In this study, 25 mg of thermite powders was loaded inside the cell (constant volume, ~13 cm^3) and ignited by a resistively heated nichrome wire. The temporal pressure and optical

emission from the thermite reaction were measured using a piezoelectric pressure sensor and a photodetector, respectively. More detailed information on the combustion cell test can be found in our previous publications [8, 40]. Each experiment was repeated at least 3 times.

5.3. Results and Discussion

Various iodine oxides/iodic acids were prepared via ASP using a previously described synthesis method [37]. All of the as-prepared iodine-containing oxides including *a*-I_2O_5, *δ*-HIO_3 and *a*-HI_3O_8 have an average particle size of about 1 μm with a relatively wide size distribution [37]. SEM images, XRD patterns and TGA/DSC results are presented in Chapter 3 and 4 [37, 38]. Commercial I_2O_5 and HIO_3 (labeled as *c*-I_2O_5 and *c*-HIO_3) and *t*-HI_3O_8 prepared via thermal treatment of c-HIO_3 were employed as comparisons. The average particle size of *c*-I_2O_5 and *c*-HIO_3 are ~30 μm and *t*-HI_3O_8 particles have an average size ~4 μm (Figure S5.1). To verify the actual compositions of *c*-I_2O_5, *c*-HIO_3 and *t*-HI_3O_8, XRD and TGA results shown in Figure S5.2 and Figure S5.3 indicate that *c*-HIO_3 is pure HIO_3, *c*-I_2O_5 has mostly hydrated (~80%) to HI_3O_8 and t-HI_3O_8 is pure HI_3O_8. As control experiments, nano-sized (< 50nm) and micro-sized (<5 μm) CuO were also included in this work.

T-Jump/TOFMS (3 ms, heating rate ~5×10^5 °C /s) was employed to study the initial events of bare oxides or thermites under rapid heating rates, enabling us to probe the reaction process on a time scale close to that of a combustion event. Figure 5.1A, shows the temporal evolution of elemental iodine and O_2 from *a*-HI_3O_8 during rapid heating. Iodine and O_2 are released at approximately the same temperature (~475 ºC) indicating that it could be a good candidate for a molecular iodine-releasing oxidizer. The single

peak in the species vs. time plots of both Iodine and O_2 suggests that a one-step decomposition of *a*-HI_3O_8.

To further explore its decomposition, time-resolved mass spectra from rapid heating of *a*-HI_3O_8 at 0.8-1.5 ms are shown in Figure 5.1B. For mass spectra taken at t<1.1 ms (before the decomposition of the oxidizer), H_2O^+ (m/z 18), OH^+ (m/z 17) and N_2^+ (m/z 28) are attributed to the background. Above the decomposition temperature (>1.2 ms), O_2^+ and I^+ are detected in addition to IO^+, IO_2^+, I_2^+, and I_2O^+. The appearance of these species implies that the high heating rate decomposition pathway does not go directly to the thermodynamic end product of molecular iodine and oxygen under the conditions of this experimental setup. The temporal profile of those oxygen-containing species is shown in Figure S5.4 in which O_2^+ has the highest signal intensity. All other iodine oxides/iodic acids have similar time-resolved mass spectra as depicted in Figure S5.5.

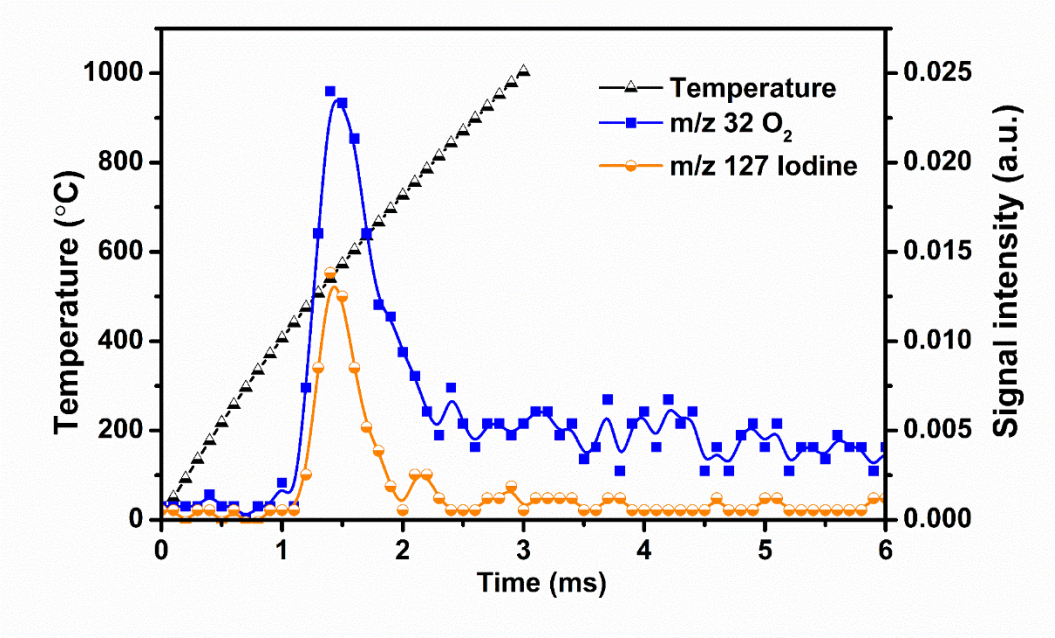

(A)

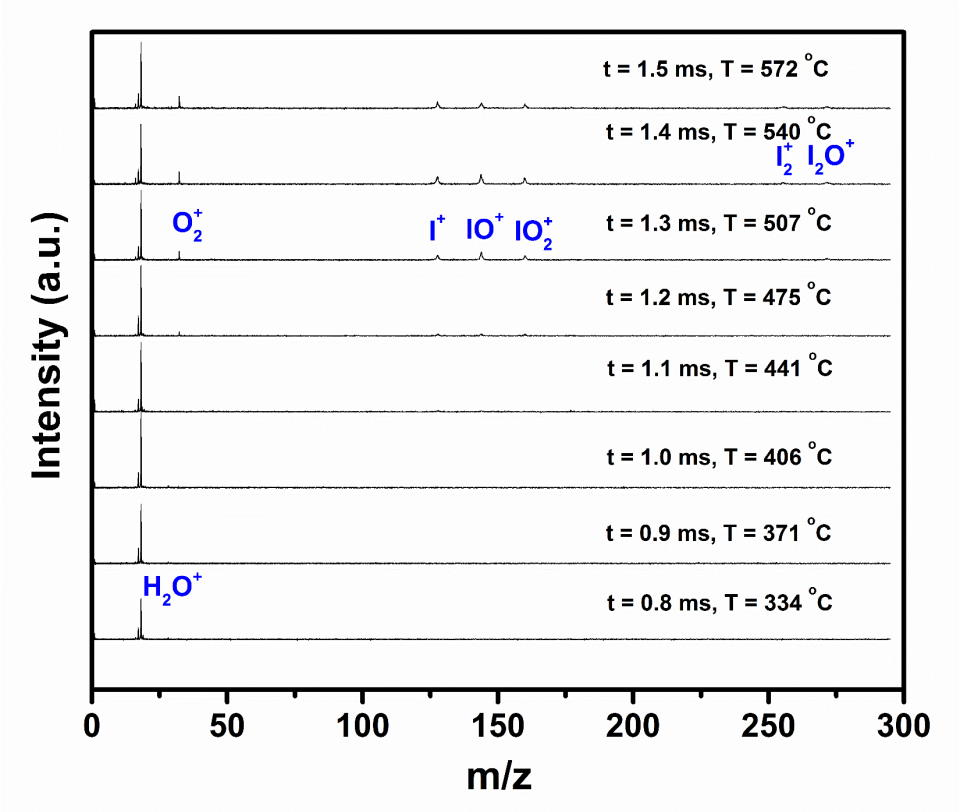

(B)

Figure 5.1. Representative plot showing the temporal profile of oxygen and iodine upon heating a-HI_3O_8 when heated at ~5×10^5 ºC/s (A); time-resolved mass spectra of a-HI_3O_8 (B).

To evaluate the performance of the iodine oxides/iodic acids as oxidizers in thermite systems, physical mixtures with nAl were made with 30 minutes sonication of nAl and iodine oxides/iodic acids in dry hexane. To indicate whether the mixing process has any influence on iodine oxides/iodic acids, XRD and TGA were performed and results of iodine oxides/iodic acids before and after mixing shown in Figure S5.6 and Figure S5.7. To be more specific about the exact compositions of each sample in Figure S5.6, Rietveld refinement was run for all the XRD patterns and the results are shown in Table 5.1. Almost for all the samples except for c-I_2O_5, a small portion of the original compounds either changed to another phase or dehydrated. As the most hygroscopic one among those samples, a-I_2O_5 made the most changes (~25% dehydrate into δ-HIO_3). Due to the sensitivities of those iodine-containing compounds to water, those minor changes could be resulted from preparation, characterization and/or handling. In addition, the TGA results shown in Figure S5.7 show no discernable effect of the thermite preparation process on the hydration state of the iodine oxides/iodic acids. As an example, the SEM images of a-HI_3O_8 and Al/a-HI_3O_8 shown in Figure S5.8 further indicate that the mixing procedure does not influence the particle size or morphologies of the iodine oxides/iodic acids.

Table 5.1. Crystalline compositions of all the samples employed in Figure S6 determined by Rietveld refinement of the corresponding XRD pattern[a].

Samples	Crystalline Phases	Samples	Crystalline Phases [b]
a-HI_3O_8	91% HI_3O_8 [c] 9% δ-HIO_3 [d]	Al/a-HI_3O_8	89% HI_3O_8 11% δ-HIO_3
t-HI_3O_8	100% HI_3O_8	Al/t-HI_3O_8	87% HI_3O_8 13% δ-HIO_3
δ-HIO_3	100% δ-HIO_3	Al/δ-HIO_3	88% δ-HIO_3 12% α-HIO_3 [e]
c-HIO_3	89% α-HIO_3 11% HI_3O_8	Al/c-HIO_3	75% α-HIO_3 25% HI_3O_8
a-I_2O_5	91% I_2O_5 [f] 9% δ-HIO_3	Al/a-I_2O_5	68% I_2O_5 32% δ-HIO_3
c-I_2O_5	100% HI_3O_8	Al/c-I_2O_5	100% HI_3O_8

[a]: *detailed results of Rietveld refinement are included in electronic supporting information as an appendix.*
[b]: *aluminum signal was found in all Al-based samples and its composition ratio is excluded here for comparison purpose.*
[c]: *PDF# 01-075-3387 HI_3O_8 [27]*
[d]: *XRD information of δ-HIO_3 could be found in [38]*
[e]: *PDF #01-079-1633 HIO_3 [41]*
[f]: *PDF #01-082-2225 I_2O_5 [42]*

Figure S5.9 shows some selected temporal snapshots of the Al/*a*-HI_3O_8 thermite reaction under vacuum of the T-jump/TOFMS chamber. Optical emission from reaction was first observed at 1.65 ms, corresponding to a wire temperature of ~664 ºC, indicating ignition of nAl/*a*-HI_3O_8 thermite. Overall, the optical emission of nAl/*a*-HI_3O_8 is not very strong [39] which suggests lower heat generation from the nAl-based thermite [43]. These snapshots also provide an alternative method to roughly determine burn time, calculated to be ~1.2 ms, and will be discussed more in the combustion test results.

From the T-jump TOFMS results, I found that the bare *a*-HI_3O_8 releases oxygen at ~475 ºC when heated at ~5×10^5 ºC/s. Under the same heating condition, the nAl/*a*-HI_3O_8 thermite showed oxygen appearance at ~575 ºC and thus 100 ºC higher than the

oxygen release temperature of the bare oxidizer (Figure 5.2A). This result is quite different from the most of Al/metal oxides thermites where oxygen release from the metal oxide is not influenced by the presence of aluminum fuel [44]. One exception I know of is Al/Bi_2O_3, which releases oxygen at a temperature that is 700 ^oC lower than that of the bare Bi_2O_3 [45]. This effect is the opposite of $nAl/a\text{-}HI_3O_8$. In this case, the interaction between the iodine ions of $a\text{-}HI_3O_8$ and the alumina shell of the fuel might form stable alumino-oxy-halides that delay the decomposition of the oxide [31, 46].

Even though the oxygen release temperature from $nAl/a\text{-}HI_3O_8$ thermite increased in comparison to the neat oxide, it is still lower than its ignition temperature (~664 ^oC). In fact, it is sufficient close to aluminum melting point to reasonable argue that aluminum mobility into aluminum oxide is the initiation process. Clearly gaseous oxygen release from $a\text{-}HI_3O_8$ at ~575 ^oC did not initiate ignition. [47]. In fact, Al/Bi_2O_3, Al/SnO_2, $Al/AgIO_3$, Al/CuO and $Al/KClO_4$ also ignited in vacuum at about the melting temperature of aluminum no matter what the oxygen release temperature is [44]. In addition, the ignition temperature of $nAl/a\text{-}HI_3O_8$ thermite in Ar environment with a 1 atm pressure was also obtained and it was decreased ~30 ^oC compared with that in vacuum. Considering the experimental uncertainty of $\pm$50 ^oC, it is reasonable to say that the ignition temperatures of $nAl/a\text{-}HI_3O_8$ in vacuum and 1 atm Ar are roughly the same, which again implies the importance of the melting phase transition of aluminum fuel.

If I consider Al/Co_3O_4, which has an ignition temperature of ~1095 ^oC, and is higher than its oxygen release temperature and the melting point of aluminum [44]. In this case, the generated gas phase oxygen also has no correlation with its ignition. However,

the nAl/*a*-HI_3O_8 ignited right after the aluminum melted. My group members have previously investigated the ignition of nAl in an oxygen environment and found that the ignition temperature decreased with increasing O_2 pressure and dropped below the melting point of bulk aluminum at >7.4 atm [47]. Why then does nAl/*a*-HI_3O_8 thermite ignite at the melting point of aluminum? Obviously, the partial pressure of O_2 during the ignition of nAl/*a*-HI_3O_8 thermite under vacuum is much lower than 7.4 atm. It has been shown in prior work that the oxygen concentration in solid oxidizers (7×10^4 mol/m^3) is much higher than that in gas (100 mol/ m^3 for 18 atm O_2 gas) [47]. Thus, in vacuum, the oxygen pressure around the fuel is likely very high. This is also supported by the combustion cell tests where a high pressurization rate is observed after ignition. Moreover, the local gas phase oxygen released from the oxidizer has a much higher temperature than the free O_2 in the pressurized ignition temperature tests described above. Both factors suggest that the gas phase oxygen from the oxidizer might also play a role in the ignition of thermites.

Time-resolved mass spectra taken at 0.1 ms intervals from a nAl/*a*-HI_3O_8 thermite reaction is shown in Figure 5.2A. As I expected,O_2^+, I^+ and I_2^+ peaks were first observed at a time of about 1.3 ms (~536 ºC), which is prior to ignition, and earlier than IO^+ and IO_2^+ species appeared. At the ignition temperature, IO^+ and IO_2^+ concentration also diminished, which implies that those intermediate iodine sub-oxide species also took part in the aluminum combustion [33].

Reactions between solids are by their nature limited by the movement of component reactive species or fragments. To further investigate the role of these oxidizers in the thermite reaction, a fuel was chosen that unlike aluminum would be immobile at least

at the point of ignition. Aluminum was replaced with tantalum as a means to potentially tweeze out the relationship between iodine and oxygen release with ignition. Similar to aluminum, tantalum also has a native oxide shell (Ta_2O_5). However, tantalum has a very high melting point of about 3017 ºC, which rules out the influence of the melting phase transition in the scope of ignition temperature test, which reaches a maximum wire temperature of ~1200 ºC. Sequential snapshots of the nTa/*a*-HI_3O_8 thermite reaction during rapid heating under vacuum were captured using a high speed camera and are shown in Figure 5.3. In contrast to nAl/*a*-HI_3O_8, the nTa/*a*-HI_3O_8 reaction is surprisingly much more vigorous with strong light emission. The images in Figure 5.3 also show that multiple ignition points appeared after ignition and propagate toward each other to ignite the whole thermite. The burn time of nTa/*a*-HI_3O_8 is roughly 1.7 ms, which is longer than that of nAl/*a*-HI_3O_8. In addition, time-resolved mass spectra of the nTa/*a*-HI_3O_8 thermite reaction (Figure 5.2B) shows that its oxygen and iodine release temperatures are ~450 ºC, which is very close to those of neat *a*-HI_3O_8 (~475 ºC). However, nTa/*a*-HI_3O_8 thermite ignited at ~400 ºC (0.96 ms) prior to the oxygen release from the bare oxidizer (~475 ºC) and Figure 5.2B also shows neither oxygen gas nor elemental iodine are detected before the ignition, which suggests a condensed phase reaction mechanism was dominant. While, considering that T-jump/TOFMS has a temperature measurement uncertainty of about ±50 ºC [44], it would be also possible that a very small amount of the oxidizer starts decomposing around the ignition temperature that ignites the thermite. As to the condensed phase mechanism, it has been found that cracks on in the oxide shell are formed when tantalum is rapidly heated to

above 500 ºC due to the amorphous to crystalline phase change of the oxide shell [48]. However, the ignition of nTa/*a*-HI_3O_8 occurs ~100 ºC earlier than this phase change.

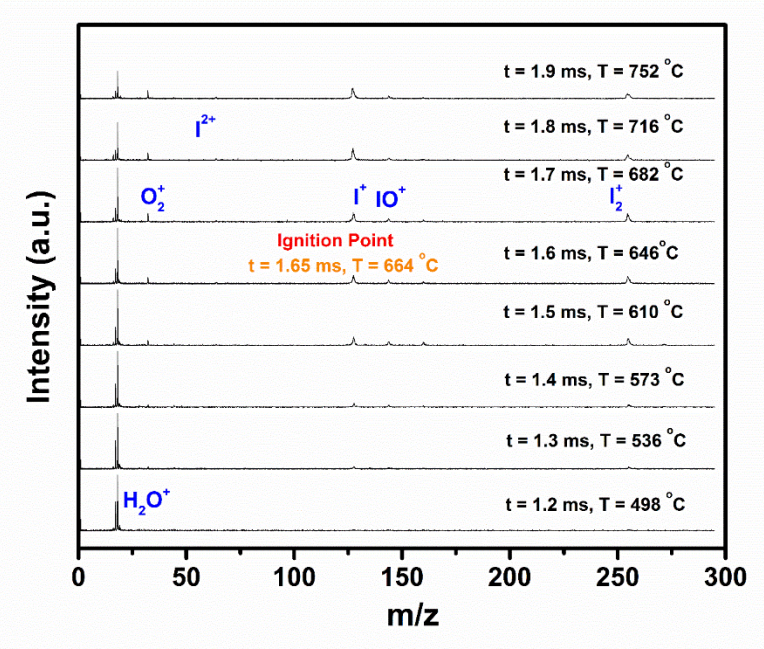

(A)

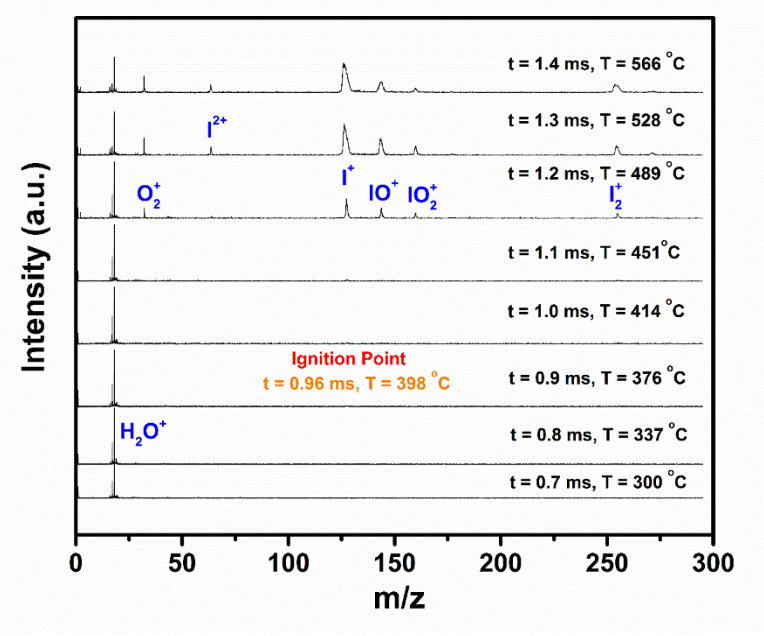

(B)

Figure 5.2. Time-resolved mass spectra of nAl/a-HI_3O_8 (A) and nTa/a-HI_3O_8 (B).

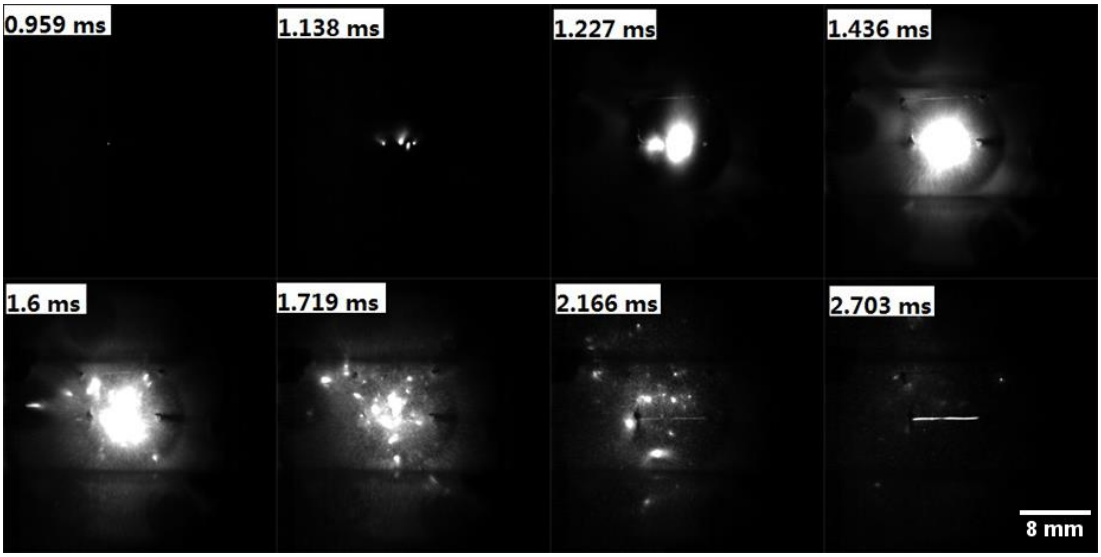

Figure 5.3. Sequential snapshots of nTa/a-HI_3O_8 thermite burning on a high rate heating (5×10^5 $^oC/s$) Pt wire under vacuum, captured by a high-speed camera. The labels in each image are the time elapsed after triggering.

The performance of all the iodine oxides/iodic acids (δ-HIO_3, *c*-HIO_3, *a*-HI_3O_8, *t*-HI_3O_8, *a*-I_2O_5 and *c*-I_2O_5) as an oxidizer using nAl or nTa as the fuel are summarized in the following figures. Figure 5.4 shows the relationship between iodine and O_2 release temperature in neat iodine oxides/iodic acids, and the ignition temperature of nAl-based and nTa-based thermites. For all iodine oxides/iodic acids, I find that oxygen and iodine occur at the same temperature which suggests iodine oxides/iodic acids directly decomposed into iodine and oxygen at high heating rate.

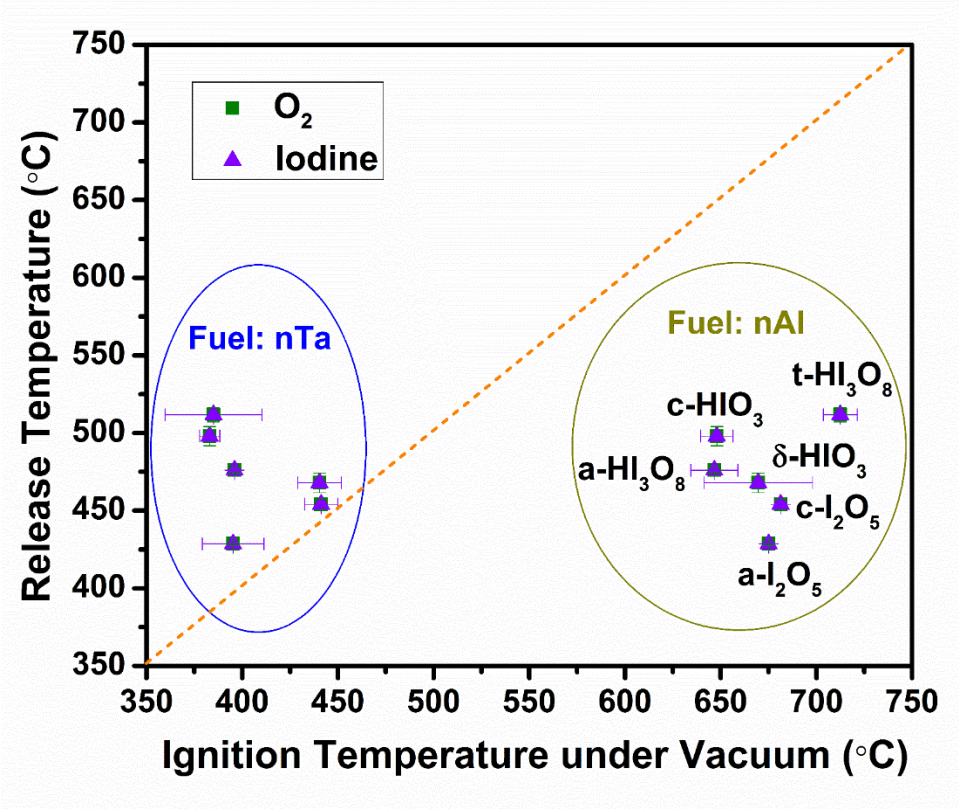

Figure 5.4. I and O_2 release temperature in neat iodine oxides/iodic acids, and the ignition temperature of corresponding nAl-based and nTa-based thermites under vacuum. Error bars correspond to at least two measurements. The orange dashed line stands for a perfect correlation.

All oxidizers when reacting with aluminum ignited about their oxygen release temperature. Moreover, they all ignited around the same temperature under vacuum, and at approximately the melting point of aluminum 660 ºC. Those results indicate that the ignition of nAl-based thermites is dominated by the melting of aluminum. Aluminum could then react with oxygen released from the oxidizer, but more likely since this experiment is conducted in vacuum, reacts heterogeneous with the oxidizer, once aluminum becomes mobile.

In contrast to aluminum, when tantalum was employed as the fuel, all nTa-based thermites ignited at temperatures lower than the oxygen release temperatures relative

to their corresponding neat oxidizers. Clearly, in this case a condensed phase reaction mechanism is dominant [44]. DeLisio et al have previously found that the Ta_2O_5 has a preferred orientation during crystalline oxide growth and this crystallization upon rapid heating result in cracking of the oxide shell that may enhance oxygen diffusion [48]. Since this is below the melting point of tantalum the oxygen from the decomposition of iodine oxides/iodic acids diffuse through the Ta_2O_5 cracked or weakened shell to the tantalum core. Moreover, even though *a*-HI_3O_8 and *a*-I_2O_5 has a significantly smaller particle size than *c*-HI_3O_8 or *c*-I_2O_5, their ignition temperatures are essentially within the measurement uncertainty which implies that particle size of the oxidizer is relatively unimportant and that the reaction of tantalum and gaseous O_2 contributed to the ignition, in agreement with the ignition of nAl/potassium oxysalts energetic composites [49].

To investigate the combustion performance of iodine oxides/iodic acids as oxidizers in nAl-based thermites at 1atm, constant volume combustion cell tests were performed on each thermite and the results are summarized in Table 5.2. Nano-sized copper oxide outperforms micro-sized copper oxide due to the huge difference between their particle sizes [50]. Given the fact that all iodine oxides/iodic acids include in this work have average particles size larger than 1 μm (~1 μm for *δ*-HIO_3, *a*-HI_3O_8 and *a*-I_2O_5; ~4 μm for *t*-HI_3O_8; ~30 μm for *c*-HIO_3 and *c*-I_2O_5), micro-sized copper oxide was chosen to be the control experiment.

Table 5.2 shows that those iodine oxides/iodic acids prepared via ASP outperform the corresponding commercial samples, with a shorter burn time and higher maximum pressure and pressurization rate. In addition, *t*-HI_3O_8 has better performance than *c*-

I_2O_5, but since they are both really HI_3O_8 the difference in performance can probably be attributed to the smaller particle size of *t*-HI_3O_8. Similar to the nano-sized and micro-sized CuO, particle size plays a very important role in combustion. In our previous work, we attributed the pressurization to the oxygen release from the oxidizer particles [43]. For nAl/micro-oxidizer thermites, the decomposition of the oxidizer is the rate-limiting step that results in the delay of the pressure rise [33, 43]. Thus, the particle size of the oxidizer is crucial for a thermite to perform well in combustion cell test because smaller particle size guarantees shorter diffusion length and higher specific surface area and therefore faster heat transfer and shorter the delay time for pressure rise [51]. In other words, the decomposition reaction of commercial iodine oxides/iodic acids that have larger particles size is the rate-limiting step during nAl-based thermites combustion, which results in slower thermite reaction rate and thus relatively poor performance in terms of pressurization rate [50]. Given the fact the only difference between commercial and aerosol synthesized iodine oxides/iodic acids is the particle size, it is reasonable to conclude that the higher pressurization rates and maximum pressures are resulted from the faster heat transfer owing to the higher contact area with employing smaller sized oxidizer particles. However, ignition with high heating rate by its nature is essentially the point where the self-heating by exothermic reaction exceeds heat loss and a non-linear reaction event occurs. In this case, the initial heat release from thermite reaction was not affected by oxidizers particles size and thus the ignition temperature is independent on particles size, which is consistent with our previous reports [51,52].

In addition, the fact that *t*-HI_3O_8 outperforms *c*-HIO_3 and *a*-HI_3O_8 outperforms *δ*-HIO_3 imply that HI_3O_8 is a better oxidizer. In fact, the pressurization rate and maximum pressure of the nAl/*a*-HI_3O_8 thermite reaction are ~450 Kpa/ms and ~384 Kpa, which is significantly above the other oxidizers evaluated, and indicate that the *a*-HI_3O_8 is the best gas generator in this study. The nAl/*a*-HI_3O_8 thermite reaction shows the highest peak optical emission and the shortest burn time, demonstrating it outperforms others in heat generation rate. Figure 5.5 shows the direct comparison between the pressure and optical trace of nAl/*m*-CuO and nAl/*a*-HI_3O_8. Based on the combustion behavior, *a*-HI_3O_8 seems to warrant further attention for biocidal applications since it features both high-pressure generation and energy release and has almost the same iodine content as I_2O_5 on a per mass basis (I_2O_5: ~76%; HIO_3: ~72%; HI_3O_8: ~75%). In a prior work it has been reported [53] that I_2O_5 showed increased reactivity with a polar solvent treatment. Since I_2O_5 likely hydrated to form HI_3O_8 and HIO_3 in the polar solvent, it is reasonable to conclude that the results were showing that I_2O_5 hydrates outperform I_2O_5 in a flame speed test. This is consistent with my results.

Table 5.2. Combustion cell test data for nAl-based thermites with different oxidizers. Each sample was repeated at least three times. All the numbers have a deviation at ~25.

Oxidizers (*n*Al, stoichiometric)	**Peak Pressure (Kpa)**	**Pressurization rate (Kpa/ms)**	**Burn time (ms)**	**Peak optical emission (Volts)**
n-CuO	405	5653	0.31	2.24
m-CuO	162	157	1.60	2.70
δ-HIO_3	281	166	1.39	6.09
c-HIO_3	104	6	12.7	0.41
a-I_2O_5	293	207	1.29	7.52
c-I_2O_5	156	31	2.49	2.88
a-HI_3O_8	384	450	0.96	11.7
t-HI_3O_8	214	175	1.25	7.79

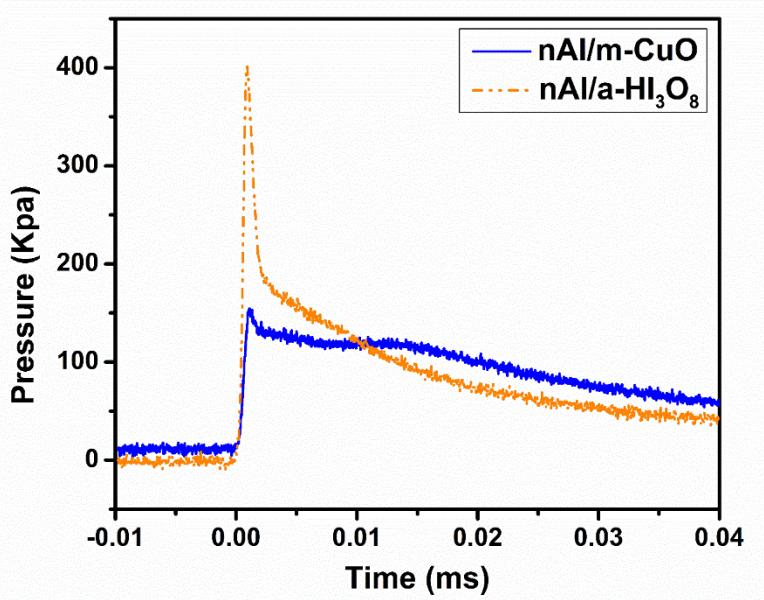

(A)

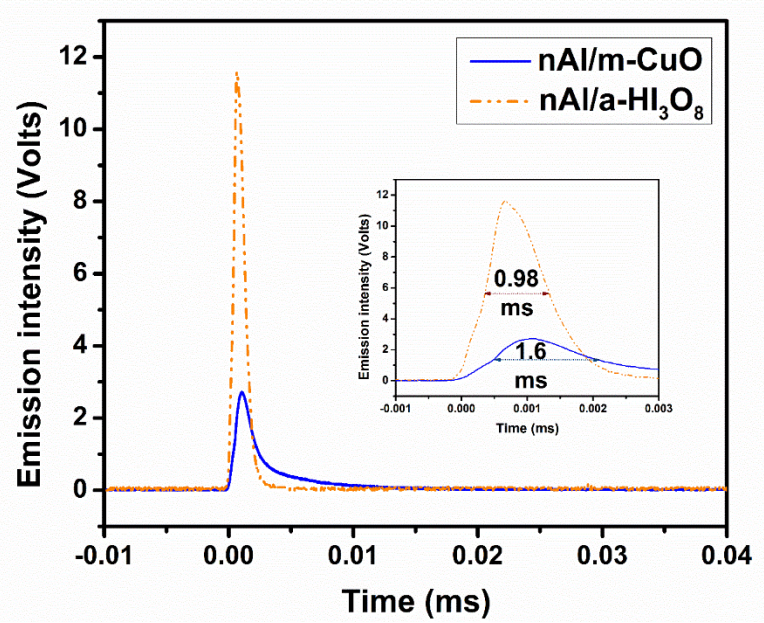

(B)

Figure 5.5. Direct comparison between the pressure (A) and optical (B) trace of nAl/m-CuO and nAl/a-HI_3O_8.

5.4. Conclusions

In this study, various iodine oxides/iodic acids, including *a*-I_2O_5, *a*-HI_3O_8 and *δ*-HIO_3, were prepared based on the aerosol route published previously, and were employed as the oxidizer in thermite systems. Their decomposition behavior was studied using T-Jump/TOFMS, which identified a single decomposition step for all oxides at high heating rates compared with the multi-steps process at low heating rate. The ignition temperatures of nAl-based thermites are all ~650 ºC which is at the melting point of aluminum (~660 ºC). This suggests that the mobility of the aluminum core is dominating the ignition/reaction while the gaseous oxygen released from the decomposition of the oxidizer does not participate in the ignition until the molten aluminum was available. Unlike nAl-based thermites, the ignition temperatures of nTa-based thermites are lower than the oxygen release temperatures from the corresponding bare oxidizers. In this case, a condensed phase reaction mechanism is proposed to dominate the ignition process. Combustion tests show that nAl/*a*-HI_3O_8 has the highest pressurization rate and peak pressure and shortest burn time, and since it also has an iodine content of ~75% which is as high as I_2O_5 on a per mass basis, this material may be a very promising candidate in biocidal application.

5.5. Supplemental Information

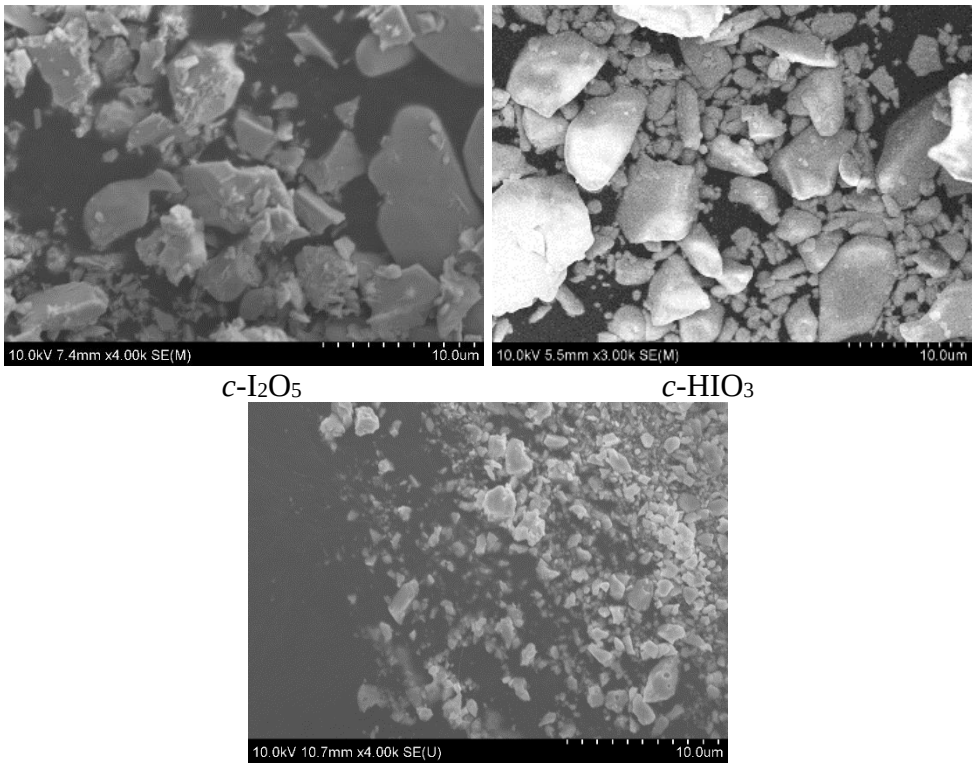

c-I_2O_5 *c*-HIO_3

t-HI_3O_8

Figure S5.1. The SEM images of c-I_2O_5, c-HIO_3 and t-HI_3O_8.

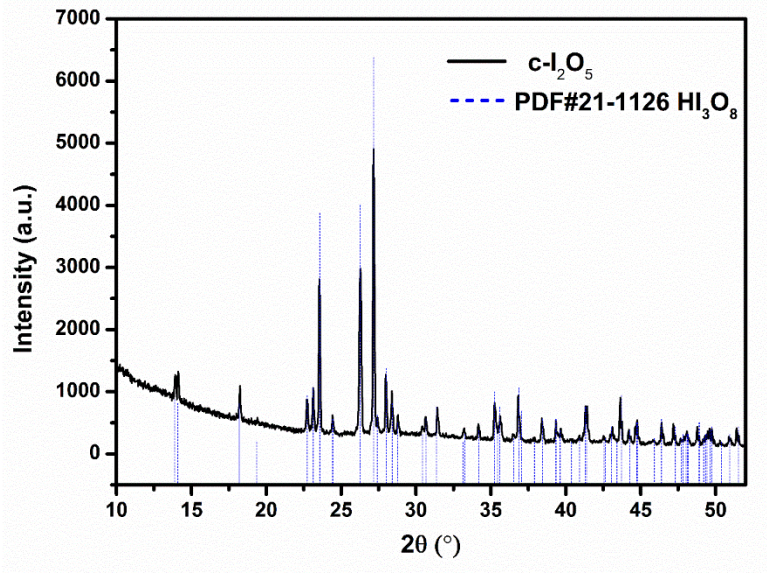

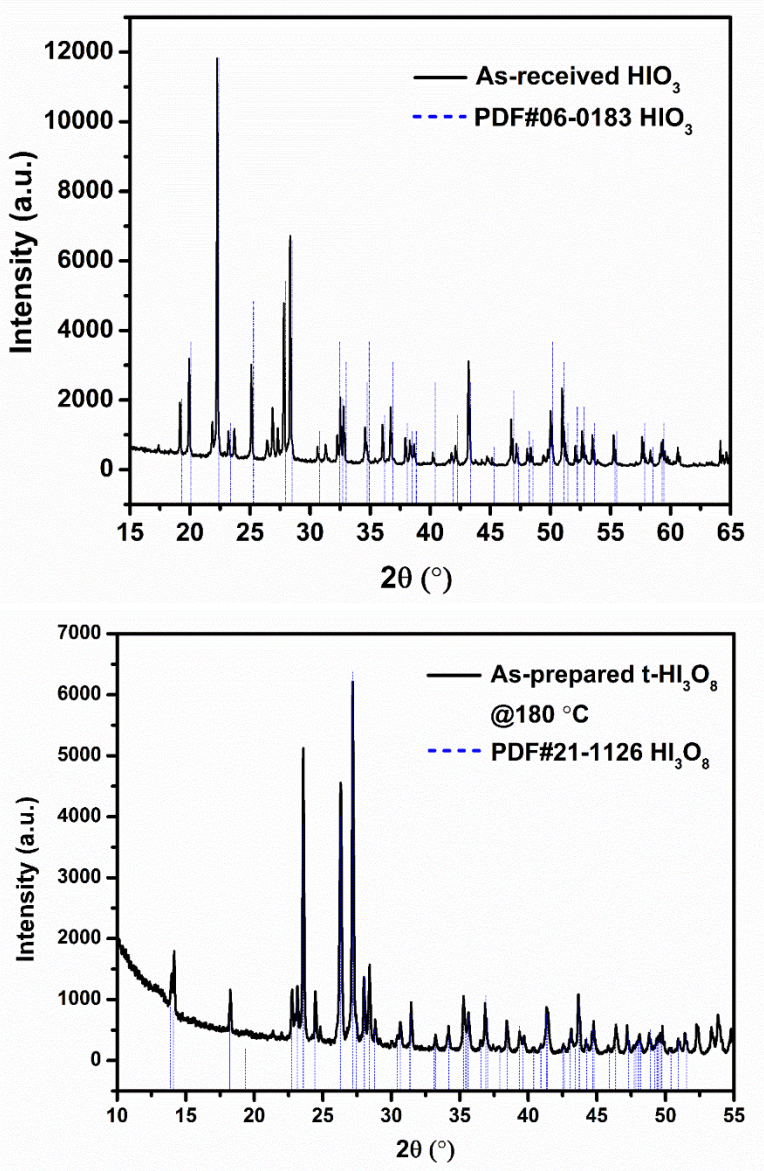

Figure S5.2. The XRD patterns of c-I_2O_5, c-HIO_3 and t-HI_3O_8.

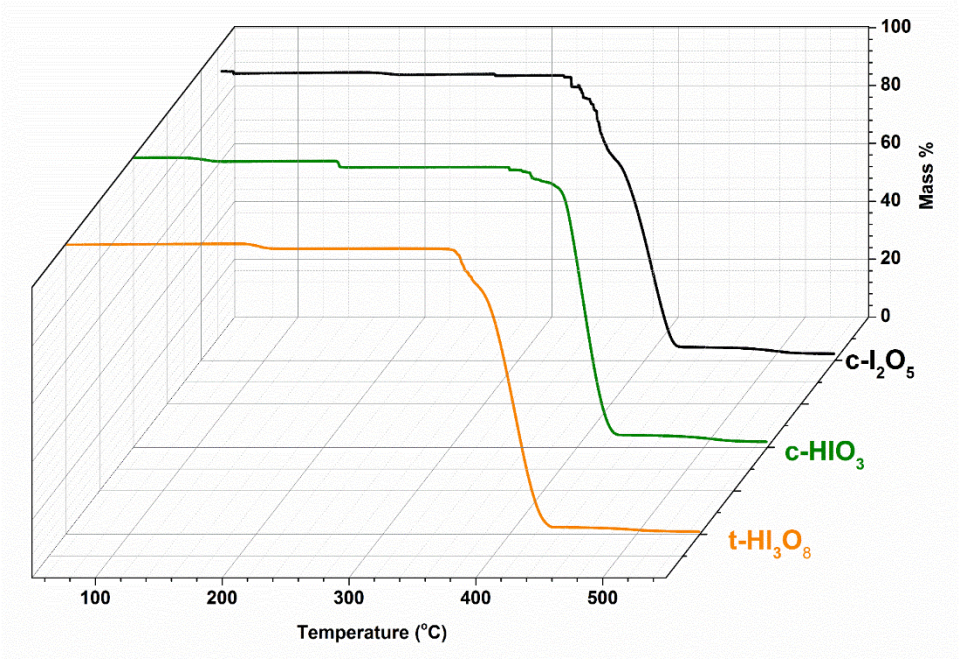

Figure S5.3. The TGA curves of c-I_2O_5, c-HIO_3 and t-HI_3O_8.

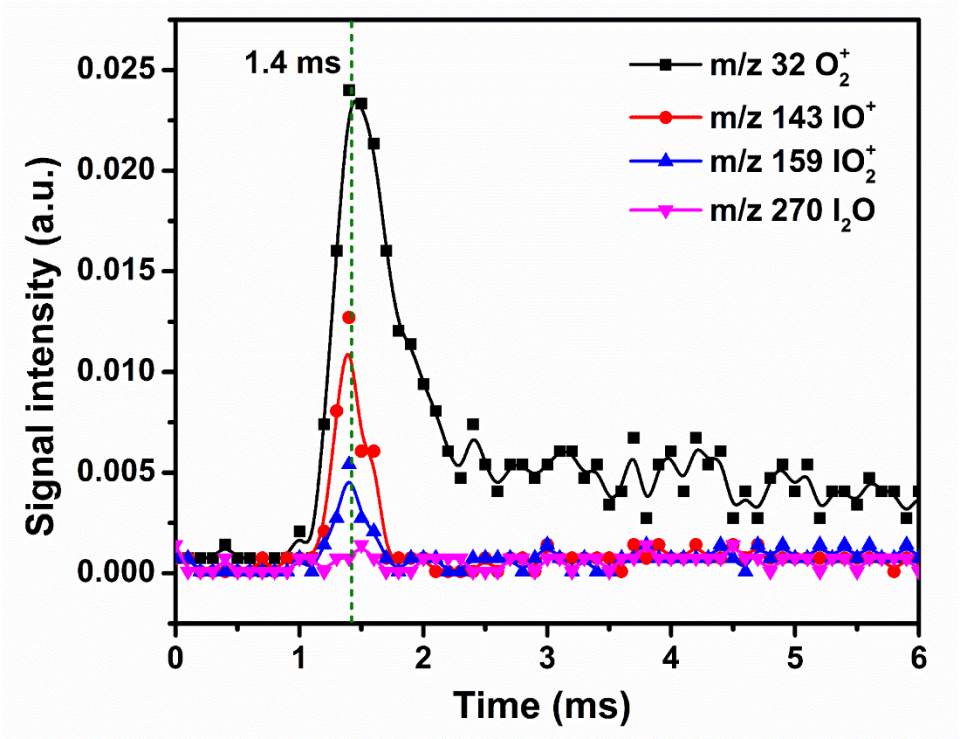

Figure S5.4. Representative plot showing the temporal profiles of oxygen and IO_x^+ upon heating a-HI_3O_8 when heated at ~5×10^5 ºC/s.

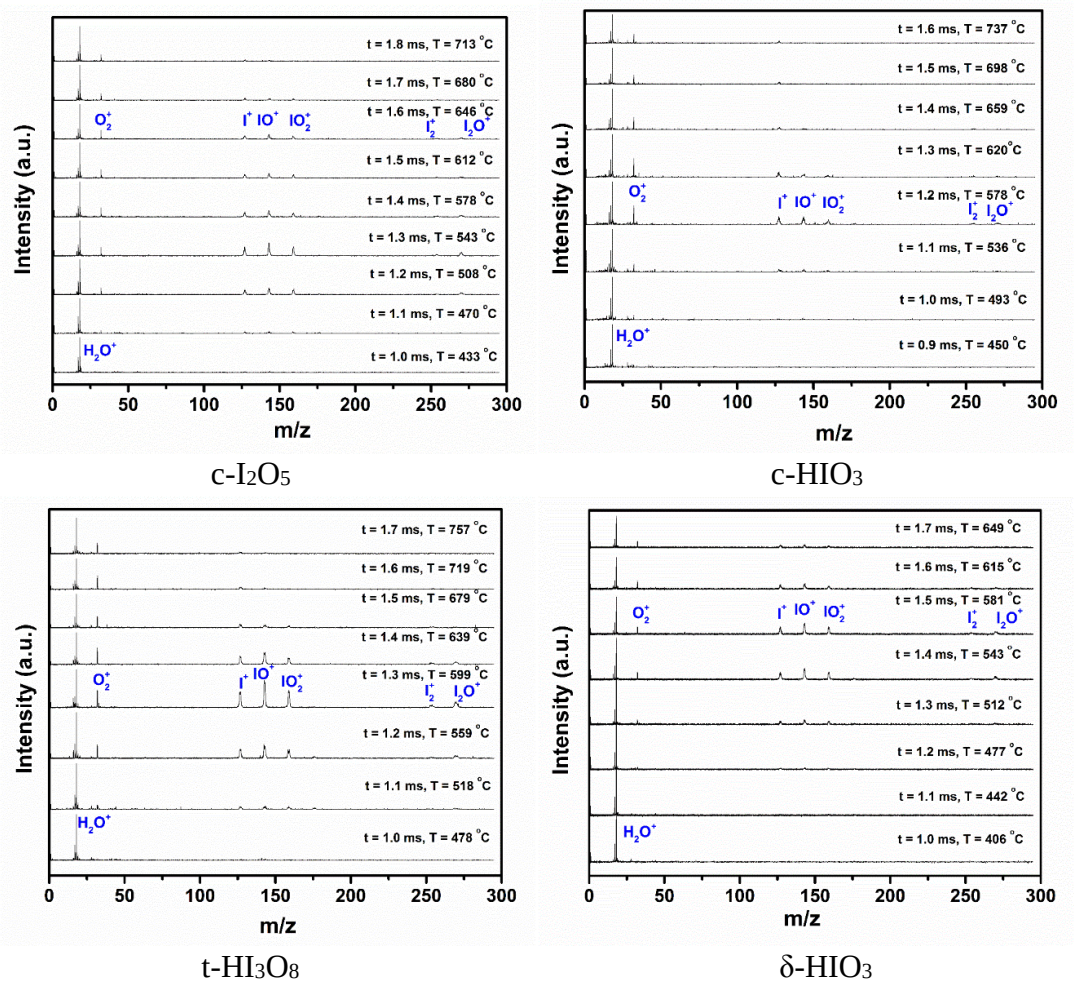

Figure S5.5. Time-resolved T-Jump mass spectra obtained at a heating rate of ~5×10^5 ºC/s.

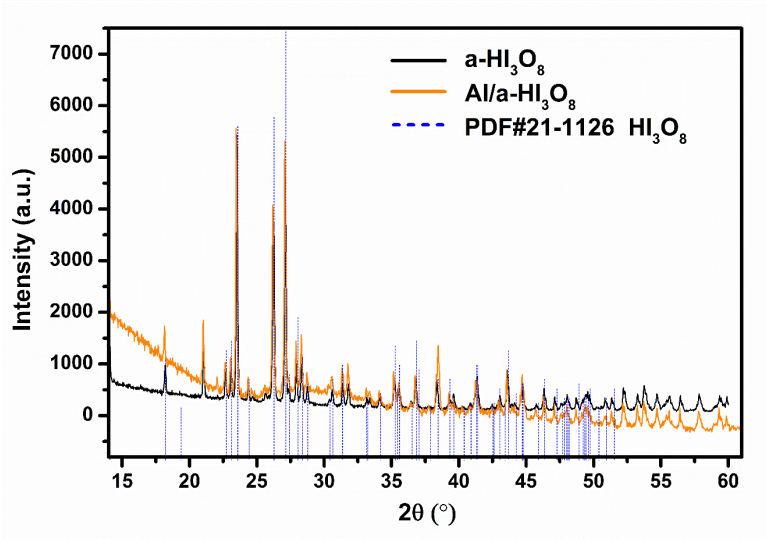
a-HI3O8
Al/a-HI3O8
PDF#21-1126 HI3O8
Intensity (a.u.)
2θ (°)

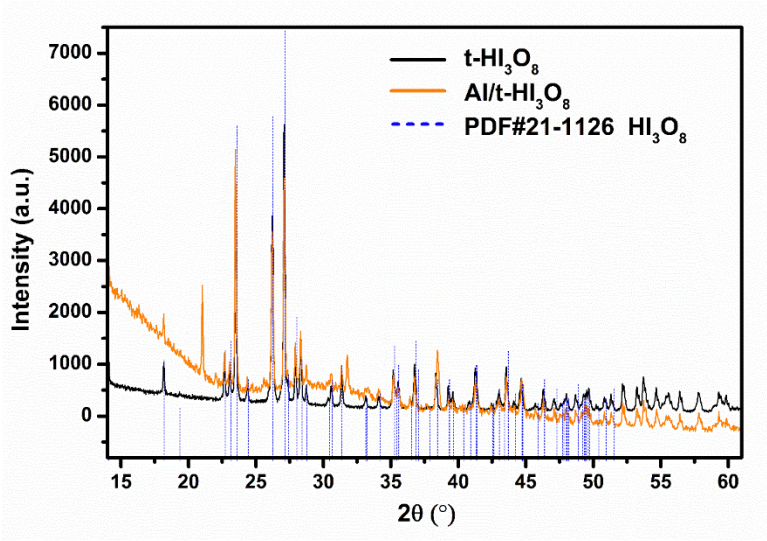
t-HI3O8
Al/t-HI3O8
PDF#21-1126 HI3O8
Intensity (a.u.)
2θ (°)

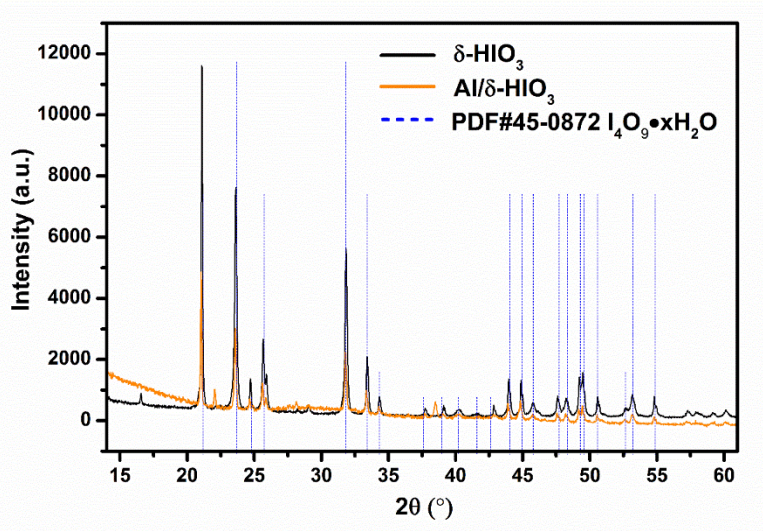
δ-HIO3
Al/δ-HIO3
PDF#45-0872 I4O9•xH2O
Intensity (a.u.)
2θ (°)

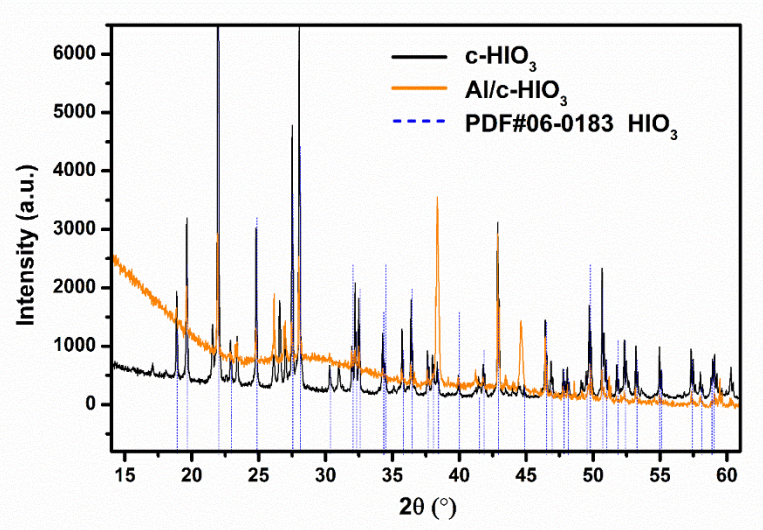
c-HIO3
Al/c-HIO3
PDF#06-0183 HIO3
Intensity (a.u.)
2θ (°)

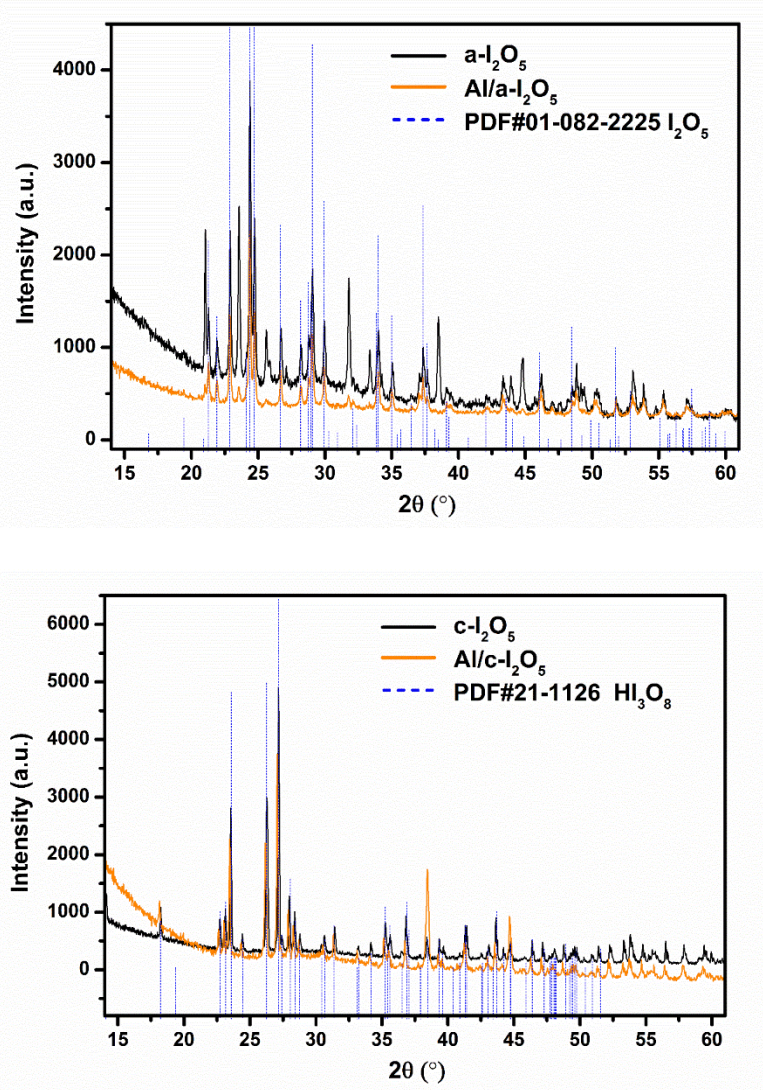

Figure S5.6. The XRD patterns of a-HI_3O_8 vs Al/a-HI_3O_8, t-HI_3O_8 vs Al/t-HI_3O_8, δ-HIO_3 vs Al/δ-HIO_3, c-HIO_3 vs Al/c-HIO_3, a-I_2O_5 vs Al/a-I_2O_5, and c-I_2O_5 vs Al/c-I_2O_5.

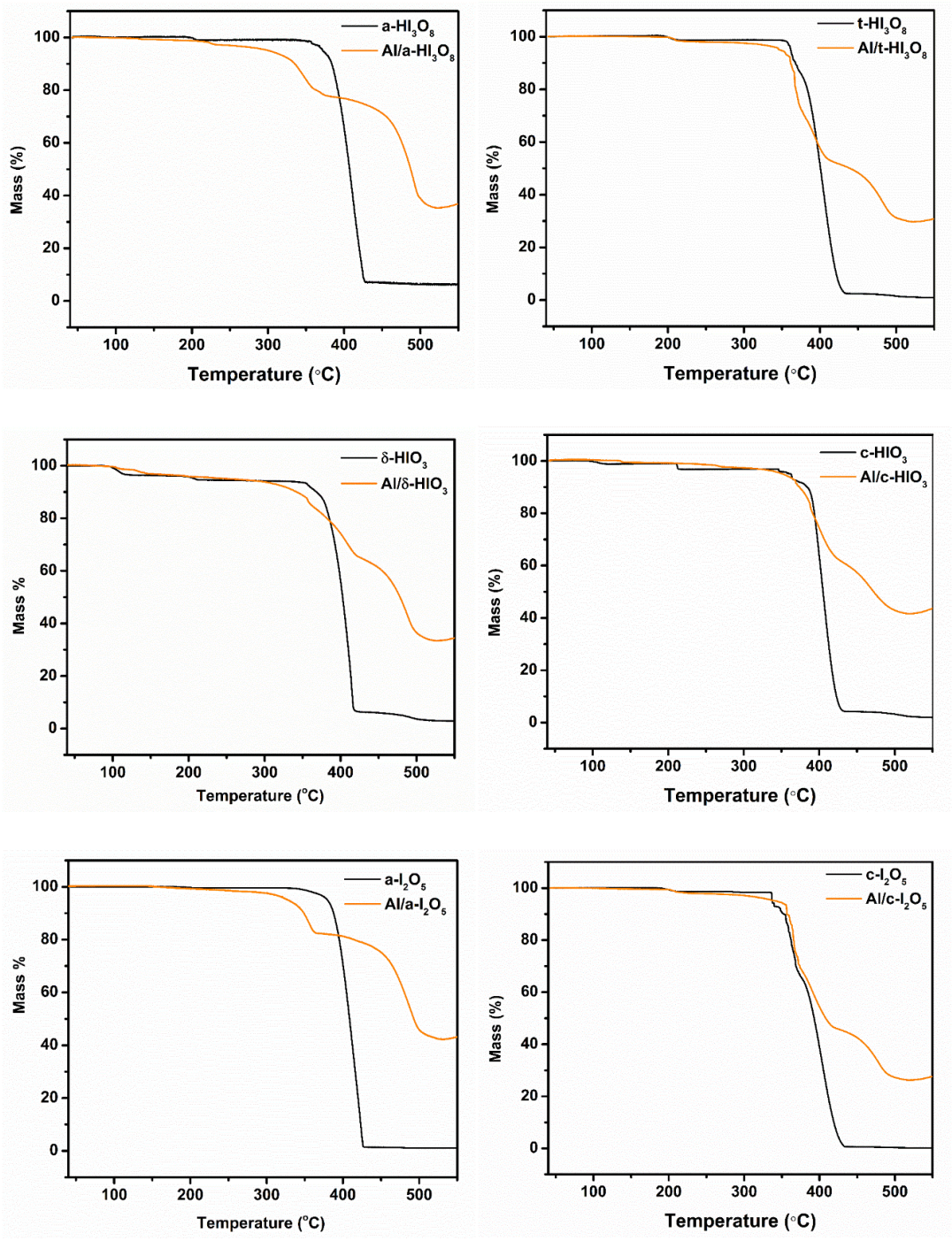

Figure S5.7. TGA results of a-HI_3O_8 vs Al/a-HI_3O_8, t-HI_3O_8 vs Al/t-HI_3O_8, δ-HIO_3 vs Al/δ-HIO_3, c-HIO_3 vs Al/c-HIO_3, a-I_2O_5 vs Al/a-I_2O_5 and c-I_2O_5 vs Al/c-I_2O_5.

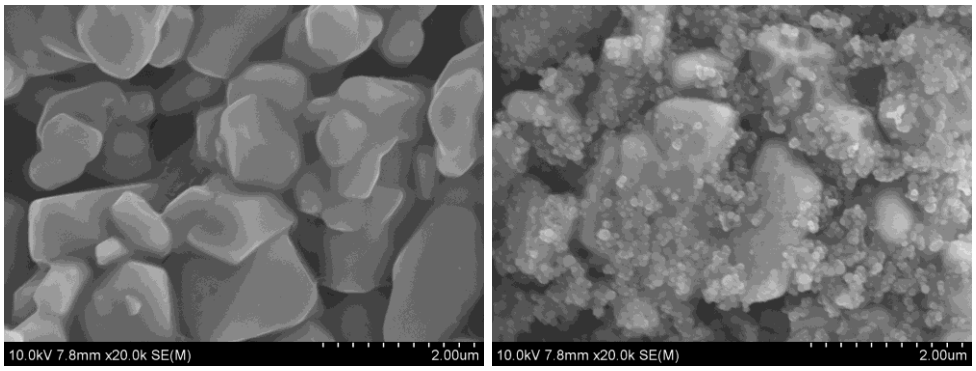

Figure S5.8. SEM images of a-HI_3O_8 and Al/a-HI_3O_8.

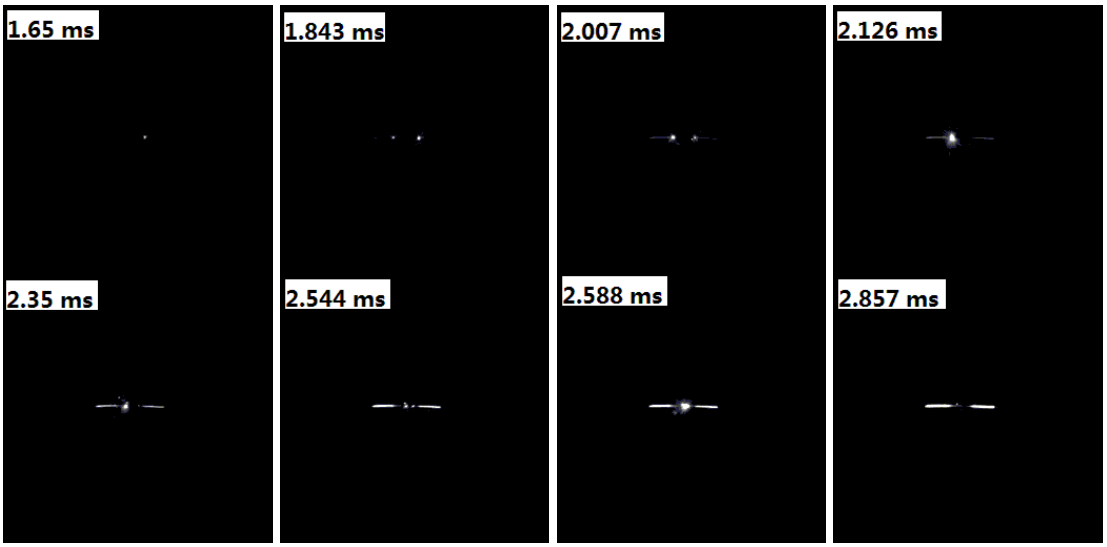

Figure S5.9. Sequential snapshots of nAl/a-HI_3O_8 thermite burning on high heating rate wire under vacuum captures by a high-speed camera. The labels in each image are time elapses after triggering.

5.6. Appendix: detailed results of Rietveld refinement

5.6.1.a-HI_3O_8.raw"

R-Values
Rexp : 5.25 Rwp : 9.25 Rp : 6.85 GOF : 1.76
Rexp`: 10.86  Rwp`: 19.14 Rp` : 18.91 DW : 0.77

Quantitative Analysis - Rietveld

Phase 1 : delta-HIO_3 9.1(3) %
Phase 2 : HI_3O_8 90.9(3) %

Specimen displacement -0.348(9)

Structure 1
Phase name delta-HIO_3
R-Bragg 2.513
Spacegroup P212121
Scale 0.0000172(5)
Cell Mass 703.642
Cell Volume (Å^3) 264.47(6)
Wt% - Rietveld 9.1(3)
Double-Voigt|Approach
Cry size Lorentzian 250(30)
k: 1 LVol-IB (nm) 158(18)
k: 0.89 LVol-FWHM (nm) 220(20)
Crystal Linear Absorption Coeff. (1/cm) 929.55(19)
Crystal Density (g/cm^3) 4.4180(9)
Preferred Orientation (Dir 1 : 1 0 0) 0.77(5)
(Dir 2 : 0 0 1) 1.4(6)
Fraction of Dir 1 0.8(3)
Lattice parameters
a (Å) 8.4486(6)
b (Å) 6.9582(9)
c (Å) 4.4988(7)

Site	Np	x	y	z	Atom	Occ	Beq
I1	4	0.27820	0.23062	0.02640	I	1	1.5
O1	4	0.34140	0.43890	0.27400	O	1	2
O2	4	0.35420	0.03720	0.25500	O	1	2
O3	4	0.08730	0.25400	0.16780	O	1	2
H1	4	0.44051	0.44433	0.28298	H	1	2

Structure 2
Phase name HI_3O_8
R-Bragg 4.346
Spacegroup P121/n1
Scale 0.00002355(14)
Cell Mass 2038.866
Cell Volume (Å^3) 666.96(4)
Wt% - Rietveld 90.9(3)
Double-Voigt|Approach
Cry size Lorentzian 277(7)
k: 1 LVol-IB (nm) 177(5)

k: 0.89 LVol-FWHM (nm) 247(7)
Crystal Linear Absorption Coeff. (1/cm) 1103.95(6)
Crystal Density (g/cm^3) 5.0762(3)
Preferred Orientation (Dir 1 : 1 0 0) 0.883(5)
(Dir 2 : 0 1 0) 1.49(10)
Fraction of Dir 1 0.82(3)
Lattice parameters
a (Å) 7.5752(2)
b (Å) 7.7169(3)
c (Å) 11.4095(4)
beta (°) 90.166(2)

Site	Np	x	y	z	Atom	Occ	Beq
I1	4	0.24144	0.22767	0.09527	I	1	1
I2	4	0.33769	0.73614	0.10361	I	1	1
I3	4	0.75579	0.04724	0.19159	I	1	1
O1	4	0.45720	0.30100	0.05390	O	1	1.5
O2	4	0.12980	0.43130	0.08700	O	1	1.5
O3	4	0.17110	0.82240	0.00800	O	1	1.5
O4	4	0.44080	0.94070	0.13590	O	1	1.5
O5	4	0.18330	0.74510	0.24070	O	1	1.5
O6	4	0.78370	0.45460	0.15790	O	1	1.5
O7	4	0.80280	0.84230	0.12420	O	1	1.5
O8	4	0.97740	0.11430	0.22530	O	1	1.5
H1	4	0.87310	0.46530	0.12130	H	1	2

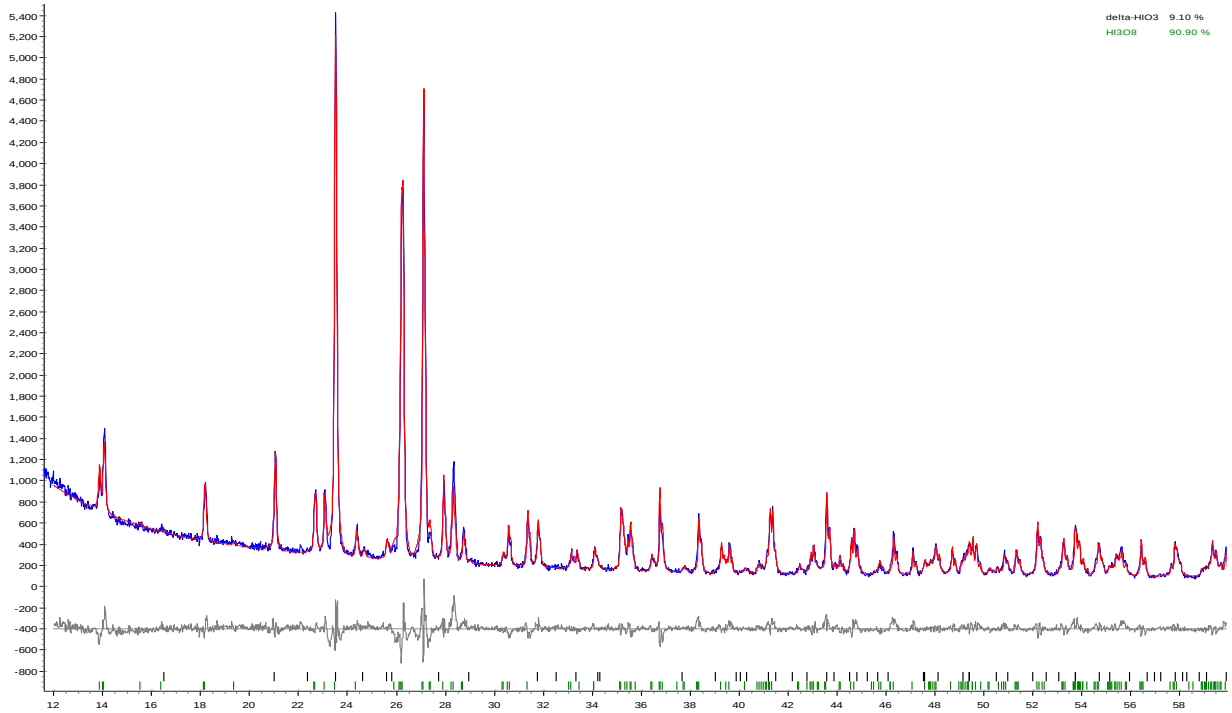

5.6.2. Al/a-HI_3O_8.raw"

R-Values
Rexp : 4.24 Rwp : 5.31 Rp : 3.93 GOF : 1.25
Rexp`: 18.76  Rwp`: 23.51 Rp` : 27.89 DW : 1.47

Quantitative Analysis - Rietveld
Phase 1 : delta-HIO3 8.3(4) %
Phase 2 : HI3O8 67.1(6) %
Phase 3 : Al 24.6(6) %

Instrument
Specimen displacement 0.142(8)

Structure 1
Phase name delta-HIO3
R-Bragg 1.678
Spacegroup P212121
Scale 0.0000135(7)
Cell Mass 703.642
Cell Volume (Å^3) 264.01(9)
Wt% - Rietveld 8.3(4)
Double-Voigt|Approach
Cry size Lorentzian 270(50)
k: 1 LVol-IB (nm) 170(30)
k: 0.89 LVol-FWHM (nm) 240(50)
Crystal Linear Absorption Coeff. (1/cm) 931.2(3)
Crystal Density (g/cm^3) 4.4258(15)
Preferred Orientation (Dir 1 : 1 0 0) 0.782(13)
Lattice parameters
a (Å) 8.4460(8)
b (Å) 6.9551(16)
c (Å) 4.4942(9)

Site	Np	x	y	z	Atom	Occ	Beq
I1	4	0.27820	0.23062	0.02640	I	1	2
O1	4	0.34140	0.43890	0.27400	O	1	2
O2	4	0.35420	0.03720	0.25500	O	1	2
O3	4	0.08730	0.25400	0.16780	O	1	2
H1	4	0.44051	0.44433	0.28298	H	1	2

Structure 2
Phase name HI3O8
R-Bragg 2.248

Spacegroup	P121/n1
Scale	0.00001497(14)
Cell Mass	2038.866
Cell Volume (Å^3)	665.86(4)
Wt% - Rietveld	67.1(6)
Double-Voigt|Approach	
Cry size Lorentzian	361(19)
k: 1 LVol-IB (nm)	230(12)
k: 0.89 LVol-FWHM (nm)	321(17)
Crystal Linear Absorption Coeff. (1/cm)	1105.77(6)
Crystal Density (g/cm^3)	5.0846(3)
Preferred Orientation (Dir 1 : 1 0 0)	0.908(7)
(Dir 2 : 0 1 0)	1.4(2)
Fraction of Dir 1	0.86(6)
Lattice parameters	
a (Å)	7.5733(2)
b (Å)	7.7109(3)
c (Å)	11.4025(4)
beta (°)	90.174(3)

Site	Np	x	y	z	Atom	Occ	Beq
I1	4	0.24144	0.22767	0.09527	I	1	1
I2	4	0.33769	0.73614	0.10361	I	1	1
I3	4	0.75579	0.04724	0.19159	I	1	1
O1	4	0.45720	0.30100	0.05390	O	1	1.5
O2	4	0.12980	0.43130	0.08700	O	1	1.5
O3	4	0.17110	0.82240	0.00800	O	1	1.5
O4	4	0.44080	0.94070	0.13590	O	1	1.5
O5	4	0.18330	0.74510	0.24070	O	1	1.5
O6	4	0.78370	0.45460	0.15790	O	1	1.5
O7	4	0.80280	0.84230	0.12420	O	1	1.5
O8	4	0.97740	0.11430	0.22530	O	1	1.5
H1	4	0.87310	0.46530	0.12130	H	1	2

Structure 3

Phase name	Al
R-Bragg	1.236
Spacegroup	Fm3m
Scale	0.00104(3)
Cell Mass	107.926
Cell Volume (Å^3)	66.371(9)
Wt% - Rietveld	24.6(6)
Double-Voigt|Approach	
Cry size Lorentzian	141(15)
k: 1 LVol-IB (nm)	90(10)

k: 0.89 LVol-FWHM (nm) 126(13)
Crystal Linear Absorption Coeff. (1/cm) 133.607(17)
Crystal Density (g/cm^3) 2.7002(4)
Lattice parameters
a (Å) 4.04879(18)

Site	Np	x	y	z	Atom	Occ	Beq
Al	4	0.00000	0.00000	0.00000	Al	1	1

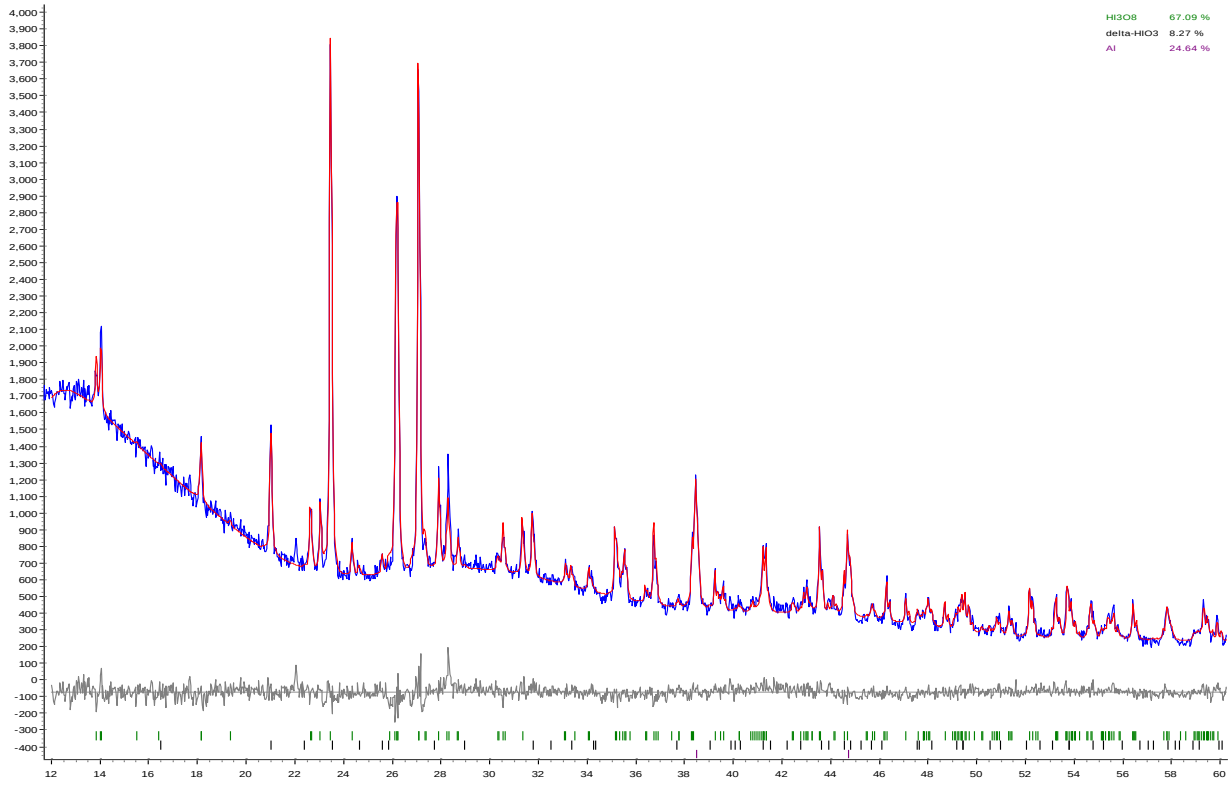

5.6.3. Al/t-HI_3O_8.raw"

R-Values
Rexp : 4.05 Rwp : 5.08 Rp : 3.72 GOF : 1.26
Rexp`: 20.51  Rwp`: 25.76 Rp` : 31.37 DW : 1.35

Quantitative Analysis - Rietveld
Phase 1 : delta-HIO3 9.668 %
Phase 2 : HI3O8 63.612 %
Phase 3 : Al 26.720 %

Instrument
Specimen displacement 0.06926433

Structure 1
Phase name delta-HIO3
R-Bragg 2.188
Spacegroup P212121
Scale 1.45283e-005
Cell Mass 703.642
Cell Volume (Å^3) 264.17053
Wt% - Rietveld 9.668
Double-Voigt|Approach
Cry size Lorentzian 347.0
k: 1 LVol-IB (nm) 220.903
k: 0.89 LVol-FWHM (nm) 308.825
Crystal Linear Absorption Coeff. (1/cm) 930.609
Crystal Density (g/cm^3) 4.423
Preferred Orientation (Dir 1 : 1 0 0) 0.7375984
Lattice parameters
a (Å) 8.4463753
b (Å) 6.9616589
c (Å) 4.4926362

Site	Np	x	y	z	Atom	Occ	Beq
I1	4	0.27820	0.23062	0.02640	I	1	2
O1	4	0.34140	0.43890	0.27400	O	1	2
O2	4	0.35420	0.03720	0.25500	O	1	2
O3	4	0.08730	0.25400	0.16780	O	1	2
H1	4	0.44051	0.44433	0.28298	H	1	2

Structure 2
Phase name HI_3O_8
R-Bragg 2.703

Spacegroup	P121/n1
Scale	1.30854e-005
Cell Mass	2038.866
Cell Volume (Å^3)	665.98220
Wt% - Rietveld	63.612
Double-Voigt|Approach	
Cry size Lorentzian	331.3
k: 1 LVol-IB (nm)	210.894
k: 0.89 LVol-FWHM (nm)	294.831
Crystal Linear Absorption Coeff. (1/cm)	1105.576
Crystal Density (g/cm^3)	5.084
Preferred Orientation (Dir 1 : 1 0 0)	0.8393051
(Dir 2 : 0 1 0)	1.136459
Fraction of Dir 1	0.632521
Lattice parameters	
a (Å)	7.5731885
b (Å)	7.7118932
c (Å)	11.4031509
beta (°)	90.17477

Site	Np	x	y	z	Atom	Occ	Beq
I1	4	0.24144	0.22767	0.09527	I	1	1
I2	4	0.33769	0.73614	0.10361	I	1	1
I3	4	0.75579	0.04724	0.19159	I	1	1
O1	4	0.45720	0.30100	0.05390	O	1	1.5
O2	4	0.12980	0.43130	0.08700	O	1	1.5
O3	4	0.17110	0.82240	0.00800	O	1	1.5
O4	4	0.44080	0.94070	0.13590	O	1	1.5
O5	4	0.18330	0.74510	0.24070	O	1	1.5
O6	4	0.78370	0.45460	0.15790	O	1	1.5
O7	4	0.80280	0.84230	0.12420	O	1	1.5
O8	4	0.97740	0.11430	0.22530	O	1	1.5
H1	4	0.87310	0.46530	0.12130	H	1	2

Structure 3

Phase name	Al
R-Bragg	1.391
Spacegroup	Fm3m
Scale	1.04188e-003
Cell Mass	107.926
Cell Volume (Å^3)	66.37367
Wt% - Rietveld	26.720
Double-Voigt|Approach	
Cry size Lorentzian	117.4
k: 1 LVol-IB (nm)	74.737

k: 0.89 LVol-FWHM (nm) 104.483
Crystal Linear Absorption Coeff. (1/cm) 133.601
Crystal Density (g/cm^3) 2.700
Lattice parameters
a (Å) 4.0488524

Site	Np	x	y	z	Atom	Occ	Beq
Al	4	0.00000	0.00000	0.00000	Al	1	1

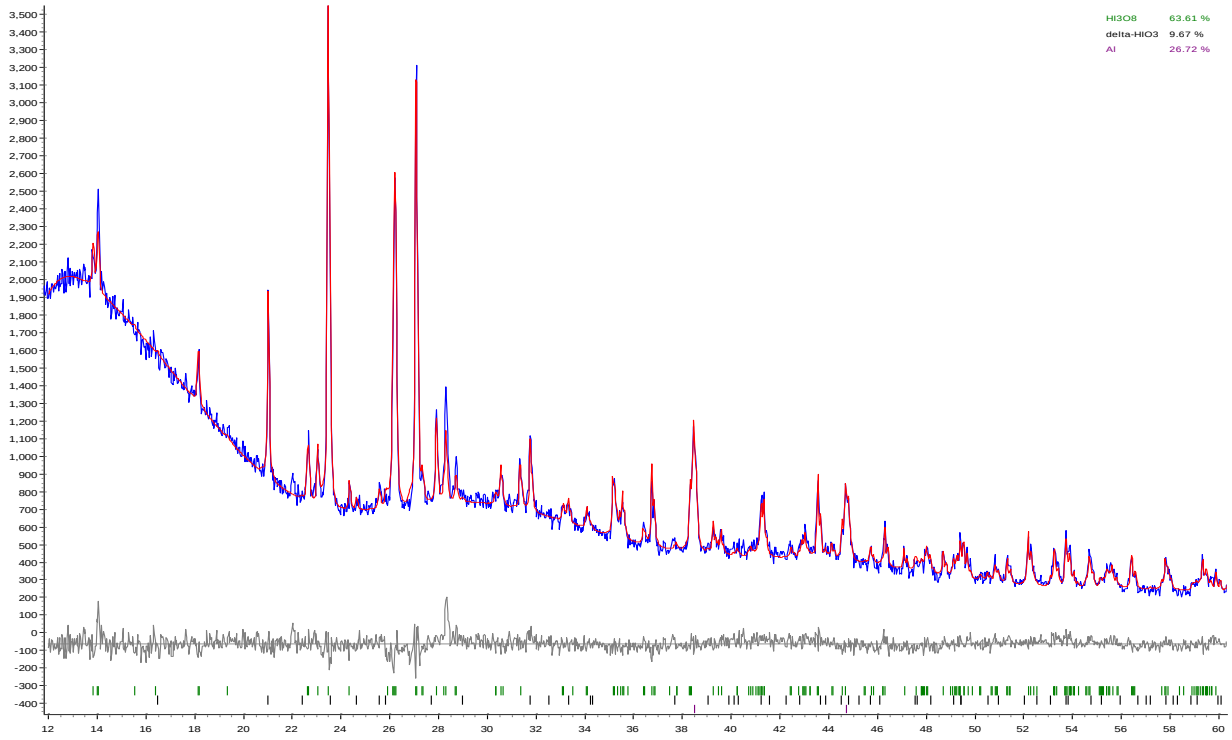

5.6.4. t-HI_3O_8.raw"

R-Values
Rexp : 5.86 Rwp : 9.87 Rp : 7.41 GOF : 1.68
Rexp`: 11.45  Rwp`: 19.26 Rp` : 18.24 DW : 0.77

Quantitative Analysis - Rietveld
Phase 1 : HI_3O_8 100.000 %

Instrument
Zero error 0.2452(18)
Specimen displacement -0.159(15)

Structure 1
Phase name HI_3O_8
R-Bragg 5.449
Spacegroup P121/n1
Scale 0.0000420(4)
Cell Mass 2038.866
Cell Volume (Å^3) 667.70(2)
Wt% - Rietveld 100.000
Double-Voigt|Approach
Cry size Lorentzian 187(3)
k: 1 LVol-IB (nm) 118.9(17)
k: 0.89 LVol-FWHM (nm) 166(2)
Crystal Linear Absorption Coeff. (1/cm) 1102.74(4)
Crystal Density (g/cm^3) 5.07059(17)
Preferred Orientation (Dir 1 : 1 0 0) 0.915(3)
(Dir 2 : 0 1 0) 1.66(14)
Fraction of Dir 1 0.915(16)
Lattice parameters
a (Å) 7.57861(14)
b (Å) 7.71950(15)
c (Å) 11.4131(2)
beta (°) 90.1621(14)

Site	Np	x	y	z	Atom	Occ	Beq
I1	4	0.24144	0.22767	0.09527	I	1	1
I2	4	0.33769	0.73614	0.10361	I	1	1
I3	4	0.75579	0.04724	0.19159	I	1	1
O1	4	0.45720	0.30100	0.05390	O	1	1.5
O2	4	0.12980	0.43130	0.08700	O	1	1.5
O3	4	0.17110	0.82240	0.00800	O	1	1.5
O4	4	0.44080	0.94070	0.13590	O	1	1.5
O5	4	0.18330	0.74510	0.24070	O	1	1.5

O6	4	0.78370	0.45460	0.15790	O	1	1.5
O7	4	0.80280	0.84230	0.12420	O	1	1.5
O8	4	0.97740	0.11430	0.22530	O	1	1.5
H1	4	0.87310	0.46530	0.12130	H	1	2

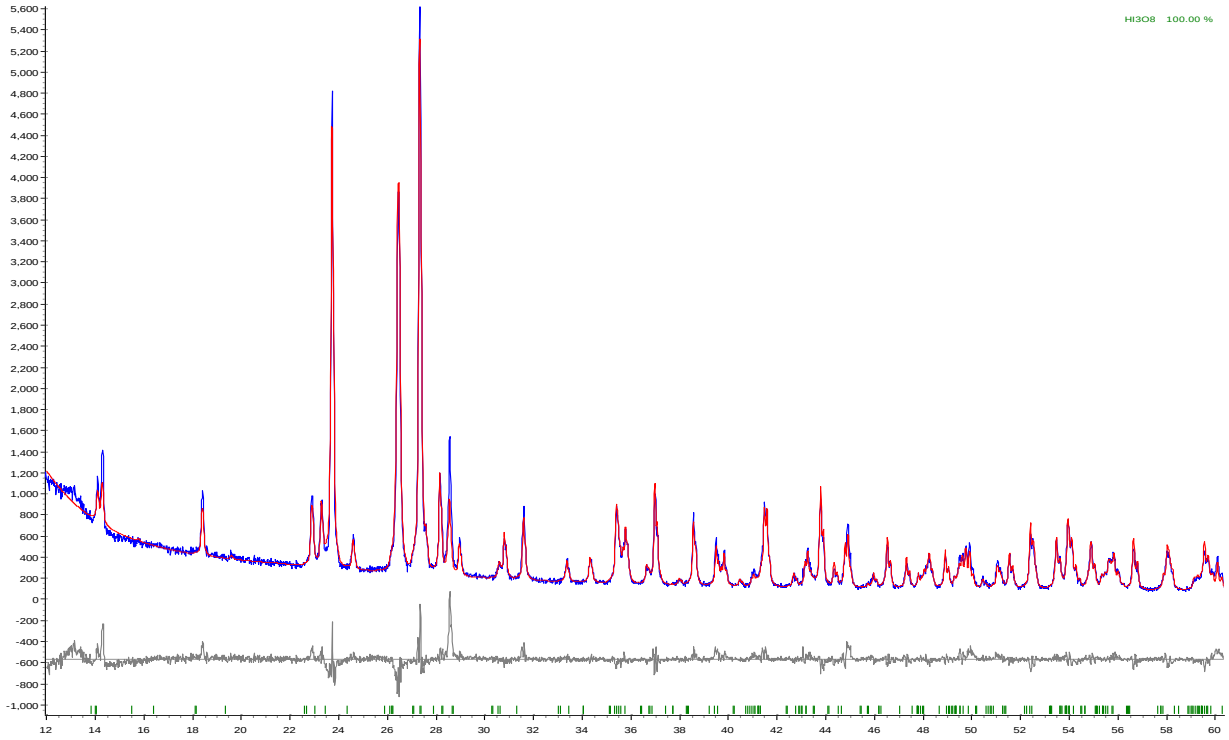

5.6.5. a-I_2O_5.raw"

R-Values
Rexp : 7.80 Rwp : 8.43 Rp : 6.45 GOF : 1.08
Rexp`: 20.61  Rwp`: 22.28 Rp` : 22.43 DW : 1.73

Quantitative Analysis - Rietveld
Phase 1 : delta-HIO3 8.6(4) %
Phase 2 : I2O5 91.4(4) %

Instrument
Zero error -0.013(3)

Structure 1
Phase name delta-HIO_3
R-Bragg 1.902
Spacegroup P212121
Scale 0.0000075(4)
Cell Mass 703.642
Cell Volume (Å^3) 264.35(13)
Wt% - Rietveld 8.6(4)
Double-Voigt|Approach
Cry size Lorentzian 93(11)
k: 1 LVol-IB (nm) 59(7)
k: 0.89 LVol-FWHM (nm) 82(10)
Crystal Linear Absorption Coeff. (1/cm) 930.0(4)
Crystal Density (g/cm^3) 4.420(2)
Preferred Orientation (Dir 1 : 1 0 0) 0.9(5)
(Dir 2 : 0 0 1) 1.1(11)
Fraction of Dir 1 1(5)
Lattice parameters
a (Å) 8.4490(19)
b (Å) 6.956(2)
c (Å) 4.4976(12)

Site	Np	x	y	z	Atom	Occ	Beq
I1	4	0.27820	0.23062	0.02640	I	1	2
O1	4	0.34140	0.43890	0.27400	O	1	2
O2	4	0.35420	0.03720	0.25500	O	1	2
O3	4	0.08730	0.25400	0.16780	O	1	2
H1	4	0.44051	0.44433	0.28298	H	1	2

Structure 2
Phase name I_2O_5

R-Bragg	1.778
Spacegroup	P121/c1
Scale	0.0000256(4)
Cell Mass	1335.224
Cell Volume (Å^3)	433.90(3)
Wt% - Rietveld	91.4(4)
Double-Voigt|Approach	
Cry size Lorentzian	131(3)
k: 1 LVol-IB (nm)	83.2(17)
k: 0.89 LVol-FWHM (nm)	116(2)
Crystal Linear Absorption Coeff. (1/cm)	1130.34(8)
Crystal Density (g/cm^3)	5.1099(4)
Preferred Orientation (Dir 1 : 1 0 0)	0.992(5)
(Dir 2 : 0 0 1)	0.36(14)
Fraction of Dir 1	0.996(5)
Lattice parameters	
a (Å)	11.0334(4)
b (Å)	5.0618(2)
c (Å)	8.1329(3)
beta (°)	107.200(3)

Site	Np	x	y	z	Atom	Occ	Beq
I1	4	0.12780	0.11700	0.21700	I	1	1
I2	4	0.37370	0.68300	0.15900	I	1	1
O1	4	0.01270	0.84700	0.15200	O	1	1.5
O2	4	0.19130	0.03500	0.43900	O	1	1.5
O3	4	0.49440	0.84900	0.33200	O	1	1.5
O4	4	0.30570	0.50000	0.29700	O	1	1.5
O5	4	0.24920	0.96900	0.11200	O	1	1.5

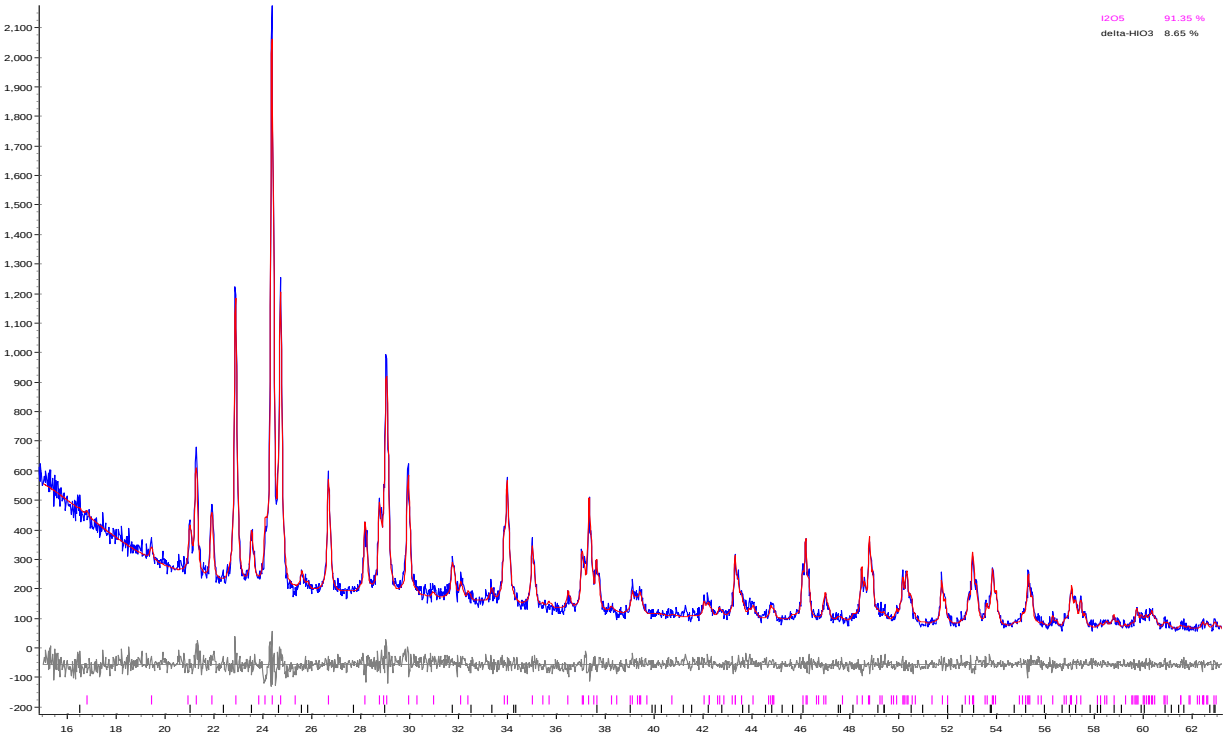
I2O5 91.35 %
delta-HIO3 8.65 %
2,100
2,000
1,900
1,800
1,700
1,600
1,500
1,400
1,300
1,200
1,100
1,000
900
800
700
600
500
400
300
200
100
0
-100
-200
16
18
20
22
24
26
28
30
32
34
36
38
40
42
44
46
48
50
52
54
56
58
60
62

5.6.6. Al/a-I_2O_5.raw"

R-Values
Rexp : 4.62 Rwp : 5.57 Rp : 4.28 GOF : 1.21
Rexp`: 15.13  Rwp`: 18.25 Rp` : 18.95 DW : 1.43

Quantitative Analysis - Rietveld
Phase 1 : delta-HIO_3 24.5(4) %
Phase 2 : I_2O_5 52.3(5) %
Phase 3 : Al 23.1(4) %

Instrument
Zero error 0.004(3)
Specimen displacement -0.04(3)

Structure 1
Phase name delta-HIO_3
R-Bragg 1.674
Spacegroup P212121
Scale 0.0000622(10)
Cell Mass 703.642
Cell Volume (Å^3) 264.08(2)
Wt% - Rietveld 24.5(4)
Double-Voigt|Approach
Cry size Lorentzian 141(5)
k: 1 LVol-IB (nm) 90(3)
k: 0.89 LVol-FWHM (nm) 126(4)
Crystal Linear Absorption Coeff. (1/cm) 930.93(9)
Crystal Density (g/cm^3) 4.4245(4)
Preferred Orientation (Dir 1 : 1 0 0) 1.1(18)
(Dir 2 : 0 0 1) 1.04(12)
Fraction of Dir 1 0(3)
Lattice parameters
a (Å) 8.4467(4)
b (Å) 6.9556(4)
c (Å) 4.4948(2)

Site	Np	x	y	z	Atom	Occ	Beq
I1	4	0.27820	0.23062	0.02640	I	1	2
O1	4	0.34140	0.43890	0.27400	O	1	2
O2	4	0.35420	0.03720	0.25500	O	1	2
O3	4	0.08730	0.25400	0.16780	O	1	2
H1	4	0.44051	0.44433	0.28298	H	1	2

Structure 2

Phase name	I_2O_5
R-Bragg	1.588
Spacegroup	P121/c1
Scale	0.0000426(6)
Cell Mass	1335.224
Cell Volume (Å^3)	433.70(3)
Wt% - Rietveld	52.3(5)
Double-Voigt|Approach	
Cry size Lorentzian	122(2)
k: 1 LVol-IB (nm)	77.5(15)
k: 0.89 LVol-FWHM (nm)	108(2)
Crystal Linear Absorption Coeff. (1/cm)	1130.86(8)
Crystal Density (g/cm^3)	5.1123(4)
Preferred Orientation (Dir 1 : 0 0 1)	0.992(3)
Lattice parameters	
a (Å)	11.0324(5)
b (Å)	5.0608(2)
c (Å)	8.1313(3)
beta (°)	107.194(3)

Site	Np	x	y	z	Atom	Occ	Beq
I1	4	0.12780	0.11700	0.21700	I	1	1
I2	4	0.37370	0.68300	0.15900	I	1	1
O1	4	0.01270	0.84700	0.15200	O	1	1.5
O2	4	0.19130	0.03500	0.43900	O	1	1.5
O3	4	0.49440	0.84900	0.33200	O	1	1.5
O4	4	0.30570	0.50000	0.29700	O	1	1.5
O5	4	0.24920	0.96900	0.11200	O	1	1.5

Structure 3

Phase name	Al
R-Bragg	0.975
Spacegroup	Fm3m
Scale	0.00152(3)
Cell Mass	107.926
Cell Volume (Å^3)	66.371(6)
Wt% - Rietveld	23.1(4)
Double-Voigt|Approach	
Cry size Lorentzian	118(6)
k: 1 LVol-IB (nm)	75(4)
k: 0.89 LVol-FWHM (nm)	105(5)
Crystal Linear Absorption Coeff. (1/cm)	133.607(13)
Crystal Density (g/cm^3)	2.7002(3)
Lattice parameters	

a (Å) 4.04879(13)

Site	Np	x	y	z	Atom	Occ	Beq
Al	4	0.00000	0.00000	0.00000	Al	1	1

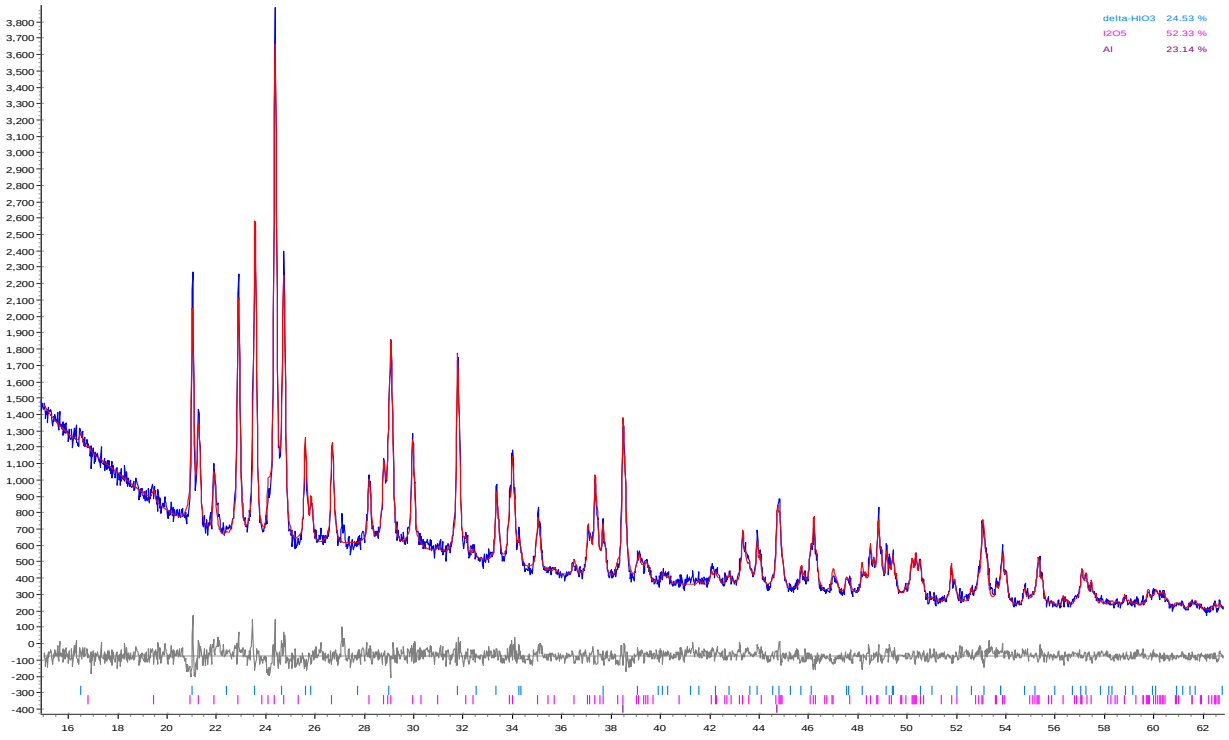

5.6.7. Al/c-I_2O_5.raw"

R-Values
Rexp : 5.21 Rwp : 7.71 Rp : 5.60 GOF : 1.48
Rexp`: 20.58  Rwp`: 30.44 Rp` : 34.94 DW : 1.38

Quantitative Analysis - Rietveld
Phase 1 : HI_3O_8 48.6(7) %
Phase 2 : Al 51.4(7) %

Instrument
Specimen displacement 0.046(6)

Structure 1
Phase name HI_3O_8
R-Bragg 3.089
Spacegroup P121/n1
Scale 0.0000103(2)
Cell Mass 2038.866
Cell Volume (Å^3) 667.69737
Wt% - Rietveld 48.6(7)
Double-Voigt|Approach
Cry size Lorentzian 330(20)
k: 1 LVol-IB (nm) 212(15)
k: 0.89 LVol-FWHM (nm) 300(20)
Crystal Linear Absorption Coeff. (1/cm) 1102.736
Crystal Density (g/cm^3) 5.071
Preferred Orientation (Dir 1 : 1 0 0) 0.996(7)
(Dir 2 : 0 1 0) 0(3)
Fraction of Dir 1 1.000(19)
Lattice parameters
a (Å) 7.5786077
b (Å) 7.7194972
c (Å) 11.4130826
beta (°) 90.16208

Site	Np	x	y	z	Atom	Occ	Beq
I1	4	0.24144	0.22767	0.09527	I	1	1
I2	4	0.33769	0.73614	0.10361	I	1	1
I3	4	0.75579	0.04724	0.19159	I	1	1
O1	4	0.45720	0.30100	0.05390	O	1	1.5
O2	4	0.12980	0.43130	0.08700	O	1	1.5
O3	4	0.17110	0.82240	0.00800	O	1	1.5
O4	4	0.44080	0.94070	0.13590	O	1	1.5
O5	4	0.18330	0.74510	0.24070	O	1	1.5

O6	4	0.78370	0.45460	0.15790	O	1	1.5
O7	4	0.80280	0.84230	0.12420	O	1	1.5
O8	4	0.97740	0.11430	0.22530	O	1	1.5
H1	4	0.87310	0.46530	0.12130	H	1	2

Structure 2

Phase name	Al
R-Bragg	0.726
Spacegroup	Fm3m
Scale	0.00206(4)
Cell Mass	107.926
Cell Volume (Å^3)	66.506(7)
Wt% - Rietveld	51.4(7)
Double-Voigt|Approach	
Cry size Lorentzian	116(7)
k: 1 LVol-IB (nm)	74(4)
k: 0.89 LVol-FWHM (nm)	104(6)
Crystal Linear Absorption Coeff. (1/cm)	133.335(13)
Crystal Density (g/cm^3)	2.6947(3)
Lattice parameters	
a (Å)	4.05154(13)

Site	Np	x	y	z	Atom	Occ	Beq
Al	4	0.00000	0.00000	0.00000	Al	1	1

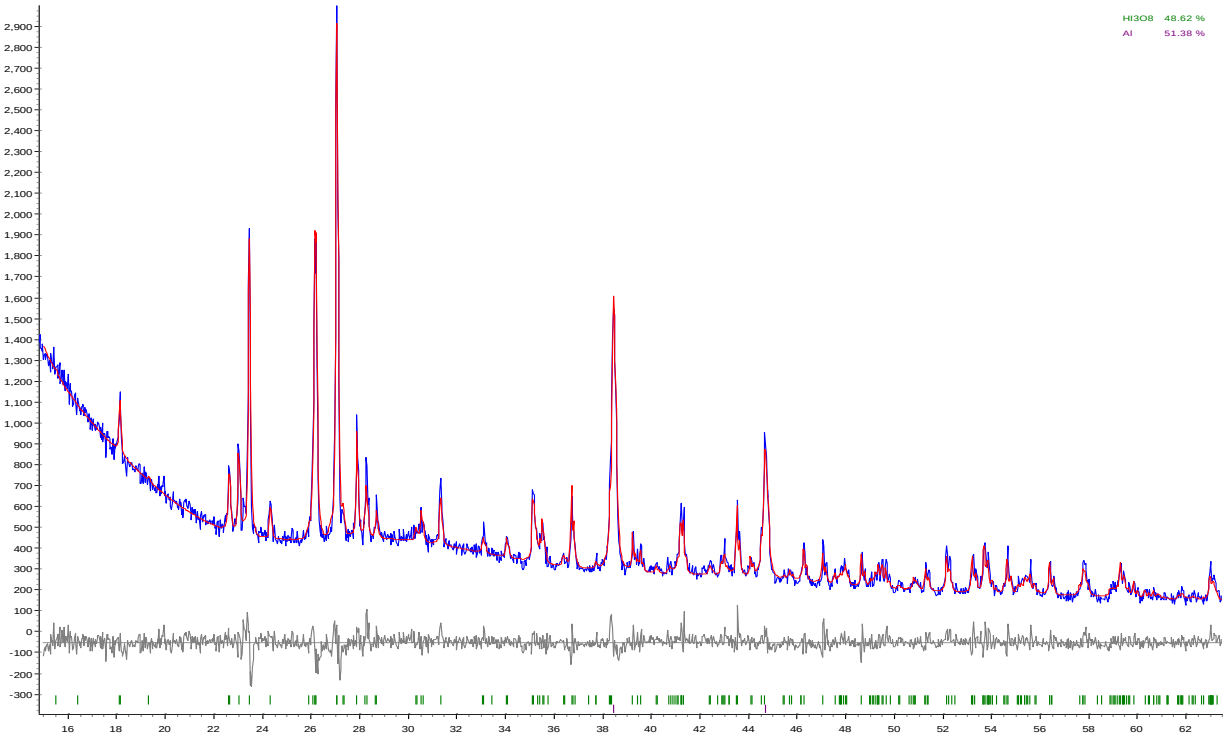
HI3O8 48.62 %
Al 51.38 %

5.6.8. c-I_2O_5.raw"

R-Values
Rexp : 5.61 Rwp : 7.22 Rp : 5.46 GOF : 1.29
Rexp`: 16.16  Rwp`: 20.80 Rp` : 23.59 DW : 1.30

Quantitative Analysis - Rietveld
Phase 1 : HI_3O_8 100.000 %

Instrument
Zero error 0.0663(17)
Specimen displacement -0.138(15)

Structure 1
Phase name HI_3O_8
R-Bragg 3.249
Spacegroup P121/n1
Scale 0.0000237(2)
Cell Mass 2038.866
Cell Volume (Å^3) 665.65(2)
Wt% - Rietveld 100.000
Double-Voigt|Approach
Cry size Lorentzian 910(80)
k: 1 LVol-IB (nm) 580(50)
k: 0.89 LVol-FWHM (nm) 810(80)
Crystal Linear Absorption Coeff. (1/cm) 1106.13(3)
Crystal Density (g/cm^3) 5.08619(15)
Preferred Orientation (Dir 1 : 0 0 1) 1.0(5)
(Dir 2 : 1 0 0) 1.0(4)
Fraction of Dir 1 1(30)
Lattice parameters
a (Å) 7.57251(13)
b (Å) 7.70991(13)
c (Å) 11.4014(2)
beta (°) 90.1792(13)

Site	Np	x	y	z	Atom	Occ	Beq
I1	4	0.24144	0.22767	0.09527	I	1	1
I2	4	0.33769	0.73614	0.10361	I	1	1
I3	4	0.75579	0.04724	0.19159	I	1	1
O1	4	0.45720	0.30100	0.05390	O	1	1.5
O2	4	0.12980	0.43130	0.08700	O	1	1.5
O3	4	0.17110	0.82240	0.00800	O	1	1.5
O4	4	0.44080	0.94070	0.13590	O	1	1.5

O5	4	0.18330	0.74510	0.24070	O	1	1.5
O6	4	0.78370	0.45460	0.15790	O	1	1.5
O7	4	0.80280	0.84230	0.12420	O	1	1.5
O8	4	0.97740	0.11430	0.22530	O	1	1.5
H1	4	0.87310	0.46530	0.12130	H	1	2

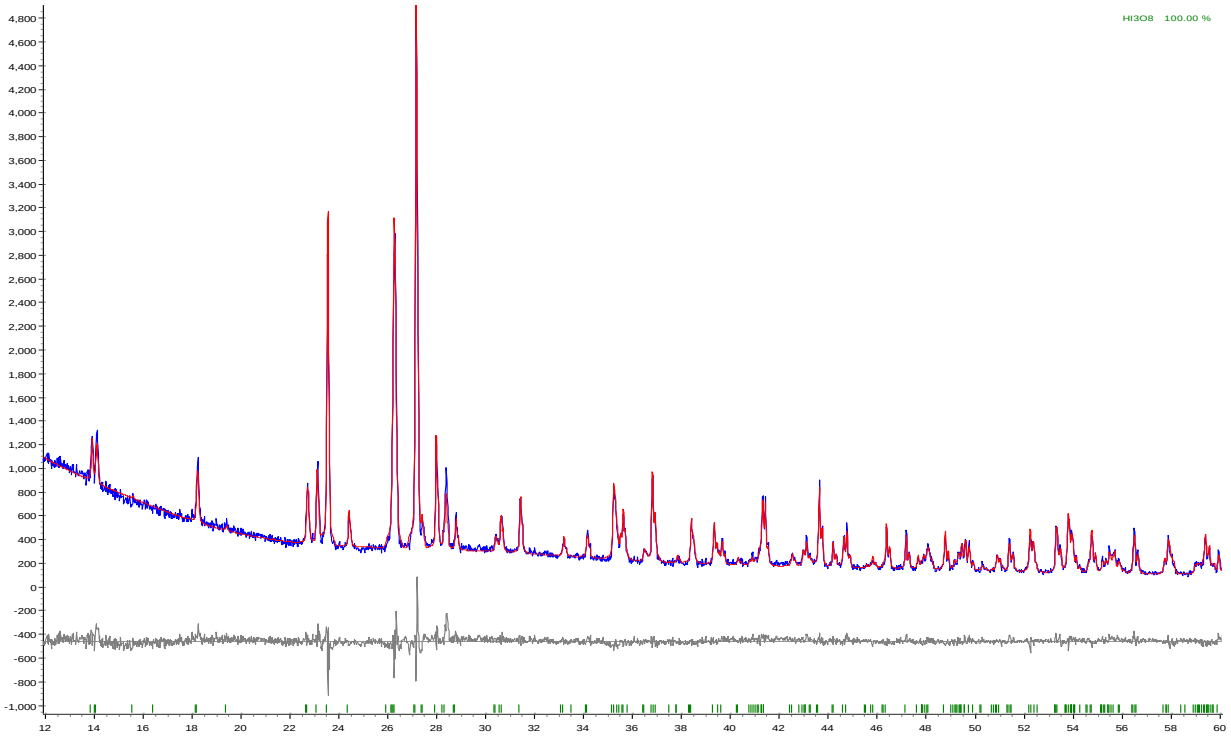

5.6.9. Al/delta-HIO_3.raw"

R-Values
Rexp : 4.45 Rwp : 5.16 Rp : 3.96 GOF : 1.16
Rexp`: 22.62  Rwp`: 26.21 Rp` : 33.46 DW : 1.55

Quantitative Analysis - Rietveld
Phase 1 : alpha-HIO_3 9.6(5) %
Phase 2 : delta-HIO_3 68.9(8) %
Phase 3 : Al 21.5(7) %

Instrument
Zero error 0.027(3)
Specimen displacement -0.10(3)

Structure 1
Phase name alpha-HIO_3
R-Bragg 3.155
Spacegroup P212121
Scale 0.0000173(9)
Cell Mass 703.642
Cell Volume (Å^3) 251.89716
Wt% - Rietveld 9.6(5)
Double-Voigt|Approach
Cry size Lorentzian 290(90)
k: 1 LVol-IB (nm) 190(60)
k: 0.89 LVol-FWHM (nm) 260(80)
Crystal Linear Absorption Coeff. (1/cm) 975.952
Crystal Density (g/cm^3) 4.639
Lattice parameters
a (Å) 5.5400000
b (Å) 5.8768000
c (Å) 7.7370000

Site	Np	x	y	z	Atom	Occ	Beq
I1	4	0.20395	-0.08538	0.15737	I	1	1.13
O1	4	-0.06832	0.02425	0.25690	O	1	1.56
O2	4	0.33409	0.19685	0.08399	O	1	1.79
O3	4	0.09469	-0.15837	-0.05215	O	1	1.73
H1	4	0.23752	0.32350	0.13452	H	1	3.07

Structure 2
Phase name delta-HIO_3
R-Bragg 1.275

Spacegroup	P212121
Scale	0.000118(3)
Cell Mass	703.642
Cell Volume (Å^3)	263.83(2)
Wt% - Rietveld	68.9(8)
Double-Voigt|Approach	
Cry size Lorentzian	870(150)
k: 1 LVol-IB (nm)	550(100)
k: 0.89 LVol-FWHM (nm)	780(130)
Crystal Linear Absorption Coeff. (1/cm)	931.83(8)
Crystal Density (g/cm^3)	4.4288(4)
Preferred Orientation (Dir 1 : 1 0 0)	0.56(2)
(Dir 2 : 0 0 1)	0.977(8)
Fraction of Dir 1	0.19(2)
Lattice parameters	
a (Å)	8.4447(3)
b (Å)	6.9575(3)
c (Å)	4.4903(3)

Site	Np	x	y	z	Atom	Occ	Beq
I1	4	0.27820	0.23062	0.02640	I	1	2
O1	4	0.34140	0.43890	0.27400	O	1	2
O2	4	0.35420	0.03720	0.25500	O	1	2
O3	4	0.08730	0.25400	0.16780	O	1	2
H1	4	0.44051	0.44433	0.28298	H	1	2

Structure 3

Phase name	Al
R-Bragg	1.023
Spacegroup	Fm3m
Scale	0.00095(4)
Cell Mass	107.926
Cell Volume (Å^3)	66.364(14)
Wt% - Rietveld	21.5(7)
Double-Voigt|Approach	
Cry size Lorentzian	121(16)
k: 1 LVol-IB (nm)	77(10)
k: 0.89 LVol-FWHM (nm)	107(15)
Crystal Linear Absorption Coeff. (1/cm)	133.62(3)
Crystal Density (g/cm^3)	2.7005(6)
Lattice parameters	
a (Å)	4.0486(3)

Site	Np	x	y	z	Atom	Occ	Beq
Al	4	0.00000	0.00000	0.00000	Al	1	1

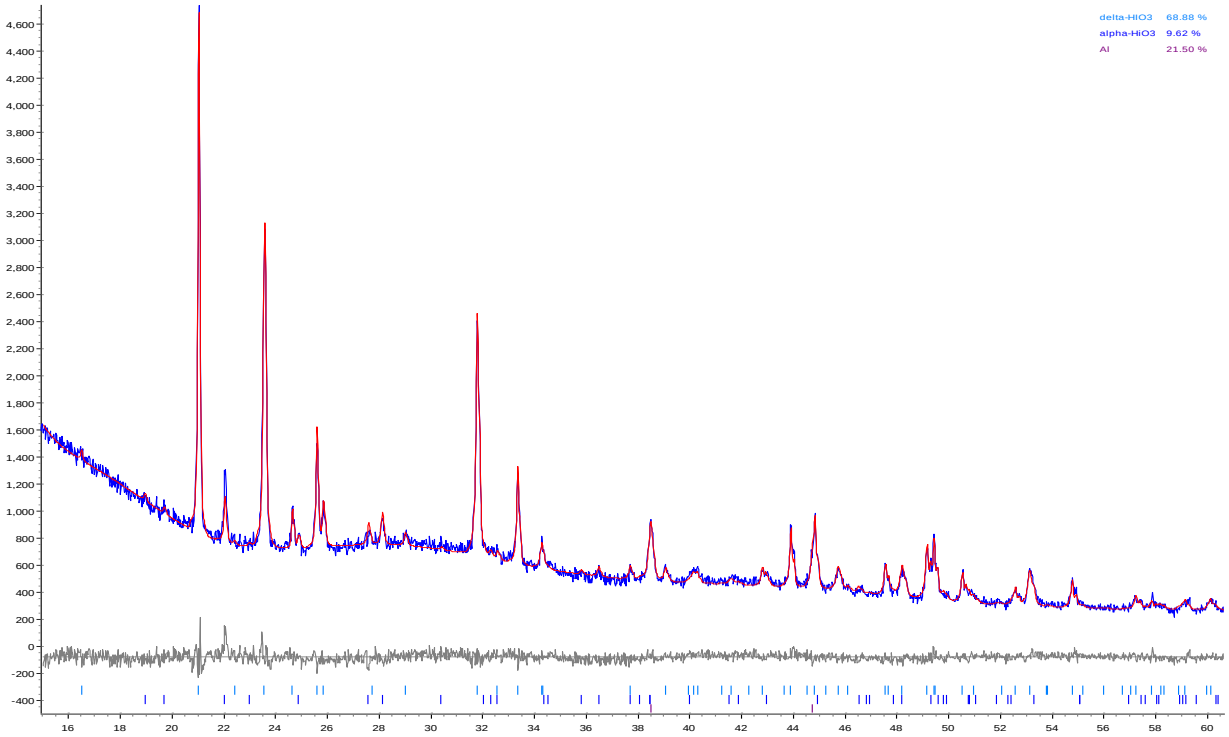
delta-HIO3 68.88 %
alpha-HIO3 9.62 %
Al 21.50 %
4,600
4,400
4,200
4,000
3,800
3,600
3,400
3,200
3,000
2,800
2,600
2,400
2,200
2,000
1,800
1,600
1,400
1,200
1,000
800
600
400
200
0
-200
-400
16
18
20
22
24
26
28
30
32
34
36
38
40
42
44
46
48
50
52
54
56
58
60

5.6.10. delta-HIO_3.raw"

R-Values
Rexp : 5.50 Rwp : 6.78 Rp : 5.08 GOF : 1.23
Rexp`: 9.45  Rwp`: 11.64 Rp` : 10.60 DW : 1.33

Quantitative Analysis - Rietveld
Phase 1 : delta-HIO_3 100.000 %

Instrument
Zero error 0.0688(12)
Specimen displacement -0.149(13)

Structure 1
Phase name delta-HIO_3
R-Bragg 1.133
Spacegroup P212121
Scale 0.000406(2)
Cell Mass 703.642
Cell Volume (Å^3) 264.161(10)
Wt% - Rietveld 100.000
Double-Voigt|Approach
Cry size Lorentzian 280(6)
k: 1 LVol-IB (nm) 178(4)
k: 0.89 LVol-FWHM (nm) 249(6)
Crystal Linear Absorption Coeff. (1/cm) 930.64(4)
Crystal Density (g/cm^3) 4.42316(17)
Preferred Orientation (Dir 1 : 1 0 0) 0.639(10)
(Dir 2 : 0 0 1) 0.987(3)
Fraction of Dir 1 0.197(11)
Lattice parameters
a (Å) 8.44609(13)
b (Å) 6.95622(15)
c (Å) 4.49614(12)

Site	Np	x	y	z	Atom	Occ	Beq
I1	4	0.27820	0.23062	0.02640	I	1	2
O1	4	0.34140	0.43890	0.27400	O	1	2
O2	4	0.35420	0.03720	0.25500	O	1	2
O3	4	0.08730	0.25400	0.16780	O	1	2
H1	4	0.44051	0.44433	0.28298	H	1	2

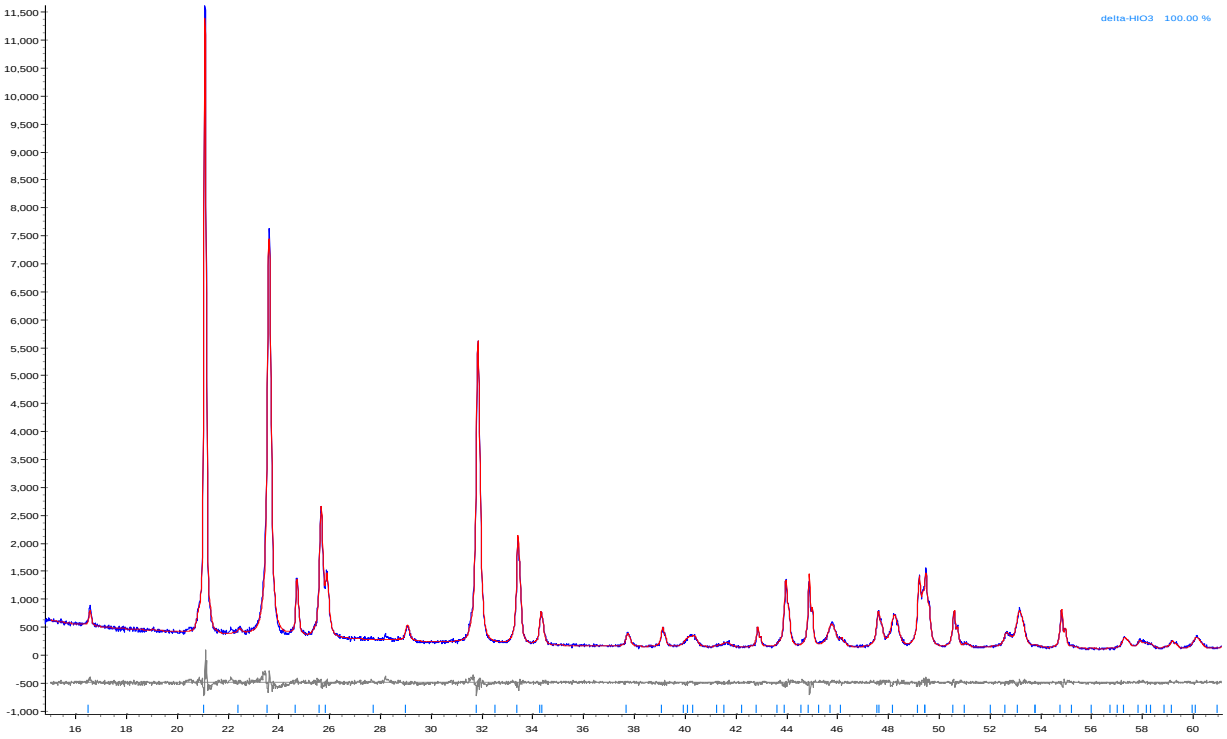
delta-HIO3 100.00 %
11,500
11,000
10,500
10,000
9,500
9,000
8,500
8,000
7,500
7,000
6,500
6,000
5,500
5,000
4,500
4,000
3,500
3,000
2,500
2,000
1,500
1,000
500
0
-500
-1,000
16
18
20
22
24
26
28
30
32
34
36
38
40
42
44
46
48
50
52
54
56
58
60

5.6.11. Al/c-HIO_3.raw"

R-Values
Rexp : 4.29 Rwp : 7.16 Rp : 4.91 GOF : 1.67
Rexp`: 24.08  Rwp`: 40.21 Rp` : 49.56 DW : 1.10

Quantitative Analysis - Rietveld
  Phase 1 : alpha-HIO_3 30(3) %
  Phase 2 : HI_3O_8 10(3) %
  Phase 3 : AL 61(3) %

Instrument
  Zero error -0.027(4)
  Specimen displacement -0.06(3)
s
Structure 1
  Phase name alpha-HIO_3
  R-Bragg 5.266
  Spacegroup P212121
  Scale 0.000080(9)
  Cell Mass 703.642
  Cell Volume (Å^3) 251.49(3)
  Wt% - Rietveld 30(3)
  Double-Voigt|Approach
    Cry size Lorentzian 1500(1100)
    k: 1 LVol-IB (nm) 1000(700)
    k: 0.89 LVol-FWHM (nm) 1400(1000)
  Strain
    Strain G 0.00(3)
    e0 0.00000(7)
  Crystal Linear Absorption Coeff. (1/cm) 977.54(11)
  Crystal Density (g/cm^3) 4.6461(5)
  Preferred Orientation (Dir 1 : 1 0 0) 0.52(5)
    (Dir 2 : 0 1 0) 0.21(12)
    Fraction of Dir 1 0.98(8)
  Preferred Orientation Spherical Harmonics
    Order 8
    y00 1
    y20 0.72(18)
    y22p -0.2(2)
    y40 -0.7(2)
    y42p 0.10(9)
    y44p -0.1(2)
    y60 0.31(17)
    y62p -0.03(8)

y64p	0.07(8)
y66p	-0.16(14)
y80	0.72(13)
y82p	-0.06(10)
y84p	-0.08(7)
y86p	-0.46(8)
y88p	-0.00(7)
Lattice parameters	
a (Å)	5.5359(3)
b (Å)	5.8743(4)
c (Å)	7.7334(5)

Site	Np	x	y	z	Atom	Occ	Beq
I1	4	0.20395	-0.08538	0.15737	I	1	1.13
O1	4	-0.06832	0.02425	0.25690	O	1	1.56
O2	4	0.33409	0.19685	0.08399	O	1	1.79
O3	4	0.09469	-0.15837	-0.05215	O	1	1.73
H1	4	0.23752	0.32350	0.13452	H	1	3.07

Structure 2

Phase name	HI_3O_8
R-Bragg	3.469
Spacegroup	P121/n1
Scale	0.0000035(12)
Cell Mass	2038.866
Cell Volume (Å^3)	663.9(2)
Wt% - Rietveld	10(3)
Double-Voigt|Approach	
Cry size Lorentzian	330(100)
k: 1 LVol-IB (nm)	210(70)
k: 0.89 LVol-FWHM (nm)	290(90)
Crystal Linear Absorption Coeff. (1/cm)	1109.1(3)
Crystal Density (g/cm^3)	5.1000(15)
Preferred Orientation (Dir 1 : 0 1 0)	0.26(19)
(Dir 2 : 1 0 0)	0.74(10)
Fraction of Dir 1	0.22(8)
Preferred Orientation Spherical Harmonics	
Order	4
y00	1
y20	2.0(10)
y22m	0.4(9)
y22p	0.2(2)
y40	-2.8(9)
y42m	-2.4(9)
y42p	0.24(15)

y44m -0.5(3)
y44p 1.0(8)
Lattice parameters
a (Å) 7.5720(12)
b (Å) 7.7119(12)
c (Å) 11.369(2)
beta (°) 90.02(3)

Site	Np	x	y	z	Atom	Occ	Beq
I1	4	0.24144	0.22767	0.09527	I	1	1
I2	4	0.33769	0.73614	0.10361	I	1	1
I3	4	0.75579	0.04724	0.19159	I	1	1
O1	4	0.45720	0.30100	0.05390	O	1	1.5
O2	4	0.12980	0.43130	0.08700	O	1	1.5
O3	4	0.17110	0.82240	0.00800	O	1	1.5
O4	4	0.44080	0.94070	0.13590	O	1	1.5
O5	4	0.18330	0.74510	0.24070	O	1	1.5
O6	4	0.78370	0.45460	0.15790	O	1	1.5
O7	4	0.80280	0.84230	0.12420	O	1	1.5
O8	4	0.97740	0.11430	0.22530	O	1	1.5
H1	4	0.87310	0.46530	0.12130	H	1	2

Structure 3
Phase name AL
R-Bragg 5.378
Spacegroup Fm3m
Scale 0.00403(10)
Cell Mass 107.926
Cell Volume (Å^3) 66.380(10)
Wt% - Rietveld 61(3)
Double-Voigt|Approach
Cry size Lorentzian 107(5)
k: 1 LVol-IB (nm) 68(3)
k: 0.89 LVol-FWHM (nm) 95(4)
Crystal Linear Absorption Coeff. (1/cm) 133.588(19)
Crystal Density (g/cm^3) 2.6999(4)
Lattice parameters
a (Å) 4.04898(19)

Site	Np	x	y	z	Atom	Occ	Beq
Al	4	0.00000	0.00000	0.00000	Al	1	1

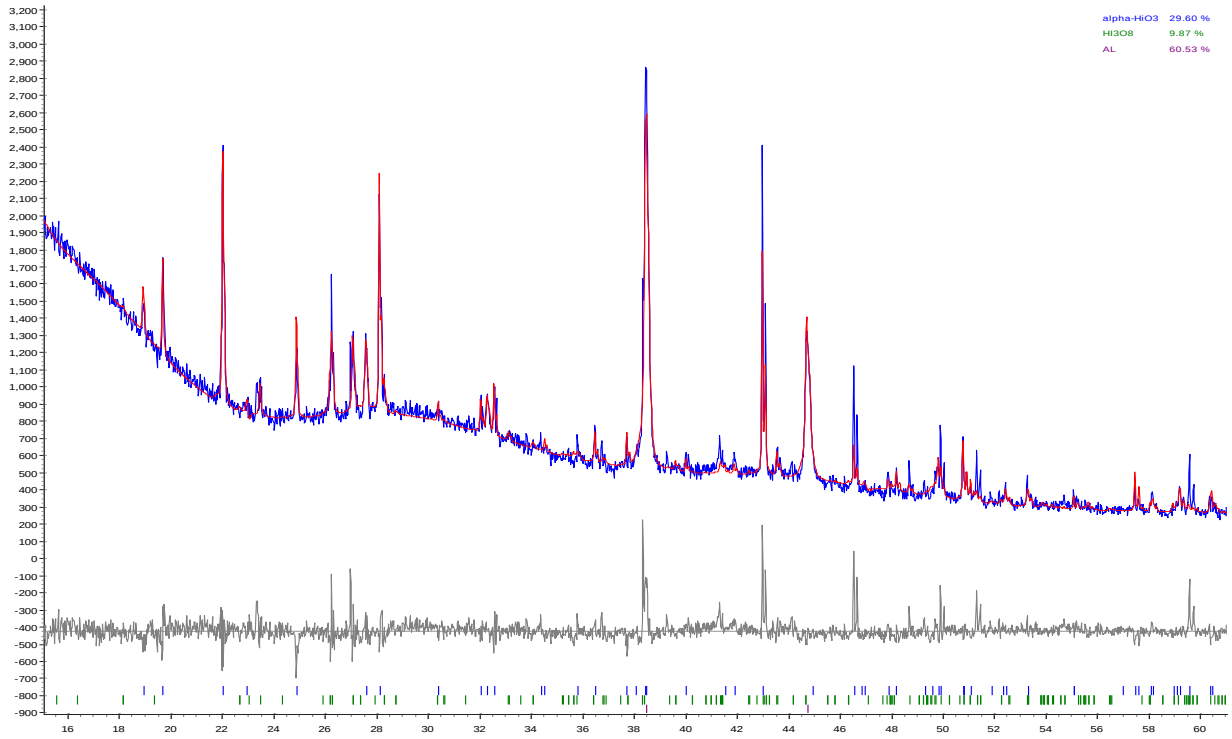
alpha-HiO3 29.60 %
HI3O8 9.87 %
AL 60.53 %

5.6.12. c-HIO_3.raw"

R-Values
Rexp : 5.31 Rwp : 11.82 Rp : 8.72 GOF : 2.23
Rexp`: 9.95  Rwp`: 22.16 Rp` : 20.75 DW : 0.53

Quantitative Analysis - Rietveld
  Phase 1 : alpha-HIO_3 88.7(3) %
  Phase 2 : HI_3O_8 11.3(3) %

Instrument
  Zero error 0.2291(12)
  Specimen displacement -0.062(10)

Structure 1
  Phase name alpha-HIO_3
  R-Bragg 8.740
  Spacegroup P212121
  Scale 0.000284(3)
  Cell Mass 703.642
  Cell Volume (Å^3) 252.308(8)
  Wt% - Rietveld 88.7(3)
  Double-Voigt|Approach
    Cry size Lorentzian 411(14)
    k: 1 LVol-IB (nm) 262(9)
    k: 0.89 LVol-FWHM (nm) 366(12)
  Crystal Linear Absorption Coeff. (1/cm) 974.36(3)
  Crystal Density (g/cm^3) 4.63096(14)
  Preferred Orientation (Dir 1 : 1 0 0) 0.86(3)
    (Dir 2 : 0 1 0) 1.13(4)
    Fraction of Dir 1 0.55(12)
  Lattice parameters
    a (Å) 5.54287(9)
    b (Å) 5.88041(11)
    c (Å) 7.74085(14)

Site	Np	x	y	z	Atom	Occ	Beq
I1	4	0.20395	-0.08538	0.15737	I	1	1.13
O1	4	-0.06832	0.02425	0.25690	O	1	1.56
O2	4	0.33409	0.19685	0.08399	O	1	1.79
O3	4	0.09469	-0.15837	-0.05215	O	1	1.73
H1	4	0.23752	0.32350	0.13452	H	1	3.07

Structure 2

Phase name	HI_3O_8
R-Bragg	3.993
Spacegroup	P121/n1
Scale	0.00000469(15)
Cell Mass	2038.866
Cell Volume (Å^3)	667.60(11)
Wt% - Rietveld	11.3(3)
Double-Voigt|Approach	
Cry size Lorentzian	270(30)
k: 1 LVol-IB (nm)	170(20)
k: 0.89 LVol-FWHM (nm)	240(30)
Crystal Linear Absorption Coeff. (1/cm)	1102.90(18)
Crystal Density (g/cm^3)	5.0714(8)
Preferred Orientation (Dir 1 : 1 0 0)	0.62(16)
(Dir 2 : 0 0 1)	1.06(2)
Fraction of Dir 1	0.11(11)
Lattice parameters	
a (Å)	7.5792(5)
b (Å)	7.7186(8)
c (Å)	11.4118(13)
beta (°)	90.181(10)

Site	Np	x	y	z	Atom	Occ	Beq
I1	4	0.24144	0.22767	0.09527	I	1	1
I2	4	0.33769	0.73614	0.10361	I	1	1
I3	4	0.75579	0.04724	0.19159	I	1	1
O1	4	0.45720	0.30100	0.05390	O	1	1.5
O2	4	0.12980	0.43130	0.08700	O	1	1.5
O3	4	0.17110	0.82240	0.00800	O	1	1.5
O4	4	0.44080	0.94070	0.13590	O	1	1.5
O5	4	0.18330	0.74510	0.24070	O	1	1.5
O6	4	0.78370	0.45460	0.15790	O	1	1.5
O7	4	0.80280	0.84230	0.12420	O	1	1.5
O8	4	0.97740	0.11430	0.22530	O	1	1.5
H1	4	0.87310	0.46530	0.12130	H	1	2

Peaks Phase 1

Phase name	Peaks Phase:0

Type	Position	I		
FP	21.608(3)	3.15(13)	Cry size Lor	174(12)
		k: 1, LVol-IB(nm)		111(8)
		k: 0.89, LVol-FWHM(nm)		155(11)
FP	26.6321(17)	8.6(2)	Cry size Lor	174(12)

k: 1, LVol-IB(nm) 111(8)
k: 0.89, LVol-FWHM(nm) 155(11)

FP 31.051(3) 3.95(18) Cry size Lor 174(12)
k: 1, LVol-IB(nm) 111(8)
k: 0.89, LVol-FWHM(nm) 155(11)

FP 44.483(6) 3.6(3) Cry size Lor 174(12)
k: 1, LVol-IB(nm) 111(8)
k: 0.89, LVol-FWHM(nm) 155(11)

FP 49.162(6) 4.4(4) Cry size Lor 174(12)
k: 1, LVol-IB(nm) 111(8)
k: 0.89, LVol-FWHM(nm) 155(11)

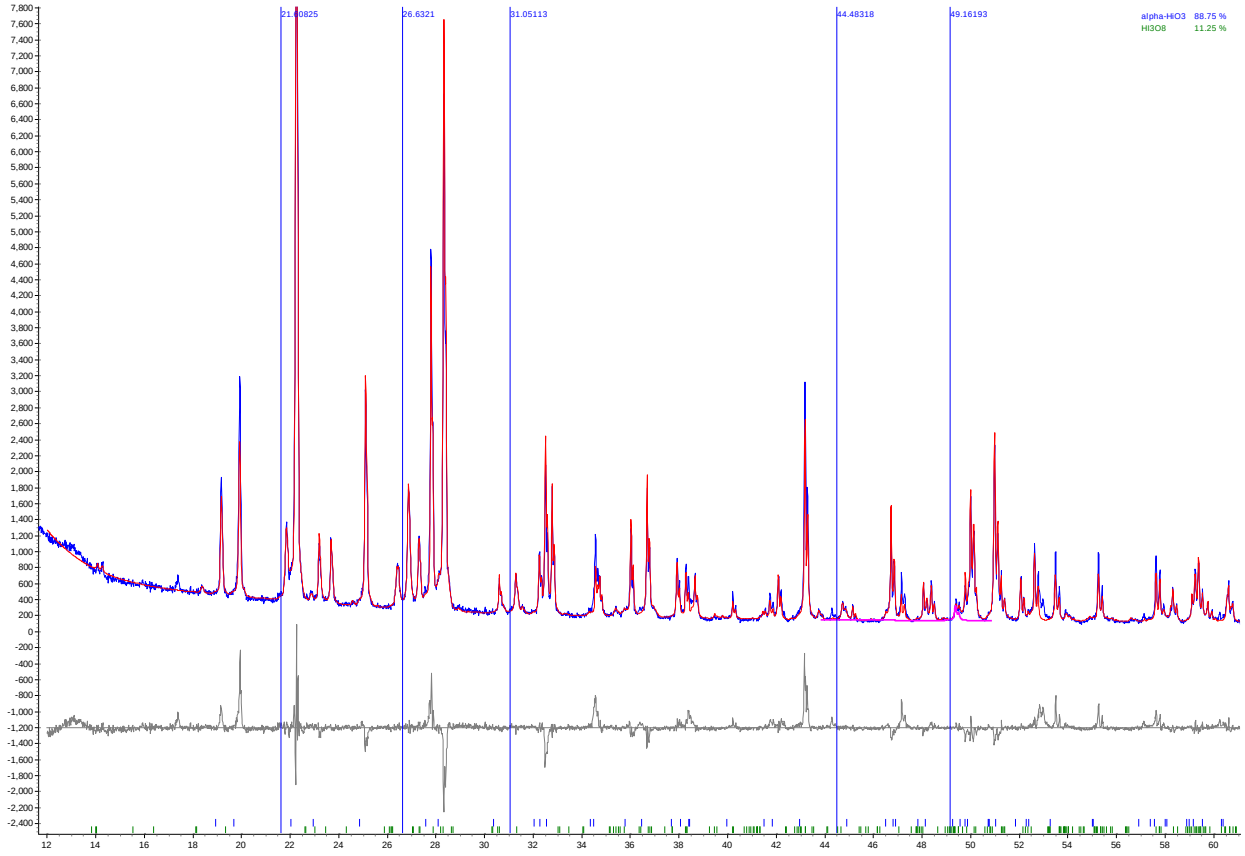

Chapter 6: Carbon addition lowers initiation and iodine release temperatures from iodine oxide-based biocidal energetic materials[*]

Overview

Iodine oxides are of significant interest as strong oxidizers in energetic formulation that also operate as iodine release agents for neutralization of spores using strong thermal pulses. In this Chapter incorporation of carbon black (CB) as the main fuel or additive into iodine oxides-based energetic materials are shown to lower both initiation and iodine release temperatures compared to those of Al/iodine oxides and Ta/iodine oxides thermites. Those lowering effects were triggered by a condensed phase CB-iodine oxides reaction explored by high heating rate time-resolved temperature-jump time-of-flight mass spectrometry and low heating rate thermogravimetric analysis/differential scanning calorimetry results. I observe that other carbon allotropes, such as carbon nanotubes and functionalized graphene sheets, also feature the similar effect as CB. Fourier transform infrared spectroscopy analysis shows that the presence of CB lowered the bond energy of iodine oxide on the surface to trigger the CB-iodine oxide initiation at a relatively lower temperature.

[*] The results presented in this chapter have been published in the following journal article: Wu, T.; Wang, X.; DeLisio, J.B.; Holdren, S.; Zachariah, M.R., Carbon addition lowers initiation and iodine release temperatures from iodine oxide-based biocidal energetic materials. *Carbon* 2018 130 410-415.

6.1. Introduction

Developing new energetic materials with high efficiency neutralization of biological warfare agents has gained increased attention due to the increased threat of bioterrorism [1-5]. Preliminary laboratory studies have suggested that an ideal neutralization process should generate not only a high temperature, but also release a long-lasting biocidal agent [6-12]. The main limitation of conventional energetic materials is low neutralization efficiency since the thermal neutralization mechanism is dominant in this case, with the lack of effective biocidal agent release [6]. Therefore, it has been proposed that simultaneously delivering a rapid thermal pulse with a remnant biocidal agent would prolong the exposure time and improve the inactivation process [13].

Halogen-containing energetic materials have shown the most promise because of their excellent biocidal properties [14], compared to other biological energetic materials [15-17]. Among all halogens, iodine stands out owing to its strong neutralization effect. Different methods have been reported for incorporating elemental iodine into energetic materials [14, 18-20]. For instance, Dreizin et al. employed mechanically alloyed aluminum-iodine composites as a fuel in energetic formulations and the initiation and combustion tests in air indicated that higher iodine concentration lowers initiation temperatures and the combustion temperatures were not substantially diminished [12]. They also found improvements in terms of pressurization rate and maximum pressure at constant volume with 15 wt.% and 20 wt.% of I_2 [12]. Furthermore, an effective inactivation of aerosolized spores has been achieved using Al/I_2 and Al/B/I_2 composites with 15-20 wt.% of iodine [14]. Another efficient method

is to use iodine-containing compounds as an oxidizer, particularly iodine oxides/iodic acids.

Among all the iodine oxides/iodic acids (I_2O_5, I_4O_9, HI_3O_8, HIO_3, H_5IO_6, etc [21-23]), I_2O_5 is the most studied in thermite systems [24-28] due to its relatively high iodine content (~76% iodine mass fraction). In these studies, aluminum particles with different sizes were chosen as the fuel due to its high reaction enthalpy, thermal conductivity and availability. With reported propagation velocities of up to ~2,000 m/s for loose ball-milled nano-aluminum and nano-scaled I_2O_5 (~10 nm) [27], I_2O_5 shows its high potential in aluminum-based thermites as an extremely aggressive oxidizer. Constant volume combustion tests also show nano-Al/micro-I_2O_5 outperforms traditional aluminum-based thermites such as Al/CuO and Al/Fe_2O_3 [28].

Aluminum has a passivating alumina shell that stabilizes the material at ambient conditions. However, once the aluminum core is heated near the melting temperature, obtaining sufficient mobility, it can diffuse through the oxide shell and interact with any available oxidizer ultimately leading to initiation [29]. However, iodine oxide releases O_2 at a relatively low temperature (~450 C) which is well below the Al melting point, where reaction is most advantaged [30]. To explore the fuel melting aspect of initiation, I have also used tantalum as a fuel since it has a much higher melting point (~3000 ºC) than Al (660 ºC), and thus would not melt at the point of initiation. However, the immobile tantalum core will not react with iodine oxide until some cracks appeared in the Ta_2O_5 shell upon heating (higher than 500 C) due to the amorphous to crystalline phase change of the oxide shell [31]. Those cracks serve as a low resistance pathway for the oxygen to react with the tantalum core [31].

In this work, I employed carbon as a fuel to better interpret the initiation process of iodine oxide-based energetic materials since it has a high melting point (3550 ºC) and no passivating shell. Therefore, there will be direct contact between the fuel and oxidizer enabling further understanding of the initiation process. Time-resolved temperature-jump time-of-flight mass spectrometry was used to study the initial events of bare oxidizers or carbon/iodine oxides thermites under rapid heating rates, enabling me to probe the reaction process on a time scale close to that of a combustion event. Slow heating rate thermogravimetric analysis and differential scanning calorimetry in an argon environment was also employed to further probe the reaction mechanism. Both methods indicate that carbon black (CB) and other carbon allotropes, such as functionalized graphene sheets and carbon nanotubes, can lower the iodine release temperature from iodine oxides such as I_2O_5, HIO_3 and HI_3O_8, via a condensed phase reaction mechanism. More importantly, I also found that CB as an additive with only 3 wt% can also significantly lower the initiation and iodine release temperatures for both Al/iodine oxides and Ta/iodine oxides thermites, indicating the potential use of CB in biocidal applications. In addition, Fourier transform infrared spectroscopy analysis was employed to examine the structural changes, specifically how the vibrations of I_2O_5 are affected by the addition of carbon black. The result implies that the presence of CB lowered the bond energy of iodine oxide on the surface and therefore triggered this condensed phase reaction.

6.2. Experimental Details

6.2.1 Materials

The aluminum nanopowders (Al) (Alex, ~80 nm) were purchased from Novacentrix. The active Al was 81 % by mass, determined by thermogravimetric analysis. Nano-tantalum powders (<50 nm, Ta) were purchased from Global Advanced Metals. Nano-sized carbon black (~50 nm, CB) was obtained from Cabot Corporation. Multi-wall carbon nanotubes and iodine pentoxide (I_2O_5) purchased from Sigma-Aldrich were directly used as received. Functionalized graphene sheets (FGS) with C:O molar ratio of 15 and 60 were obtained from Aksay et.al [32] and labeled as FGS_{15} and FGS_{60}, respecrively. All the other chemicals were of analytical grade and used as purchased without further treatment. HI_3O_8 was prepared via thermal treatment of commercial HIO_3 at ~180 ºC for 30 minutes.

6.2.2 Preparation of thermites

Aluminum, tantalum or CB was stoichiometrically mixed with I_2O_5, HIO_3 and HI_3O_8 based on the following equations, respectively, in hexane followed by 30 minutes of sonication.

$$3C + 2HIO_3 \rightarrow 3I_2 + H_2 + 3CO_2$$

$$8C + 2HI_3O_8 \rightarrow 3I_2 + H_2 + 8CO_2$$

$$5C + 2I_2O_5 \rightarrow 2I_2 + 5CO_2$$

$$4Al + 2HIO_3 \rightarrow I_2 + 2Al_2O_3 + H_2$$

$$32Al + 6HI_3O_8 \rightarrow 9I_2 + 16Al_2O_3 + 3H_2$$

$$10Al + 3I_2O_5 \rightarrow 3I_2 + 5Al_2O_3$$

After room temperature evaporation of the solvent in a desiccator, the solid thermite powders were used. To show the morphology of the thermites, as an example, the SEM images of CB/Ta/HI_3O_8 along with Ta/HI_3O_8 and HI_3O_8 are shown in Figure S6.1. The fact that fuel (CB, Ta) nanoparticles were well distributed on the surface of HI_3O_8 indicates a good mixing of fuel and oxidizer.

6.2.3. T-Jump/TOFMS measurement and high-speed imaging

The decomposition of oxide particles was investigated using a T-Jump/TOFMS [6]. Typically, a ~1 cm long platinum wire (76 um in width) with a thin layer coating of oxidizer sample was rapidly joule-heated to about 1200 °C by a 3 ms pulse at a heating rate of 5 × ~10^5 °C/s. The current and voltage signals were recorded, and the temporal temperature of the wire was measured according to the Callendar–Van Dusen equation [29]. However, the sample temperature can be different than the wire temperature, and we are only able to directly measure the wire temperature by this method. To address this concern, we have previously developed a heat transfer model to estimate the true sample temperature during the heating event [33, 34]. The major conclusion from this quantitative model is that the characteristic heating time of nanoparticles on the wire is sufficiently fast, that even though we are using a high heating rate, the nanoparticles on the wire are expected to be essentially at the wire temperature ($\pm$ 5 °C). Therefore, initiation/ignition temperatures of the materials in contact with the wire is equal to the wire temperature within any experimental and practical effect. Adding a material with a higher thermal conductivity such as carbon would only improve the situation. The temperature of the wire corresponding to the initial release of O_2 or iodine was regarded

as the O_2 or iodine release temperature. Mass spectra were measured every 0.1 ms. The detailed experimental set-up is given in our previous papers [6, 29].

To identify the point of initiation, a high-speed camera (Vision Research Phantom v12.0) was employed to record the combustion on the wire during heating. Initiation temperatures of thermite reactions in vacuum were measured from the correlation of optical emission from high speed imaging and temporal temperature of the wire and were further analyzed in combination with the temporal mass spectra. Each measurement was repeated 3 times.

6.2.4. Thermogravimetric analysis/differential scanning calorimetry (TGA/DSC) measurement

Thermogravimetric analysis and Differential Scanning Calorimetry were conducted using an SDT Q600 (TA instruments). The measurement was performed under a 100 mL min^{-1} argon flow with ~ 1.0 mg samples placed into an alumina pan and heated from room temperature up to 550 °C (or higher temperature) at a rate of 5 °C/min.

6.2.5. Fourier Transform Infrared Spectroscopy (FTIR) analysis

Attenuated total reflection (ATR) FTIR spectra of I_2O_5 samples with and without CB were collected using a Nicolet iS-50R spectrometer equipped with a room temperature deuterated triglycine sulfate (DTGS) detector FTIR spectroscopy. A Thermo Scientific Smart iTX accesory was installed to collect the ATR spectra shown here at 4 cm^{-1}resolution and averaged over 25 scans.

6.3. Results and Discussion

To investigate the performance of iodine oxides/iodic acids as oxidizers in thermite systems, I have previously employed Al and Ta as fuels in Chapter 5. However, both aluminum and tantalum have an oxide shell, which to some extent restricted our understanding on how those thermites react during initiation [35], and thus motivated the use of carbon. Commercial iodine pentoxide was first examined because it is the most extensively studied and can be obtained easily [36].

T-Jump/TOFMS was employed to study the initial events of bare oxidizers or thermites under rapid heating [37]. I plot in Figure 6.1 both the iodine and oxygen release temperatures vs. the reaction initiation temperature. Different initiation temperatures were obtained for thermites with different fuels including Al, Ta and CB. I have previously argued that the initiation of Al-based and Ta-based thermites is dominated by the melting of aluminum and the phase change of the Ta_2O_5 shell, respectively [35]. As to CB, the initiation temperature of CB/I_2O_5 is ~330 ºC (determined from release of CO_2 product since there is virtually no optical signature of initiation), and more than 100 ºC lower than the iodine release temperature from the neat I_2O_5, which implies a condensed phase reaction mechanism may be dominant here.

Ignition by its nature is essentially the point where self-heating by exothermic reaction exceeds heat loss and product formation occurs. It should be noted that the light emission of metal based thermites aligns well with the product release profile based on our previous work [29]. One major conclusion from this paper is that the product formation determined by mass spectrometry correlates well with the temperature at which light emission begins. Therefore, ignition/initiation in these

experiments is defined at the point of CO_2 production for C-based thermites (Figure S6.2) and the light emission of Al/Ta-based thermites.

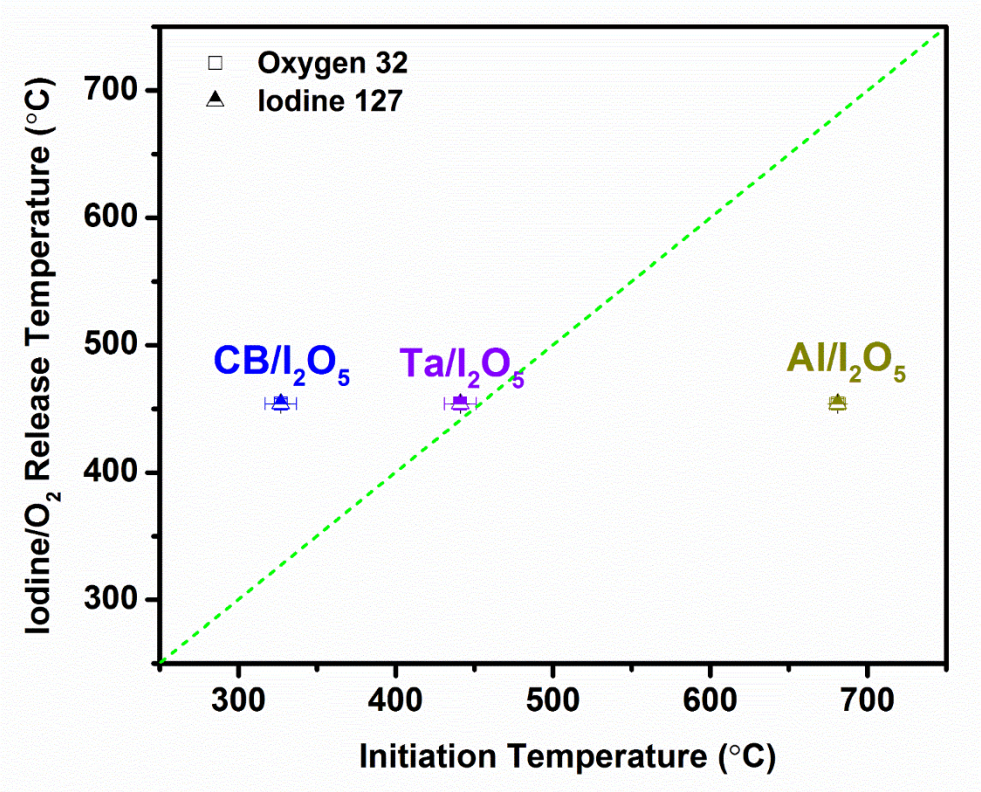

Figure 6.1. Release temperature of I and O_2 from neat I_2O_5 vs. initiation temperature of corresponding Al-based, Ta-based and CB-based thermites under vacuum. Error bars represent two replicates. The diagonal dashed line would imply a perfect correlation between initiation and release temperature.

To understand the relationship between iodine release and initiation, I plotted iodine release temperatures vs initiation temperatures in Figure 6.2. The dotted red line represents the iodine/O_2 release temperatures (~450 °C) from neat I_2O_5 obtained through a high heating method. Note that, the y-axis in Figure 6.2 is the iodine/O_2 release temperature of the fuel/I_2O_5 mixture; however, the y-axis in Figure 6.1 is the iodine/O_2 release temperature of the neat I_2O_5. Since CB/I_2O_5 ignition was initiated at

a very low temperature, 3 wt% CB was introduced into both Al/I_2O_5 and Ta/I_2O_5 systems to investigate the effect of CB as an additive.

Results in Figure 6.2 shows that the initiation temperature is correlated with the iodine release temperature for all cases except for Al/I_2O_5 in which its initiation was controlled by the mobilization of the aluminum core. When aluminum is employed as the fuel, iodine release is actually delayed to a significantly higher temperature compared with neat I_2O_5 (550 vs. 450 ^oC). This delay might be caused by the interaction between the alumina shell and I_2O_5, which to some extent stabilizes I_2O_5 and therefore delays its decomposition. Similar effects of halogen interactions have been reported in previous studies [26, 38].

Figure 6.2 also shows that addition of just 3 wt% CB into Al/I_2O_5 system, not only lowers the iodine release temperature but also the initiation temperature. The incorporated CB offsets the influence of aluminum on the iodine release from I_2O_5 and makes it behave like that of the bare oxidizer. As to why initiation seems not limited by the melting point of Al: the condensed phase reaction of CB/I_2O_5 is initiated first and presumably the energy generated kicks the temperature above the point of making the Al core mobile. Thus, addition of CB lowers the initiation temperature of an aluminum-based thermite.

As a comparison, $CB_{3wt\%}/I_2O_5$ (non-stoichiometric) shows a lower initiation and iodine release temperatures than $CB_{3wt\%}/Al/I_2O_5$, which indicates the presence of aluminum inhibits the condensed phase reaction of CB/I_2O_5 and therefore delays the iodine release from I_2O_5. On the other hand, with only 3wt% addition of CB, the iodine release temperature of I_2O_5 was brought lower by about 50 ^oC compared to the neat

I_2O_5, which indicates that the condensed phase CB/I_2O_5 reaction occurred before the I_2O_5 decomposition. Furthermore, the addition of 3 wt% CB into Ta/I_2O_5 system also bring both iodine release and initiation to lower temperatures, indicating the general effect of CB additive on different fuel/I_2O_5 systems. In addition, time resolved images of $CB_{3wt\%}$/Al/I_2O_5 and $CB_{3wt\%}$/Ta/I_2O_5 thermite reactions during rapid heating under vacuum were captured using a high-speed camera and are shown in Figure S6.3. In contrast to $CB_{3wt\%}$/Al/I_2O_5, the $CB_{3wt\%}$/Ta/I_2O_5 reaction is much more vigorous with strong light emission.

In fact, similar results (Figure S6.4) were also obtained for HI_3O_8-based or HIO_3-based thermites indicating the general effect of CB on iodine oxides/iodic acids.

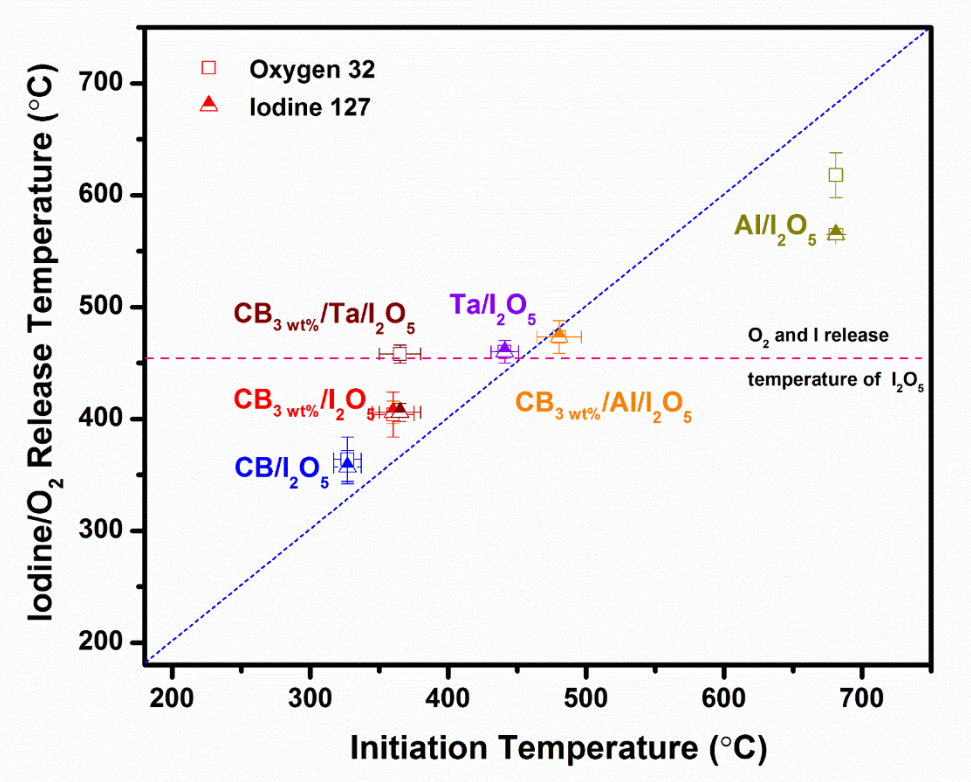

Figure 6.2. Release temperatures of iodine/oxygen vs. initiation temperatures of different thermites.

I now turn to mechanistic effects, which I limit to the CB/I_2O_5 reaction mechanism since the other oxidizers showed similar behavior.

To explore the CB/I_2O_5 reaction further, time-resolved T-Jump mass spectra of I_2O_5 and CB/I_2O_5 were obtained and shown in Figure 6.3. For neat I_2O_5, above the decomposition temperature (>1.1 ms, 470°C), O_2^+ and I^+ are detected in addition to IO^+, IO_2^+, I_2^+, and I_2O^+, which is consistent with our previous result of HI_3O_8. Since IO^+ and IO_2^+ were reported previously as the primary species of iodic acid, we conclude that the commercial I_2O_5 is partially hydrated to form HI_3O_8. In fact, the XRD and TGA/DSC results (Figure S6.5) of commercial I_2O_5 also prove it is ~80% hydrated to HI_3O_8 [35, 36]. For CB/I_2O_5, both the disappearance of the O_2^+ peak and the appearance of a CO_2^+ peak prove CB reacted with I_2O_5. The time-resolved mass spectra of bare CB (Figure S6.6) clearly eliminates the possibility that the CO_2^+ peak is from CB. The new CO^+ peak is either a fragment of CO_2 or a product of incomplete reaction of CB/I_2O_5 energetic composite. Considering both facts that the reaction is extremely fast (less than several milliseconds) and the formed O_2 could rapidly escape the reaction interface at very low pressure, the partially incomplete reaction between the fuel and oxidizer is not a surprise.

Figure 6.3 also shows that CB/I_2O_5 released iodine at ~360 ºC, which occurred slightly later than its initiation temperature (~340 ºC), indicating a condensed phase reaction mechanism was involved here. More importantly, the onset release temperature of iodine from CB/I_2O_5 is about 100 ºC lower than that of neat I_2O_5, which is probably due to that the condensed phase reaction of CB extracts oxygen from I_2O_5, and thus promoting a quicker release of iodine.

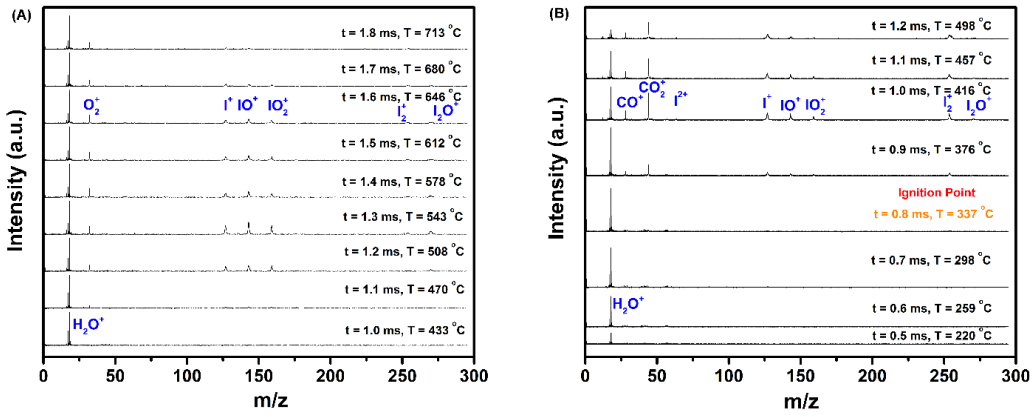

Figure 6.3. Time-resolved mass spectra of I_2O_5 (A) and CB/I_2O_5 (B).

Slow heating rate TGA in argon is shown in Figure 6.4. Neat I_2O_5 shows one minor weight loss at around 210 ºC that corresponds to the dehydration of HI_3O_8 and another major weight loss at around 370 ºC that results from the decomposition of I_2O_5. The DSC curve of I_2O_5 shows that both steps are endothermic (black curve in Figure S6.7).

When CB was mixed with I_2O_5 (red curve in Figure 6.4) the onset decomposition temperature is 140 ºC lower than that of neat I_2O_5. In addition, the DSC (red curve in Figure S6.7) shows an exotherm around 250 ºC presumably from reaction between CB and I_2O_5. Even with only 3wt% of CB, the TGA curve of I_2O_5 follows the same kinetics as CB/I_2O_5 at temperatures below 250 ºC. However, as temperature increases (250<T<300 ºC), the reaction effectively stops until it reaches the neat I_2O_5 condition resuming decomposition at a rate the same as neat I_2O_5. In fact, the actual weight loss of $CB_{3wt\%}/I_2O_5$ at 300 ºC, ~35%, is very close the theoretical weight loss ~37% based on the reaction of 3 wt% CB and I_2O_5 (accounted for the 80% hydration HI_3O_8 specie).

The unchanged TGA result of Al/I_2O_5 compared with that of I_2O_5 indicates that aluminum does not pose any significant influence on the decomposition of I_2O_5 at low

heating rates, which is quite different from the T-jump/TOFMS experiment in which the presence of aluminum delays the iodine release of I_2O_5. Moreover, for $CB_{3wt\%}/Al/I_2O_5$, the decomposition started at a temperature very close to that of CB/I_2O_5, thus aluminum does not influence the CB/I_2O_5 reaction at a low heating rate and again differs from the T-jump/TOFMS experiment.

The TGA curve (Figure S6.8A) of Ta/I_2O_5 starts decreasing at a lower temperature than that of bare I_2O_5, which suggests Ta/I_2O_5 reaction was probably initiated prior to I_2O_5 decomposition at low heating rate and thus causing the weight loss. The TGA/DSC of Ta in O_2 at a heating rate of 20 ^oC/min (Figure S6.9) shows oxidation is a one step process beginning at ~300 ^oC and finishing at ~500 ^oC, indicating that gaseous O_2 can diffuse through the Ta_2O_5. Thus, the Ta/I_2O_5 reaction was probably initiated by the interaction between the Ta core and the oxidizer I_2O_5 following a condensed phase reaction mechanism. The 3 wt% addition CB into Ta/I_2O_5 system, decreases the onset decomposition temperature, but the kinetics were found to be faster (Figure S6.8A) and a small exotherm was observed (Figure S6.8B).

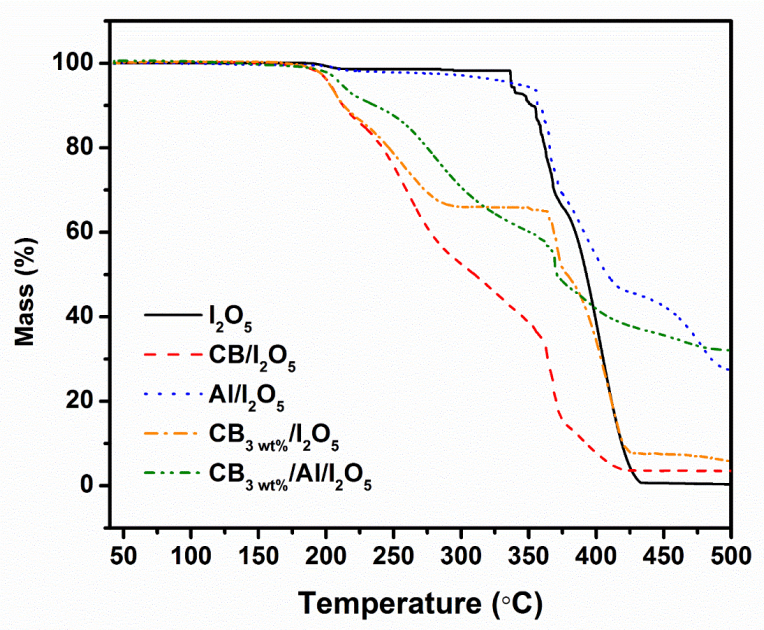

Figure 6.4. TGA results of neat I_2O_5, CB/I_2O_5, Al/I_2O_5 and $CB_{3\ wt\%}/Al/I_2O_5$ thermites.

Additional carbon allotropes including CNT and FGS were evaluated by stoichiometrically mixing with I_2O_5. Figure 6.5 shows the relation between iodine release temperatures and initiation temperature of those energetic composites employing carbon allotropes as the fuel from T-Jump mass spectrometry. The horizontal dotted red line represents the oxygen and iodine release temperatures of neat I_2O_5, and the dotted blue line would refer to the perfect correlation between iodine release and the onset reaction temperature. For all samples, the initiation temperatures are either lower to or the same as the corresponding iodine release temperatures and the iodine release temperature is lower than bare I_2O_5. All four stoichiometric thermites employing FGS_{15}, FGS_{60}, CNT or CB as the fuel initiated almost at the same temperature ~310 ºC, implying that the different properties among those carbon materials [39-42] appear to have no significant effect on initiation. We also note that

above a threshold level of carbon the ignition temperature is not affected. So, 3% and 8% of CB addition have essentially the same ignition temperature. Additionally, the low heating rate TGA/DSC results (Figure S6.10) show similar onset decomposition temperatures and exothermic peaks as to CB/I_2O_5, which are in consistent with the initiation results.

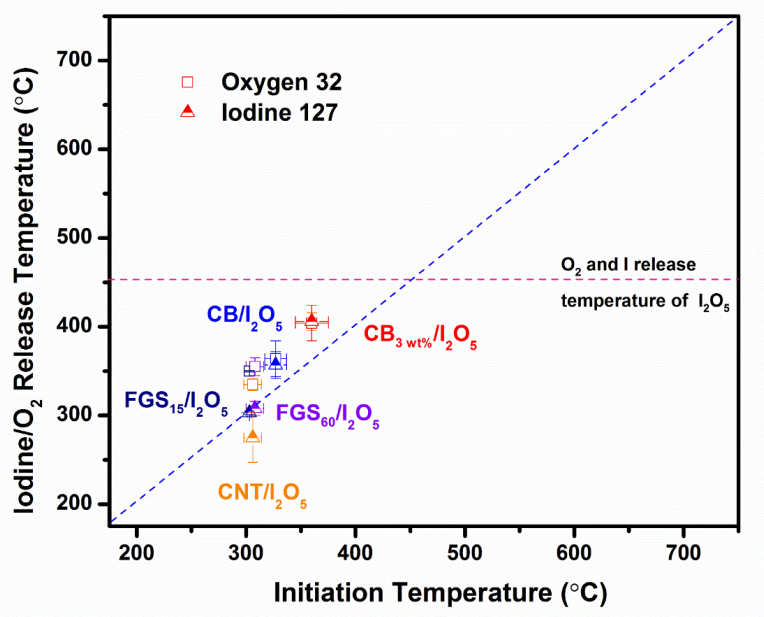

Figure 6.5. The relation between iodine/oxygen release temperatures and initiation temperatures of thermites employing carbon allotropes as the fuel.

Since I conclude that surface reaction is clearly playing a significant role, FTIR attenuated total reflection (ATR, surface) and transmission measurements (KBr pellet) were both employed to deduce any structure changes just prior to reaction [43]. FTIR-ATR spectra of bare I_2O_5, $CB_{3wt\%}/I_2O_5$ and stoichiometric CB/I_2O_5 at room temperature and 200 °C, is shown in Figure 6.7. The spectra show a steady red-shift (too lower wavenumbers) with increasing CB content. For clarity, the stoichiometric CB/I_2O_5 is labeled as $CB_{8wt\%}/I_2O_5$. The redshifts indicate weaker iodine-oxygen bonds due to the

presence of CB. In addition, no new peak is detected with CB-added samples which suggests no new carbon-iodine or carbon-oxide bonds are formed between CB and iodine oxide. Transmission FTIR-KBr pellet spectra (Figure S6.11) show no discernable changes in the spectra. Keeping in mind that the ATR is a surface sensitive technique while the KBr pellet method is a bulk technique I can conclude that the surface of I_2O_5 particles even under room temperature conditions is affected by CB in a manner to enable a lower decomposition temperature.

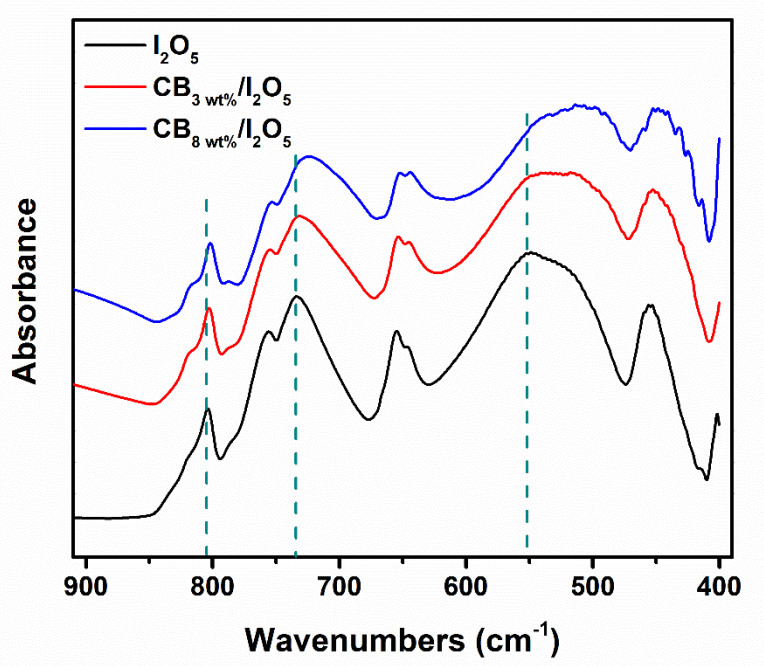

Figure 6.6. ATR-FTIR spectra of bare I_2O_5, $CB_{3wt\%}/I_2O_5$ and $CB_{8wt\%}/I_2O_5$ at room temperature showing I-O bond red-shift upon addition of CB

6.4. Conclusions

In this paper, I employed carbon (CB, CNT and FGS) as both a fuel and as an additive to aluminum and tantalum fuels to study the influence of a fuel without nascent oxide shell on initiation of iodine oxide-based thermites. I found that the initiation

temperature of CB/I_2O_5 is much lower than the initiation temperature of Al/I_2O_5 and Ta/I_2O_5. When CB is used as an additive to other fuels I observe a decrease in the overall initiation temperature and a lowering of the iodine release temperature to below that of the nascent oxidizer. Other carbon allotropes showed similar results. FTIR analysis indicated at CB lowered the iodine-oxygen bond energy of I_2O_5 on the surface and thus triggered this condensed phase reaction. These results indicate that CB can be employed as an additive to any metal fuel as a means to lower both the initiation and iodine release temperature.

6.5. Supplementary Information

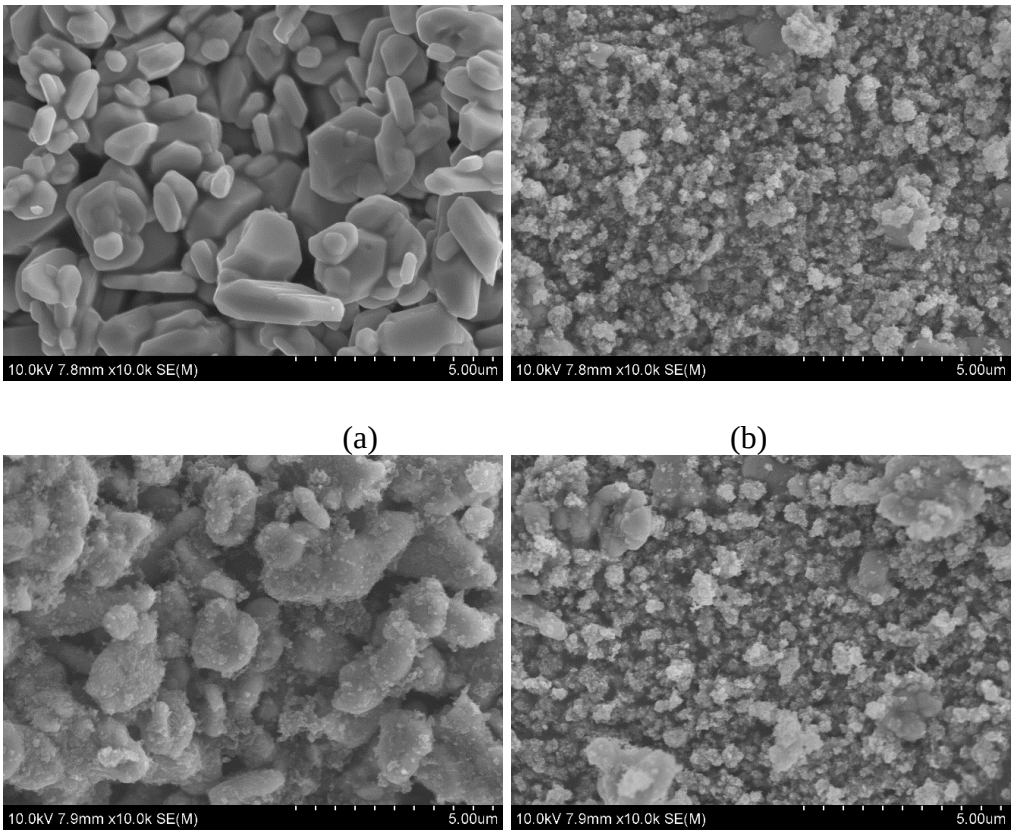

Figure S6.1. SEM images of (a) HI_3O_8, (b) Ta/HI_3O_8, (c) CB/HI_3O_8 and (d) CB/Ta/HI_3O_8.

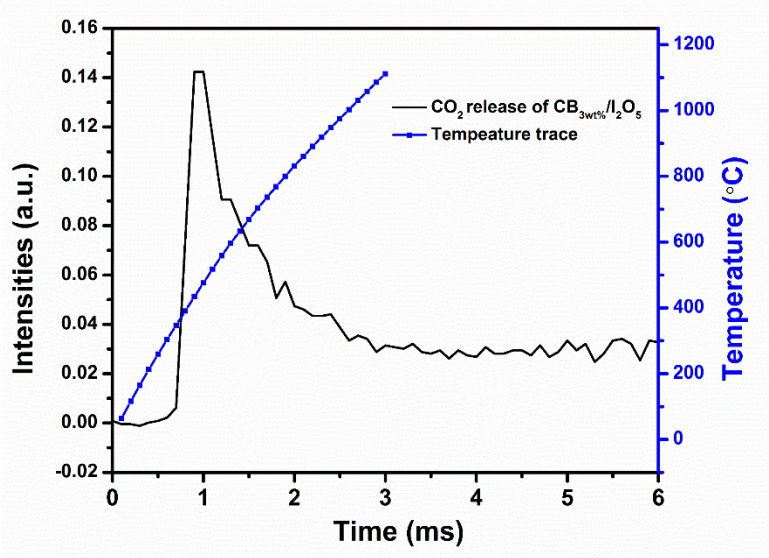

Figure S6.2. Representative plot showing the temporal release of CO_2 from $CB_{3wt\%}/I_2O_5$ when heated at ~5 × 10^5 °C/s.

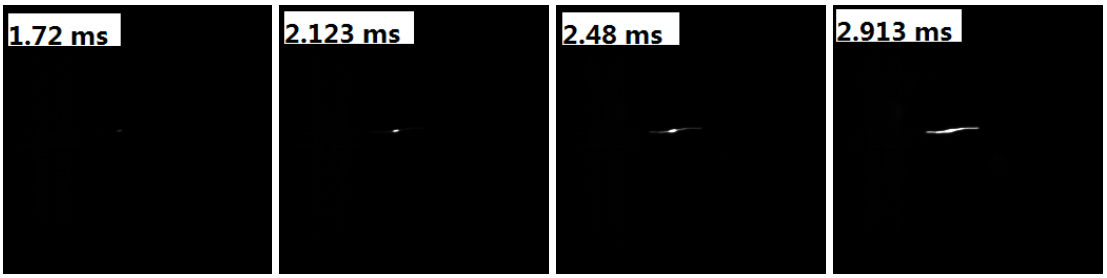

(A)

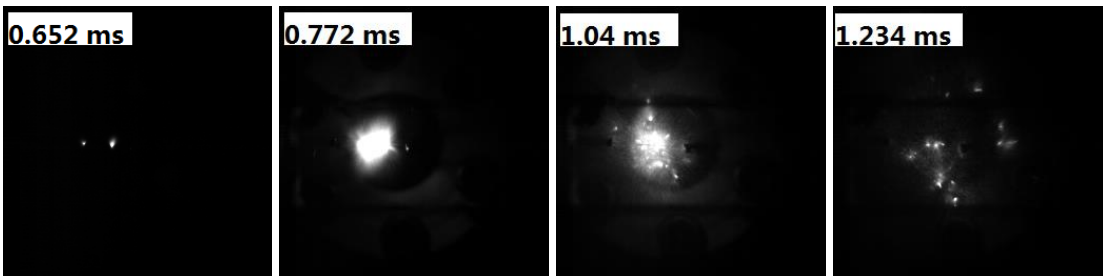

(B)

Figure S6.3. Sequential snapshots of (A) $CB_{3wt\%}/Al/I_2O_5$ and (B) $CB_{3wt\%}/Ta/I_2O_5$ thermites burning on a high rate heating (5 x 10^5 °C/s) Pt wire under vacuum, captured by a high-speed camera. The labels in each image are the time elapsed after triggering.

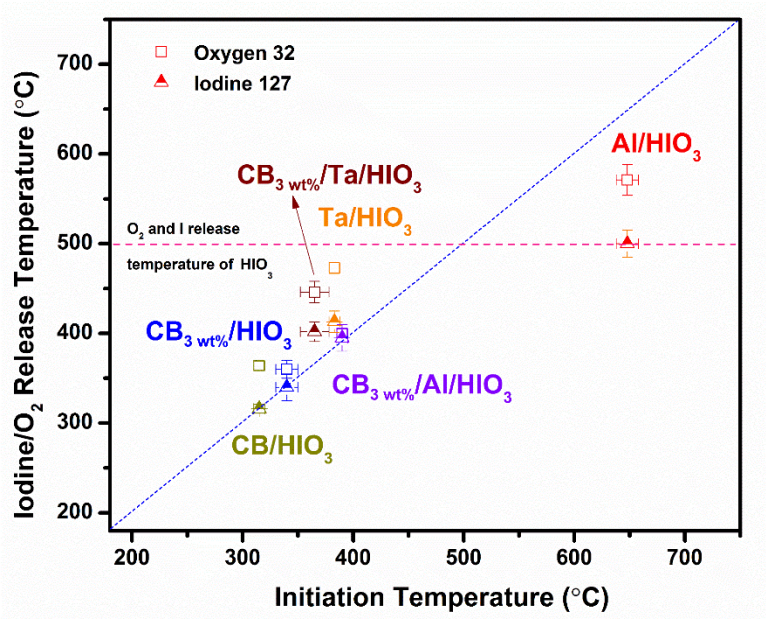

(A)

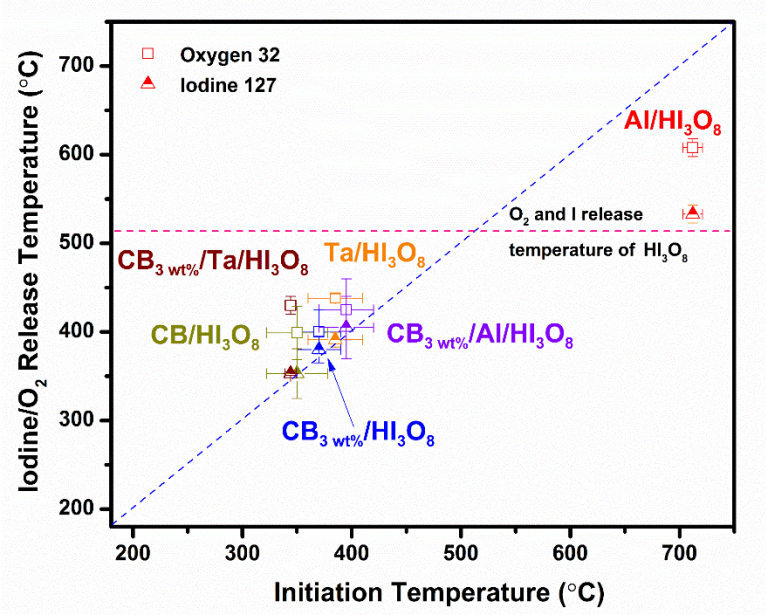

(B)

Figure S6.4. The relation between iodine/oxygen release and ignition temperatures of HIO_3-based (A) and HI_3O_8-based thermites (B).

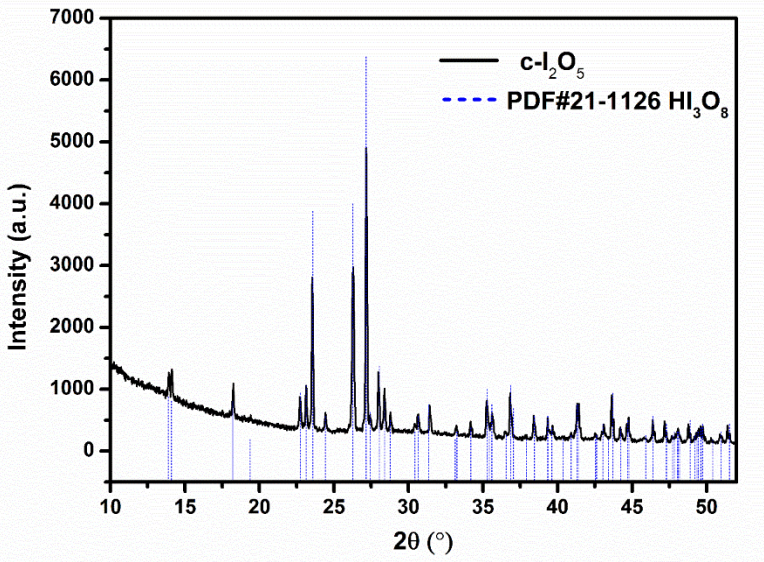

(A)

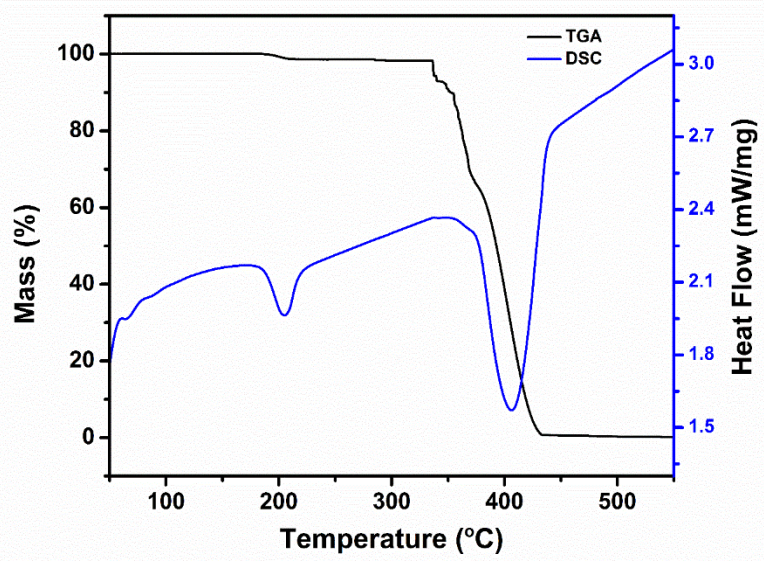

(B)

Figure S6.5. XRD and TGA/DSC results of commercial I_2O_5.

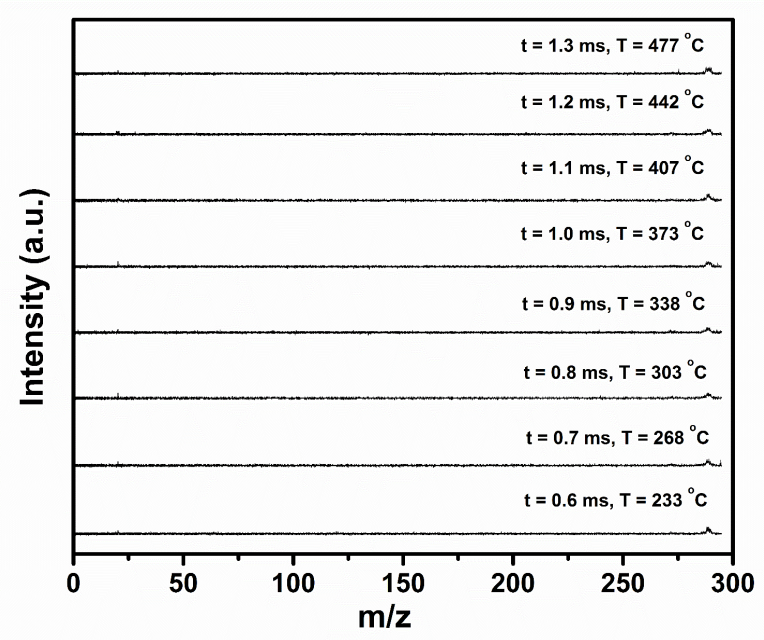

Figure S6.6. Time-resolvedmass spectra of CB.

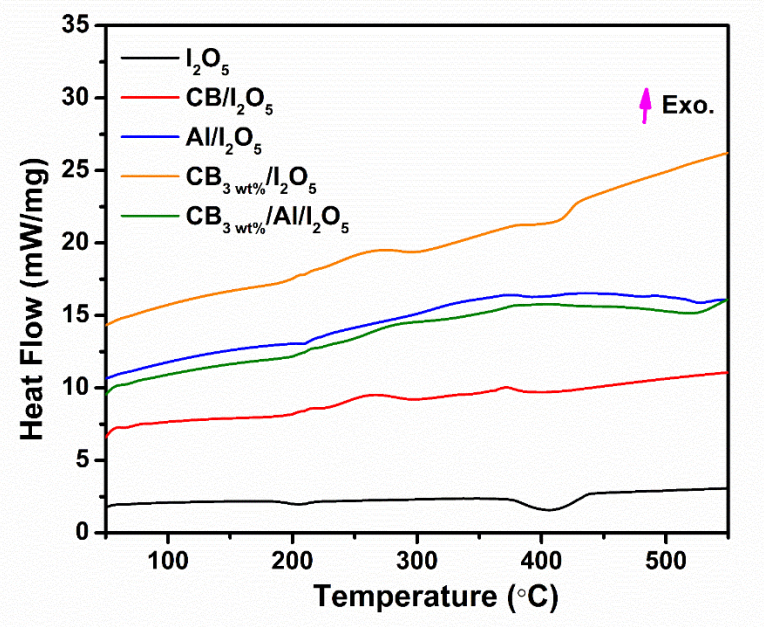

Figure S6.7. DSC results of neat I_2O_5 and I_2O_5–based thermites.

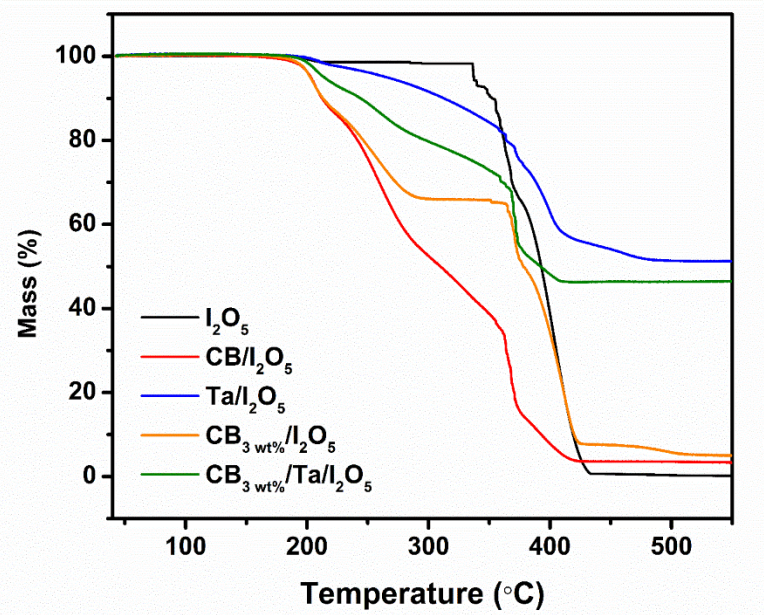

(A)

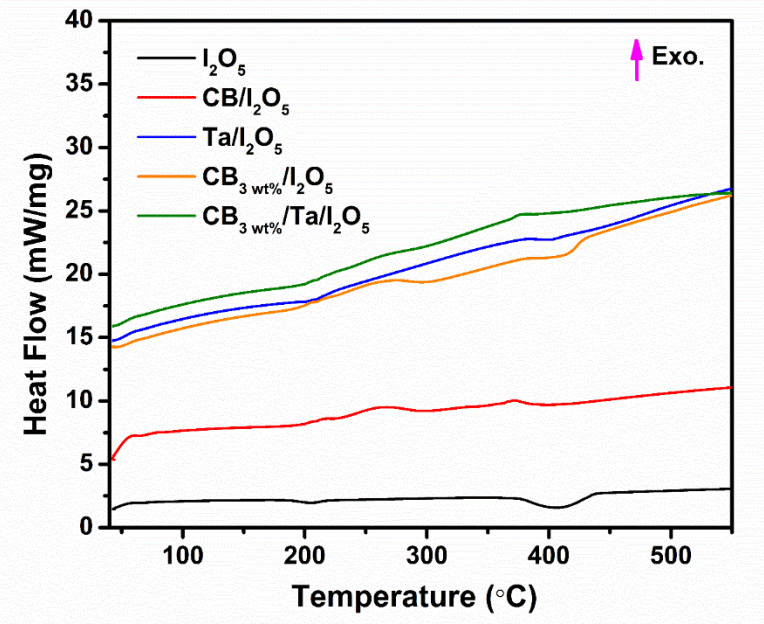

(B)

Figure S6.8. TGA (A) and DSC (B) results of neat I_2O_5, CB/I_2O_5, Ta/I_2O_5 and $CB_{3\ wt\%}/Ta/I_2O_5$ thermites.

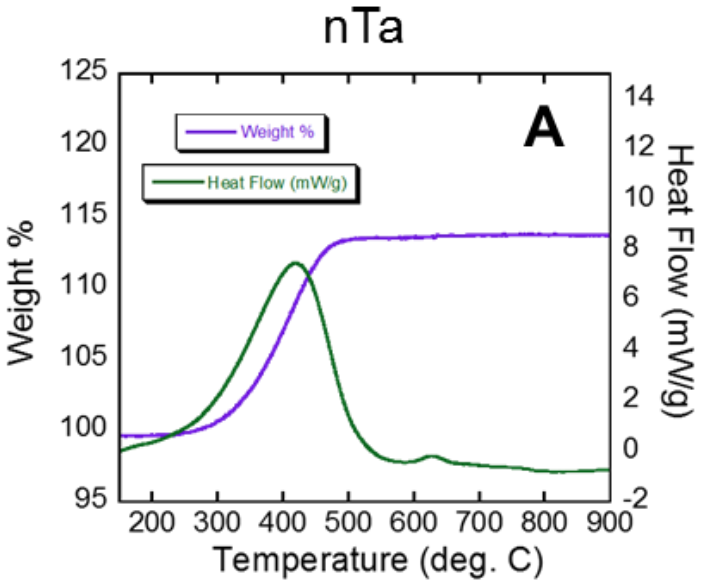

Figure S6.9. TGA/DSC of Ta under 100 mL/min of O_2 at a heating rate of 20 ^{o}C/min.

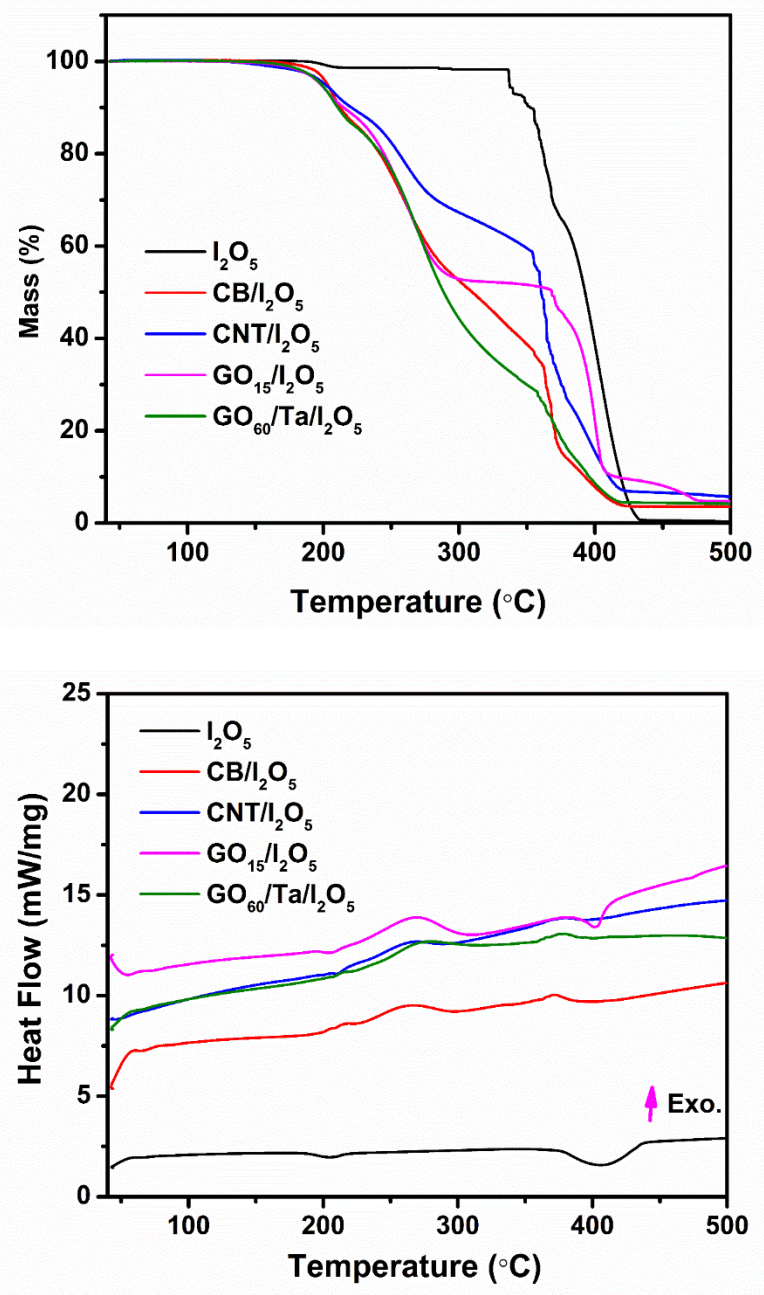

Figure S6.10. TGA/DSC results of thermites employing carbon allotropes as the fuel.

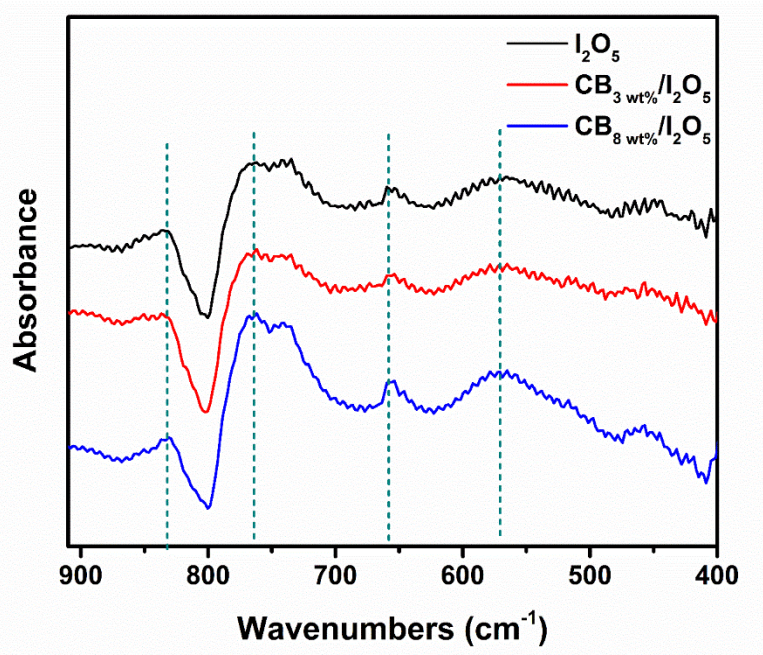

Figure S6.11. FTIR-KBr pellet spectra of bare I_2O_5, $CB_{3wt\%}/I_2O_5$ and $CB_{8wt\%}/I_2O_5$ at room temperature.

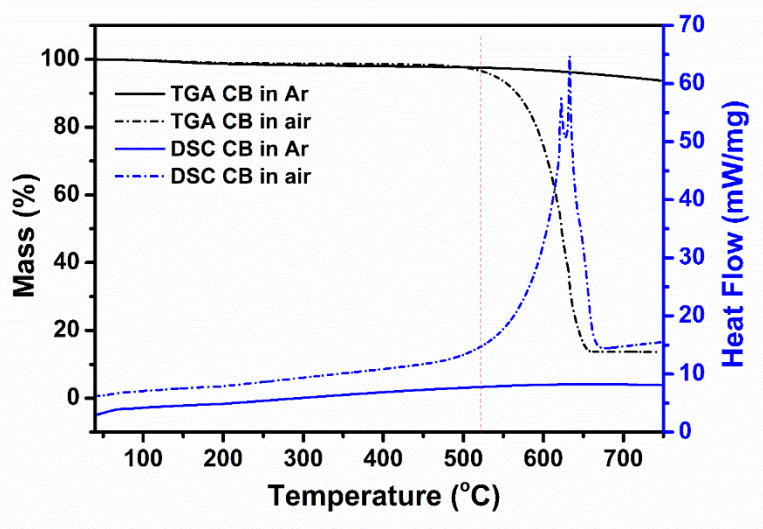

Figure S6.12. TGA and DSC results of CB in Ar or air.

Chapter 7: Enhancement to the combustion of Al/I_2O_5 thermites by addition of a secondary oxidizer*

Overview

Developing new iodine-containing energetic materials is attracting growing interest due to its high energy release and potential high efficiency neutralization functions. One interesting phenomenon was found for all iodine-containing energetic materials: an ignition delay was always present in their pressure profiles while combusting. Considering the fact that some Al/iodine oxides have similar performance as to Al/CuO in term of peak pressure, an instant ignition for Al/iodine oxides might boost their combustion performance further. Here, this particularly unsolved question is going to be thoroughly investigated in this chapter. To shorten or eliminate this ignition delay, a secondary oxidizer CuO is incorporated into Al/I_2O_5 system and four different Al/I_2O_5/CuO thermites by varying the mass ratio between two oxidizers are prepared and studied in a constant volume combustion cell. Significant enhancement is observed for all four thermites and their peak pressures and pressurization rates are much higher than that of Al/I_2O_5 or Al/CuO. The disappearance of the ignition delay in their pressure profiles and the shortened burn time imply CuO addition indeed does work on accelerating the ignition of Al/I_2O_5 thermite and the overall reaction. To further understand the mechanism behind this improvement, the flame temperatures of the thermites while reacting are obtained via two different methods: color camera

* I would like to thank my collaborators for this study, Dylan J. Kline, Dr. Haiyang Wang, Miles C. Rehwoldt, and Dr. Michael R. Zachariah for all their hard work and input that made this chapter possible.

pyrometry and optical spectrometer measurement. The results confirm the flame temperature of $Al/I_2O_5/CuO$ thermites are comparable to Al/I_2O_5, indicating the CuO addition doesn't sacrifice the high flame temperature of Al/I_2O_5 system. In fact, the high flame temperature potentially promotes the decomposition of oxidizers and therefore improving the combustion performance of Al/I_2O_5 system. Furthermore, to expand the types of the secondary oxidizer, a weaker oxidizer Ag_2O and stronger oxidizer $AgFeO_2$ compared to CuO is also incorporated into Al/I_2O_5 thermite and demonstrate similar effects on promoting the combustion performance of Al/I_2O_5. And a synergetic effect is proposed here to explain the significant enhancement on the combustion performance of Al/I_2O_5 by introducing a secondary oxidizer.

7.1. Introduction

Biological warfare agents with high efficiency neutralization functions has gained increased attention due to the increased threat of bioterrorism and various new energetic materials has been developed over the past few decades [1-5]. Preliminary laboratory studies have suggested that an ideal neutralization process should generate not only a high temperature, but also release a long-lasting biocidal agent [6-12]. With the lack of effective biocidal agent release, conventional energetic materials suffer from low neutralization efficiency since the thermal neutralization mechanism is dominant in this case [6]. Therefore, it has been proposed that simultaneously delivering a rapid thermal pulse with a remnant biocidal agent would prolong the exposure time and improve the inactivation process [13].

Iodine-containing energetic materials have shown the most promise because of their excellent biocidal properties [14], compared to other biological energetic materials [15-17]. Different methods have been reported for incorporating elemental iodine into energetic materials [14, 18-20]. Dreizin et al. employed mechanically alloyed aluminum-iodine composites as a fuel in energetic formulations and the initiation and combustion tests in air indicated that higher iodine concentration lowers initiation temperatures and the combustion temperatures were not substantially diminished [12]. They also found improvements in terms of pressurization rate and maximum pressure at constant volume with 15 wt.% and 20 wt.% of I_2 [12]. Wang et al physically incorporated iodine molecules into Al/CuO thermite systems and found that the Al/CuO/I_2 thermite reaction rate was significantly decreased with increasing the iodine content while a decent burn rate could be achieved with high iodine content (67 wt.%) if special laminated structure was used.[19, 21]. Another efficient approach is to use iodine-containing oxy-compounds as an oxidizer, particularly iodine oxides/iodic acids.

Among all the iodine oxides/iodic acids (I_2O_5, I_4O_9, HI_3O_8, HIO_3, H_5IO_6, etc [22-24]), I_2O_5 is the most studied oxidizer in thermite systems [25-29] due to its relatively high iodine content (~76% iodine mass fraction). In these studies, aluminum particles with different sizes were chosen as the fuel due to its high reaction enthalpy, thermal conductivity and availability. With reported propagation velocities of up to ~2,000 m/s for loose ball-milled nano-aluminum and nano-scaled I_2O_5 (~10 nm) [28], I_2O_5 shows its high potential in aluminum-based thermites as an extremely aggressive oxidizer. Constant volume combustion tests also show nano-Al/micro-I_2O_5 outperforms

traditional aluminum-based thermites such as Al/micro-CuO and Al/micro-Fe_2O_3 [29]. A pre-ignition reaction was proposed to be the ignition trigger in which ionic I_2O_5 fragments diffused into the alumina passivated shell and to create some reactive complexes exothermically.[27, 30] However, this mechanism is far from clear as Smith et al reported that such pre-ignition reaction was not found for Al/nano crystalline I_2O_5.[31] I reported that aerosol route synthesized iodine oxides/iodic acids outperform the corresponding commercial ones in combustion cell tests, where in particular Al/a-HI_3O_8 has the highest pressurization rate and peak pressure and shortest burn time among all iodine-containing composites.[32] Later, I employed carbon as an additive or main fuel into iodine oxides-based energetic materials and reported that carbon addition can lower initiation and iodine release temperatures due to a surface interaction between carbon and iodine oxide.[33]

In this work, I conduct further studies on enhancing the combustion performance of Al/I_2O_5 thermite materials and understanding the mechanisms. For the fuel, once the aluminum core is heated near its melting point (~660 ^oC), obtaining sufficient mobility, it can diffuse through the passivated alumina shell and interact with any available oxidizer ultimately leading to initiation [34]. When aluminum combined with iodine oxides/iodic acids, an ignition delay with a constant time period (~0.16 ms) was found in the pressure profiles of all iodine oxides-based energetic materials based on the results in our previously published work.[32] To be more focused on understanding the mechanism behind this ignition delay, I_2O_5 was chosen as the subject in this work because it is relatively easier to prepare compare to other iodine oxides via aerosol spray pyrolysis and the yield is the highest according to Chapter 3.[18, 32]

The goal of this work is to shorten or even eliminate the ignition delay of Al/I_2O_5. To achieve that, a secondary oxidizer CuO featuring instant ignition (no delay) when mixed with aluminum is incorporated into the system. Various Al/I_2O_5 thermites with different CuO addition are prepared and examined in the combustion cell. Meanwhile, the flame temperatures of those employed thermites are also obtained in order to help us understanding the mechanism via two different methods: color camera pyrometry and optical spectrometer measurement. To expand the types of the secondary oxidizer, a weaker oxidizer Ag_2O and stronger oxidizer $AgFeO_2$ compared to CuO is also incorporated into Al/I_2O_5 thermite. Furthermore, a synergetic effect is proposed here to explain the significant enhancement on the reactivity of Al/I_2O_5 by introducing a secondary oxidizer.

7.2. Experimental

7.2.1 Materials:

The aluminum nanopowders (Al) (Alex, ~80 nm) were purchased from Novacentrix. The active Al was 81 % by mass, determined by thermogravimetric analysis. Iodic acid and CuO purchased from Sigma-Aldrich were directly used as received. All the other chemicals were of analytical grade and used as purchased without further treatment.

7.2.2 Preparation of thermites:

Aluminum was stoichiometrically mixed with I_2O_5 based on the following equation in hexane followed by 30 minutes of sonication.

$$10Al + 3I_2O_5 \rightarrow 3I_2 + 5Al_2O_3$$

After room temperature evaporation of the solvent in a desiccator, the solid thermite powders were used.

7.2.3 T-Jump/TOFMS measurement and high-speed imaging:

The decomposition of oxide particles was investigated using a T-Jump/TOFMS [6]. Typically, a ~1 cm long platinum wire (76 um in width) with a thin layer coating of oxidizer sample was rapidly joule-heated to about 1200 °C by a 3 ms pulse at a heating rate of 5 × ~10^5 °C/s. The current and voltage signals were recorded, and the temporal temperature of the wire was measured according to the Callendar–Van Dusen equation [34]. Mass spectra were measured every 0.1 ms. The detailed experimental set-up is given in our previous papers [6, 34].

To identify the point of initiation, a high-speed camera (Vision Research Phantom v12.0) was employed to record the combustion on the wire during heating. Initiation temperatures of thermite reactions in vacuum were measured from the correlation of optical emission from high speed imaging and temporal temperature of the wire and were further analyzed in combination with the temporal mass spectra. Each measurement was repeated 3 times.

7.2.4. High speed 32-channel spectrometer

The high-speed 32-channel spectrometer used to collect emission spectra and analyze temperature of combusting samples in the constant-volume combustion cell has been previously described and is only done so briefly here.[34] From the inner edge of the vessel, an assembly consisting of a Sapphire window, a plano convex lens (1f

from inner edge), an ND2 filter, and 455nm color glass filter are in a 0.5“ lens tube which is terminated with a SMA fiber optic adapter. Light is transmitted via the fiber optic cable to a 500mm, triple-grating, Czerny-Turner Imaging Spectrometer (Acton SP 500i) set to 150 groove/mm and slit width of 100µm to give a dispersion of 13nm/mm over 464-867nm wavelengths. The light is then passed into a 32-channel photomultiplier tube (Hamamatsu MC-PMT, H7260) which is interfaced to a high-speed data acquisition system (Vertilon IQSP580) which terminates the MC-PMT to 50Ω and measures current with a 14-bit resolution. The system is capable of measure at rates up to ~390kHz and MC-PMT voltages and spectrometer integration times are chosen to avoid sensor saturation and to remain within the linearity limit of the MC-PMT. Here I would like to acknowledge Dylan Kline for his help on the temperature measurements of thermites in combustion tests.

7.2.5. Combustion cell and optical spectrometer temperature measurement

Combustion properties of themites were evaluated in a constant-volume combustion cell, with simultaneous pressure and optical emission measurements. In this study, 25 mg of thermite powders was loaded inside the cell (constant volume, ~20 cm^3) and ignited by a resistively heated nichrome wire. The temporal pressure and optical emission from the thermite reaction were measured using a piezoelectric pressure sensor and a photodetector, respectively. Another port houses an optical assembly that collects and relays the emission to a spectrometer.[35] The cell was placed inside an artificial environment bag which was purged with argon to elminate the influence of atmospheric oxygen while operating. More detailed information on the combustion cell

test can be found in our previous publications.[32, 35] Each sample was measured at least 3 times.

7.3. Results and discussion

Different iodine oxides and iodic acids had been studied within aluminum-based and tantalum-based thermite systems previously.[32] However, by comparing their pressure profile obtained from a constant volume combustion cell with that of Al/CuO, I noticed that there is an ignition delay for all Al/iodine oxides and Al/iodic acids thermites after trigger. Unlike those iodine-containing thermite systems, Al/CuO was ignited almost at the same time as the trigger. To present the difference clearer, a zoom-in view of the pressure profiles of Al/CuO and Al/I_2O_5 are shown in Figure 7.1. There is an ~0.3 ms ignition delay between the two pressure history profiles of the two nanothermites systems. Considering the burn time of Al/CuO is 0.31 ms, an ignition delay with a length almost the same as the ignition process itself cannot be ignored. Since aerosol-route synthesized I_2O_5 have particles size at around several micrometers, the ignition delay might be caused by the difference between the particle sizes of these two oxidizers.[32] To prove this theory, we plotted the pressure profiles of Al/micro-sized CuO, Al/a-HI_3O_8, Al/nano-sized CuO and Al/a-I_2O_5, data was obtained from our previous work and the result is shown in Figure S7.1. The fact that all micro-sized oxidizer-based thermites have ignition delay compare to Al/CuO proves our assumption. And the long burn time, about 1.3 ms, of Al/I_2O_5 might also be a consequence due to the size effect of the oxidizer.

To get rid of or even shorten this ignition delay, an obvious method is to incorporate nano-sized CuO into Al/I_2O_5 system. The thermal energy release by the instant ignition of Al/CuO might help ignite Al/I_2O_5 right away.

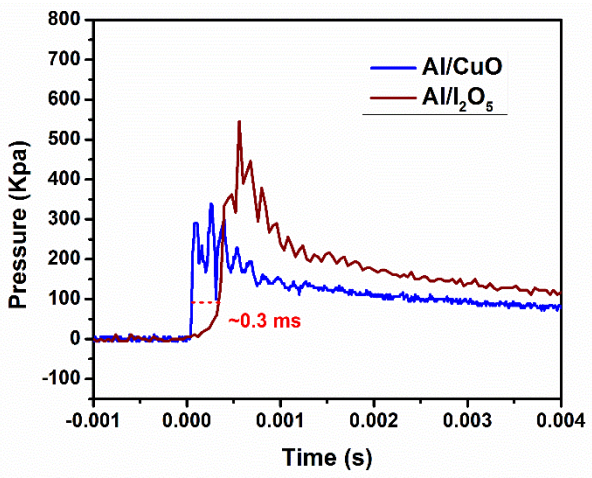

Figure 7.1. Temporal pressure traces of Al/CuO and Al/I_2O_5.

Thus, nano-sized CuO is incorporated into Al/I_2O_5 formulations with different ratios to form a series of Al/I_2O_5/CuO ternary systems. All thermites remain stoichiometric to avoid uncontrollable influences. Four ternary samples are prepared by varying the mass ratio between these two oxidizers and are referred as Al/I_2O_5/82% CuO, Al/I_2O_5/68% CuO, Al/I_2O_5/42% CuO and Al/I_2O_5/20% CuO (percentages represent the weight ratio of CuO in the oxidizers). Along with Al/I_2O_5 and Al/CuO, these six samples are examined in combustion cell and their pressure profiles are presented in Figure 7.2. As I expected, the ignition delay disappeared for all four ternary systems indicating the addition of nano-sized CuO can overcome the ignition difficulty of

Al/I_2O_5. However, what I do not expect is the fact that all four ternary systems significantly outperform Al/I_2O_5 and Al/CuO in term of the peak pressure.

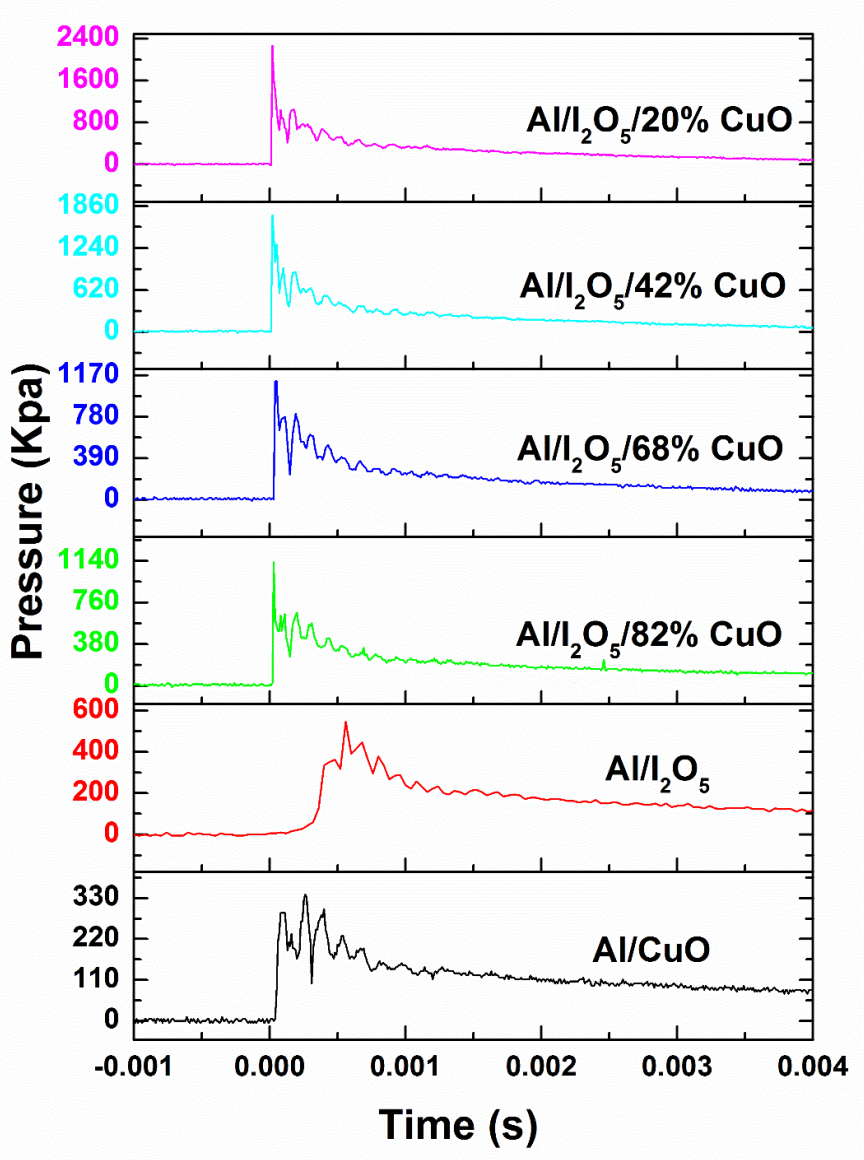

Figure 7.2. Temporal pressure traces of different Al/I_2O_5/CuO thermites. The number listed after the series name represent the weight fraction of CuO within oxidizers in each thermite.

To have a close look at the combustion performance of these thermites, the combustion cell results of all six samples are summarized and presented in Figure 7.3. Al/CuO with a lower peak pressure features a higher pressurization rate compare to

Al/I_2O_5 indicates the ignition delay/burn time of the later is much longer than the former. Again, strengthening our proposed method by incorporating CuO into Al/I_2O_5 to eliminate or shorten the ignition delay and hence further boost its combustion performance.

Figure 7.3A and 7.3B implies that the addition of CuO remarkably increase the peak pressure and pressurization rate of Al/I_2O_5. Apparently, these improvements are independent on the amount of incorporated CuO. As long as CuO is included in Al/I_2O_5, its combustion performance will be improved no matter how much CuO is added.

Surprisingly, by adding 20% of CuO within the oxidizers part, the peak pressure and pressurization rate of Al/I_2O_5 increased by about 4 and 26 times, respectively, the strongest improvement among all. Thus, a ternary system significantly outperforms each binary system. A similar result has been published previously as Al/Fe_2O_3/70% WO_3 outperforms both Al/Fe_2O_3 and Al/WO_3 in term of combustion cell results.[35] The authors explained: the lower ignition temperature of Al/WO_3 help igniting the ternary composite and its higher flame temperature promoting the further decomposition of Fe_2O_3, thus more gaseous oxygen participating the combustion, all those factors are the reason why Al/Fe_2O_3/70% WO_3 outperforms both Al/Fe_2O_3 and Al/WO_3. However, the peak pressure increase is only about 1.5 times compare to 4 times in this work and let alone with 26 times boost for the pressurization rate.

Among those ternary thermites systems, peak pressure and pressurization rate decreases when the CuO content increases. However, they all outperform the other binary thermite systems. With higher weight ratio of CuO in the oxidizers, the overall

combustion performance weakens within these four ternary systems. It could mean that Al/CuO combustion is acting as an on-site trigger to help the ignition of Al/I_2O_5 thermite, but excessive amount could weaken the overall combustion performance of Al/I_2O_5/CuO system.

From Figure 7.3C, it could be seen that all four Al/I_2O_5/CuO thermites have a shorter burn time compare with Al/I_2O_5, indicating CuO addition can also accelerate the combustion of Al/I_2O_5. However, the results are more complicated when comparing with Al/CuO. In particular, the burn times of the Al/I_2O_5/CuO composites with more than 40% of CuO addition is almost the same as to Al/CuO indicating the rest iodine oxide plays no or insignificant effect on elongating burn time. As for Al/I_2O_5/20% CuO, it features a burn time three quarters of Al/CuO. With less incorporated CuO, the combustion of Al/I_2O_5/CuO composite is more violent and gives higher pressurization rate as well. Therefore, CuO and I_2O_5 apparently are responsible for different functions in the ignition/reaction of Al/I_2O_5/CuO. The reaction process of these ternary systems could be summarized as follows: first Al/CuO helps shortening the ignition delay and overall burn time; then Al/I_2O_5 ignites by the thermal shock of Al/CuO and then further combust violently contributing to the pressurization of the cell. To better understand the causes behind these phenomena, we need to turn our focus on the max emission results.

As discussed in our previous works, maximum optical emission in combustion cell test is positively correlated with the temperature in the system.[36] As shown in Figure 3D, the maximum optical emission of Al/I_2O_5 is much higher than the others, demonstrating Al/I_2O_5 reaction release lots of heat. This result is in a good correlation

with the thermal dynamic calculated data shown in Table 7.1 where Al/I_2O_5 reaction feature a very high adiabatic temperature (3952 ^oC). Even though Al/I_2O_5 reaction lasts a longer burn time, it can potentially lift the temperature inside the combustion cell up to a very high value. On the opposite, with a much lower adiabatic temperature, Al/CuO addition significantly lowers the maximum optical emission and in other word temperature. For Al/I_2O_5/20% CuO, its maximum optical emission (~2 V) lowers to half of Al/I_2O_5 reaction (3.6 V). And all the other three Al/I_2O_5/CuO composites give a similar maximum optical emission (0.8 V) as to Al/CuO. Thus, it is reasonable to conclude that the amount of CuO addition can affect the value of the temperature inside the combustion cell and probably the overall combustion performance even though it reaches a plateau when more than 40% of CuO is added. To prove these perspectives, temperature measurements were performed, and the results are going to be discussed below.

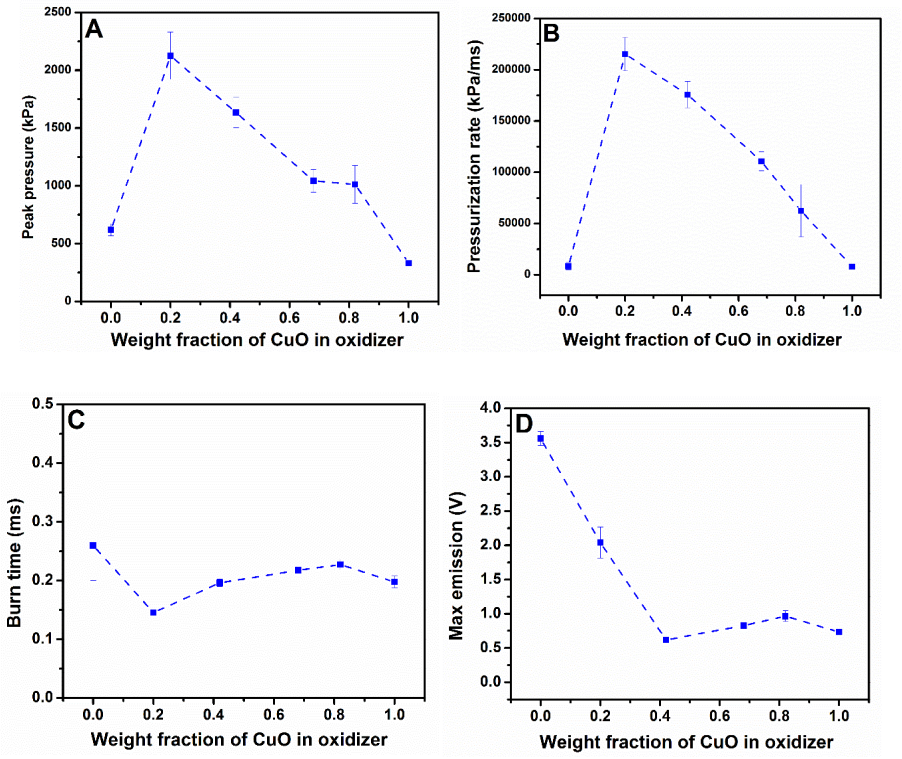

Figure 7.3. Combustion cell results of Al/I_2O_5 with different amount of nano-sized CuO addition.

Table 7.1. Thermodynamic equilibrium predictions of Al/I_2O_5, Al/CuO and Al/Ag2O thermites.[a]

Thermite Reaction	*Adiabatic Temperature (C)*	*Gas Production (mmol/g)*	*Major Gas Species*
$10Al + 3I_2O_5 \rightarrow 5Al_2O_3 + 3I_2$	3952	6.3	I_2
$2Al + 3CuO \rightarrow Al_2O_3 + 3Cu$	2570	5.4	Cu
$2Al + 3Ag_2O \rightarrow Al_2O_3 + 6Ag$	2163	4.3	Ag

[a]: Assumptions: constant enthalpy and pressure with phase changes; without taking account of the oxide shell of aluminum. Data is taken from Fisher and Grubelich.[36]

The ignition temperature measurements were performed inside a T-Jump/TOFMS chamber and the whole event was simultaneously recorded by a high-speed color camera. Then the flame temperatures were obtained by color ratio pyrometry following a previously published method.[35] The typical snapshots and corresponding flame temperature map of Al/I_2O_5 are shown in Figure S7.2 as an example to show the process of color ratio pyrometry. The summarized average flame temperatures of all tested samples are plotted and presented in Figure 7.4. Consistent with the result shown in Figure 7.3D, Al/CuO thermite has the lowest flame temperature. However, all four ternary thermites have either similar or higher flame temperature than Al/I_2O_5. These results indicate the maximum optical emission results have some relation to the flame temperature but not in a significant way. As results shown in Figure 7.4, the addition of CuO into Al/I_2O_5 system affects its flame temperature differently according to the amount of additive secondary oxidizer. With less than 68% CuO addition, the flame temperature of Al/I_2O_5 reaches the maximum increase about 500 K for Al/I_2O_5/42% CuO sample. When the amount of CuO addition increases to 82%, the flame temperature of Al/I_2O_5 remains almost the same as its original value indicating Al/I_2O_5 could remain the flame temperature to a high value even with only 18% of I_2O_5 in the oxidizer. A more convincing result could be seen if we change the subject to Al/CuO. The flame temperature of Al/CuO jumps from 3500 K to 4760 K with just 18% of incorporated I_2O_5 within the system, again confirms the reaction between aluminum and I_2O_5 generates much more heats than that of aluminum and CuO.

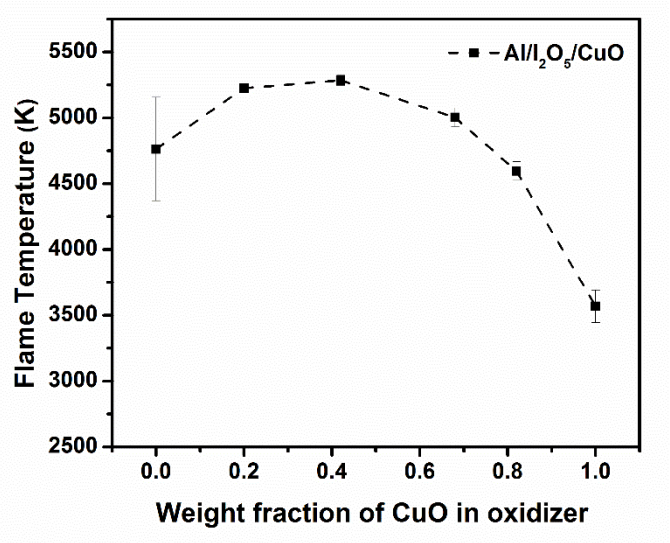

Figure 7.4. Flame temperatures of Al/I_2O_5 with different amount of nano-sized CuO addition obtained via color camera pyrometry.

To verify whether the flame temperature data obtained from color camera pyrometry is solid, the flame temperature of Al/I_2O_5 and Al/I_2O_5/20% CuO thermites in a combustion cell were obtained according to a previous published method and the results are presented in Figure 7.5.[35] The average flame temperatures of Al/I_2O_5 and Al/I_2O_5/20% CuO thermites are both located at ~5000 K, which is very close to the temperatures obtained from the color camera pyrometry method.

Therefore, the reasons for the significant enhancement of the combustion performance of Al/I_2O_5 by addition of a small amount of CuO could be summarized as follows: the additive Al/CuO shortens the ignition delay of Al/I_2O_5 (as shown in Figure 7.2); that leads to enormous amount of gas formation for aluminum to react with and then the extremely high flame temperature of Al/I_2O_5 boost the pressure inside the combustion cell further. All those events happen around the same time and produce a synergetic effect on enhancing the overall combustion performance of Al/I_2O_5.

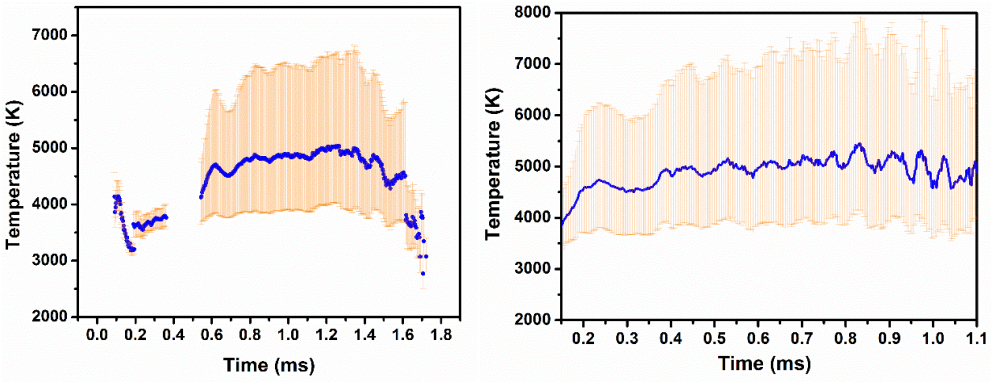

Figure 7.5. Temporal reaction temperature profiles of Al/I_2O_5 (A) and Al/I_2O_5/20% CuO (B) obtained via high speed spectrometer temperature measurement.

As for the ignition mechanism of Al/I_2O_5/CuO thermites, heat released from the instant ignition of Al/CuO helps igniting Al/I_2O_5; then the enormous amount of heat released from Al/I_2O_5 thermite reaction further promoting the decomposition of the oxidizers; with more oxygen gas and higher temperature, the oxidization of aluminum is further accelerated.

To expand the option for the secondary oxidizer, a previously reported very weak oxidizer Ag_2O was incorporated into Al/I_2O_5 system to investigate its effect on the combustion performance of Al/I_2O_5.[2] Three Al/I_2O_5/Ag_2O ternary thermites were prepared and tested, including Al/I_2O_5/19% Ag_2O, Al/I_2O_5/41% Ag_2O and Al/I_2O_5/68% Ag_2O. Along with Al/CuO, Al/I_2O_5 and Al/Ag_2O, their pressure profiles are plotted in Figure S7.3. and the combustion cell results are summarized in Figure 6. The fact that the pressure profile of Al/Ag_2O is almost like a flat line implies the additive Al/Ag_2O is very much a dead weight for the ternary thermites. In other words, the Al/Ag_2O addition could not assist the combustion performance of Al/I_2O_5.

However, all three $Al/I_2O_5/Ag_2O$ thermites outperform Al/I_2O_5, just like what CuO has done for Al/I_2O_5.

Similar to $Al/I_2O_5/CuO$ thermites, the peak pressure and pressurization rate of $Al/I_2O_5/Ag_2O$ thermite decreases when the amount of Ag_2O increases. As shown in Figure 7.6A and 7.6B, although Al/I_2O_5/68% Ag_2O thermite has a similar peak pressure as to Al/I_2O_5, its pressurization rate is still higher than either Al/I_2O_5 or Al/Ag_2O, implies the combustion performance of Al/I_2O_5 can be enchanted even with incorporating a much weaker secondary oxidizer. The burn time of $Al/I_2O_5/Ag_2O$ thermites is very close to that of Al/Ag_2O and is slightly shorter than that of Al/I_2O_5, except for Al/I_2O_5/68% Ag_2O thermite that feature a burn time twice longer than that of Al/I_2O_5. A longer burn time means less violent thermite reactions probably due to the inefficient decomposition of Ag_2O and/or the bad thermal conductivity of I_2O_5.[32] In addition, the pressure profile (the purple dotted line) of Al/I_2O_5/68% Ag_2O thermite (Figure S7.3) shows a similar trend as to Al/Ag_2O but with a higher peak pressure. The appearance of an obvious ignition delay indicates the combustion performance of $Al/I_2O_5/Ag_2O$ thermite would be further weakening with increasing Ag_2O amount. Considering no ignition delay was found in the pressure profiles of $Al/I_2O_5/CuO$ thermites, a much weaker oxidizer does have its limitation on influencing the ignition and combustion performance of Al/I_2O_5.

The ignition/reaction mechanism of $Al/I_2O_5/Ag_2O$ thermite should be very similar to that of $Al/I_2O_5/CuO$ thermite with only one exception that Ag_2O being a much weaker oxidizer and affecting the gas formation and the oxidization of aluminum. What interesting is that ignition delay exists in both Al/I_2O_5 and Al/Ag_2O cases but not for

$Al/I_2O_5/Ag_2O$ thermite. The ignition temperature results shown in Figure S7.4 indicate Al/I_2O_5 and Al/Ag_2O have almost the same ignition temperature; however, $Al/I_2O_5/Ag_2O$ thermites feature a lower ignition temperature especially for Al/I_2O_5/41% Ag_2O that has a ignition temperature of ~350 ^oC. Therefore, it has to be Al/Ag_2O thermite the one who ignites first and the generated heat help igniting Al/I_2O_5 thermite. Otherwise, Al/I_2O_5 thermite could not be ignited instantly based on the results shown in Figure S7.2. Even though the limitation is there, an enhancement on the combustion performance of Al/I_2O_5 is still observed when Ag_2O is incorporated into the system.

$AgFeO_2$, a stronger oxidizer than CuO, is also tested in this work and the combustion results are presented in Figure 7.6 as well. As I expected, $AgFeO_2$ shares a similar effect as to CuO. Therefore, it is reasonable to assume that the combustion performance of Al/I_2O_5 can always be enhanced by addition of a secondary metal oxidizer. However, more oxidizers are needed to be added into Al/I_2O_5 system to further verify this argument.

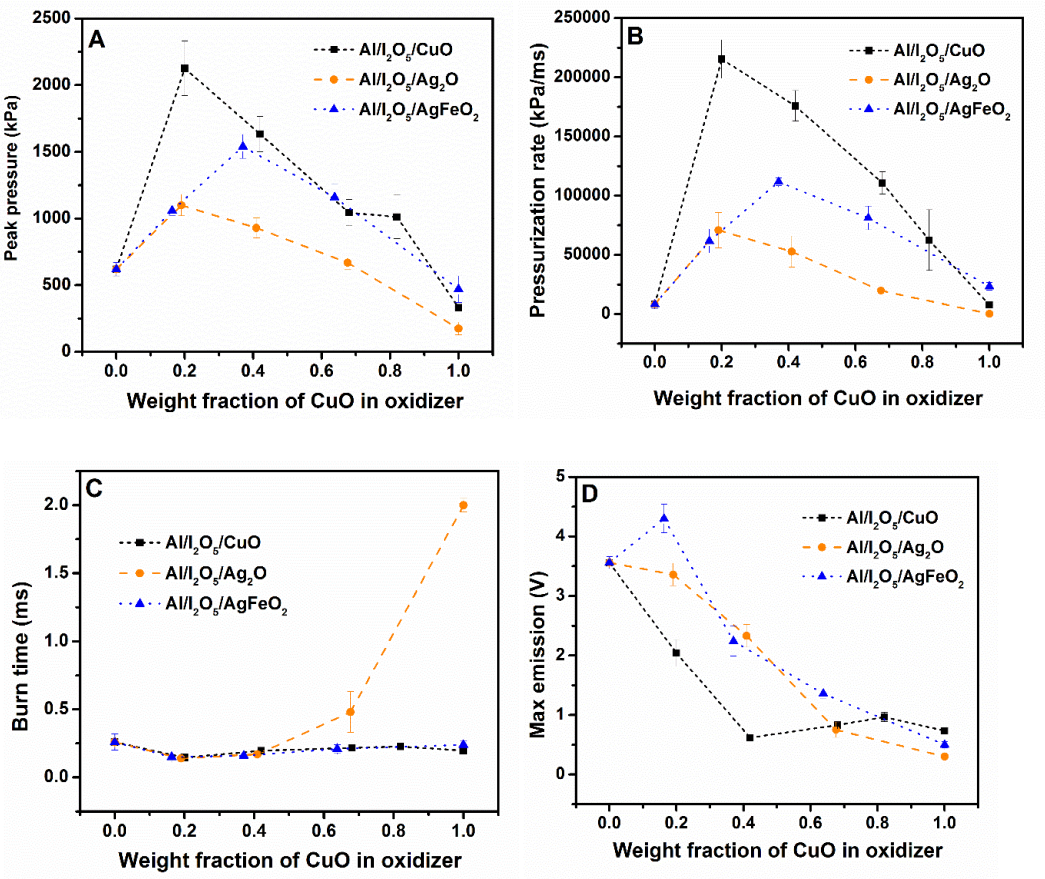

Figure 7.6. Combustion cell results of Al/I_2O_5 thermites with addition of different secondary oxidizer.

7.4. Conclusions

A secondary oxidizer CuO was incorporated into Al/I_2O_5 system to shorten or eliminate the ignition delay of the combustion of Al/I_2O_5. By investigating the combustion performance of four different Al/I_2O_5/CuO thermites varying the mass ratio between two oxidizers and the other two Al/I_2O_5 and Al/CuO thermites in a constant volume combustion cell, significant enhancement is observed for all four thermites and their peak pressures and pressurization rates are much higher than that of Al/I_2O_5 or Al/CuO. The disappearance of the ignition delay in their pressure profiles

and the shortened burn time imply CuO addition indeed does work on accelerating the ignition of Al/I_2O_5 thermite and the overall reaction. In addition, the flame temperatures of the thermites while reacting were obtained and the results indicate the flame temperature of Al/I_2O_5/CuO thermites are almost the same as to Al/I_2O_5, indicating the CuO addition will not sacrifice the high flame temperature of Al/I_2O_5 system.

Therefore, a mechanism was proposed in this work to account for this unexpected improvement: the additive Al/CuO shortens the ignition delay of Al/I_2O_5; that leads to enormous amount of gas formation for aluminum to react and then the extremely high flame temperature of Al/I_2O_5 boost the pressure inside the combustion cell further. All those events happen around the same time and produce a synergetic effect to enhance the combustion performance of Al/I_2O_5.

A weaker oxidizer Ag_2O and stronger oxidizer $AgFeO_2$ compared to CuO is also incorporated into Al/I_2O_5 thermite, respectively, in order to potentially expand the options for the secondary oxidizer. The results demonstrate both Ag_2O and $AgFeO_2$ have similar effects on promoting the combustion performance of Al/I_2O_5. Although more oxidizers need to be examined furthermore, it is reasonable to assume the combustion performance of Al/I_2O_5 could be enhanced by just incorporating a secondary oxidizer, which make the iodine-containing energetic materials more tunable and controllable.

7.5. Supplemental Information

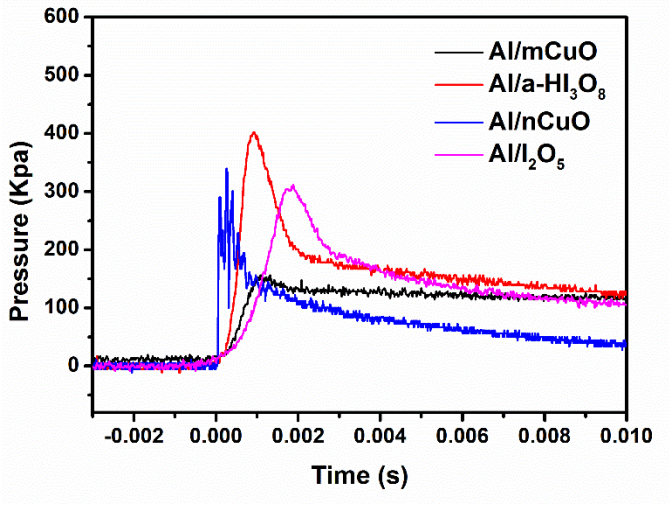

Figure S7.1. Temporal pressure traces of different thermites from ref (combustion and flame paper).

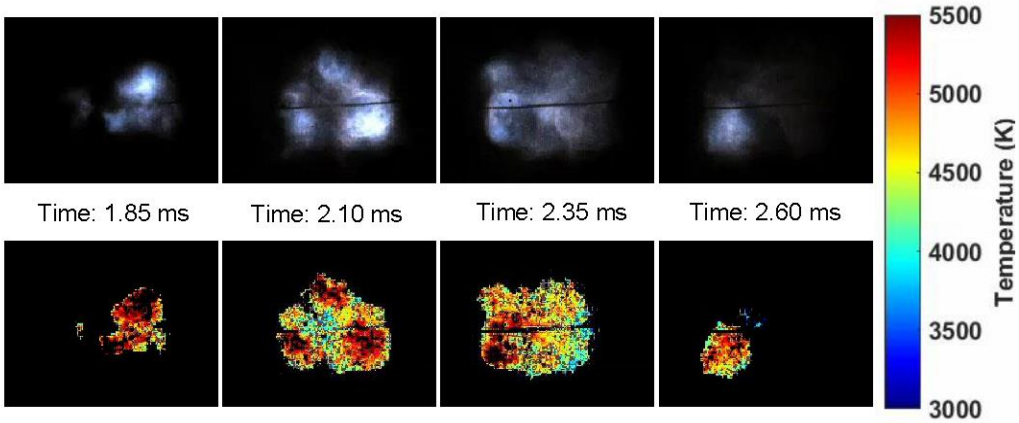

Figure S7.2. The typical snapshots and corresponding flame temperature map of Al/I_2O_5.

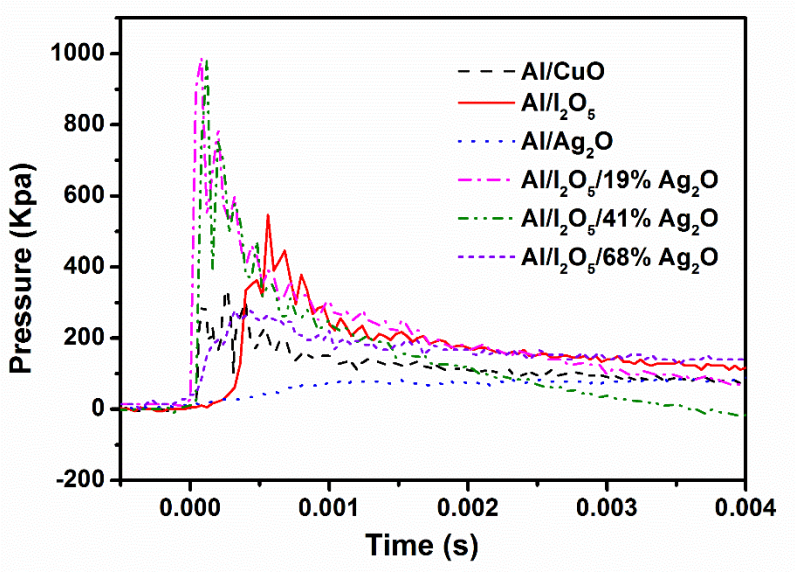

Figure S7.3. Temporal pressure traces of different $Al/I_2O_5/CuO$ thermites. The number listed after the series name represent the weight fraction of CuO within oxidizers in each thermite.

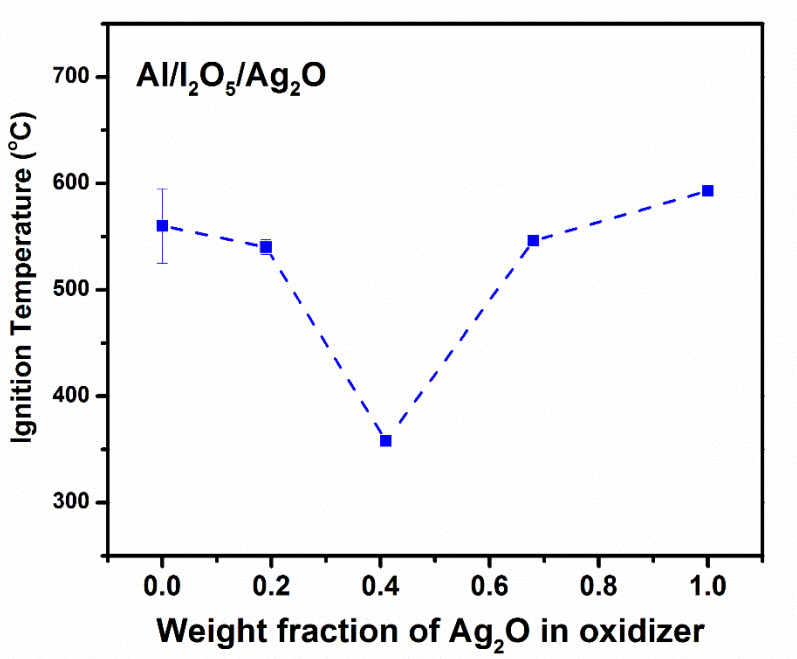

Figure S7.4. The ignition temperatures of $Al/I_2O_5/Ag_2O$ thermites within T-Jump/TOFMS.

Chapter 8: Silver Ferrite: a superior oxidizer for thermite-driven biocidal nanoenergetic materials*

Overview

Silver-containing oxidizers are of interest as biocidal components in energetic application such as thermites due to their biocidal agent delivery. In this study, $AgFeO_2$, was evaluated as an oxidizer in aluminum-based thermite system. This novel oxidizer $AgFeO_2$ particles were prepared via a wet-chemistry method and the structure, morphologies and thermal behavior were investigated using X-ray diffraction (XRD), scanning electron microscopy (SEM), thermogravimetric analysis and differential scanning calorimetry, and time-resolved temperature-jump time-of-flight mass spectrometry (T-Jump/TOFMS). The results indicate the decomposition pathways of $AgFeO_2$ vary with heating rates from a two-step at low heating rate to a single step at high heating rate. Ignition of Al/$AgFeO_2$ at a temperature just above the oxygen release temperature and is very similar to Al/CuO. However, with a pressurization rate three times of Al/CuO, Al/$AgFeO_2$ yields a comparable result as to Al/hollow-CuO or Al/$KClO_4$/CuO, with a simpler preparation method. The post combustion products demonstrated that the Al/$AgFeO_2$ thermite reaction produces a fine dispersion of elemental nanosized silver particles which coats the larger alumina particles and is thus bioavailable.

* The results presented in this chapter have been submitted in the following journal article: Wu, T.; Zachariah, M.R., Silver Ferrite: a superior oxidizer for thermite-driven biocidal nanoenergetic materials. *Journal of Materials Chemistry C* 2018.

8.1. Introduction

High efficiency neutralization of biological warfare agents has become of increased importance due to the enhanced threat of bioterrorism [1-4]. Preliminary laboratory studies have suggested that an ideal neutralization process should contain not only a high thermal event but also a long-lasting biocidal agent release [5-11]. The main problem with conventional energetic materials is low neutralization efficiency since a thermal neutralization mechanism is nominally dominant [5]. Therefore, it has been proposed that simultaneously delivering a rapid thermal pulse with a remnant biocidal agent would prolong the exposure time and improve the inactivation process [12].

Reactive materials are a class of energetic materials containing separated fuels and oxidizers and featuring an extremely high exothermicity, intensive light emission and shock generation by the self-sustained reaction [13-15]. When metal and metal oxide are employed as the fuel and oxidizer, respectively, the intense exothermic metal/metal oxide reaction is commonly referred to a thermite reaction. This reaction is self-propagating once the ignition starts and the kinetics of the reaction are known to be accelerated when the fuel and oxidizer are at the nanoscale, resulting from the increased interfacial contact and reduced characteristic diffusion length scale. The most widely adopted metal is aluminum due to its abundance and competitive reactivity when compared with other metals [16]. Various oxidizers, such as metal oxides [17-25], iodine oxides [26-31], sulfates [32, 33], iodates [12, 34, 35], potassium salts [36, 37] and etc, have been employed in formulation of thermites. Among all, halogens-containing and silver-containing oxidizers have drawn attention because of their excellent biocidal properties [38-42]. For halogens, iodine stands out owing to its

strong neutralization effect and different iodine-containing oxy-compounds, such as metal iodates and iodine oxides [5, 12, 18-32, 34-36, 43], have been studied in thermite systems.

As to silver, it has been pointed out that silver exhibits biocidal properties in the forms of metallic Ag particles and silver ions in a humid environment [44]. Since most of the products of thermite combustion tend to be primarily in the condensed phase [2], metallic silver particles are the focus of this work. As indicated by Morones et al [45] and Smetana et al [46], small particle sizes are necessary for silver particles to perform well in biocidal activities. To deliver not only a high thermal event but also a large amount of small silver particles as the active biocidal sites is the goal of this work.

When it comes to silver-containing oxidizers, Ag_2O was the obvious choice to be considered as an oxidizer in an aluminum-based thermite system. In 2010, Clark et al [47] investigated the combustion performance and biocidal abilities of both Al/I_2O_5 and Al/Ag_2O thermites using a homemade biocidal reaction chamber. They concluded Al/I_2O_5 thermite exhibited significant spore neutralization owing to the generation of lot of iodine gas. In 2011, Russell et al [48] further studied the flame propagation behaviors of Al/I_2O_5 and Al/Ag_2O thermites using mechanical impact and thermal initiation. The results show that Al/Ag_2O features a lower average flame propagation by about 2.5 times in thermal ignition tests but produce much more energy than Al/I_2O_5 in impact-driven ignition tests. They also argued that the energy release of the thermite reactions is significantly enhanced by reducing the sizes of the oxidizers particles. In the same year, Sullivan et al [5] investigated the performance of $AgIO_3$ as an oxidizer in aluminum-based thermite because it decomposed to O_2, O and I gases when heated

at an ultra-high heating rate. Silver was not observed in the mass spectra probably because the temperature was high enough to reach the adiabatic flame temperature and thus could not vaporize silver. However, Al/$AgIO_3$ considerably outperformed Al/CuO in pressurization rate due to a large number of gaseous products released from $AgIO_3$; however, its high combustion performance was mitigated by the fact that the reaction products were found to form AgI instead of elemental silver and iodine, thus obstructing its usage in biocidal applications.

Sullivan et al [2] subsequently synthesized nano-Ag_2O particles and investigated its reactivity as an oxidizer in biocidal energetic systems since it produces high yields of antimicrobial silver as one of the combustion products. They found that Ag_2O alone performs poorly in terms of pressurization rate and burn time, but its performance is significantly improved when combined with one more reactive oxidizer, such as $AgIO_3$ or CuO. The morphology of the final products was also studied and indicated that abundant active sites of silver particles were sacrificed since some silver particles were trapped within the interior of other products, which might to some extent affect its biocidal activity. Inspired by the fact that CuO addition improve the performance of Al/Ag_2O extensively, I embed the extra oxidizer into Ag_2O molecularly, which means the oxidizer used in this work is going to be a composite metal oxide. Lately, $NiCo_2O_4$ [49] and $NiFe_2O_4$ [50] have been employed as oxidizer in aluminum-based thermites and both feature excellent heat release and intense thermite reaction. Among all Ag-containing composite metal oxides, $AgFeO_2$ as a molecularly mixed oxidizer of Ag_2O and Fe_2O_3 with a delafossite structure becomes the first one to explore this idea here. In addition, Fe_2O_3 has been proven to be very poor oxidizer in Al-based thermite system

[36], it could potentially make our point even more sound if $AgFeO_2$ made of two poor oxides (Ag_2O and Fe_2O_3) became a strong oxidizer.

A wet-chemistry method was adopted here for the preparation of $AgFeO_2$ and its thermal behavior were investigated using a low heating rate thermogravimetric analysis and differential scanning calorimetry in an argon environment. Time-resolved temperature-jump time-of-flight mass spectrometry (T-Jump/TOFMS) was also employed to evaluate the decomposition behaviors of bare $AgFeO_2$ or Al/$AgFeO_2$ thermites under rapid heating rates, enabling me to probe the reaction process on a time scale close to that of a combustion event. The results indicate that the decomposition pathways of $AgFeO_2$ vary in term of heating rates. For a comparison purpose, Al/CuO, Al/Ag_2O and Al/Ag_2O/Fe_2O_3 were also included in this chapter. A high-speed camera coupled with T-Jump/TOFMS simultaneously captured optical emission from the ignition/reaction of the thermites allowing us to obtain the ignition time, and corresponding ignition temperature. In addition, constant volume combustion cell tests were performed on aluminum-based thermites. The post combustion products were characterized by X-ray diffraction, scanning electron microscopy, transmission electron microscopy and energy-disperse X-ray spectroscopy. The results demonstrated that the Al/$AgFeO_2$ thermite reaction produce an enormous amount of nanosized silver particles and feature the best combustion performance in this work.

8.2. Experimental Details

8.2.1. Materials

The aluminum nanopowders (Al) (Alex, ~80 nm) was purchased from Novacentrix. The active Al was 81 % by mass, determined by TGA. All metal oxide nanopowders (< 50 nm) purchased from Sigma-Aldrich was directly used as received. All the other chemicals were of analytical grade and used as purchased without further treatment.

8.2.2. Preparation of $AgFeO_2$

$AgFeO_2$ powders were prepared via a co-precipitation method. For this, 2.66 mmol of $Fe(NO_3)_3 \cdot 9H_2O$ and 2.66 mmol of $AgNO_3$ were dissolved in 20 mL of water and stirred for 30 minutes. The solution was then heated to 80 °C and stirred for one hour. Then, 1.5 M of NaOH solution was added dropwise into the solution until its pH reaches 13, followed by another 6 hours of stirring on a hot plate (80 °C). The prepared $AgFeO_2$ powders could be easily iolated from the solution by vacuum filtration and were purified by successively washing with copious amount of distilled water and absolute ethanol. Finally, the product was dried in a oven at 70 °C.

8.2.3. Preparation of Ag_2O

Ag_2O powders were prepared by adding 0.025 M NaOH solution dropwise into 80 mL of $AgNO_3$ solution (0.005 M) with stirring until the solution become a grey-yellow colloidal suspension. The suspension was kept at 60 °C for another 2 hours to ensure complete reaction. The prepared Ag_2O powders were collected by centrifugation and

washed with distilled water and then absolute ethanol three times. The solid pure Ag_2O was obtained after being dried in an oven at 70 °C for 10 hours.

8.2.4. Preparation of thermites

Aluminum nanopowders was stoichiometric mixed with $AgFeO_2$, Ag_2O, CuO and Fe_2O_3 based on the following equations, respectively, in dry hexane followed by 30 minutes sonication. After room temperature evaporation of the solvent the solid thermite powders were collected.

$4Al + 3AgFeO_2 \rightarrow 3Ag + 3Fe + 2Al_2O_3$, $\Delta H_{calculated}$ = -1760 kJ/mol

$2Al + 3Ag_2O \rightarrow 6Ag + Al_2O_3$, $\Delta H_{calculated}$ = -1374 kJ/mol

$2Al + 3CuO \rightarrow 3Cu + Al_2O_3$, $\Delta H_{calculated}$ = -1109 kJ/mol

$4Al + 3Ag_2O + Fe_2O_3 \rightarrow 6Ag + 2Fe + 2Al_2O_3$, $\Delta H_{calculated}$ = -2125 kJ/mol

8.2.5. T-Jump/TOFMS measurement and high-speed imaging

The decomposition of oxides particles was investigated using a custom T-Jump/TOFMS [5] Typically, a ~1 cm long platinum wire (76 um in width) with a thin coating of oxidizer or thermite sample was rapidly joule-heated to about 1200 °C by a 3 ms pulse at a heating rate of ~10^5 °C/s. The current and voltage signals were recorded, and the temporal temperature on the wire was measured according to the Callendar–Van Dusen equation. MS spectra were measured every 0.1 ms. The detailed experimental set-up is given in our previous papers [5, 32].

To identify the point of ignition a high-speed camera (Vision Research Phantom v12.0) was employed to record the combustion on the wire during heating. Ignition temperatures of thermite reactions in vacuum were measured from the correlation of

optical emission from high speed imaging and temporal temperature of the wire and were further analyzed in combination with the temporal mass spectra. Each experiment was repeated 3 times.

8.2.6. X-Ray Diffraction (XRD) measurement and Rietveld refinement

The as-prepared samples were characterized by powder X-ray diffraction. Diffraction pattern was measured using Cu Kα radiation in Bragg-Brentano geometry on Bruker D8 Advance powder diffractometer equipped with incident beam Soller slits, Ni β-filter and LynxEye position sensitive detector. Data were collected from 10º to 90º 2θ with a step size of 0.01578º and counting time of 1 sec per step (total exposure time of 180 sec per step).

8.2.7. Thermogravimetric analysis/differential scanning calorimetry (TGA/DSC) measurement

Thermogravametric analysis and differential scanning calorimetry (TGA/DSC) was performed using a TA Instruments SDT Q600. The analysis was performed under a 100 mL min^{-1} argon flow with ~ 1.0 mg samples placed into an alumina pan and heated from room temperature up to 1000 °C at a rate of 10 °C min^{-1} in argon atmosphere.

8.2.8. Morphologies and structures characterizations Transmission Electronic Microscopy (TEM)

Transmission electronic microscopy (TEM, JEOL JEM 2100 FEG) and scanning electronic microscopy (SEM, Hitachi Su-70) were used to investigate morphologies

and structures of thermites. Elemental distribution in the thermites was analyzed by Energy-disperse X-rat spectroscopy (EDS) on both SEM and TEM.

8.2.9. Combustion test

Combustion properties of themites were evaluated in a constant-volume combustion cell, with simultaneous pressure and optical emission measurements. In this study, 25 mg of thermite powders was loaded inside the cell (constant volume, ~13 cm^3) and ignited by a resistively heated nichrome wire. The temporal pressure and optical emission from the thermite reaction were measured using a piezoelectric pressure sensor and a photodetector, respectively. More detailed information on the combustion cell test can be found in our previous publications [21, 25, 29]. Each experiment was repeated at least 3 times.

8.3. Results and discussions

8.3.1. Synthesis and characterization of $AgFeO_2$

XRD of as-prepared materials shown in Figure 8.1A indicates that silver ferrite was successfully prepared. The particles have an oval shape with particle size of ~40 nm based on the SEM image shown in Figure 8.1B, and suggests it might be a very good oxidizer in a thermite system due to its small size [32].

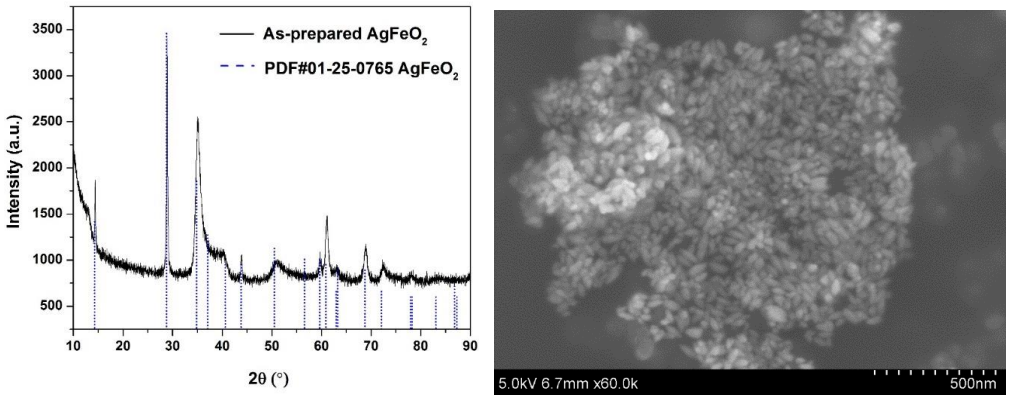

A B

Figure 8.1. XRD spectrum (A) and SEM image (B) of $AgFeO_2$ prepared via co-precipitation

The thermal stability of $AgFeO_2$ was studied with a TGA in Ar at a heating rate of 10 °C/min. The result shown in Figure 8.2 indicates a ~4% weigh loss at around 650 °C, corresponding to O_2 gas release based on equation (8.1). To determine the composition of the remaining material, XRD shown in Figure 8.2B indicates the formation of both Fe_2O_3 and Ag.

$2AgFeO_2 \rightarrow 2Ag + Fe_2O_3 + ½\ O_2$ Equation (8.1)

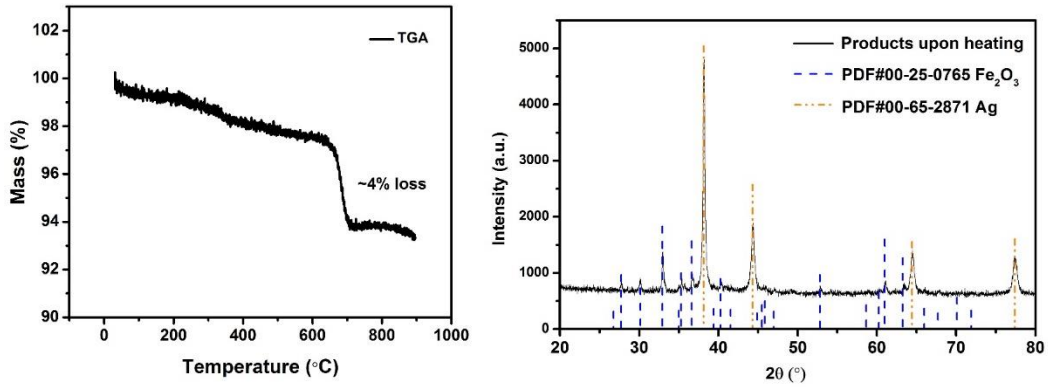

A B

Figure 8.2. TGA result of $AgFeO_2$ in Ar at a heating rate of 10 °C/min (A); $AgFeO_2$ decomposed product after heated to 1000 °C (B).

High heating rate decomposition of $AgFeO_2$ was investigated using TOFMS/T-Jump (3 ms, heating rate ~5×10^5 °C /s). Figure 8.3 shows the temporal evolution of O_2 from $AgFeO_2$ during rapid heating. Oxygen was first detected at around 685 °C which is slightly higher than the onset decomposition temperature under low heating rate TGA. Only one O_2 signal stage is observed indicating the decomposition of $AgFeO_2$ is a one-step event at high heating rates conditions, as compared to its multistage decomposition behavior at low heating rates as discussed previously.

Time-resolved T-jump mass spectra from rapid heating of $AgFeO_2$ at 1.6-2.2 ms is shown in Figure S8.1 to further explore its decomposition process. Apparently, the onset decomposition of $AgFeO_2$ started at around 1.8 ms (685 °C) with the appearance of a small O_2 peak. For mass spectra taken at prior times, H_2O^+, OH^+, CO^+/N_2^+ peaks are attributed to the background [18]. Above the decomposition temperature, no new peak except for O_2 peak is found again suggests a one-step decomposition of $AgFeO_2$ at high heating rate. CO_2^+ was also observed we attribute to decomposition products of the precursor salt residue on the $AgFeO_2$ surface [17].

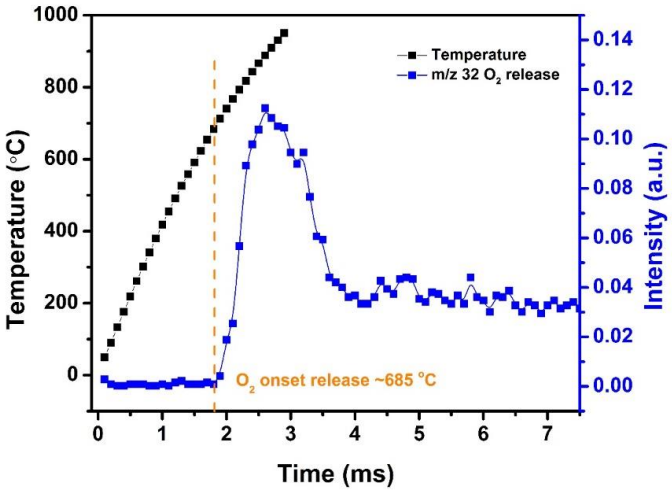

Figure 8.3. Temperature and O_2 temporal profile of $AgFeO_2$.

8.3.2. Ignition of Al/$AgFeO_2$ nanothermite

To evaluate the performance of $AgFeO_2$ as an oxidizer in Al-based thermite, physical mixtures of nanosized aluminum and $AgFeO_2$ were made, following 30 min sonication of the mixture in dry hexane. Sequential snapshot of Al/$AgFeO_2$ ignition during high-rate heating under vacuum were captured using a high-speed camera and is shown in Figure 8.4. Optical emission from Al/$AgFeO_2$ reaction was first observed at 1.662 ms with a corresponding wire temperature of ~740 °C as a sign of ignition. Multiple ignition points are observed in the prior time and then merge into a large bright flame indicating the generation of a lot of heat. One should also notice that, upon ignition, thousands of bright dots were rapidly ejected out from the reactants coated on the Pt wire (even more bright dots appeared when ignited in an argon environment as shown in Figure S8.2). The burn time of the thermite in T-jump chamber could be roughly obtained based on the visual flame and is about 0.3 ms, which is almost the same as the value obtained from the combustion cell test discussed below.

Ag_2O was included as an oxidizer in Al-based thermites as a control. As the most common used oxidizer, CuO was also included as a standard reference. Since $AgFeO_2$ ($Ag_2Fe_2O_4$) can be molecularly written as Ag_2O and Fe_2O_3, a binary mixture Ag_2O-Fe_2O_3 with 1/1 molar ratio is also included for comparison.

Figure 8.5 shows the relationship between O_2 release temperature in neat oxides and the ignition temperature of corresponding thermites under vacuum. There is a good correlation between the oxygen release from the bare oxidizer and ignition of Al/Fe_2O_3 and Al/$AgFeO_2$. Al/Fe_2O_3 has a very high ignition temperature due to the poor performance of Fe_2O_3 as an oxidizer [24]. On the other hand, Al/Ag_2O thermite ignited

at around ~660 ºC, essentially the melting temperature of aluminum. Considering Ag_2O releases oxygen at around 520 °C, it is reasonable to conclude that the ignition of Al/Ag_2O thermite is limited to the melting phase of aluminum like most Al/metal oxides systems [19]. In fact, the ignition temperatures of the other three samples are all higher than the melting point of aluminum indicates that gaseous oxygen released from the decomposition of oxidizers, was insufficient to ignite aluminum when it is still in the solid phase.

$Al/Ag_2O/Fe_2O_3$ ternary thermite ignited at around 800 °C much higher than its oxygen release temperature (520 °C). Considering Al/Ag_2O and Al/Fe_2O_3 ignited at around 660 and 940 °C, respectively, an ignition temperature of about 800 °C is reasonable for the ternary system $Al/Ag_2O/Fe_2O_3$. The Fe_2O_3 addition is more likely hindering/weakening the ignition/reaction of the ternary system due to its weak reactivity in Al-based thermites [36].

As to $Al/AgFeO_2$, it ignited at a temperature close to the oxygen release temperature of the corresponding oxidizer and higher than the melting temperature of aluminum following an ignition mechanism similar to Al/Fe_2O_3 and Al/CuO [18, 19]. Moreover, the fact that the ignition temperature of Al/Fe_2O_3 is much higher than that of $Al/AgFeO_2$ implies the oxygen involved with $Al/AgFeO_2$ ignition come from $AgFeO_2$ rather than the first-stage decomposed product Fe_2O_3 as indicated in TGA. Since only one oxygen release stage appeared at the mass spectra and the violent reaction of $Al/AgFeO_2$ at 1.7 ms (~780 °C) implies decomposition of $AgFeO_2$ is a one-step process during $Al/AgFeO_2$ thermite reaction at high heating rate.

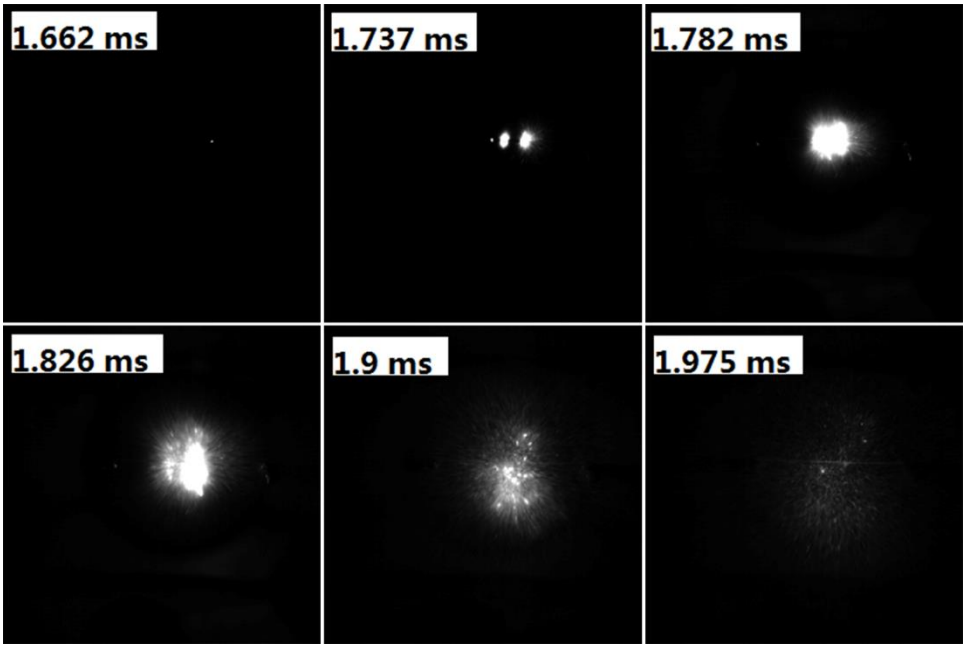

Figure 8.4. Sequential snapshots of $Al/AgFeO_2$ burning on a high-rate heating Pt wire in T-Jump chamber (in vacuum). The labels in each image are the time elapse after triggering.

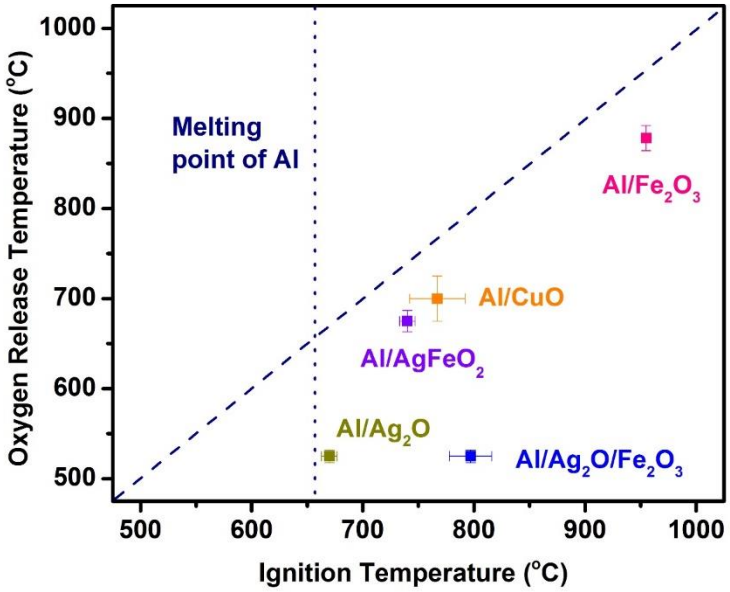

Figure 8.5. Ignition temperature vs. oxygen release temperature from the corresponding oxidizer. The diagonal dash line presents a perfect correlation.

8.3.3. Combustion performance of Al/$AgFeO_2$ nanothermite

The combustion performance of Al/$AgFeO_2$ at room atmosphere was studied using a constant volume combustion cell, and the results are summarized in Table 8.1. The pressurization rate and peak pressure in Al/$AgFeO_2$ reaction are 6200 kPa/ms and 325 kPa, respectively, which are considerably higher than those of nanothermite reaction of Al/CuO. A direct comparison between the temporal pressure traces of Al/$AgFeO_2$ and Al/CuO was shown in Figure 8.6A in which the first peak was used to determine the corresponding pressurization rate. Clearly, Al/$AgFeO_2$ reaction reaches its first peak with a faster rate and higher peak value compared with Al/CuO. It has been claimed in our previous works that gaseous species release from the decomposition of the oxidizer is the main cause for the pressurization, which can occur much earlier than ignition/combustion [36, 51]. The fact that $AgFeO_2$ (~16%) which has a lower oxygen weight ratio than CuO (~20%) suggests the O_2 release rate of $AgFeO_2$ must be higher than that of CuO in order to output such high pressure. In addition, the optical signals peak much later than the corresponding pressure peaks for both Al/CuO (~0.5 ms) and Al/$AgFeO_2$ (0.9 ms) implying a similar mechanism [51, 52]. Therefore, similar to Al/CuO [36], the ignition/reaction mechanism of Al/$AgFeO_2$ is summarized as follows: $AgFeO_2$ releases O_2 gas (~690 °C) and the aluminum core becomes mobile (633 °C); and the mixture ignites (~740 °C, Figure 8.5) and the generated heat further promote the decomposition of $AgFeO_2$ to pressurize the system.

Moreover, with a pressurization rate three times of Al/CuO, Al/$AgFeO_2$ yields a comparable result as prior work on Al/hollow-CuO [25] or Al/KClO4/CuO [36], which

make $AgFeO_2$ a powerful replacement owing to its simpler and cheaper preparation method.

Sullivan et al [2] has previously reported that Al/Ag_2O suffers a poor combustion performance in terms of both pressurization rate and peak pressure and incorporation of a small fraction of CuO into the Al/Ag_2O system improved its combustion performances extensively to even close to the reactivity of Al/CuO. An explanation was provided by Sullivan et al that CuO addition can increase the reaction temperature and thus further enhance the performance of Ag_2O as an oxidizer. Consistent with this reported result, Al/Ag_2O performs poorly in the combustion cell test due to to early a release of O_2 [2]; however, Fe_2O_3 addition does not show much improvement to Al/Ag_2O system as CuO does. Instead of improving, Fe_2O_3 even weaken the combustion performance of Al/Ag_2O system considering $Al/Ag_2O/Fe_2O_3$ features the worst pressurization rate and burn time. Thermodynamic equilibrium predictions of Al/CuO, Al/Ag_2O and Al/Fe_2O_3 thermites by Fisher and Grubelich [2, 26, 53] are shown in Table 8.2 where we can see that both CuO and Ag_2O should perform significantly better than Fe_2O_3 in terms of gas production. And this is consistent with our experimental data shown in Table 8.1. In detail, unlike CuO that can rapidly release O_2, Fe_2O_3 cannot efficiently decompose and upon decomposition most of the oxygen is still fixed as solid FeO [36], which leads to its decomposition as the rate-limiting step for $Al/Ag_2O/Fe_2O_3$ reaction and therefore weakened combustion performance. In fact, Fe_2O_3 has been introduced previously as a moderator to weaken the reactivities of $Al/KMnO_4$ [24] and $Al/KClO_4$ [36].

$Al/AgFeO_2$ significantly outperforms $Al/Ag_2O/Fe_2O_3$ by a scale of almost 100 in pressurization rate and about 4 in peak pressure. The fact that $Al/AgFeO_2$ and $Al/Ag_2O/Fe_2O_3$ share the exact same elemental compositions indicates molecularly incorporation of Ag_2O into Fe_2O_3 outperforms the mechanically mixed Ag_2O/Fe_2O_3 when they were employed as oxidizers in aluminum-based thermites.

The burn time of the thermite reactions measured in the combustion cell are shown in Table 8.1. Clearly, $Al/AgFeO_2$ features the shortest burn time which makes it the most violent thermite among the four examined. A direct comparison of the optical emission trace of $Al/AgFeO_2$ and Al/CuO was shown in Figure 8.6B. The Al/CuO reaction has a four-times higher peak optical emission but 0.1 ms longer burn time compare with those of $Al/AgFeO_2$. This result indicates that $Al/AgFeO_2$ is a weaker heat generator than Al/CuO; but reacts more rapidly. In general, $AgFeO_2$ is the best oxidizer among those four in the aluminum-based thermite system from both pressurization and optical emission perspectives.

Table 8.1. Combustion performance of mixed thermites of $Al/AgFeO_2$.

Thermites (stoichiometric)	**Peak Pressure (Kpa)**	**Pressurization rate (Kpa/ms)**	**Burn time (ms)**	**Peak optical emission (Volts)**
Al/n-CuO	226	2045	0.46	4.3
Al/Ag_2O	75	25.7	3.6	0.3
$Al/Ag_2O/Fe_2O_3$	74	21	5	0.4
$Al/AgFeO_2$	**325**	**6200**	0.3	1

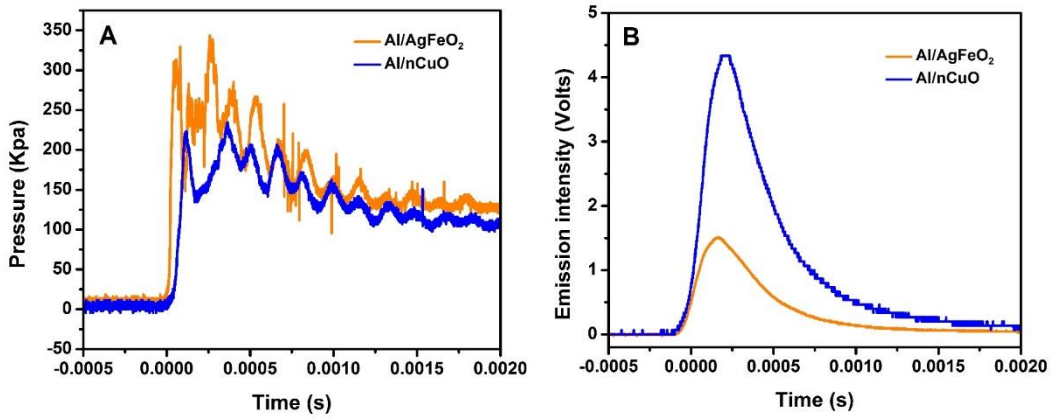

Figure 8.6. Direct comparison between the pressure and optical trace of Al/AgFeO2 and Al/nCuO.

Table 8.2. Thermodynamic equilibrium predictions of Al/CuO, Al/Ag_2O and Al/Fe_2O_3 thermites. Data is taken from Fisher and Grubelich[a] [53].

Thermite reaction	Adiabatic Temperature (C)	Gas production (mmol/g)	Major gas species
2Al + 3CuO -> Al_2O_3 (l) + 3Cu (l, g)	2570	5.4	Cu
2Al + 3Ag_2O -> Al_2O_3 (l) + 6Ag (l, g)	2163	4.3	Ag
2Al + Fe_2O_3 -> Al_2O_3 (l) + 2Fe (l, g)	2862	1.4	Fe

[a] *Assumptions: constant enthalpy and pressure with phase changes; without taking account of the oxide shell of aluminum.*

8.3.4. Post-combustion-product characterization

It has been pointed out previously that the nature and dispersion of the products from a thermite combustion plays an important role in biocidal applications [26]. XRD evaluation of crystalline product species is shown in Figure 8.7 and show no evidence of the parent starting materials, but five new strong peaks indexed to elemental silver

are seen. The fact that no peak corresponding to Al_2O_3 or Fe was observed might suggest they are both amorphous.

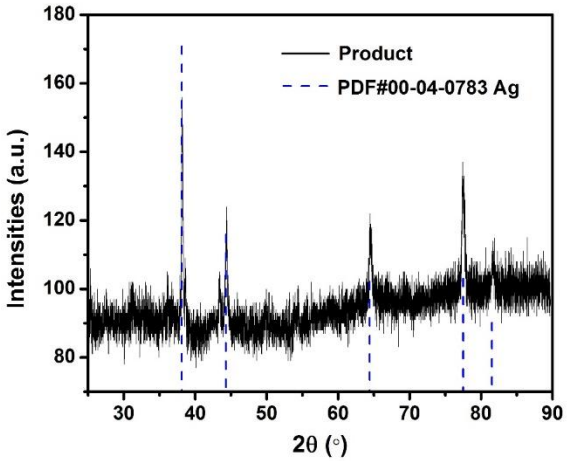

Table 8.3. The XRD pattern of Al/$AgFeO_2$ reaction product.

For SEM evaluation of the reaction product a 7 mm × 5 mm rectangular double-sided carbon tape was placed inside the combustion cell chamber. Two representative SEM images of the product were shown in Figure 8.8A-B, show there are mainly two populations of product particle sizes. One has relatively larger dimension and another with a dimension as small as ~80 nm. 2D elemental mapping using EDS shown in Figure 8.8, indicate the larger spherical particles are Al_2O_3 while the smaller particles are Ag. This was also confirmed with 1D elemental line-scan coupled with elemental analysis shown in Figure S8.3. Most importantly for the application as a biocide, is that the smaller Ag particles randomly decorate the larger Al_2O_3 particles.

Overall, the intensity of iron signal is the weakest among those four elements under EDS mapping implying the random distribution of iron.

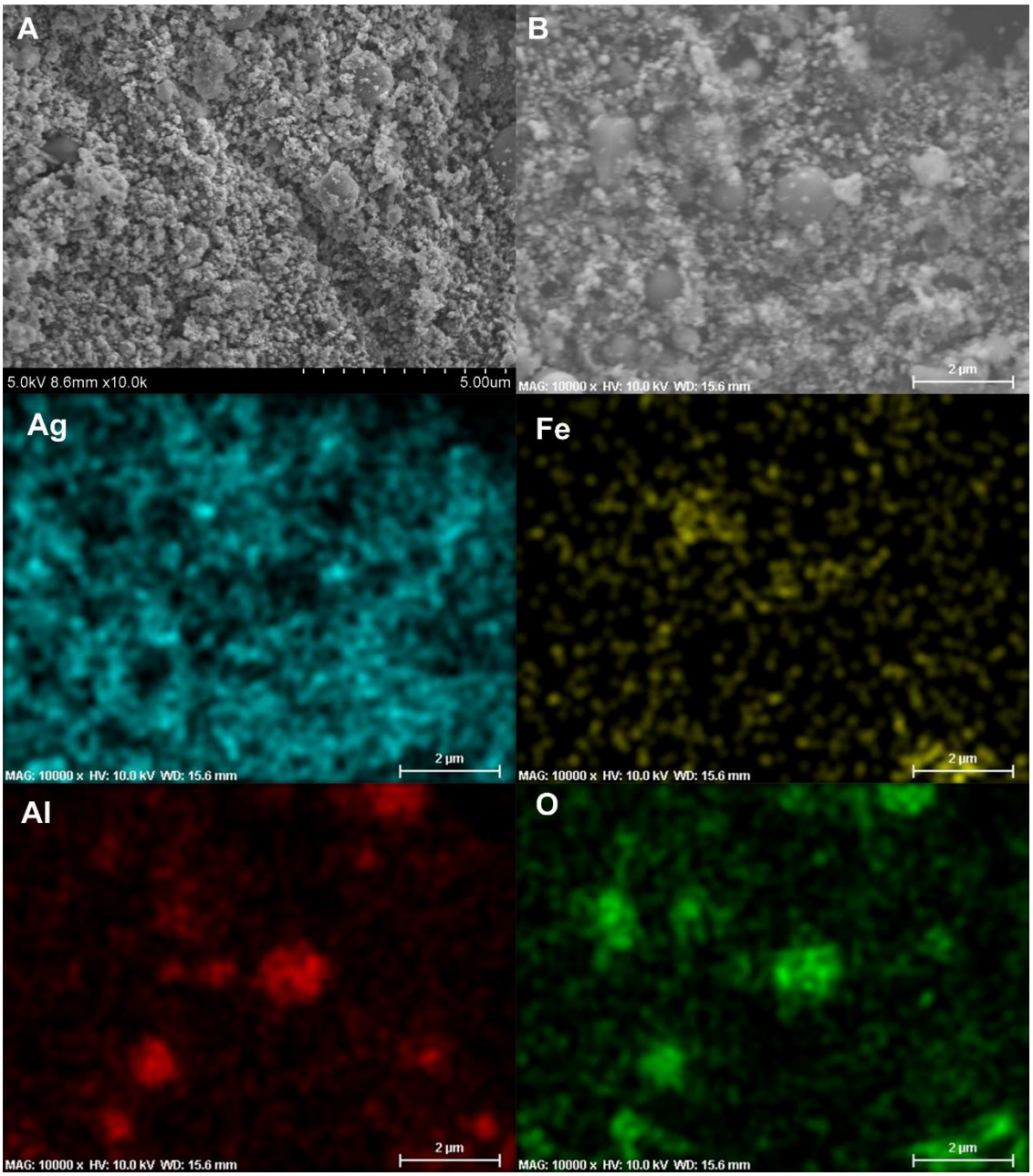

Table 8.4. Representative SEM images (A and B) of the Al/$AgFeO_2$ reaction product collected inside the combustion cell; 2D elemental mapping (Ag, Fe, Al and O) of Figure 8B using EDS.

TEM of the reaction product along with an EDS elemental mapping result is shown in Figure 8.9. As can be seen, there are two different types of particles similar to the SEM result. One has a spherical shape with a relatively larger particle size and low

contrast; another has a spherical/oval shape with smaller size and dark contrast. In the EDS elemental mapping, red represents silver, blue iron, yellow aluminum and green oxygen. Clearly, the three larger spherical particles are Al_2O_3. Since the mixing of red and blue gives purple, it is reasonable to conclude that the silver and iron positions are mostly overlapped. It could mean a formation of Ag-Fe alloy; however, the SEM results indicate the iron signal is much weaker and always appears with the presence of both aluminum and oxygen signals. To clarify this speculation, an EDS line-scan analysis was employed, and the result will be discussed below. It should also be noted that some white pixels were found in the purple area, implying the presence of oxygen (green plus red and blue equals to white). Thus, those silver- and iron-containing particles might be partially oxidized that could be a result from handling the product in air.

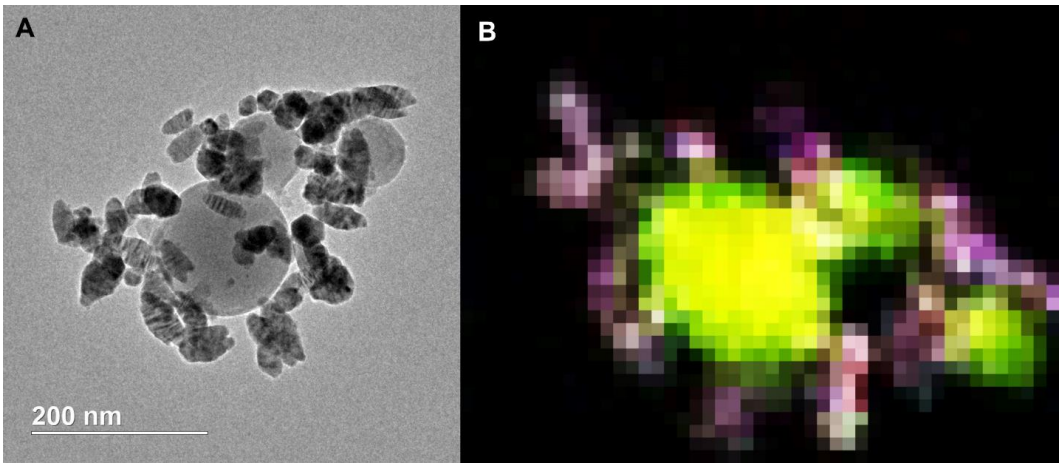

Figure 8.7. TEM image (A) and 2D elemental mapping (B) of the Al/$AgFeO_2$ reaction product. Red represents Ag, blue represents Fe, yellow represents Al and green represents O.

As one can see from the EDS line-scan result shown in Figure 8.10, excerpt for the small oxygen signal peak at ~0.4 um, the aluminum and oxygen signals are almost synchronous in positions indicating Al_2O_3. Like the SEM EDS mapping result, iron is

the weakest among all four elements. It overlaps with aluminum and silver, respectively, implying the iron is randomly distributed and excluding the hypothesis of Ag-Fe alloy formation.

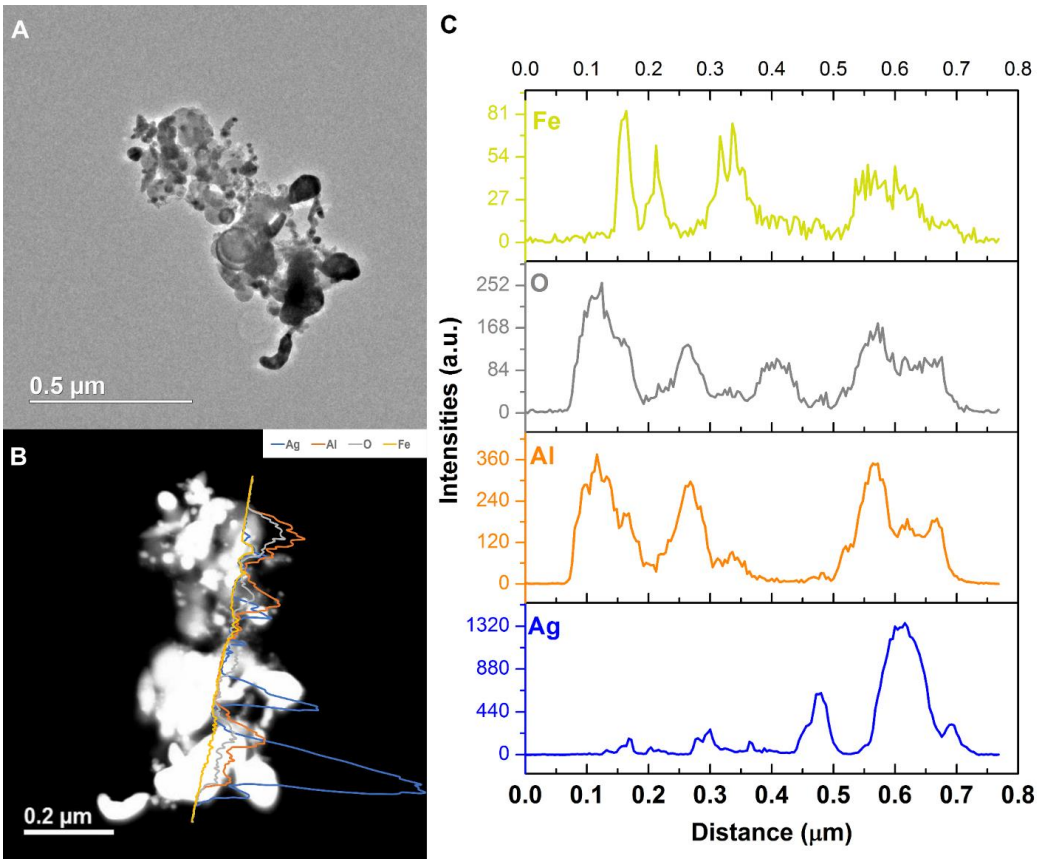

Figure 8.8. A representative TEM image and the corresponding EDS line-scan data of the Al/$AgFeO_2$ reaction product.

Comparing these two representative TEM images Figure 8.9A and Figure 8.10A, the morphologies of the silver particles are quite different. The ones in Figure 8.9A are nanosized with spherical/oval shapes and are decorated on/near the Al_2O_3 surface that suggests silver product had vaporized and re-condensed [2]. This mechanism is beneficial to biocidal applications due to the wide distribution of small sized silver particles during the violent combustion event. As to the one in Figure 8.10A, particles

at the bottom right with oddly shapes clearly underwent some sintering while silver. Those results are consistent to a previously reported sintering reaction mechanism of Al-based thermites [54, 55]. However, it seems much less reactants were following the sintering mechanism according to the SEM image shown in Figure 8.8 where the majority of silver product has small particle size and distributed randomly.

8.4. Conclusions

In this study, the $AgFeO_2$ was prepared via a wet-chemistry method to yield phase pure ~ 40 nm particles. The decomposition pathways of $AgFeO_2$ were found to depend on heating rates: decomposition to Ag, O_2 and Fe_2O_3 at ~600 °C at low heating rate and direct decomposition ~685 °C at high heating rates.

The ignition of $Al/AgFeO_2$ was found to slightly higher than the oxygen release temperature and thus with a similar mechanism to Fe_2O_3 although ignites and a much lower temperature. Fast video imaging indicates a fine smoke dispersing particle.

Combustion cell test showed that $Al/AgFeO_2$ outperformed other thermites in maximum pressure, pressurization rate and burn time. Moreover, with a pressurization rate three times and 5% less oxygen content of Al/CuO, $Al/AgFeO_2$ yields a comparable result as to Al/hollow-CuO or $Al/KClO_4/CuO$. The fact that $Al/AgFeO_2$ and $Al/Ag_2O/Fe_2O_3$ share the exact same elemental compositions but feature the highest and lowest pressurization rate, respectively, indicates molecularly incorporation of Ag_2O into Fe_2O_3 outperforms the mechanically mixed Ag_2O/Fe_2O_3 when they were employed as oxidizers in aluminum-based thermites. Post combustion products indicate the formation of elemental silver nanoparticles (~ < 80 nm) decorating larger Al_2O_3 and is this bioavailable.

8.5. Supplemental Information

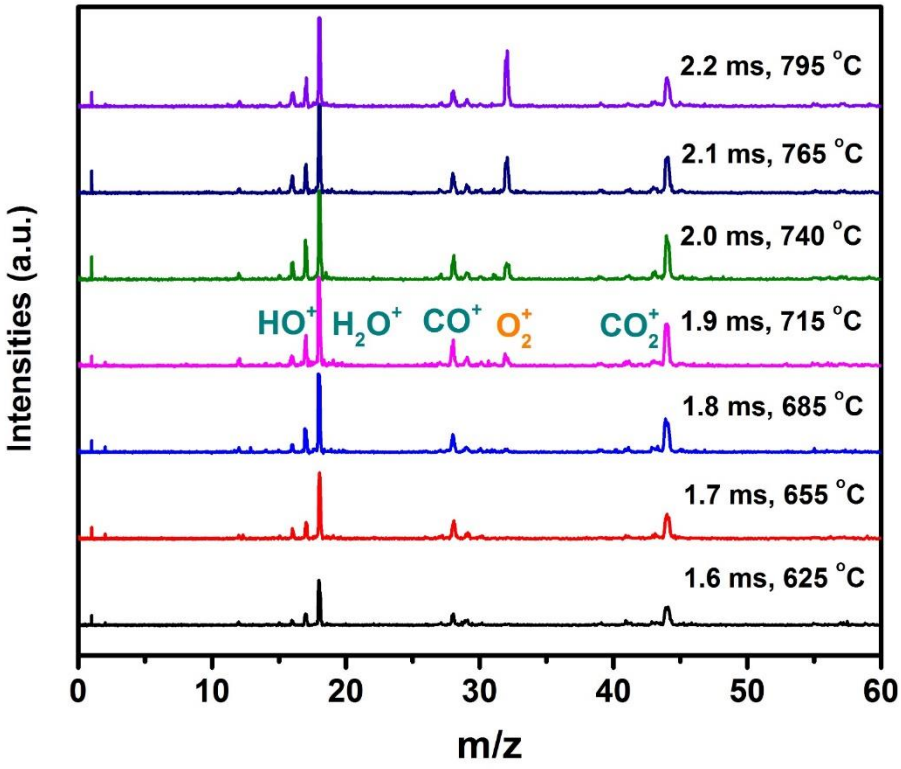

Figure S8.1. Multiple mass spectra of $AgFeO_2$

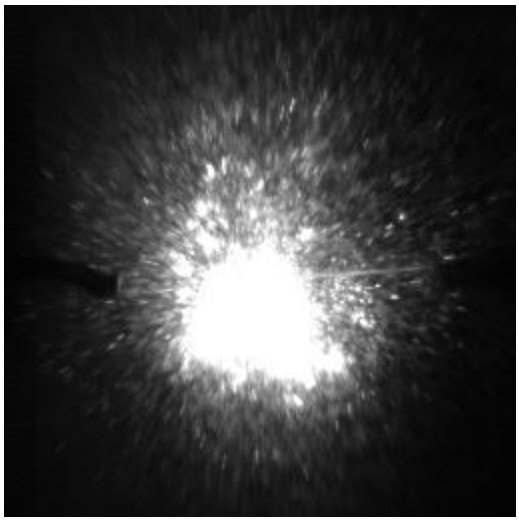

Figure S8.2. A snapshot of Al/$AgFeO_2$ burning on a high-rate heating Pt wire in T-Jump chamber (in argon).

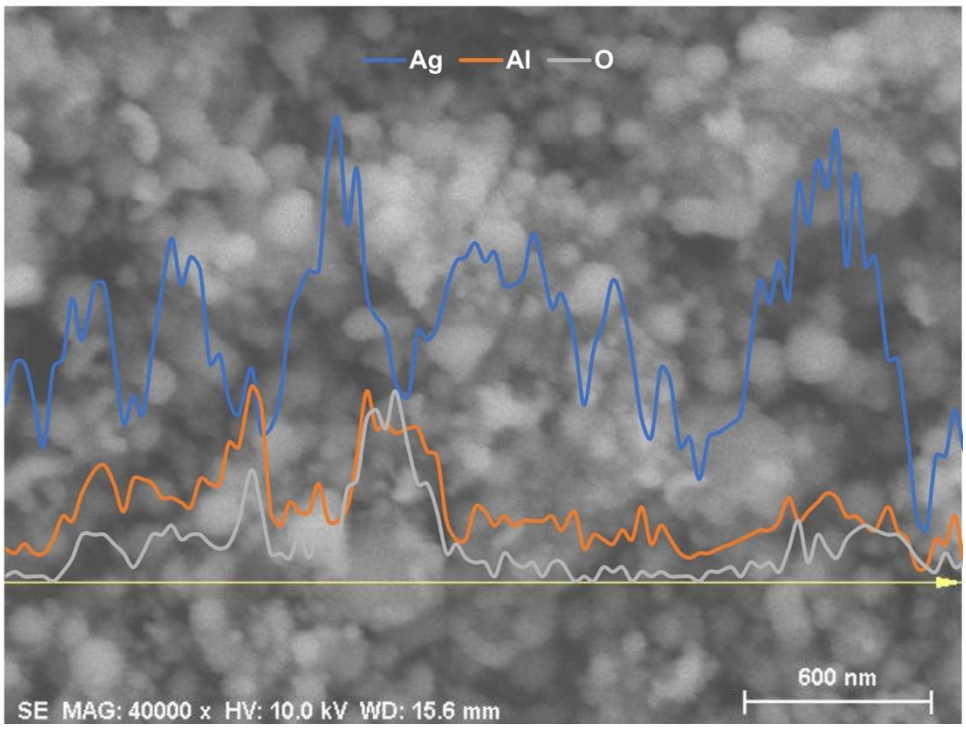

Figure S8.3. One-dimensional elemental line-scan using EDS of the Al/$AgFeO_2$ reaction product collected inside the combustion cell.

Chapter 9: Understanding Ignition Mechanism of boron-based Nanothermites

Overview

The goal of this work it to explain why boron-based thermites show the lowest ignition temperature comparing with other fuel-based thermite systems when using the same oxidizers. To do so, boron as the one feature the highest maximum combustion enthalpy when it was employed as the fuel is stoichiometrically mixed with CuO, Bi_2O_3, KIO_3, Fe_2O_3, Co_3O_4 and MoO_3 to form boron-based nanothermites. Time-resolved temperature-jump time-of-flight mass spectrometer (T-Jump/TOFMS) was used to study the ignition and decomposition of boron-based thermites. A high-speed camera simultaneously captured optical emission from the ignition/reaction of the thermites allowing for the ignition time, and corresponding ignition temperature. In addition, the ignition behaviors of bare boron nanopowders and boron-based nanothermites at various gaseous oxygen pressure were investigated using the T-Jump method. High-heating rate transmission electron microscopy studies were performed on both B/CuO and B/Bi_2O_3 nanothermites to evaluate the ignition process. I propose a co-sintering effect between B_2O_3 and the oxidizer play an important role in the ignition process of boron-based nanothermites.

9.1 Introduction

Reactive materials are a class of energetic materials containing separated fuels and oxidizers and featuring an extremely high exothermicity, intensive light emission and

shock generation by the self-sustained reaction [1-3]. When metal and metal oxide are employed as the fuel and oxidizer, respectively, the intense exothermic metal/metal oxide reaction is commonly referred to a thermite reaction. This reaction is self-propagating once the ignition happens and the kinetics of the reaction are known to be accelerated when the fuel and oxidizer are at the nanoscale, resulting from the increased interfacial contact and reduced characteristic diffusion length scale. The most widely adopted metal is aluminum due to its abundance and competitive reactivity when compared with other metals [4]. It has been used as an additive in numerous types of rocket propellants and pyrotechnic mixtures. However, aluminum is currently not the only commercially available nanosized metal fuel [2]. Investigating other fuels, such as boron, tantalum and carbon, with different properties than aluminum can be used to tweeze out mechanisms for ignition and combustion. Figure 9.1 shows the maximum reaction enthalpy for different metal fuels in a thermite composition with copper (II) oxide (CuO) [5] as the oxidizer. It is obvious that boron features the highest maximum combustion enthalpy when it was employed as the fuel. Thus, boron theoretically could be an attractive alternate for aluminum.

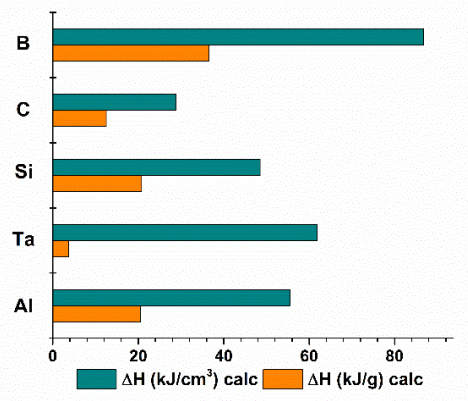

Figure 9.1. Maximum combustion enthalpy for the reaction of various metals with CuO.

Like aluminum, boron particles also have a passivated oxide shell, B_2O_3. Since B_2O_3 melts at a much lower temperature (450 ^oC) than the core (2100 ^oC), the burning scenario of boron is very different from aluminum. Upon heating, the molten B_2O_3 shell will surround the outside which prevent oxygen source from diffusing through. Over the last few decades, the ignition and combustion of boron particles were extensively studied both theoretically and experimentally.

Prentice [6] observed a two-stage combustion process for the ignition of boron particles in air and in oxygen-argon mixtures at atmospheric pressures. The low-temperature stage involves a surface burning process followed by a high-temperature stage is corresponding to gas-phase combustion. Later, Macek and Semple [7] investigated combustion of boron particles at atmospheric pressure in hot oxidizing gases of different compositions and found that boron combustion always happens in a two-stages process verifying what Prentice has claimed previously. The first short stage involves the removal of the oxide layer and can be a kinetic and/or diffusion-controlled process. The second stage involves the burnout of a bare boron particle is controlled by gas-phase diffusion of oxidants. The burn time of each stage is found to be inversely proportional to the oxygen molar ratio and merge as the mole fraction of oxygen decreases. Macek and Semple [8] then studied the combustion of boron particles at elevated pressures and found that the low-temperature stage was nonreproducible at pressure above ~10 atm.

There are contradictory theories about the mechanism that dominate species diffusing into the liquid boron oxide layer during the first stage of boron particles

ignition. Glassman et al [9] claimed that boron oxide production during first ignition stage results from boron diffusion across the oxide layer rather than oxygen diffusion claimed by King [10, 11]. Yeh and Kuo [12] later verifies that the diffusion of dissolved boron into molten boron oxide dominates the diffusion process. They also found the boron oxide layer of boron particles changed from a crystalline to an amorphous structure at elevated temperatures and its chemical composition was identified as a polymeric vitreous $(BO)_n$ complex through the reaction between dissolved boron and molten boron oxide. Theoretical models were also developed to simulate each of the two-stages combustion of boron particles by Knipe [13], Mohan and Williams [14] and others.

The influence of initial thickness of boron oxide layer on ignition and combustion of boron particles was studied by Ao et al [15]. They reported the oxide layer has little effect on the reactivity of the oxidation of boron particles below 775 ^{o}C. With increasing boron oxide layer thickness, the combustion efficiency decreases, and the time required for complete removal of the oxide layer is longer, while the ignition delay time significantly increases, and the oxide layer removal rate is raised.

In recent years, more efforts have been devoted to the ignition and combustion of boron-based thermites system. As mentioned previously, thermites involve an exothermic reaction of a metal fuel and a metal oxide. Sullivan et al [16] studied the reaction of nano-B/Al/CuO metastable intermolecular composites and reported the addition of nanoboron to Al/CuO can enhance the reactivity when the boron is less than 50 mol% of the fuel, while no enhancement was observed for microboron. From both experimental and theoretical results, they speculated that the sensible heating, removal

of the oxide shell and the melting of the boron are all critical for fast reaction. Liu et al[17] prepared B/CuO nanothermite through a chemistry precipitation method. They reported an improved thermochemistry behavior of boron particles with a coating of nano-CuO and a lower onset reaction temperature. Recently, Wang et al[18] reported a clear relationship between molecular properties of the oxidizer and ignition temperature as well as combustion performance of boron-based nanothermites in which larger oxygen vacancy concentration and smaller metal-oxygen bond energy lead to lower ignition temperature.

In this work, boron nanopowder stoichiometrically mixed with CuO, Bi_2O_3, KIO_3, Fe_2O_3, Co_3O_4 and MoO_3 were evaluated. Time-resolved temperature-jump time-of-flight mass spectrometer (T-Jump/TOFMS) was used to study the ignition and decomposition of boron-based thermites. A high-speed camera simultaneously captured optical emission from the ignition/reaction of the thermites allowing for the ignition time, and corresponding ignition temperature. In addition, the ignition behaviors of bare boron nanopowders, B/CuO, B/KIO_3 and B/Bi_2O_3 nanothermites at various gaseous oxygen pressure were investigated using the T-Jump method. High-heating rate transmission electron microscopy studies were performed on both B/CuO and B/Bi_2O_3 nanothermites to evaluate the ignition process. Pressure cell tests evaluated combustion performance.

9.2. Experimental

9.2.1 Materials:

The aluminum nanopowders (Al) (Alex, ~80 nm) were obtained from Novacentrix. The active Al was 81 % by mass, determined by TGA. The nanoboron powders were obtained from the SB Boron Corporation [16]. The active B was 72% by mass, determined by TGA. All metal oxide nanopowders (< 50 nm) purchased from Sigma-Aldrich were directly used as received. All the other chemicals were of analytical grade and used as purchased without further treatment.

9.2.2. Preparation of thermites:

Nanoboron was stoichiometrically mixed with CuO, Bi_2O_3, KIO_3, Fe_2O_3, Co_3O_4 and MoO_3 based on the following equations, respectively, in hexane followed by 30 minutes sonication. After room temperature evaporation of the solvent the solid thermite powders were collected for use.

$$2B + 3CuO \rightarrow 3Cu + B_2O_3$$

$$2B + Bi_2O_3 \rightarrow 2Bi + B_2O_3$$

$$2B + KIO_3 \rightarrow KI + B_2O_3$$

$$2B + Fe_2O_3 \rightarrow 2Fe + B_2O_3$$

$$8B + 3Co_3O_4 \rightarrow 9Co + 4B_2O_3$$

$$2B + MoO_3 \rightarrow Mo + B_2O_3$$

9.2.3. T-Jump/TOFMS measurement and high-speed imaging:

The decomposition of oxides particles was investigated using a custom T-Jump/TOFMS [19]. Typically, a ~1 cm long platinum wire (76 um in width) with a thin layer coating of oxidizer sample was rapidly joule-heated to about 1200 °C by a 3 ms pulse at a heating rate of ~10^5 °C/s. The current and voltage signals were recorded, and the temporal temperature on the wire was measured according to the Callendar–Van Dusen equation. MS spectra were measured every 0.1 ms. The detailed experimental set-up is given in our previous papers [19, 20].

To identify the point of ignition a high-speed camera (Vision Research Phantom v12.0) was employed to record the combustion on the wire during heating. Ignition temperatures of thermite reactions in vacuum were measured from the correlation of optical emission from high speed imaging and temporal temperature of the wire and were further analyzed in combination with the temporal mass spectra. Each experiment was repeated 3 times.

9.2.4. TGA/DSC characterization

Thermogravametric analysis and differential scanning calorimetry (TGA/DSC) was performed using a TA Instruments SDT Q600. For both nTa and nAl oxidation analysis runs, a heating rate of 20 ^{o}C/min and O_2 flow rate of 100 mL/min were employed.

9.2.5. In situ high heating rate TEM

Protochips Arduro heating chips were used with a Protochips TEM holder in a JEM 2100 FEG TEM/STEM, equipped with Oxford EDS and Gatan Tridiem EELS systems, with an accelerating voltage of 200 kV. Ta nanopowders were deposited onto an

Arduro chip and heated in air whereas the Ta based nanothermites were heated under vacuum within the TEM. All samples were heated at 10^5 ^oC /s and held for a period between 1 and 100 ms.

9.3. Results and Discussion

Over the past decades, different fuels such as aluminum, [21-26] carbon, [27-29] tantalum, [30] etc, had been studied in thermite systems and different ignition mechanisms have also been developed to interpret their unique ignitions. Since the same oxidizers have been investigated previously in those fuel systems, the initiation temperatures in vacuum environment of CuO, Bi_2O_3, Fe_2O_3 and KIO_3, with different fuels are listed in Table 9.1 to demonstrate the particularity of boron-based nanothermites. The measured oxygen release temperatures, and literature melting points of the bare oxidizers are also included in Table 1. It can be clearly seen that boron-based nanothermites give the lowest ignition temperature for those oxidizers.

As previously demonstrated that the ignition of Al-based nanothermites is dominated by the mobility of the aluminum core and the reactive sintering only play a partial role, this explains why Al/oxidizer nanothermites feature the highest initiation temperatures for all the listed oxidizers.[21, 25, 31] Reactive sintering was introduced in our previous works to describe the ignition mechanism of aluminum-based nanothermites where reaction initiates at an Al/oxidizer interface and the exothermic reaction led to further melting/sintering of adjacent particles. Then those newly melted materials are rapidly delivered to the reactive interface via strong capillary/surface tension forces and followed by the formation of the sintered product. [25, 31] As for

carbon, it remains immobile upon heating to a temperature within the regime of our set-up. The reactive sintering of metal oxide increases the effective contact area between carbon and oxidizer and thus further promoting sintering/heating, which helps to initiate condensed phase reaction and expand the effective reaction zone. [32] Those effects are the reasons why carbon/oxidizer nanothermites initiate at a much lower temperature than Al/oxidizer nanothermites. In addition, a rapid oxide shell crystallization of nano tantalum has been proposed to be the dominant factor for the ignition of tantalum-based thermites where the crystallization contributes enough energy to the shell/oxidizer interface and therefore promoting the reactive sintering to take place.[30]

Even though the reactive sintering has been observed in aluminum-based, carbon-based and boron-based nanothermites (boron case will be discussed later), the extremely different ignition temperatures obtained on those different types of nanothermites suggest there are other impactors influencing the ignition except for reactive sintering.

Boron has an oxide shell featuring an extremely low melting point that is very different from either aluminum, carbon or tantalum, and boron-based nanothermites feature the lowest initiation temperature among these four types of thermites. It has been reported in a recent work that B/Bi_2O_3 shows the second least negative ΔG_r and ΔH_r compared to Al/Bi_2O_3 and Ta/Bi_2O_3, which eliminating the possibility of ascribing the low ignition temperature of B/Bi_2O_3 to the thermodynamically causes.[23] Both facts imply the boron oxide shell may play some role in the ignition of boron-based nanothermites.

Ignition temperatures of B/CuO, B/Bi_2O_3, B/KIO_3, and B/Fe_2O_3 are higher than the melting point of B_2O_3, and close to the Tamman temperature of corresponding oxidizer, which means both B_2O_3 shell and the oxidizer are to some extent mobile prior to ignition. Those results are suggesting that the molten B_2O_3 shell might participate in or even promote the sintering of metal oxides to feature a co-sintering effect in which oxygen can diffuse through the mixed B_2O_3/metal oxide area and react with the boron core and thus resulting in a low initiation temperature. According to a recent published work, an interface was created due to the wetting of Bi_2O_3 by the molten B_2O_3 where high mobility solid-state oxygen can diffuse through and reacts with boron core[18]. However, Bi_2O_3 is a very special oxidizer that features the highest known oxygen ion conductivity and usually undergoes a condensed phase reaction mechanism in thermites system where oxygen transfers to be in contact with the fuel within solids.[28] Here, I propose that such co-sintering effect is present not just in B/Bi_2O_3 but also in other boron-based nanothermites and further attributing to their low ignition temperature.

Table 9.1. Ignition temperatures for different fuel-based thermites

Oxidizer	**O_2 release temperature (^oC)**	**Melting point (^oC)**	**Ignition temperature of nanothermites (^oC)**			
			Al/Oxidizer	CB/Oxidizer	Ta/Oxidizer	B/Oxidizer
CuO	730	1325	765	665	725	640
Bi_2O_3	965	820	575	695	650	550
KIO_3	630	560	625	565		510
Fe_2O_3	1065	1565	1135	805	715	670

To further prove my proposal, I first look into the boron particles and then move on to boron-based nanothermites.

Figure 9.2 shows the SEM images of the boron nanoparticles are mostly spheroids that are agglomerated with hard aggregates, with average primary particle diameter ~60 nm.

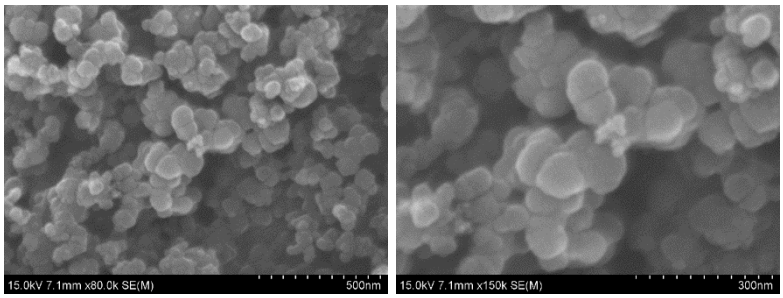

Figure 9.2. SEM images of boron nanoparticles.

To learn how boron reacts in different systems, the oxidation of boron nanoparticles was first studied in an air environment using standard low heating rate TGA/DSC and the results are shown in Figure S9.1. The one-step exothermic oxidation of boron nanoparticles starts at ~500 ^{o}C, which is slightly higher than the melting point of B_2O_3 shell (450 ^{o}C, Table S9.1). Thus, the molten phase B_2O_3 shell might play a role in the oxidation and will be discussed below. TEM images of boron nanoparticles before and after in-situ heating up to 800 C (Figure S9.2) show no significant changes upon heating, indicating the boron nanoparticles do not sinter even with the molten B_2O_3 shell, suggesting that the necking between particles occurred during the synthesis of the boron, and before the passivating shell was created. Considering the boron active content is about 72% in boron nanoparticles, complete oxidation of boron nanoparticles

would result in a final weight % of ~262% (final product is assumed to be B_2O_3), which is slightly lower than the final weight 280% shown in Figure S9.1.

The oxidation of boron particles at high heating rate was obtained by T-jump system. Boron was ignited in gaseous oxygen at various pressures within a high heating rate T-jump chamber and the measured ignition temperatures as a function of oxygen pressure are shown in Figure 9.3. The fact that boron nanoparticles always ignited at ~850 ^oC even at elevated oxygen pressures suggests its ignition is not controlled by a gas phase mechanism where the oxidizer first decomposed into gaseous oxygen and then those oxygen diffuse through the molten Al_2O_3 shell and reacts with the fuel core.[21] This in contrast to what is observed with aluminum which shows a decrease in ignition temperature with increasing oxygen concentration [22].Considering the B_2O_3 shell is molten at ~850 ^oC, it is reasonable to speculate that the ignition of boron nanoparticles is strongly related to the oxide shell. In another words, gas phase oxygen cannot diffuse through B_2O_3 shell under those pressurized atmospheres. [22]

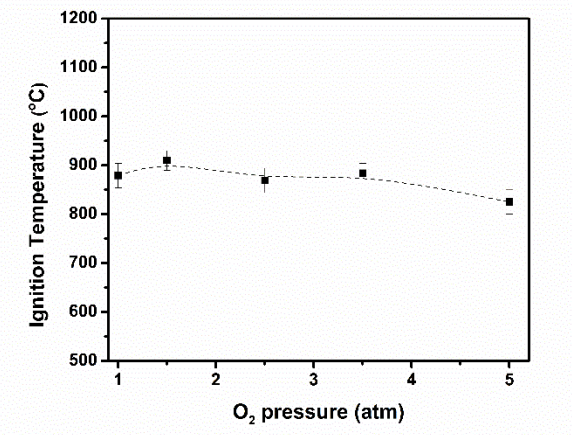

Figure 9.3. Ignition temperature of boron measured using the T-Jump ignition at varying O_2 pressures.

Since the ignition of boron nanoparticles is apparently not controlled by gas phase oxygen, different solid oxidizers were stoichiometrically mixed with boron nanoparticles and their ignition temperatures obtained via the high heating rate T-jump method are listed in Table 9.2. The oxygen release temperature and the melting point of each oxidizer are also included in this table. B/MoO_3 and B/Sb_2O_3, ignited at ~650 and 630 ºC, respectively, but since neither of these oxides release any gas upon heating up to 1200 ºC it is reasonable to conclude that they are initiated through condensed phase reactions. [21] For the other boron-based thermites shown in Figure 9.4, I find their ignition temperatures are lower than the oxygen release temperature from the corresponding neat oxidizers. This also implies a condensed phase reaction since reaction occurs before oxygen release.

To further investigate the ignition mechanism of boron-based nanothermites, boron coped with CuO (a known gas phase oxidizer in Al-based thermite systems), Bi_2O_3 (a known condensed phase oxidizer in Al-based thermite systems) and a salt oxidizer KIO_3 were ignited in oxygen atmosphere with different O_2 pressure. Figure 9.5 shows not surprisingly the oxygen has no synergistic effects in ignition and that the ignition temperature is independent of oxygen concentration. Perhaps more interesting is that the ignition temperatures with bonded oxygen is lower than in free oxygen. An integrated oxidizer greatly enhance combustion due to mass transfer limits of free oxygen in a bulk sample, thus in a wire coated sample test, such transport limits were seen. The reader is reminded that reaction with free oxygen leads to the highest adiabatic flame temperature relative to the other oxidizers.

Table 9.2. Ignition temperature of various B based nanothermites with different oxidizers. The oxygen release temperature from neat oxidizer as detected by TOFMS and the melting point of the oxidizers are also included. Heating rate ~ 5×10^5 °C/s.

B/Oxidizer nanothermites	Ignition temperature (°C) ± 30 °C	O_2 release temperature from neat oxidizer (°C) ± 30 °C	Melting point of the oxidizer (°C)
CuO	640	730	1320
Bi_2O_3	550	960	820
Fe_2O_3	670	1060	1560
Co_3O_4	660	740	895
KIO_3	510	630	560
MoO_3	650		790
Sb_2O_3	630		650

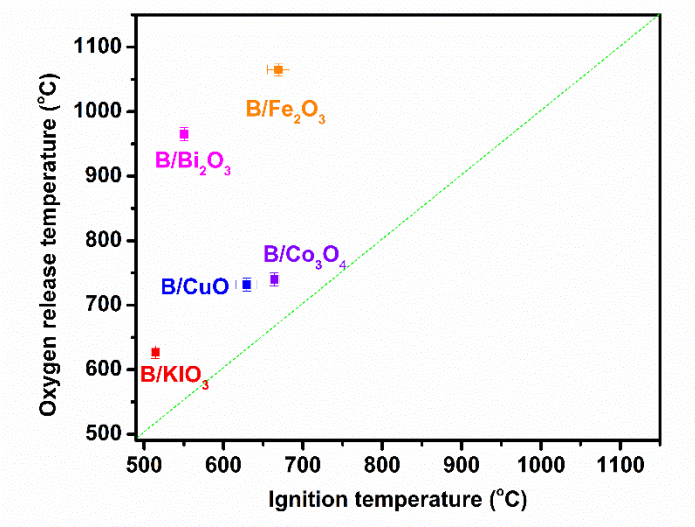

Figure 9.4. Oxygen release temperature of various oxidizers vs ignition temperature of various B based nanothermites.

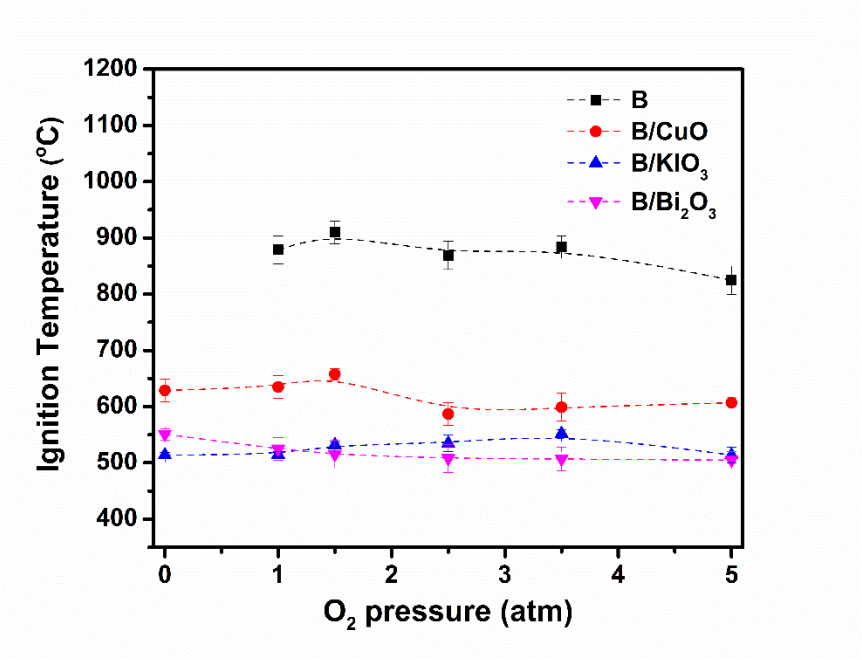

Figure 9.5. The ignition temperature of B-based nanothermites as a function of O_2 pressure.

Since B_2O_3 melts at a much lower temperature (450 °C) than the core (2076 °C) and lower than the measured ignition temperature, for reaction to occur, oxygen must be diffusing through the liquid layer or the boron core must be exposed to the oxygen source in some way, such as by de-wetting. Thus, solid state oxygen must find a way to diffuse into the boron core and initiated the fuel-oxidizer reaction.

To examine the ignition process, high-heating rate in-situ TEM were employed here. Two oxidizers were mixed with boron to form boron-based nanothermites: CuO (gas phase oxide) and Bi_2O_3 (condensed phase oxide)

Figure 9.6 shows images of B/CuO nanothermites before and after heating, where the lighter aggregates are boron, and the darker particles are CuO. Figure 9.6A shows that all CuO particles are in good contact with boron prior to heating. After rapid in situ

heating to 800 ºC for 10 ms, comparing Figure 9.6A and 9.6B, it is clear that those CuO particles that are in good physical contact with boron nanoparticles underwent significant morphological changes, and the isolated boron nanoparticles retain their original form. EELS results show that the darker particles with irregular spherical shape observed in Figure 9.6B are copper particles (Figure S9.3). Similar to the reactive sintering mechanism of aluminum-based thermites[31], the surface contact between the boron and CuO is essential to initiate their reaction.

Similar experiments on B/Bi_2O_3 nanothermites were also conducted. EDS line scans in Figure 9.7A2 indicates the darker particles are Bi_2O_3. After rapid heating, B/Bi_2O_3 nanothermites underwent dramatic morphological changes. All Bi_2O_3 particles aggregated/sintered together and formed much larger particles with irregular shapes that later proved to be bismuth. The EDS line scan (Figure 9.7B2) of the same spots as to those of Figure 7A2 shows that those darker particles are bismuth and the lighter ones are B_2O_3. In addition, it seems that all bismuth atoms are moved to the edge of the plane and formed much bigger particles, where B_2O_3 particles are intended to stay in the middle of the plane.

It has been previously reported the importance of reactive sintering in which the interfacial reaction upon heating can lead to an increased mobility and sintering of the particles into larger structures [25, 31]. As Jian et al points out [21] partial sintering of metal oxides can commence at a much lower temperature; at the Tammann temperature ~ ½ melting point. Once the metal oxide becomes mobile, the contact area between fuel and oxidizer increases extensively, favoring ignition. However, all boron-based nanothermites except for B/Fe_2O_3 ignited at temperatures higher than the Tammann

temperatures of their corresponding oxidizers. Therefore, the partial sintering of metal oxides might not play a controlling role for the ignition of boron-based nanothermites.

Both B/CuO and B/Bi_2O_3 nanothermites show evidence of reactive sintering having occurred on the interfacial area where boron has good contact with the oxidizers. Once the reaction was initiated, the generated heat will transfer to the adjacent particles and either promote initiation or draw them towards the reacting interface, where the final products are formed.

The major difference between aluminum and boron is that the isolated boron remains almost the same after rapid heating, but aluminum particles either undergoes crystallization of its aluminum oxide shell or evolve heterogeneities near the surface. The rather stable property of boron further indicates the importance of the contact between boron and the oxidizer to ignition. Considering aluminum-based nanothermites show even higher ignition temperature than boron-based nanothermites, it is reasonable to conclude that the co-sintering effect between B_2O_3 and the oxidizer play an important role in its ignition process.

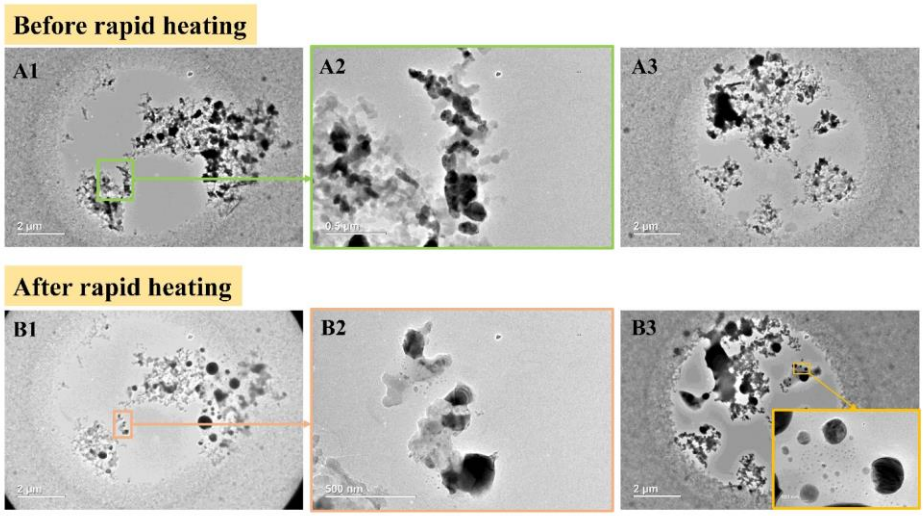

Figure 9.6. TEM images of B/CuO nanothermites prior to (A) and after (B) in situ heating at 4×10^5 °C/s to 800 °C/s for 10 ms. A and B are the same position.

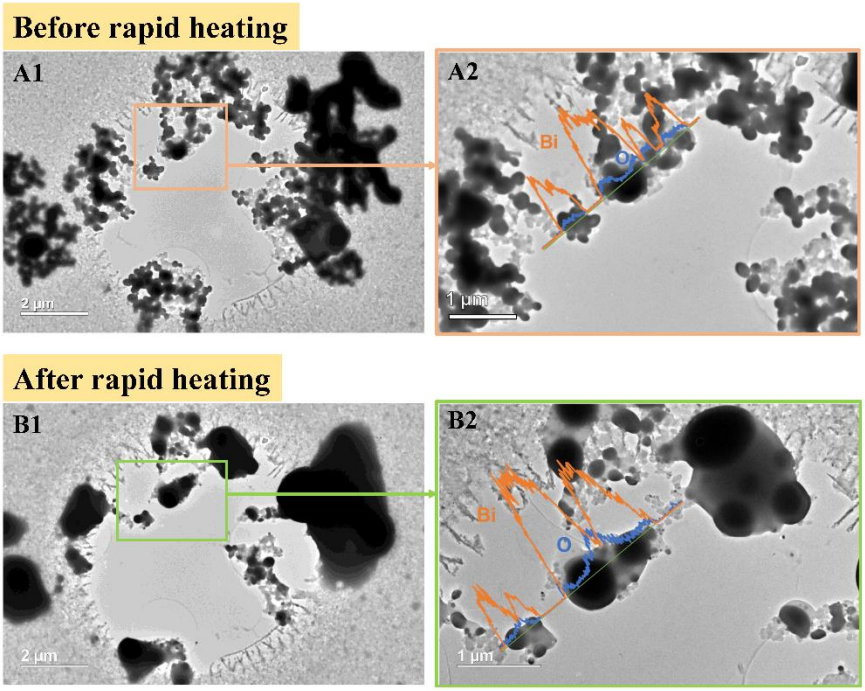

Figure 9.7. TEM images and elemental line scan of B/Bi_2O_3 nanothermites prior to (A) and after (B) in situ heating at 4×10^5 °C/s to 800 °C/s for 10 ms.

9.4. Conclusions

The ignition mechanisms of boron and boron-based nanothermites are investigated in this work. It is noted that boron nanoparticles always ignited at ~850 ^{o}C even at elevated oxygen pressures suggests its ignition is not controlled by a gas phase mechanism. Different oxidizers were mixed with boron nanoparticles to examine the possibility of condensed phase reaction mechanism and the results show that boron-based nanothermites have the lowest ignition temperatures compare with that of other fuel-based samples and the ignition of boron-based nanothermites is independent of gaseous oxygen pressure. Therefore, a condensed phase mechanism is controlling the ignition mechanism of boron-based nanothermites. Since the ignition temperatures of boron-based nanothermites are higher than the melting point of B_2O_3, and close to the Tamman temperature of corresponding oxidizer, where both B_2O_3 and the oxidizers are to some extent mobile prior to ignition, suggesting that the low ignition temperature of boron-based nanothermites might be contributed to a co-sintering effect between B_2O_3 and the oxidizers. In detail, the molten B_2O_3 shell might participate in or even promote the sintering of metal oxides to feature a co-sintering effect in which oxygen can diffuse through the mixed B_2O_3/metal oxide area and react with the boron core and thus resulting in a low initiation temperature.

Then, High-heating rate TEM measurements B/CuO and B/Bi_2O_3 nanothermites provide evidence of reactive sintering having occurred on the interfacial area where boron has good contact with the oxidizers, like Al-based nanothermites. However, Al-based nanothermites show even higher ignition temperature than boron-based

nanothermites, it is reasonable to conclude that the co-sintering effect between B_2O_3 and the oxidizer play an important role in its ignition process.

9.5. Supplemental Information

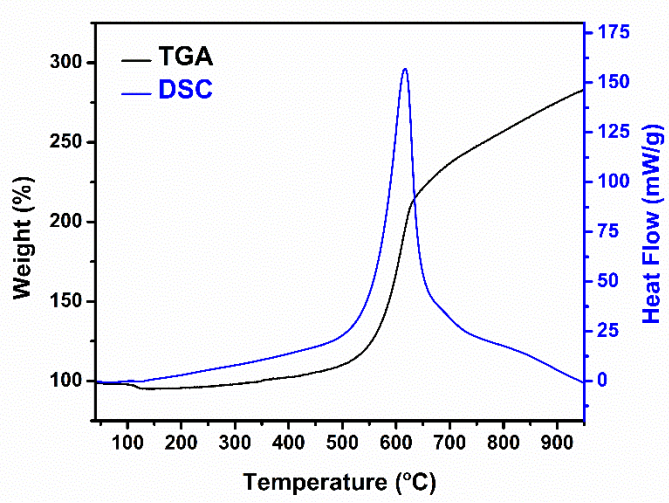

Figure S9.1. TGA/DSC of boron nanoparticles under 100 mL/min of air at a heating rate of 25 ^{o}C/min.

Table S9.1. The general properties of boron and B_2O_3.

	Melting point (^{o}C)	**Boiling point (^{o}C)**
Boron	2076	3927
B_2O_3	450	1860

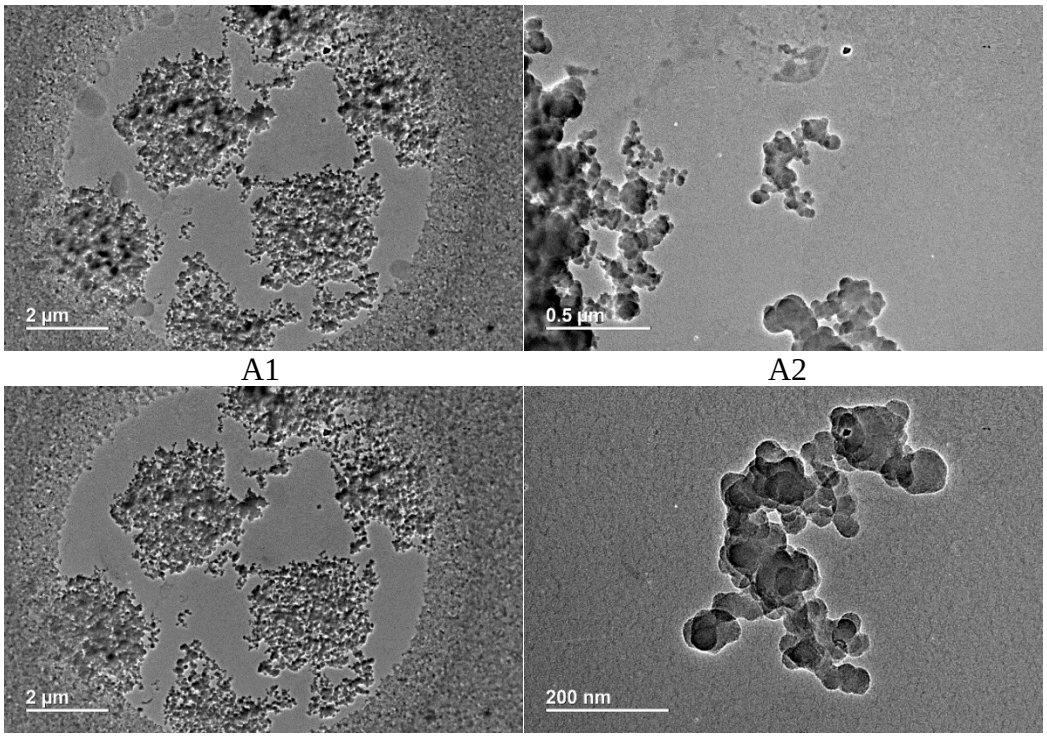

Figure S9.2. The TEM images of boron nanoparticles before (A) and after (B) heating to 800 C.

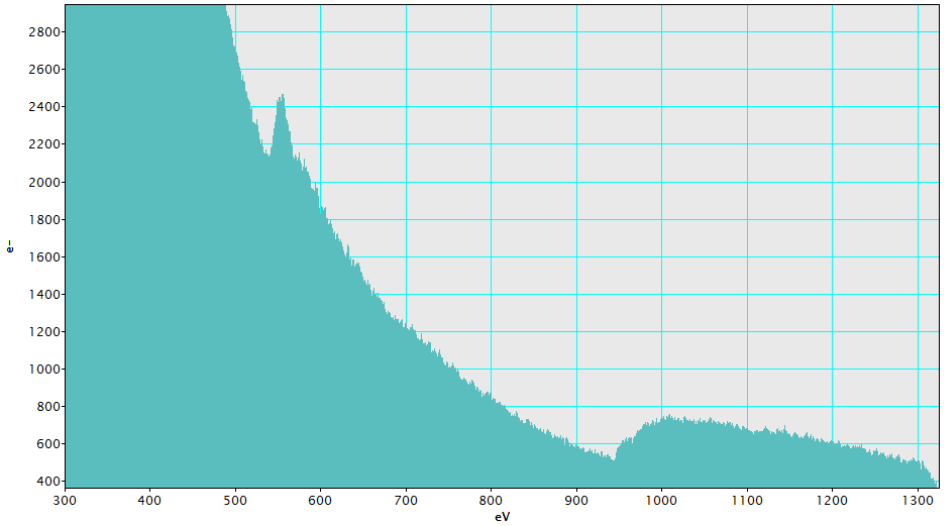

Figure S9.3. EELS spectrum of B/CuO (Cu: major edges at 951 and 931 eV).

Chapter 10: Summary

10.1 Conclusions

The objective of this dissertation study was to develop new energetic materials with biocidal capabilities and apply them in various nanothermites systems to explore the relationships between fuel and oxidizer reactions. To achieve this goal, oxidizers that consist of element like iodine or silver were prepared via various synthetic methods and then incorporated into different fuel-based nanothermites for ignition/reaction studies. Various fuels or oxidizers were added into the system to create ternary nanothermites in order to further understand their ignition/reaction properties.

As discussed in Chapter 1, nanothermites have so much potential in various energetic applications because they offer high energy densities and high reaction rates. By employing biocidal agents within the system, they can be the potential solution for counterfeit the threat of bioterrorism. The detailed experimental techniques are presented in Chapter 2 in order to let the readers know how those experiments were performed.

In Chapter 3, three different products, δ-HIO_3, HI_3O_8 and I_2O_5, were obtained via aerosol spray pyrolysis. Both temperature and humidity control in silica gel preparation were necessary to obtain all three products without post-processing. This chapter demonstrates a facile and environmentally friendly aerosol spray pyrolysis method to prepare various iodine oxides/iodic acids using a single precursor HIO_3. By tuning the furnace temperature and the humidity I was able in a single step to produce near phase pure δ-HIO_3, HI_3O_8 and I_2O_5.

As one of the products produced in Chapter 3, δ-HIO_3, was demonstrated to be a new polymorph of iodic acid, which crystallizes in the orthorhombic space group $P2_12_12_1$. Its crystal structure is reported in Chapter 4. *Ab initio* crystal structure determination of δ-phase reveals that previously known $I_4O_9.xH_2O$ phase is actually HIO_3.

In Chapter 5, those prepared iodine oxides/iodic acids, including *a*-I_2O_5, *a*-HI_3O_8 and *δ*-HIO_3, were employed as the oxidizer in thermite systems. Their decomposition behaviour was studied using T-Jump/TOFMS, which identified a single decomposition step for all oxides at high heating rates compared with the multi-steps process at low heating rate. The ignition temperatures of nAl-based thermites are all ~650 ºC which is at the melting point of aluminum (~660 ºC). This suggests that the mobility of the aluminum core is dominating the ignition/reaction while the gaseous oxygen released from the decomposition of the oxidizer does not participate in the ignition until the molten aluminum was available. Unlike nAl-based thermites, the ignition temperatures of nTa-based thermites are lower than the oxygen release temperatures from the corresponding bare oxidizers. In this case, a condensed phase reaction mechanism is proposed to dominate the ignition process. Combustion tests show that nAl/*a*-HI_3O_8 has the highest pressurization rate and peak pressure and shortest burn time, and since it also has an iodine content of ~75% which is as high as I_2O_5 on a per mass basis, this material may be a very promising candidate in biocidal application.

In Chapter 6, I employed carbon (CB, CNT and FGS) as both a fuel and as an additive to aluminium and tantalum fuels to study the influence of a fuel without

nascent oxide shell on initiation of iodine oxide-based thermites. I found that the initiation temperature of CB/I_2O_5 is much lower than the initiation temperature of Al/I_2O_5 and Ta/I_2O_5. When CB is used as an additive to other fuels, I observe a decrease in the overall initiation temperature and a lowering of the iodine release temperature to below that of the nascent oxidizer. Other carbon allotropes showed similar results. FTIR analysis indicated at CB lowered the iodine-oxygen bond energy of I_2O_5 on the surface and thus triggered this condensed phase reaction. These results indicate that CB can be employed as an additive to any metal fuel as a means to lower both the initiation and iodine release temperature.

In Chapter 7, a secondary oxidizer CuO was incorporated into Al/I_2O_5 system to shorten or eliminate the ignition delay of the combustion of Al/I_2O_5. By investigating the combustion performance of four different Al/I_2O_5/CuO thermites varying the mass ratio between two oxidizers and the other two Al/I_2O_5 and Al/CuO thermites in a constant volume combustion cell, significant enhancement is observed for all four thermites and their peak pressures and pressurization rates are much higher than that of Al/I_2O_5 or Al/CuO. The disappearance of the ignition delay in their pressure profiles and the shortened burn time imply CuO addition indeed does work on accelerating the ignition of Al/I_2O_5 thermite and the overall reaction. a mechanism was proposed in this work to account for this unexpected improvement: the additive Al/CuO shortens the ignition delay of Al/I_2O_5; that leads to enormous amount of gas formation for aluminum to react and then the extremely high flame temperature of Al/I_2O_5 boost the pressure inside the combustion cell further. All those events happen around the same time and

produce a synergetic effect to enhance the combustion performance of Al/I_2O_5. Although more oxidizers need to be examined furthermore, it is reasonable to assume the combustion performance of Al/I_2O_5 could be enhanced by just incorporating a secondary oxidizer.

In Chapter 8, the $AgFeO_2$ was prepared via a wet-chemistry method to yield phase pure ~ 40 nm particles. The decomposition pathways of $AgFeO_2$ were found to depend on heating rates: decomposition to Ag, O_2 and Fe_2O_3 at ~600 °C at low heating rate and direct decomposition ~685 °C at high heating rates. The ignition of $Al/AgFeO_2$ was found to slightly higher than the oxygen release temperature and thus with a similar mechanism to Fe_2O_3 although ignites and a much lower temperature. Fast video imaging indicates a fine smoke dispersing particle. Combustion cell test showed that $Al/AgFeO_2$ outperformed other thermites in maximum pressure, pressurization rate and burn time. Moreover, with a pressurization rate three times and 5% less oxygen content of Al/CuO, $Al/AgFeO_2$ yields a comparable result as to Al/hollow-CuO or $Al/KClO_4$/CuO. Post combustion products indicate the formation of elemental silver nanoparticles (~ < 80 nm) decorating larger Al_2O_3 and is this bioavailable.

In Chapter 9, the ignition mechanisms of boron and boron-based nanothermites are investigated in this work. It is noted that boron nanoparticles always ignited at ~850 ^oC even at elevated oxygen pressures suggests its ignition is not controlled by a gas phase mechanism. Different oxidizers were mixed with boron nanoparticles to examine the possibility of condensed phase reaction mechanism and the results show that boron-based nanothermites have the lowest ignition temperatures compare with that of other fuel-based samples and the ignition of boron-based nanothermites is independent of

gaseous oxygen pressure. Therefore, based on the experimental results, I proposed a co-sintering mechanism to explain the causes of the low ifnition temperature of boron-based nanothermites: the molten B_2O_3 shell might participate in or even promote the sintering of metal oxides to feature a co-sintering effect in which oxygen can diffuse through the mixed B_2O_3/metal oxide area and react with the boron core and thus resulting in a low initiation temperature.

10.2. Recommendations for future work

10.2.1. The effect of boron addition to iodine release, ignition and combustion of Al/I_2O_5 thermite

In my dissertation, carbon addition has been added into Al/I_2O_5 system and the results show it can lower the iodine release temperature and ignition temperature of Al/iodine oxide thermites owing to a condensed phase interaction between carbon and I_2O_5 according to the FTIR results. Recently, our group also studied the effect of titanium addition to Al/I_2O_5 system and found the ignition temperature decreases as the titanium fraction in the fuel increases and that titanium can accelerate the release of iodine and oxygen gas from Ti/Al/I_2O_5 ternary system. And the reactivity and combustion performance of Al/I_2O_5 thermite was significantly enhanced with addition of titanium. Therefore, carbon, a fuel without an oxide shell and with an extremely high melting temperature core, and titanium, a fuel with a partially reactive titanium (II) oxide shell, have all been proven to be an efficient additive to boost the combustion performance and lower the ignition temperature Al/I_2O_5.

In one of the previous chapters in my dissertation, "Understanding Ignition Mechanism of boron-based Nanothermites", I found out that B/I_2O_5 cannot ignited in either argon or air environment. The oxide layer outside of boron fuel has a very low melting temperature ~440 ^oC compare to the boron core that features a very high melting point. This unique property of boron nanoparticles may bring some new insights to improving the ignition and combustion of Al/I_2O_5 system.

Considering boron with other oxidizers do not have this problem, I started looking into the reasons that causing this problem. First, I studied the decomposition behaviors of B/I_2O_5 under both high and low heating rate and the results are shown in Figure 10.1. Figure 10.1A indicates that the boron lowers the iodine release temperature of I_2O_5 from 450 to as low as 280 ^oC at high heating rate. However, at low heating rate, boron does not affect the thermal behavior of I_2O_5.

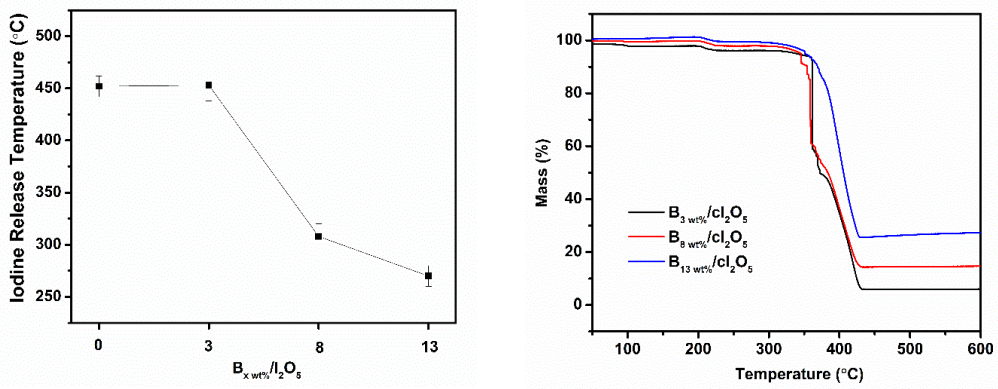

A B

Figure 100.1. The iodine release temperature (A) and the TGA results (B) of B/I2O5 composite with different weight ratio of boron.

Figure 10.2 shows the ignition temperatures and iodine release temperatures of B/Al/I_2O_5 composites with different boron content. The iodine release temperature was determined from the time-resolved mass spectra of thermites. Both ignition and iodine

release temperature decrease when the boron content increases and both reach plateau when 4 w.t.% of boron is incorporated into B/Al/I_2O_5 system. In addition, the iodine release temperature is always more than 100 °C lower than the corresponding ignition temperature indicating I_2O_5 decomposes prior to the exothermic reaction between boron and I_2O_5. The fact all B/Al/I_2O_5 composites with different boron content can be ignited under argon environment implies boron alone could not exothermically react with I_2O_5 and it can only be used as an additive for Al/I_2O_5 system.

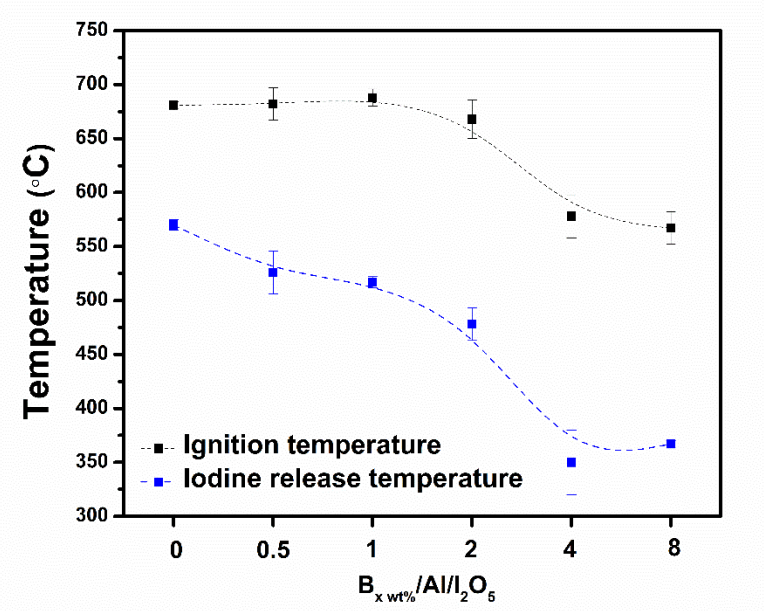

Figure 100.2. The ignition temperatures and iodine release temperatures of B/Al/I_2O_5 composites with different weight ratio of boron.

To figure out the reason why addition of boron lower both ignition and iodine release temperature, inert oxides such as Al_2O_3 and SiO_2 were introduced into Al/I_2O_5 system as comparisons. (Al_2O_3 and SiO_2 have similar particle size as Boron). Giving the fact that addition of both Al_2O_3 and SiO_2 have no discernible effect on either ignition or

iodine release temperatures of Al/I_2O_5 system as shown in Figure 10.3, it is reasonable to conclude that heat transfer among the fuel and oxidizer is not the cause for the lowering effect.

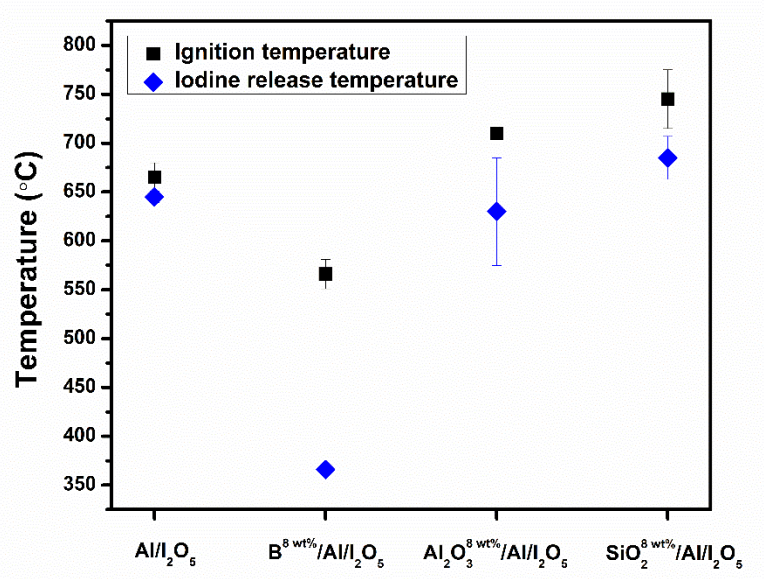

Figure 100.3. The ignition temperatures and iodine release temperatures of Al/I_2O_5 composites with different oxides additives.

Based on the digital image shown in Figure 10.4 of $B/Al/I_2O_5$ suspension after sonication treatment, the color of the suspension changes from transparent colorless to purple that indicates the formation of iodine. Thus, iodine somehow was draws out from I_2O_5 compound with the presence of boron and later suspend in the solvent as I_2.

Figure 100.4. Digital image of $B/Al/I_2O_5$ suspensions after sonication treatment.

To evaluate the interaction between boron and I_2O_5, I_2O_5, boron, physical mixed B/I_2O_5 and sonicate mixed B/I_2O_5 composites have been characterized by FTIR. The results shown in Figure 10.5 reveal no significant change was found in B/I_2O_5 compared to the spectra of I_2O_5, which rule out the possibility of a condensed phased effect. Thus, I_2O_5 becomes very unstable and can easily decompose and deliver iodine when boron is in the system might be a catalytic effect, which need to be further investigated.

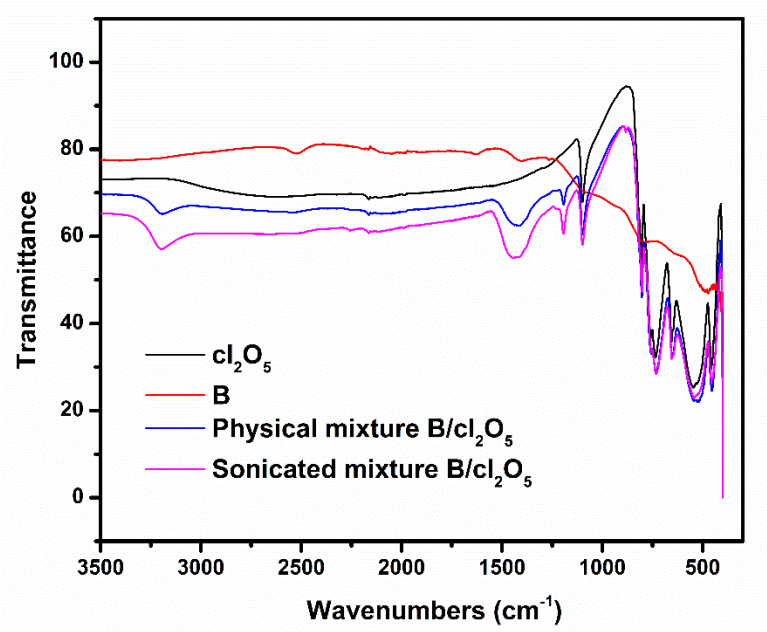

Figure 100.5. FTIR results of I_2O_5, boron, physical mixed B/I_2O_5 and sonicate mixed B/I_2O_5 composites.

10.2.2. Incorporate silver into MnO_2 molecularly: silver hollandite $Ag_x(MnO_2)_y$.

In previous chapter, I have proved that the molecularly incorporation of Ag_2O into Fe_2O_3 significantly outperforms the physical combination of Ag_2O and Fe_2O_3. To

further explore this idea, I propose to incorporate silver element, a rather inactive material to the thermite reaction but features biocidal prosperity, into an oxidizer to see the effect. By looking into literature, I finally chose silver hollandite $Ag_x(MnO_2)_y$ as the subject to study here. By breaking silver hollandite formula, one can see it is a combination of silver element and manganese oxide, which would be the perfect materials to test the idea.

Then, the silver hollandite was prepared by refluxing a mixture solution of $Mn(NO_3)_2$ and $AgMnO_4$ in an acidic condition. Its XRD pattern shown in Figure 10.6 indicate the crystal structure of silver hollandite match to a previously reported structure, $Ag_{1.8}Mn_8O_{16}$. And its SEM images show silver hollandite materials are in fiber-like shape with a diameter about 30 nm and length of 500 nm.

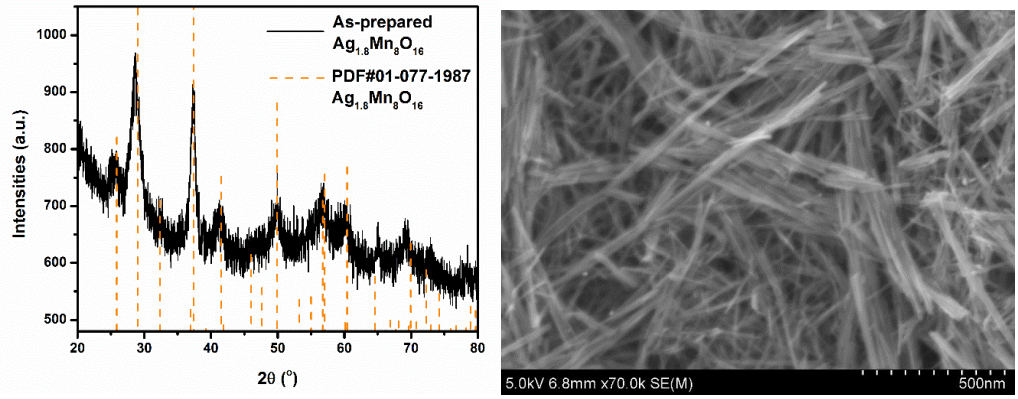

Figure 100.6. XRD spectrum and SEM image of $Ag_{1.8}Mn_8O_{16}$ prepared via wet chemistry method.

Silver hollandite was heated in an argon environment with a heating rate of 10 C/min up to 1000 C and the decomposition products are collected and characterized. The XRD pattern of the product shown in Figure 10.7 indicates the formation of both silver and

Mn_3O_4. Considering Mn_3O_4 is a good oxidizer in aluminum-based thermites and silver is biocidal, it is promising to obtain positive results by further studying the ignition, combustion and biocidal applications of Al/$Ag_{1.8}Mn_8O_{16}$ system.

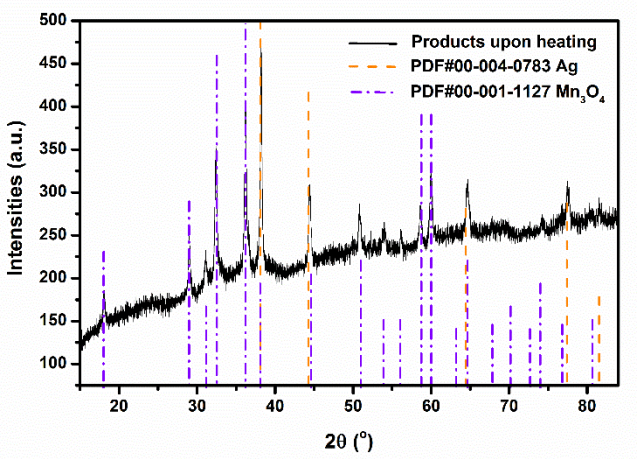

Figure 100.7. XRD spectrum of $Ag_{1.8}Mn_8O_{16}$ decomposed products after heated to 1000 ^oC in Ar.

10.2.3. To deliver independent silver and iodine products from a single system for biocidal application.

As mentioned in previous chapters, both iodine and silver exhibit biocidal properties. Various efforts have been devoted into studying the performance of either iodine-containing or silver-containing oxidizers within thermite systems. Silver iodate, as a highly insoluble salt containing both silver and iodine elements, has been considered and studied for its potential use in thermite-driven biocidal applications. However, Sullivan from our research group had found that the silver and iodine products intends to form silver iodide that leads to inactive biocidal cites. Therefore, to

design a system that could deliver independent silver and iodine elements after thermite reaction could be a major achievement in this field.

Since I_2O_5 is the most commonly used iodine oxides, it was chosen as the iodine-containing oxidizer. Then, Ag_2O, $AgFeO_2$ and $Ag_{1.8}Mn_8O_{16}$ introduced and studied in previous chapters are employed here for the silver-containing oxidizers. Combines with aluminum fuel, a ternary system is being investigated.

Figure 10.8A shows a snapshot of $Al/I_2O_5/Ag_2O$ thermite burning on a high rate heating Pt wire under vacuum capture by a high-speed camera. Large number of particles formed during the ignition/combustion and could potentially be the biocidal active cites. By applying color ratio pyrometry to the captured image, the corresponding flame temperature map of $Al/I_2O_5/Ag_2O$ thermite is shown in Figure 10.8B. The flame temperature can reach as high as 5500 K guarantees a delivery of a very high thermite release.

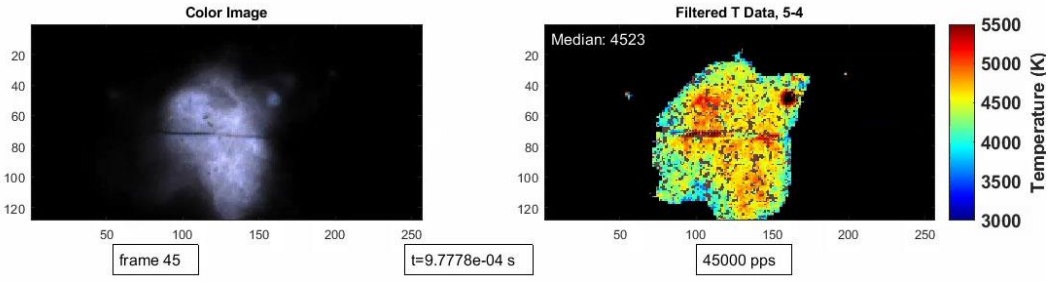

Figure 100.8. A snapshot of $Al/I_2O_5/Ag_2O$ thermite burning on a high rate heating Pt wire under vacuum capture by a high-speed camera and its corresponding high speed pyrometry frame.

To thoroughly investigate the ternary system, four different mass ratios of iodine oxide and silver-containing oxidizer are used. By characterizing the combustion products of $Al/I_2O_5/Ag_2O$, $Al/I_2O_5/AgFeO_2$ and $Al/I_2O_5/Ag_{1.8}Mn_8O_{16}$, there is only one

sample with no detection of AgI in the combustion products proved by the XRD patterns (Figure 10.9), that is of $Al/I_2O_5/Ag_{1.8}Mn_8O_{16}$ with 72% I_2O_5 (weight fraction in oxidizers). Therefore, a system with the potential to deliver two different biocidal cites and a strong thermal shock should be carried on further.

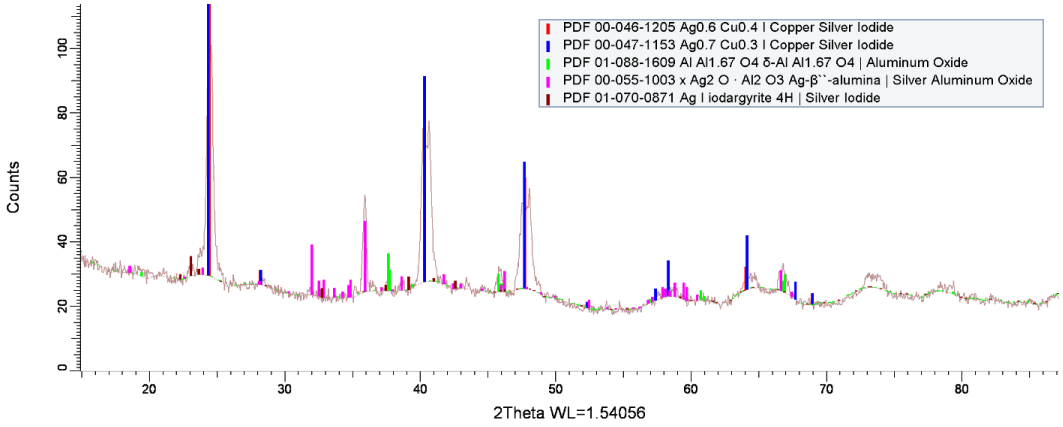

Figure 100.9. The XRD result of the combustion products of $Al/I_2O_5/Ag_{1.8}Mn_8O_{16}$ with 0.72 I_2O_5 in the oxidizer collected inside the pressure cell chamber.

10.2.4. Florine-containing thermite system; to deliver Florine gas considering it is biocidal.

Besides iodine and silver, fluorine is also known to be a biocide. As proved in previous chapters, molecularly incorporated silver or iodine into oxidizers performs much better than physically adding the elements. Therefore, a promising idea to create an energetic system that delivers not only a long-lasting thermal shock but also fluorine gas is to figure out a way to incorporate fluorine into an oxidizer. By looking into literatures, fluorine-containing oxidizers draw my attention. Especially for bismuth oxyfluoride BiO_xF_{3-2x}, bismuth oxide alone is a very strong oxidizer and the addition of fluorine (one with an even higher electronegativity) might boost its performance

even more. Other alternatives include iron oxyfluoride Fe_2OF_4, selenium oxyfluoride F_2OSn, etc. By employing those metal oxyfluoride oxidizers in aluminum-based thermite system, it might fulfill the goal of producing both thermal and biocidal events. To prevent the combination of aluminum and fluorine, the content of fluorine should be very excess.

Bibliography

Chapter 1:

[1] E.L. Dreizin, Metal-based reactive nanomaterials, Prog Energ Combust 35 (2009) 141-167.

[2] R.A. Yetter, G.A. Risha, S.F. Son, Metal particle combustion and nanotechnology, P Combust Inst 32 (2009) 1819-1838.

[3] J.P. Agrawal, High Energy Materials: Propellants, Explosives and Pyrotechnics, Wiley2010.

[4] D. Cressy, The Mother of Gunpowder, Oxford University Press2012.

[5] D. Sundaram, V. Yang, R.A. Yetter, Metal-based nanoenergetic materials: Synthesis, properties, and applications, Prog Energ Combust 61 (2017) 293-365.

[6] N.H. Yen, L.Y. Wang, Reactive Metals in Explosives, Propell Explos Pyrot 37 (2012) 143-155.

[7] C.E. Aumann, G.L. Skofronick, J.A. Martin, Oxidation Behavior of Aluminum Nanopowders, J Vac Sci Technol B 13 (1995) 1178-1183.

[8] C. Rossi, K. Zhang, D. Esteve, P. Alphonse, P. Tailhades, C. Vahlas, Nanoenergetic materials for MEMS: A review, J Microelectromech S 16 (2007) 919-931.

[9] C. Rossi, A. Esteve, P. Vashishta, Nanoscale energetic materials, J Phys Chem Solids 71 (2010) 57-58.

[10] K.S. Martirosyan, Nanoenergetic Gas-Generators: principles and applications, J Mater Chem 21 (2011) 9400-9405.

[11] M.R. Zachariah, NanoEnergetics: Hype, Reality and Future, Propell Explos Pyrot 38 (2013) 7-7.

[12] T. Wu, X.Z. Wang, P.Y. Zavalij, J.B. Delisio, H.Y. Wang, M.R. Zachariah, Performance of iodine oxides/iodic acids as oxidizers in thermite systems, Combust Flame 191 (2018) 335-342.

[13] G. Jian, N.W. Piekiel, M.R. Zachariah, Time-Resolved Mass Spectrometry of Nano-Al and Nano-Al/CuO Thermite under Rapid Heating: A Mechanistic Study, J Phys Chem C 116 (2012) 26881-26887.

[14] M.A. Trunov, M. Schoenitz, X.Y. Zhu, E.L. Dreizin, Effect of polymorphic phase transformations in Al2O3 film on oxidation kinetics of aluminum powders, Combust Flame 140 (2005) 310-318.

[15] R. Nakamura, D. Tokozakura, H. Nakajima, J.G. Lee, H. Mori, Hollow oxide formation by oxidation of Al and Cu nanoparticles, J Appl Phys 101 (2007).

[16] A. Rai, K. Park, L. Zhou, M.R. Zachariah, Understanding the mechanism of aluminium nanoparticle oxidation, Combust Theor Model 10 (2006) 843-859.

[17] K.T. Sullivan, W.A. Chiou, R. Fiore, M.R. Zachariah, In situ microscopy of rapidly heated nano-Al and nano-Al/WO3 thermites, Appl Phys Lett 97 (2010) 133104.

[18] D. Stamatis, E.L. Dreizin, K. Higa, Thermal Initiation of Al-MoO3 Nanocomposite Materials Prepared by Different Methods, J Propul Power 27 (2011) 1079-1087.

[19] K.T. Sullivan, N.W. Piekiel, C. Wu, S. Chowdhury, S.T. Kelly, T.C. Hufnagel, K. Fezzaa, M.R. Zachariah, Reactive sintering: An important component in the combustion of nanocomposite thermites, Combust Flame 159 (2012) 2-15.

[20] G.Q. Jian, S. Chowdhury, K. Sullivan, M.R. Zachariah, Nanothermite reactions: Is gas phase oxygen generation from the oxygen carrier an essential prerequisite to ignition?, Combust Flame 160 (2013) 432-437.

[21] W.B. Zhou, J.B. DeLisio, X.Z. Wang, G.C. Egan, M.R. Zachariah, Evaluating free vs bound oxygen on ignition of nano-aluminum based energetics leads to a critical reaction rate criterion, J Appl Phys 118 (2015).

[22] R.J. Jacob, D.J. Kline, M.R. Zachariah, High speed 2-dimensional temperature measurements of nanothermite composites: Probing thermal vs. Gas generation effects, J Appl Phys 123 (2018).

[23] A. Prakash, A.V. McCormick, M.R. Zachariah, Tuning the reactivity of energetic nanoparticles by creation of a core-shell nanostructure, Nano Lett 5 (2005) 1357-1360.

[24] X.Z. Wang, W.B. Zhou, J.B. DeLisio, G.C. Egan, M.R. Zachariah, Doped delta-bismuth oxides to investigate oxygen ion transport as a metric for condensed phase thermite ignition, Phys Chem Chem Phys 19 (2017) 12749-12758.

[25] X.Z. Wang, T. Wu, M.R. Zachariah, Doped Perovskites To Evaluate the Relationship between Fuel-Oxidizer Thermite Ignition and Bond Energy, Electronegativity, and Oxygen Vacancy, J Phys Chem C 121 (2017) 147-152.

[26] J.L. Prentice, METAL PARTICLE COMBUSTION PROGRESS REPORT, (1967).

[27] A. MaČEic, J.M. Semple, Combustion of Boron Particles at Atmospheric Pressure, Combust Sci Technol 1 (1969) 181-191.

[28] A. MačekJ, J.M. Semple, Combustion of boron particles at elevated pressures, Symposium (International) on Combustion 13 (1971) 859-868.

[29] I. Glassman, F.A. Williams, P. Antaki, A physical and chemical interpretation of boron particle combustion, Symposium (International) on Combustion 20 (1985) 2057-2064.

[30] M.K. King, Boron Ignition and Combustion in Air-Augmented Rocket Afterburners, Combust Sci Technol 5 (1972) 155-164.

[31] M.K. King, Boron Particle Ignition in Hot Gas Streams, Combust Sci Technol 8 (1973) 255-273.

[32] C.L. Yeh, K.K. Kuo, Ignition and combustion of boron particles, Prog Energ Combust 22 (1996) 511-541.

[33] R.H. Knipe, Condensed phase effects in the combustion of boron particles, WSCI-70-9, Western States Section/The Combustion Institue, Berkeley, California, 1970.

[34] G. Mohan, F.A. Williams, Ignition and combustion of boron in O2/inert atmospheres, AIAA Journal 10 (1972) 776-783.

[35] W. Ao, Y. Wang, H.P. Li, J.F. Xi, J.Z. Liu, J.H. Zhou, Effect of Initial Oxide Layer on Ignition and Combustion of Boron Powder, Propell Explos Pyrot 39 (2014) 185-191.

[36] K. Sullivan, G. Young, M.R. Zachariah, Enhanced reactivity of nano-B/Al/CuO MIC's, Combust Flame 156 (2009) 302-309.

[37] T. Liu, X. Chen, A.J. Han, M.Q. Ye, S.T. Zhang, Preparation and Properties of Boron-Based Nano-B/CuO Thermite, KnE Materials Science | IV Sino-Russian ASRTU Symposium on Advanced Materials and Processing Technology (ASRTU), 2016, pp. 95-102.

[38] X.Z. Wang, T. Wu, H.Y. Wang, J.B. DeLisio, Y. Yang, M.R. Zachariah, Boron ignition and combustion with doped delta-Bi2O3: Bond energy/oxygen vacancy relationships, Combust Flame 197 (2018) 127-133.

[39] J.B. DeLisio, X.Z. Wang, T. Wu, G.C. Egan, M.R. Zachariah, Investigating the oxidation mechanism of tantalum nanoparticles at high heating rates. , J Appl Phys 122 (2017) 245901.

[40] M.C. Rehwoldt, Y. Yang, H.Y. Wang, S. Holdren, M.R. Zachariah, Ignition of Nanoscale Titanium/Potassium Perchlorate Pyrotechnic Powder: Reaction Mechanism Study, J Phys Chem C 122 (2018) 10792-10800.

[41] X.Z. Wang, R. Jayathilake, D.D. Taylor, E.E. Rodriguez, M.R. Zachariah, Study of C/Doped delta-Bi2O3 Redox Reactions by in Operando Synchrotron X-ray Diffraction: Bond Energy/Oxygen Vacancy and Reaction Kinetics Relationships, J Phys Chem C 122 (2018) 8796-8803.

[42] N.W. Piekiel, L. Zhou, K.T. Sullivan, S. Chowdhury, G.C. Egan, M.R. Zachariah, INITIATION AND REACTION IN Al/Bi2O3 NANOTHERMITES: EVIDENCE FOR THE PREDOMINANCE OF CONDENSED PHASE CHEMISTRY, Combust Sci Technol 186 (2014) 1209-1224.

[43] E.R. Blatchley, A. Meeusen, A.I. Aronson, L. Brewster, Inactivation of Bacillus spores by ultraviolet or gamma radiation, J Environ Eng-Asce 131 (2005) 1245-1252.

[44] K.T. Sullivan, C.W. Wu, N.W. Piekiel, K. Gaskell, M.R. Zachariah, Synthesis and reactivity of nano-Ag2O as an oxidizer for energetic systems yielding antimicrobial products, Combust Flame 160 (2013) 438-446.

[45] M. Schoenitz, T.S. Ward, E.L. Dreizin, Fully dense nano-composite energetic powders prepared by arrested reactive milling, P Combust Inst 30 (2005) 2071-2078.

[46] G.J. Feng, Z.R. Li, Z. Zhou, Y. Wang, Joining of C-f/Al composites and TiAl intermetallics by laser-induced self-propagating high-temperature synthesis using the Ni-Al-Zr interlayer, Mater Design 110 (2016) 130-137.

[47] K. Zhang, C. Rossi, G.A.A. Rodriguez, C. Tenailleau, P. Alphonse, Development of a nano-Al/CuO based energetic material on silicon substrate, Appl Phys Lett 91 (2007).

[48] K.T. Sullivan, N.W. Piekiel, S. Chowdhury, C. Wu, M.R. Zachariah, C.E. Johnson, Ignition and Combustion Characteristics of Nanoscale Al/AgIO3: A Potential Energetic Biocidal System, Combust Sci Technol 183 (2011) 285-302.

[49] W.B. Zhou, M.W. Orr, V.T. Lee, M.R. Zachariah, Synergistic effects of ultrafast heating and gaseous chlorine on the neutralization of bacterial spores, Chem Eng Sci 144 (2016) 39-47.

[50] W. Zhou, M.W. Orr, G. Jian, S.K. Watt, V.T. Lee, M.R. Zachariah, Inactivation of bacterial spores subjected to sub-second thermal stress, Chem Eng J 279 (2015) 578-588.

[51] F.T. Tabit, E. Buys, The effects of wet heat treatment on the structural and chemical components of Bacillus sporothermodurans spores, Int J Food Microbiol 140 (2010) 207-213.

[52] S.S. Zhang, M. Schoenitz, E.L. Dreizin, Mechanically alloyed Al-I composite materials, J Phys Chem Solids 71 (2010) 1213-1220.

[53] S.S. Zhang, M. Schoenitz, E.L. Dreizin, Iodine Release, Oxidation, and Ignition of Mechanically Alloyed Al-I Composites, J Phys Chem C 114 (2010) 19653-19659.

[54] S.S. Zhang, C. Badiola, M. Schoenitz, E.L. Dreizin, Oxidation, ignition, and combustion of Al center dot I-2 composite powders, Combust Flame 159 (2012) 1980-1986.

[55] H. Wang, G. Jian, W. Zhou, J.B. DeLisio, V.T. Lee, M.R. Zachariah, Metal Iodate-Based Energetic Composites and Their Combustion and Biocidal Performance, Acs Appl Mater Inter 7 (2015) 17363-17370.

[56] Y. Aly, S. Zhang, M. Schoenitz, V.K. Hoffmann, E.L. Dreizin, M. Yermakov, R. Indugula, S.A. Grinshpun, Iodine-containing aluminum-based fuels for inactivation of bioaerosols, Combust Flame 161 (2014) 303-310.

[57] C.L. He, J.H. Zhang, J.M. Shreeve, Dense Iodine-Rich Compounds with Low Detonation Pressures as Biocidal Agents, Chem-Eur J 19 (2013) 7503-7509.

[58] C.E. Johnson, K.T. Higa, Iodine-Rich Biocidal Reactive Materials, MRS Proceedings 1521 (2013).

[59] O. Mulamba, E.M. Hunt, M.L. Pantoya, Neutralizing bacterial spores using halogenated energetic reactions, Biotechnol Bioproc E 18 (2013) 918-925.

[60] J.B. DeLisio, X.L. Hu, T. Wu, G.C. Egan, G. Young, M.R. Zachariah, Probing the Reaction Mechanism of Aluminum/Poly(vinylidene fluoride) Composites, J Phys Chem B 120 (2016) 5534-5542.

[61] T. Wu, A. SyBing, X.Z. Wang, M.R. Zachariah, Aerosol synthesis of phase pure iodine/iodic biocide microparticles, J Mater Res 32 (2017) 890-896.

[62] H.Y. Wang, J.B. DeLisio, G.Q. Jian, W.B. Zhou, M.R. Zachariah, Electrospray formation and combustion characteristics of iodine-containing Al/CuO nanothermite microparticles, Combust Flame 162 (2015) 2823-2829.

[63] S.E. Guerrero, E.L. Dreizin, E. Shafirovich, Combustion of thermite mixtures based on mechanically alloyed aluminum-iodine material, Combust Flame 164 (2016) 164-166.

[64] D. Fischer, T.M. Klapotke, J. Stierstorfer, Synthesis and Characterization of Guanidinium Difluoroiodate, [C(NH2)(3)](+)[IF2O2](-) and its Evaluation as an Ingredient in Agent Defeat Weapons, Z Anorg Allg Chem 637 (2011) 660-665.

[65] X.L. Hu, W.B. Zhou, X.Z. Wang, T. Wu, J.B. Delisio, M.R. Zachariah, On-the-fly green generation and dispersion of AgI nanoparticles for cloud seeding nuclei, J Nanopart Res 18 (2016).

[66] X.L. Hu, J.B. DeLisio, X.Y. Li, W.B. Zhou, M.R. Zachariah, Direct Deposit of Highly Reactive Bi(IO3)3- Polyvinylidene Fluoride Biocidal Energetic Composite and its Reactive Properties, Adv Eng Mater 19 (2017) 1500532.

[67] A. Fischer, Redetermination of HI3O8, an adduct of formula HIO3 center dot I2O5, Acta Crystallogr E 61 (2005) I278-I279.

[68] B.K. Little, S.B. Emery, J.C. Nittinger, R.C. Fantasia, C.M. Lindsay, Physiochemical Characterization of Iodine(V) Oxide, Part 1: Hydration Rates, Propell Explos Pyrot 40 (2015) 595-603.

[69] A. Wikjord, P. Taylor, D. Torgerson, L. Hachkowski, Thermal-Behavior of Corona-Precipitated Iodine Oxides, Thermochim Acta 36 (1980) 367-375.

[70] B.K. Little, E.J. Welle, S.B. Emery, M.B. Bogle, V.L. Ashley, A.M. Schrand, C.M. Lindsay, Chemical dynamics of nano-aluminum/iodine (V) oxide, J Phys Conf Ser 500 (2014).

[71] C. Farley, M. Pantoya, Reaction kinetics of nanometric aluminum and iodine pentoxide, J Therm Anal Calorim 102 (2010) 609-613.

[72] G. Jian, Chowdhury, S., Feng, J., Zachariah, M.R., The ignition and combustion study of nano-al and iodine pentoxide thermite, 8th U. S. National Combustion Meeting, Western States Section of the Combustion Institute, Utah, 2013, pp. 1-13.

[73] K.S. Martirosyan, L. Wang, D. Luss, Development of nanoenergetic materials based on Al/I2O5 system, NSTI-Nanotech 2 (2010) 137.

[74] D.K. Smith, K. Hill, M.L. Pantoya, J.S. Parkey, M. Kesmez, Reactive characterization of anhydrous iodine (v) oxide (I2O5) with aluminum: amorphous versus crystalline microstructures, Thermochim Acta 641 (2016) 55-62.

[75] D.K. Smith, M.L. Pantoya, J.S. Parkey, M. Kesmez, Reaction Kinetics and Combustion Dynamics of I4O9 and Aluminum Mixtures, Jove-J Vis Exp, doi:ARTN e54661

10.3791/54661(2016).

[76] E. Rentz Do Comm Cnmo, Viral Pathogens and Severe Acute Respiratory Syndrome: Oligodynamic Ag+ for Direct Immune Intervention, Journal of Nutritional & Environmental Medicine 13 (2009) 109-118.

[77] J.R. Morones, J.L. Elechiguerra, A. Camacho, K. Holt, J.B. Kouri, J.T. Ramirez, M.J. Yacaman, The bactericidal effect of silver nanoparticles, Nanotechnology 16 (2005) 2346-2353.

[78] A.B. Smetana, K.J. Klabunde, G.R. Marchin, C.M. Sorensen, Biocidal activity of nanocrystalline silver powders and particles, Langmuir 24 (2008) 7457-7464.

[79] B.R. Clark, M.L. Pantoya, The aluminium and iodine pentoxide reaction for the destruction of spore forming bacteria, Phys Chem Chem Phys 12 (2010) 12653-12657.

[80] R. Russell, S. Bless, M. Pantoya, Impact-Driven Thermite Reactions with Iodine Pentoxide and Silver Oxide, J Energ Mater 29 (2011) 175-192.

[81] L. Palou, C.H. Crisosto, D. Garner, L.M. Basinal, J.L. Smilanick, J.P. Zoffoli, Minimum Constant Sulfur Dioxide Emission Rates to Control Gray Mold of Cold-Stored Table Grapes, American Journal of Enology and Viticulture 53 (2002) 110-115.

[82] V.C. Papadimitriou, R.W. Portmann, D.W. Fahey, J. Muhle, R.F. Weiss, J.B. Burkholder, Experimental and Theoretical Study of the Atmospheric Chemistry and Global Warming Potential of SO2F2, J Phys Chem A 112 (2008) 12657-12666.

[83] W.B. Zhou, J.B. DeLisio, X.Y. Li, L. Liu, M.R. Zachariah, Persulfate salt as an oxidizer for biocidal energetic nano-thermites, J Mater Chem A 3 (2015) 11838-11846.

[84] M. Comet, G. Vidick, F. Schnell, Y. Suma, B. Baps, D. Spitzer, Sulfates-Based Nanothermites: An Expanding Horizon for Metastable Interstitial Composites, Angew Chem Int Edit 54 (2015) 4458-4462.

Chapter 2:

[1] T. Wu, X. Wang, J.B. DeLisio, H. Wang, M.R. Zachariah, Performance of iodine oxides/iodic acids as oxidizers in thermite systems, Combust Flame 191 (2017) 335-342.

[2] X.Z. Wang, T. Wu, H.Y. Wang, J.B. DeLisio, Y. Yang, M.R. Zachariah, Boron ignition and combustion with doped delta-Bi2O3: Bond energy/oxygen vacancy relationships, Combust Flame 197 (2018) 127-133.

[3] J.B. DeLisio, X.Z. Wang, T. Wu, G.C. Egan, M.R. Zachariah, Investigating the oxidation mechanism of tantalum nanoparticles at high heating rates. , J Appl Phys 122 (2017) 245901.

[4] J.B. DeLisio, X.L. Hu, T. Wu, G.C. Egan, G. Young, M.R. Zachariah, Probing the Reaction Mechanism of Aluminum/Poly(vinylidene fluoride) Composites, J Phys Chem B 120 (2016) 5534-5542.

[5] J.B. DeLisio, Understanding the relationships between architecture, chemistry, and energy release of energetic nanocomposites, thesis, University of Maryland College Park, 2017.

Chapter 3:

[1] R-D. Chapman, D. Thompson, G. Ooi, D. Wooldridge, P-N. Cash, R-A. Hollins: Presented at the Joint 66th Southwest and 62nd Southeast Regional Meeting of the American Chemical Society, New Orleans, LA, December (2012).

[2] K-T. Sullivan, C-W. Wu, N-W. Piekiel, K. Gaskell, M-R. Zachariah: Synthesis and reactivity of nano-Ag_2O as an oxidizer for energetic systems yielding antimicrobial products. *Combust. Flame* **160**(2), 438 (2013).

[3] M. Schoenitz, T-S.Ward, E-L. Dreizin: Fully dense NanoComposite Energetic Powders Prepared by Arrested Reactive Milling. *Proc. Combust. Inst.* **30**, 2071 (2005).

[4] K-J. Blobaum, A-J. Wagner, J-M. Plitzko, D. Van Heerden, D-H. Fairbrother, T-P. Weihs, Investigating the Reaction Path and Growth Kinetics in CuO_x/Al Multilayer Foils. *J. Appl. Phys*. **94**, 2923 (2003).

[5] K. Zhang, C. Rossi, G-A. Ardila Rodriguez, Development of a Nano-Al/CuO Based Energetic Material on Silicon Substrate. *Appl. Phys. Lett*. **91**, 113117 (2007).

[6] S-M. Umbrajkar, S. Seshadri, M. Schoenitz, V-K. Hoffmann, E-L. Dreizin, Aluminum-Rich Al-MoO_3 Nanocomposite Powders Prepared by Arrested Reactive Milling. *J. Propul. Power* **24**, 192−

198(2008).

[7] T-S. Ward, W. Chen, M. Schoenitz, R-N. Dave, E-L. Dreizin, A Study of Mechanical Alloying Processes Using Reactive Milling and Discrete Element Modeling. *Acta Mater*. **53**, 2909−2918(2005).

[8] S-H. Kim, M-R. Zachariah, Enhancing the Rate of Energy Release from Nanoenergetic Materials by Electrostatically Enhanced Assembly. *Adv. Mater*. **16**, 1821 (2004).

[9] T-M. Tillotson, A-E. Gash, R-L. Simpson, L-W. Hrubesh, J-H. Satcher Jr., J-F. Poco, Nanostructured Energetic Materials Using Sol−Gel Methodologies. *J. Non-Cryst. Solids* **285**, 338 (2001).

[10] H-S. Seo, J-K. Kim, J-W. Kim, H-S. Kim, K-K. Koo, Thermal Behavior of Al/MoO_3 Xerogel Nanocomposites. *J. Ind. Eng. Chem*. **20**, 189 (2014).

[11] C. Rossi, K. Zhang, D. Esteve, P. Alphonse, P. Tailhades, C. Vahlas, Nanoenergetic Materials for MEMS: a Review. *J. Microelectromech. Syst*. **16**, 919 (2007).

[12] J-Y. Malchi, T-J. Foley, R-A. Yetter, Electrostatically Selfassembled Nanocomposite Reactive Microspheres. *ACS Appl. Mater. Interfaces* **1**, 2420 (2009).

[13] H-Y. Wang, G-Q. Jian, G-C. Egan, M-R. Zachariah, Assembly and Reactive Properties of Al/CuO Based Nanothermite Microparticles. *Combust. Flame* **161**, 2203 (2014).

[14] K. Sullivan, N. Pickiel, S. Chowdhury, C. Wu, C. Johnson, M.R. Zachariah, Ignition and Combustion Characteristics of Nanoscale Al/$AgIO_3$: A Potential Energetic Biocidal System, *Combust. Sci. Technol.* **183**, 205 (2011).

[15] W. Zhou, M-W. Orr, V-T. Lee, M-R. Zachariah, Synergistic effects of ultrafast heating and gaseous chlorine on the neutralization of bacterial spores, *Chem. Eng. Sci*. **144**, 39 (2016);

[16] W. Zhou, M-W. Orr, G. Jian, S. Watt, V-T. Lee, M-R. Zachariah, Inactivation of Bacterial Spores Subjected to Sub-Second Thermal Stress, *Chem. Eng. J.* **279**, 578 (2015).

[17] F-T. Tabit, E. Buys, The effects of wet heat treatment on the structural and chemical components of Bacillus sporothermodurans spores, *Int. J. Food Microbiol*. **140**, 207 (2010).

[18] S. Zhang, M. Schoenitz, E-L. Dreizin, Mechanically alloyed Al–I composite materials, *J. Phys. Chem. Solids* **71**, 1213 (2010).

[19] S. Zhang, M. Schoenitz, E-L. Dreizin, Iodine Release, Oxidation, and Ignition of Mechanically Alloyed Al−I Composites, *J. Phys. Chem. C* **114**, 19653 (2010);

[20] S. Zhang, C. Badiola, M. Schoenitz, E-L. Dreizin, Oxidation, ignition, and combustion of Al·I_2 composite powders, *Combust. Flame* **159**, 1980 (2012).

[21] H. Wang, G. Jian, W. Zhou, J. DeLisio, V. Lee, M-R. Zachariah, Metal Iodate-based Energetic Composites and their Combustion and Biocidal Performance, *ACS Appl. Mater. Interfaces* **7**, 17363 (2015).

[22] C-E. Johnson, K-T. Higa, Iodine Rich Biocidal Reactive Materials. Presented at MRS Meeting, Boston, **11**, 25 (2012).

[23] O. Mulamba, E-M. Hunt, M-L. Pantoya, Neutralizing Bacterial Spores Using Halogenated Energetic Reactions. *Biotechnol. Bioprocess Eng*. **18**, 918 (2013).

[24] C. He, J. Zhang, J-M. Shreeve, Dense Iodine-Rich Compounds with Low Detonation Pressures as Biocidal Agents. *Chem. - Eur. J.* **19**, 7503 (2013).

[25] Y. Aly, S. Zhang, M. Schoenitz, V-K. Hoffmann, E-L. Dreizin, M. Yermakov, R. Indugula, S-A. Grinshpun, Iodine-containing Aluminum-based Fuels for Inactivation of Bioaerosols. *Combust. Flame* **161**, 303 (2014).

[26] J-Y. Feng, G-Q. Jian, Q. Liu, M-R. Zachariah, Passivated Iodine Pentoxide Oxidizer for Potential Biocidal Nanoenergetic Applications. *ACS Appl. Mater. Interfaces* **5**, 8875 (2013).

[27] D. Fischer, T-M. Klapçtke, J. Stierstorfer, Synthesis and Characterization of Guanidinium Difluoroiodate,$[C(NH_2)_3]^+[IF_2O_2]^-$ and its Evaluation as an Ingredient in Agent Defeat Weapons, *Anorg. Allg. Chem*. **637**, 660 (2011).

[28] K-S. Martirosyan, Nanoenergetic Gas-Generators: principles and applications, *J. Mater. Chem.* **21**, 9400 (2011).

[29] B-K. Little, E-J. Welle, S-B. Emery, M-B. Bogle, V-L. Ashley, A-M. Schrand, M-C. Lindsay, Chemical dynamics of nano-aluminum/iodine (V) oxide. *J. Phys. Conf. Ser*. **500**(5), 052025 (2014).

[30] C. Farley, M. Pantoya, Reaction kinetics of nanometric aluminum and iodine pentoxide, *J. Therm. Anal. Calorim.* **102**, 609 (2010).

[31] K-S. Martirosyan, L. Wang, D. Luss, Development of nanoenergetic materials based on Al/I_2O_5 system, *NSTI-Nanotech*, ISBN 978-1-4398-3402-2, 2 (2010).

32 G. Jian, S. Chowdhury, J. Feng, M-R. Zachariah, The ignition and combustion study of NanoAl and iodine pentoxide thermite, *Combustion Institute* **2**, 1287 (2013).

[33] K. Stahl, M-A. Szafranski, Single-Crystal Neutron Diffraction Study of HIO_3 at 295 and 30 K and of DIO_3 at 295 K. *Acta Chemica Scandinavica* **46**, 1146 (1992);

[34] M-T. Rogers, L. Helmholz, The crystal structure of iodic acid. *J. Am. Chem. Soc*. **63**, 278 (1941).

[35] A. Fischer, M. Lindsjö, γ-HIO_3 – a Metastable, Centrosymmetric Polymorph of Iodic Acid. *Z. Anorg. Allg. Chem*. **631**, 1574 (2005).

[36] B-K. Little, S-B. Emery, J-C. Nittinger, R-C. Fantasia, M-C. Lindsay, Physiochemical Characterization of Iodine (V) Oxide, Part 1: Hydration Rates, Propellants. *Explos. Pyrotech.* **40**, 595 (2015).

[37] A. Fischer, Redetermination of HI_3O_8, an adduct of formula HIO_3•I_2O_5, *Acta Cryst.* **E61**, i278 (2005).

[38] C-M. Sorensen, Q. Li, H-K. Xu, Z-X. Tang, K-J. Klabunde, G-C. Hadjipanayis, Aerosol spray pyrolysis synthesis techniques, *Nanophase Materials*, **260**, 109 (1994).

[39] L. Liu, M-R. Zachariah, S-I. Stoliarov, J. Li, Enhanced thermal decomposition kinetics of poly(lactic acid) sacrificial polymer catalyzed by metal oxide nanoparticles. *RSC Adv.* **5**, 101745 (2015).

[40] A. Wikjord, P. Taylor, D. Torgerson, L. Hachkowski, Thermal behavior of corona-precipitated iodine oxides, *Thermochimica Acta* **36**, 367 (1980).

Chapter 4:

[1]K. Stahl and M. Szafranski, *Acta Chem. Scand.* 1992, **46**, 1146-1148.

[2]J. G. Bergman Jr., G. D. Boyd, and A. Ashkin, S. K. Kurtz, *J. Appl. Phys.* 1969, **40**, 2860-2862.

[3]H. Naito and H. Inaba, *Opto-electronics* 1972, **4**, 335-337.

[4]M. T. Rogers and L. Helmholz, *J. Am. Chem. Soc.* 1941, **63**, 278-284.

[5]A. Fischer and M. Lindsjö, (2005), *Z. Anorg. Allg. Chem.* 2005, **631**, 1574–1576.

[6]B. K. Little, S. B. Emery, J. C. Nittinger, R. C. Fantasia and C. M. Lindsay, *Propellants Explos. Pyrotech.* 2015, **40**, 595–603.

[7]L. Liu, D. Taylor, E. Rodriguez and M.R. Zachariah, *Chem. Comm.* 2016, **52**, 10369-10372.

[8]W. Zhou, J. B. DeLisio, X. Li, L. Liu and M. R. Zachariah, *J. Mater. Chem. A* 2015, **3**, 11838-11846.

[9]H. D. Jang, S. K. Kim, H. Chang, J.-W. Choi, J. Luo and J. Huang, *Aerosol Science and Technology* 2013, **47**, 93–98.

[10] D. Kaplowitz, G, Jain, K. Gaskell, A. Ponce, P. Shang and M.R. Zachariah, *Part. Part. Syst. Charact.* 2013, ***30***, 881–887.

[11] T. Wu, A. SyBing, X. Wang and M. R. Zachariah, *J. Mater. Res.* 2016, in press.

[12] Wikjord, P. Taylor, D. Torgerson and L. Hachkowski, *Thermochimica Acta* 1980, **36**, 367-375.

[13] G. M. Sheldrick, *Acta Cryst.* 2015, **A71**, 3-8.

[14] R. W. Cheary and A. Coelho, *J. Appl. Crystallogr.* 1992, **25**, 109-121.

[15] A. Fischer, *Acta Cryst.* 2005, **E61**, i278-i279.

Chapter 5:

[1] E.R. Blatchley, A. Meeusen, A.I. Aronson, L. Brewster, Inactivation of Bacilus spores by ultraviolet or gamma radiation. J. Environ. Eng. 13 (2005) 1245.

[2] K.T. Sullivan, C.W. Wu, N.W. Piekiel, K. Gaskell, M.R. Zachariah, Synthesis and reactivity of nano-Ag_2O as an oxidizer for energetic systems yielding antimicrobial products. Combust. Flame 160 (2013) 438.

[3] M. Schoenitz, T.S.Ward, E.L. Dreizin, Fully dense NanoComposite Energetic Powders Prepared by Arrested Reactive Milling. Proc. Combust. Inst. 30 (2005) 2071.

[4] K.J. Blobaum, A.J. Wagner, J.M. Plitzko, D. Van Heerden, D.H. Fairbrother, T.P. Weihs, Investigating the Reaction Path and Growth Kinetics in CuO_x/Al Multilayer Foils. J. Appl. Phys. 94 (2003) 2923.

[5] K. Zhang, C. Rossi, G.A. Rodriguez, Development of a nAl/CuO Based Energetic Material on Silicon Substrate. Appl. Phys. Lett. 91 (2007) 113117.

[6] S.M. Umbrajkar, S. Seshadri, M. Schoenitz, V.K. Hoffmann, E.L. Dreizin, Aluminum-Rich Al-MoO_3 Nanocomposite Powders Prepared by Arrested Reactive Milling. J. Propul. Power 24 (2008) 192.

[7] T.S. Ward, W. Chen, M. Schoenitz, R.N. Dave, E.L. Dreizin, A Study of Mechanical Alloying Processes Using Reactive Milling and Discrete Element Modeling. Acta Mater. 53 (2005) 2909.

[8] K. Sullivan, N. Pickiel, S. Chowdhury, C.W. Wu, C. Johnson, M.R. Zachariah, Ignition and Combustion Characteristics of Nanoscale Al/$AgIO_3$: A Potential Energetic Biocidal System, Combust. Sci. Technol. 183 (2011) 205.

[9] W. Zhou, M.W. Orr, V.T. Lee, M.R. Zachariah, Synergistic effects of ultrafast heating and gaseous chlorine on the neutralization of bacterial spores, Chem. Eng. Sci. 144 (2016) 39.

[10] W. Zhou, M.W. Orr, G. Jian, S. Watt, V.T. Lee, M.R. Zachariah, Inactivation of Bacterial Spores Subjected to Sub-Second Thermal Stress, Chem. Eng. J. 279 (2015) 578.

[11] F.T. Tabit, E. Buys, The effects of wet heat treatment on the structural and chemical components of Bacillus sporothermodurans spores, Int. J. Food Microbiol. 140 (2010) 207.

[12] S. Zhang, M. Schoenitz, E.L. Dreizin, Mechanically alloyed Al–I composite materials, J. Phys. Chem. Solids 71 (2010) 1213.

[13] S. Zhang, M. Schoenitz, E.L. Dreizin, Iodine Release, Oxidation, and Ignition of Mechanically Alloyed Al−I Composites, J. Phys. Chem. C 114 (2010) 19653.

[14] S. Zhang, C. Badiola, M. Schoenitz, E-L. Dreizin, Oxidation, ignition, and combustion of Al·I_2 composite powders, Combust. Flame 159 (2012) 1980.

[15] H. Wang, G. Jian, W. Zhou, J. DeLisio, V. Lee, M-R. Zachariah, Metal Iodate-based Energetic Composites and their Combustion and Biocidal Performance, ACS Appl. Mater. Interfaces **7** (2015) 17363.

[16] Y. Aly, S. Zhang, M. Schoenitz, V.K. Hoffmann, E.L. Dreizin, M. Yermakov, R. Indugula, S.A. Grinshpun, Iodine-containing Aluminum-based Fuels for Inactivation of Bioaerosols. Combust. Flame 161 (2014) 303.

[17] C.E. Johnson, K.T. Higa, Iodine Rich Biocidal Reactive Materials. Presented at MRS Meeting, Boston, 11 (2012) 25.

[18] O. Mulamba, E.M. Hunt, M.L. Pantoya, Neutralizing Bacterial Spores Using Halogenated Energetic Reactions. Biotechnol. Bioprocess Eng. 18 (2013) 918.

[19] C. He, J. Zhang, J.M. Shreeve, Dense Iodine-Rich Compounds with Low Detonation Pressures as Biocidal Agents. Chem. - Eur. J. 19 (2013) 7503.

[20] J.Y. Feng, G.Q. Jian, Q. Liu, M.R. Zachariah, Passivated Iodine Pentoxide Oxidizer for Potential Biocidal Nanoenergetic Applications. ACS Appl. Mater. Interfaces **5** (2013) 8875.

[21] H. Wang, J. Delisio, G. Jian, W. Zhou and M.R. Zachariah, Electrospray Formation and Combustion Characteristics of Iodine-Containing Al/CuO Nanothermite Microparticles, Combustion and Flame 162 (2015) 2823.

[22] S.E. Guerrero, E.L. Dreizin, E. Shafirovich. Combustion of thermite mixtures based on mechanically alloyed aluminum–iodine material, Combustion and Flame 164 2016 164.

[23] D. Fischer, T.M. Klapçtke, J. Stierstorfer, Synthesis and Characterization of Guanidinium Difluoroiodate,$[C(NH_2)_3]^+[IF_2O_2]^-$ and its Evaluation as an Ingredient in Agent Defeat Weapons, Anorg. Allg. Chem. 637 (2011) 660.

[24] X. Hu, W. Zhou, X. Wang, T. Wu, J.B. DeLisio, M.R. Zachariah, On-the-fly green generation and dispersion of AgI nanoparticles for cloud seeding nuclei, J. Nanopart. Res. 18 (2016) 214.

[25] X. Hu, J. B. DeLisio, X. Li, W. Zhou, M.R. Zachariah, Direct Deposit of Highly Reactive $Bi(IO_3)^{3-}$ Polyvinylidene Fluoride Biocidal Energetic Composite and its Reactive Properties . Adv. Eng. Mater. (2016), doi:10.1002/adem.201500532.

[26] B.K. Little, S.B. Emery, J.C. Nittinger, R.C. Fantasia, M.C. Lindsay, Physiochemical Characterization of Iodine (V) Oxide, Part 1: Hydration Rates, Propellants. Explos. Pyrotech. 40 (2015) 595.

[27] A. Fischer, Redetermination of HI_3O_8, an adduct of formula HIO_3•I2O5, Acta Cryst. E61 (2005) i278.

[28] A. Wikjord, P. Taylor, D. Torgerson, L. Hachkowski, Thermal behavior of corona-precipitated iodine oxides, Thermochimica Acta 36 (1980) 367.

[29] K.S. Martirosyan, Nanoenergetic Gas-Generators: principles and applications, J. Mater. Chem. 21 (2011) 9400.

[30] B.K. Little, E.J. Welle, S.B. Emery, M.B. Bogle, V.L. Ashley, A.M. Schrand, M.C. Lindsay, Chemical dynamics of nAl/iodine (V) oxide. J. Phys. Conf. Ser. 500 (2014) 052025.

[31] C. Farley, M. Pantoya, Reaction kinetics of nanometric aluminum and iodine pentoxide, J. Therm. Anal. Calorim. 102 (2010) 609.

[32] K.S. Martirosyan, L. Wang, D. Luss, Development of nanoenergetic materials based on Al/I_2O_5 system, NSTI-Nanotech, 2 (2010) 137.

[33] G. Jian, S. Chowdhury, J. Feng, M.R. Zachariah, The ignition and combustion study of NanoAl and iodine pentoxide thermite, Combustion Institute 2 (2013) 1287.

[34] O. Mulamba, M. Pantoya. Exothermic surface reactions in alumina–aluminum shell–core nanoparticles with iodine oxide decomposition fragments, J Nanopart Res 16 (2014) 2310.

[35] D.K. Smith, K. Hill, M.L. Pantoya, J.S. Parkey, M. Kesmez. Reactive characterization of anhydrous iodine (v) oxide (I_2O_5) with aluminum: amorphous versus crystalline microstructures, Thermochimica Acta 641 (2016) 55.

[36] D. K. Smith, M.L. Pantoya, J.S. Parkey, M. Kesmez, Reaction Kinetics and Combustion Dynamics of I_4O_9 and Aluminum Mixtures, J. Vis.Exp. 117 (2016) e54661.

[37] T. Wu, A. SyBing, X. Wang, M.R. Zachariah, Aerosol Synthesis of Phase Pure Iodine/Iodic Biocide Microparticles, J. Mater. Res. 4 (2017) 890.

[38] T. Wu, P.Y. Zavalij, M.R. Zachariah, Crystal Structure of a New Polymorph of Iodic Acid, HIO_3, from Powder Diffraction, Powder Diffraction (2017) 1

https://doi.org/10.1017/S0885715617000859

[39] G. Jian, N. W. Piekiel, M.R. Zachariah, Time-resolved mass spectrometry of nAl and nAl/CuO thermite under rapid heating: a mechanistic study. J. Phys. Chem. C 116 (2012) 26881.

[40] W. Zhou, J.B. DeLisio, X. Li, L. Liu, M.R. Zachariah, Persulfate salt as an oxidizer for biocidal energetic nano-thermites, J. Mater. Chem. A 3 (2015) 11838.

[41] K. Stahl, M. Szafranski, A Single-Crystal Neutron Diffraction Study of HIO_3 at 295 and 60 K and DIO_3 at 295 K, Acta Chemica Scandinavica 46 (1992) 1146.

[42] H. Fjellvag, A. Kjekshus, The Crystal Structure of I2O4 and its Relations to Other Iodine-oxygen-containing Compounds, Acta Chemica Scandinavica 48 (1994) 815.

[43] K. Sullivan, M.R. Zachariah, Simultaneous Pressure and Optical Measurements of Nanoaluminum Thermites: Investigating the Reaction Mechanism, J Propul. Powder 26 (2009) 467.

[44] G. Jian, S. Chowdhury, K. Sullivan, M.R. Zachariah, Nanothermite reactions: Is gas phase oxygen generation from the oxygen carrier an essential prerequisite to ignition? Combust. Flame 160 (2013) 432.

[45] N. Piekiel, L. Zhou, K. T. Sullivan , S. Chowdhury, G. Eagan and M,.R. Zachariah. Initiation and Reaction in Al/Bi_2O_3 Nanothermites: Evidence for the Predominance of Condensed Phase Chemistry, Combustion Science and Technology, 186 (2014) 1209.

[46] M. Toyohara, M. Kaneko, N. Mitsutsuka, H. Fujihara, N. Saito, T. Murase, Contribution to understanding iodine sorption mechanism onto mixed solid alumina cement and calcium compounds. J Nucl Sci Technol. 39 (2002) 950.

[47] W. Zhou, J.B. DeLisio, X. Wang, G. Eagan, M.R. Zachariah, Evaluating Free vs. Bound Oxygen on Ignition of Nanoaluminum Energetics Leads to a Critical Reaction Rate Criterion, J. Applied Physics 118 (2015) 114303.

[48] J.B. DeLisio, G.C. Egan, S.C. Liou, W.A. Chiou, M.R. Zachariah, Probing the oxidation mechanism of Ta nanoparticles via in-situ and ex-situ ultra-fast heating TEM/STEM. Microsc. Microanal. 22 (2016) Suppl 3.

[49] W. Zhou, J.B. Delisio, X. Wang, M.R. Zachariah, Reaction mechanisms of potassium oxysalts based energetic composites, Comb. Flame. 177 (2017) 1.

[50] M.R. Weismiller, J.Y. Malchi, J.G. Lee, R.A. Yetter, T.J. Foley, Effects of fuel and oxidizer particle dimensions on the propagation of aluminum containing thermites, Proc. Combust. Inst. 33 (2011) 1989.

[51] E.L. Dreizin, Metal-based reactive nanomaterials, Progress in Energy and Combustion Science 35 (2009) 141.

[52] G. Egan, K. Sullivan, T. Olson, T. Han, M. Worlsey, M.R. Zachariah, Ignition and Combustion Characteristics of Nanoaluminum with Copper Oxide Nanoparticles of Differing Oxidation State, Journal of Physical Chemistry C 120 (2016) 29023.

[53] D. K.Smith, J. McCollum, M. L, Pantoya, Effect of Environment of Iodine Oxidation State on Reactivity with Aluminum. Phys. Chem. Chem. Phys. 18 (2016) 11243.

Chapter 6:

[1] E.R. Blatchley, A. Meeusen, A.I. Aronson, L. Brewster, Inactivation of Bacillus spores by ultraviolet or gamma radiation, J Environ Eng-Asce 131(9) (2005) 1245-1252.

[2] K.T. Sullivan, C.W. Wu, N.W. Piekiel, K. Gaskell, M.R. Zachariah, Synthesis and reactivity of nano-Ag2O as an oxidizer for energetic systems yielding antimicrobial products, Combust Flame 160(2) (2013) 438-446.

[3] M. Schoenitz, T.S. Ward, E.L. Dreizin, Fully dense nano-composite energetic powders prepared by arrested reactive milling, P Combust Inst 30 (2005) 2071-2078.

[4] G.J. Feng, Z.R. Li, Z. Zhou, Y. Wang, Joining of C-f/Al composites and TiAl intermetallics by laser-induced self-propagating high-temperature synthesis using the Ni-Al-Zr interlayer, Mater Design 110 (2016) 130-137.

[5] K. Zhang, C. Rossi, G.A.A. Rodriguez, C. Tenailleau, P. Alphonse, Development of a nano-Al/CuO based energetic material on silicon substrate, Appl Phys Lett 91(11) (2007).

[6] K.T. Sullivan, N.W. Piekiel, S. Chowdhury, C. Wu, M.R. Zachariah, C.E. Johnson, Ignition and Combustion Characteristics of Nanoscale Al/AgIO3: A Potential Energetic Biocidal System, Combust Sci Technol 183(3) (2011) 285-302.

[7] W.B. Zhou, M.W. Orr, V.T. Lee, M.R. Zachariah, Synergistic effects of ultrafast heating and gaseous chlorine on the neutralization of bacterial spores, Chem Eng Sci 144 (2016) 39-47.

[8] W. Zhou, M.W. Orr, G. Jian, S.K. Watt, V.T. Lee, M.R. Zachariah, Inactivation of bacterial spores subjected to sub-second thermal stress, Chem Eng J 279 (2015) 578-588.

[9] F.T. Tabit, E. Buys, The effects of wet heat treatment on the structural and chemical components of Bacillus sporothermodurans spores, Int J Food Microbiol 140(2-3) (2010) 207-213.

[10] S.S. Zhang, M. Schoenitz, E.L. Dreizin, Mechanically alloyed Al-I composite materials, J Phys Chem Solids 71(9) (2010) 1213-1220.

[11] S.S. Zhang, M. Schoenitz, E.L. Dreizin, Iodine Release, Oxidation, and Ignition of Mechanically Alloyed Al-I Composites, J Phys Chem C 114(46) (2010) 19653-19659.

[12] S.S. Zhang, C. Badiola, M. Schoenitz, E.L. Dreizin, Oxidation, ignition, and combustion of Al center dot I-2 composite powders, Combust Flame 159(5) (2012) 1980-1986.

[13] H. Wang, G. Jian, W. Zhou, J.B. DeLisio, V.T. Lee, M.R. Zachariah, Metal Iodate-Based Energetic Composites and Their Combustion and Biocidal Performance, Acs Appl Mater Inter 7(31) (2015) 17363-17370.

[14] Y. Aly, S. Zhang, M. Schoenitz, V.K. Hoffmann, E.L. Dreizin, M. Yermakov, R. Indugula, S.A. Grinshpun, Iodine-containing aluminum-based fuels for inactivation of bioaerosols, Combust Flame 161(1) (2014) 303-310.

[15] C.E. Johnson, K.T. Higa, Iodine-Rich Biocidal Reactive Materials, MRS Proceedings 1521 (2013).

[16] O. Mulamba, E.M. Hunt, M.L. Pantoya, Neutralizing bacterial spores using halogenated energetic reactions, Biotechnol Bioproc E 18(5) (2013) 918-925.

[17] C.L. He, J.H. Zhang, J.M. Shreeve, Dense Iodine-Rich Compounds with Low Detonation Pressures as Biocidal Agents, Chem-Eur J 19(23) (2013) 7503-7509.

[18] T. Wu, A. SyBing, X.Z. Wang, M.R. Zachariah, Aerosol synthesis of phase pure iodine/iodic biocide microparticles, J Mater Res 32(4) (2017) 890-896.

[19] H.Y. Wang, J.B. DeLisio, G.Q. Jian, W.B. Zhou, M.R. Zachariah, Electrospray formation and combustion characteristics of iodine-containing Al/CuO nanothermite microparticles, Combust Flame 162(7) (2015) 2823-2829.

[20] S.E. Guerrero, E.L. Dreizin, E. Shafirovich, Combustion of thermite mixtures based on mechanically alloyed aluminum-iodine material, Combust Flame 164 (2016) 164-166.

[21] B.K. Little, S.B. Emery, J.C. Nittinger, R.C. Fantasia, C.M. Lindsay, Physiochemical Characterization of Iodine(V) Oxide, Part 1: Hydration Rates, Propell Explos Pyrot 40(4) (2015) 595-603.

[22] A. Fischer, Redetermination of HI3O8, an adduct of formula HIO3 center dot I2O5, Acta Crystallogr E 61 (2005) I278-I279.

[23] A. Wikjord, P. Taylor, D. Torgerson, L. Hachkowski, Thermal-Behavior of Corona-Precipitated Iodine Oxides, Thermochim Acta 36(3) (1980) 367-375.

[24] K.S. Martirosyan, Nanoenergetic Gas-Generators: principles and applications, J Mater Chem 21(26) (2011) 9400-9405.

[25] B.K. Little, E.J. Welle, S.B. Emery, M.B. Bogle, V.L. Ashley, A.M. Schrand, C.M. Lindsay, Chemical dynamics of nano-aluminum/iodine (V) oxide, J Phys Conf Ser 500 (2014).

[26] C. Farley, M. Pantoya, Reaction kinetics of nanometric aluminum and iodine pentoxide, J Therm Anal Calorim 102(2) (2010) 609-613.

[27] E.L. Dreizin, M. Schoenitz, Correlating ignition mechanisms of aluminum-based reactive materials with thermoanalytical measurements, Prog Energ Combust 50 (2015) 81-105.

[28] G. Jian, Chowdhury, S., Feng, J., Zachariah, M.R., The ignition and combustion study of nano-al and iodine pentoxide thermite, 8th U. S. National Combustion Meeting, Western States Section of the Combustion Institute, Utah, 2013, pp. 1-13.

[29] G. Jian, N.W. Piekiel, M.R. Zachariah, Time-Resolved Mass Spectrometry of Nano-Al and Nano-Al/CuO Thermite under Rapid Heating: A Mechanistic Study, J Phys Chem C 116(51) (2012) 26881-26887.

[30] G.Q. Jian, S. Chowdhury, K. Sullivan, M.R. Zachariah, Nanothermite reactions: Is gas phase oxygen generation from the oxygen carrier an essential prerequisite to ignition?, Combust Flame 160(2) (2013) 432-437.

[31] J.B. DeLisio, G.C. Egan, S.-C. Liou, W.-A. Chiou, M.R. Zachariah, Probing the Oxidation Mechanism of Ta Nanoparticles via In-Situ and Ex-Situ Ultra-Fast Heating TEM/STEM, Microscopy and Microanalysis 22(S3) (2016) 780-781.

[32] C. Punckt, M.A. Pope, Y.F.M. Liu, I.A. Aksay, Structure-Dependent Electrochemistry of Reduced Graphene Oxide Monolayers, J Electrochem Soc 163(7) (2016) H491-H498.

[33] L. Zhou, Development of ion-mobility and mass spectrometry for probing the reactivity of nanoparticles and nanocomposites, University of Maryland, College Park, Md., 2009.

[34] S. Chowdhury, K. Sullivan, N. Piekiel, L. Zhou, M.R. Zachariah, Diffusive vs Explosive Reaction at the Nanoscale, J Phys Chem C 114(20) (2010) 9191-9195.

[35] T. Wu, X. Wang, J.B. DeLisio, H. Wang, M.R. Zachariah, Performance of iodine oxides/iodic acids as oxidizers in thermite systems, Combust Flame In press (2017).

[36] D.K. Smith, K. Hill, M.L. Pantoya, J.S. Parkey, M. Kesmez, Reactive characterization of anhydrous iodine (v) oxide (I2O5) with aluminum: amorphous versus crystalline microstructures, Thermochim Acta 641 (2016) 55-62.

[37] X.Z. Wang, W.B. Zhou, J.B. DeLisio, G.C. Egan, M.R. Zachariah, Doped delta-bismuth oxides to investigate oxygen ion transport as a metric for condensed phase thermite ignition, Phys Chem Chem Phys 19(20) (2017) 12749-12758.

[38] J.B. DeLisio, X.L. Hu, T. Wu, G.C. Egan, G. Young, M.R. Zachariah, Probing the Reaction Mechanism of Aluminum/Poly(vinylidene fluoride) Composites, J Phys Chem B 120(24) (2016) 5534-5542.

[39] T. Wu, M.X. Chen, L. Zhang, X.Y. Xu, Y. Liu, J. Yan, W. Wang, J.P. Gao, Three-dimensional graphene-based aerogels prepared by a self-assembly process and its excellent catalytic and absorbing performance, J Mater Chem A 1(26) (2013) 7612-7621.

[40] B. Lian, J. Deng, G. Leslie, H. Bustamante, V. Sahajwalla, Y. Nishina, R.K. Joshi, Surfactant modified graphene oxide laminates for filtration, Carbon 116 (2017) 240-245.

[41] D.M. Hu, W.B. Gong, J.T. Di, D. Li, R. Li, W.B. Lu, B.H. Gu, B.Z. Sun, Q.W. Li, Strong graphene-interlayered carbon nanotube films with high thermal conductivity, Carbon 118 (2017) 659-665.

[42] S. Kim, M. Jang, M. Park, N.H. Park, S.Y. Ju, A self-assembled flavin protective coating enhances the oxidative thermal stability of multi-walled carbon nanotubes, Carbon 117 (2017) 220-227.

[43] P.M. Sherwood, J.J. Turner, Vibrational Spectra of Compounds in Iodine Pentoxide-Water System and Sodium Iodate, Spectrochim Acta a-M A 26(10) (1970) 1975-&.

Chapter 7:

[1] E.R. Blatchley, A. Meeusen, A.I. Aronson, L. Brewster, Inactivation of Bacillus spores by ultraviolet or gamma radiation, J Environ Eng-Asce 131 (2005) 1245-1252.

[2] K.T. Sullivan, C.W. Wu, N.W. Piekiel, K. Gaskell, M.R. Zachariah, Synthesis and reactivity of nano-Ag2O as an oxidizer for energetic systems yielding antimicrobial products, Combust Flame 160 (2013) 438-446.

[3] M. Schoenitz, T.S. Ward, E.L. Dreizin, Fully dense nano-composite energetic powders prepared by arrested reactive milling, P Combust Inst 30 (2005) 2071-2078.

[4] G.J. Feng, Z.R. Li, Z. Zhou, Y. Wang, Joining of C-f/Al composites and TiAl intermetallics by laser-induced self-propagating high-temperature synthesis using the Ni-Al-Zr interlayer, Mater Design 110 (2016) 130-137.

[5] K. Zhang, C. Rossi, G.A.A. Rodriguez, C. Tenailleau, P. Alphonse, Development of a nano-Al/CuO based energetic material on silicon substrate, Appl Phys Lett 91 (2007).

[6] K.T. Sullivan, N.W. Piekiel, S. Chowdhury, C. Wu, M.R. Zachariah, C.E. Johnson, Ignition and Combustion Characteristics of Nanoscale Al/AgIO3: A Potential Energetic Biocidal System, Combust Sci Technol 183 (2011) 285-302.

[7] W.B. Zhou, M.W. Orr, V.T. Lee, M.R. Zachariah, Synergistic effects of ultrafast heating and gaseous chlorine on the neutralization of bacterial spores, Chem Eng Sci 144 (2016) 39-47.

[8] W. Zhou, M.W. Orr, G. Jian, S.K. Watt, V.T. Lee, M.R. Zachariah, Inactivation of bacterial spores subjected to sub-second thermal stress, Chem Eng J 279 (2015) 578-588.

[9] F.T. Tabit, E. Buys, The effects of wet heat treatment on the structural and chemical components of Bacillus sporothermodurans spores, Int J Food Microbiol 140 (2010) 207-213.

[10] S.S. Zhang, M. Schoenitz, E.L. Dreizin, Mechanically alloyed Al-I composite materials, J Phys Chem Solids 71 (2010) 1213-1220.

[11] S.S. Zhang, M. Schoenitz, E.L. Dreizin, Iodine Release, Oxidation, and Ignition of Mechanically Alloyed Al-I Composites, J Phys Chem C 114 (2010) 19653-19659.

[12] S.S. Zhang, C. Badiola, M. Schoenitz, E.L. Dreizin, Oxidation, ignition, and combustion of Al center dot I-2 composite powders, Combust Flame 159 (2012) 1980-1986.

[13] H. Wang, G. Jian, W. Zhou, J.B. DeLisio, V.T. Lee, M.R. Zachariah, Metal Iodate-Based Energetic Composites and Their Combustion and Biocidal Performance, Acs Appl Mater Inter 7 (2015) 17363-17370.

[14] Y. Aly, S. Zhang, M. Schoenitz, V.K. Hoffmann, E.L. Dreizin, M. Yermakov, R. Indugula, S.A. Grinshpun, Iodine-containing aluminum-based fuels for inactivation of bioaerosols, Combust Flame 161 (2014) 303-310.

[15] C.E. Johnson, K.T. Higa, Iodine-Rich Biocidal Reactive Materials, MRS Proceedings 1521 (2013).

[16] O. Mulamba, E.M. Hunt, M.L. Pantoya, Neutralizing bacterial spores using halogenated energetic reactions, Biotechnol Bioproc E 18 (2013) 918-925.

[17] C.L. He, J.H. Zhang, J.M. Shreeve, Dense Iodine-Rich Compounds with Low Detonation Pressures as Biocidal Agents, Chem-Eur J 19 (2013) 7503-7509.

[18] T. Wu, A. SyBing, X.Z. Wang, M.R. Zachariah, Aerosol synthesis of phase pure iodine/iodic biocide microparticles, J Mater Res 32 (2017) 890-896.

[19] H.Y. Wang, J.B. DeLisio, G.Q. Jian, W.B. Zhou, M.R. Zachariah, Electrospray formation and combustion characteristics of iodine-containing Al/CuO nanothermite microparticles, Combust Flame 162 (2015) 2823-2829.

[20] S.E. Guerrero, E.L. Dreizin, E. Shafirovich, Combustion of thermite mixtures based on mechanically alloyed aluminum-iodine material, Combust Flame 164 (2016) 164-166.

[21] B.K. Little, S.B. Emery, J.C. Nittinger, R.C. Fantasia, C.M. Lindsay, Physiochemical Characterization of Iodine(V) Oxide, Part 1: Hydration Rates, Propell Explos Pyrot 40 (2015) 595-603.

[22] A. Fischer, Redetermination of HI3O8, an adduct of formula HIO3 center dot I2O5, Acta Crystallogr E 61 (2005) I278-I279.

[23] A. Wikjord, P. Taylor, D. Torgerson, L. Hachkowski, Thermal-Behavior of Corona-Precipitated Iodine Oxides, Thermochim Acta 36 (1980) 367-375.

[24] K.S. Martirosyan, Nanoenergetic Gas-Generators: principles and applications, J Mater Chem 21 (2011) 9400-9405.

[25] B.K. Little, E.J. Welle, S.B. Emery, M.B. Bogle, V.L. Ashley, A.M. Schrand, C.M. Lindsay, Chemical dynamics of nano-aluminum/iodine (V) oxide, J Phys Conf Ser 500 (2014).

[26] C. Farley, M. Pantoya, Reaction kinetics of nanometric aluminum and iodine pentoxide, J Therm Anal Calorim 102 (2010) 609-613.

[27] E.L. Dreizin, M. Schoenitz, Correlating ignition mechanisms of aluminum-based reactive materials with thermoanalytical measurements, Prog Energ Combust 50 (2015) 81-105.

[28] G. Jian, Chowdhury, S., Feng, J., Zachariah, M.R., The ignition and combustion study of nano-al and iodine pentoxide thermite, 8th U. S. National Combustion Meeting, Western States Section of the Combustion Institute, Utah, 2013, pp. 1-13.

[29] O. Mulamba, M.L. Pantoya, Exothermic surface chemistry on aluminum particles promoting reactivity, Appl Surf Sci 315 (2014) 90-94.

[30] D.K. Smith, K. Hill, M.L. Pantoya, J.S. Parkey, M. Kesmez, Reactive characterization of anhydrous iodine (v) oxide (I2O5) with aluminum: amorphous versus crystalline microstructures, Thermochim Acta 641 (2016) 55-62.

[31] T. Wu, X.Z. Wang, P.Y. Zavalij, J.B. Delisio, H.Y. Wang, M.R. Zachariah, Performance of iodine oxides/iodic acids as oxidizers in thermite systems, Combust Flame 191 (2018) 335-342.

[32] T. Wu, X.Z. Wang, J.B. DeLisio, S. Holdren, M.R. Zachariah, Carbon addition lowers initiation and iodine release temperatures from iodine oxide-based biocidal energetic materials, Carbon 130 (2018) 410-415.

[33] G. Jian, N.W. Piekiel, M.R. Zachariah, Time-Resolved Mass Spectrometry of Nano-Al and Nano-Al/CuO Thermite under Rapid Heating: A Mechanistic Study, J Phys Chem C 116 (2012) 26881-26887.

[34] R.J. Jacob, D.J. Kline, M.R. Zachariah, High speed 2-dimensional temperature measurements of nanothermite composites: Probing thermal vs. Gas generation effects, J Appl Phys 123 (2018).

[35] K. Sullivan, M.R. Zachariah, Simultaneous Pressure and Optical Measurements of Nanoaluminum Thermites: Investigating the Reaction Mechanism, J Propul Power 26 (2010) 467-472.

[36] S.H. Fischer, M.C. Grubelich, Theoretical energy release of thermites, intermetallics, and combustible metals, 24th International Pyrotechnics Seminar, The International Pyrotechnics Society, Monterey, California, USA, 1998.

Chapter 8:

[1] E.R. Blatchley, A. Meeusen, A.I. Aronson, L. Brewster, Inactivation of Bacillus spores by ultraviolet or gamma radiation, J Environ Eng-Asce 131 (2005) 1245-1252.

[2] K.T. Sullivan, C.W. Wu, N.W. Piekiel, K. Gaskell, M.R. Zachariah, Synthesis and reactivity of nano-Ag2O as an oxidizer for energetic systems yielding antimicrobial products, Combust Flame 160 (2013) 438-446.

[3] M. Schoenitz, T.S. Ward, E.L. Dreizin, Fully dense nano-composite energetic powders prepared by arrested reactive milling, P Combust Inst 30 (2005) 2071-2078.

[4] T.S. Ward, W.L. Chen, M. Schoenitz, R.N. Dave, E.L. Dreizin, A study of mechanical alloying processes using reactive milling and discrete element modeling, Acta Mater 53 (2005) 2909-2918.

[5] K.T. Sullivan, N.W. Piekiel, S. Chowdhury, C. Wu, M.R. Zachariah, C.E. Johnson, Ignition and Combustion Characteristics of Nanoscale Al/AgIO3: A Potential Energetic Biocidal System, Combust Sci Technol 183 (2011) 285-302.

[6] W. Zhou, M.W. Orr, G. Jian, S.K. Watt, V.T. Lee, M.R. Zachariah, Inactivation of bacterial spores subjected to sub-second thermal stress, Chem Eng J 279 (2015) 578-588.

[7] W.B. Zhou, M.W. Orr, V.T. Lee, M.R. Zachariah, Synergistic effects of ultrafast heating and gaseous chlorine on the neutralization of bacterial spores, Chem Eng Sci 144 (2016) 39-47.

[8] F.T. Tabit, E. Buys, The effects of wet heat treatment on the structural and chemical components of Bacillus sporothermodurans spores, Int J Food Microbiol 140 (2010) 207-213.

[9] S.S. Zhang, C. Badiola, M. Schoenitz, E.L. Dreizin, Oxidation, ignition, and combustion of Al center dot I-2 composite powders, Combust Flame 159 (2012) 1980-1986.

[10] S.S. Zhang, M. Schoenitz, E.L. Dreizin, Mechanically alloyed Al-I composite materials, J Phys Chem Solids 71 (2010) 1213-1220.

[11] S.S. Zhang, M. Schoenitz, E.L. Dreizin, Iodine Release, Oxidation, and Ignition of Mechanically Alloyed Al-I Composites, J Phys Chem C 114 (2010) 19653-19659.

[12] H. Wang, G. Jian, W. Zhou, J.B. DeLisio, V.T. Lee, M.R. Zachariah, Metal Iodate-Based Energetic Composites and Their Combustion and Biocidal Performance, Acs Appl Mater Inter 7 (2015) 17363-17370.

[13] E.L. Dreizin, Metal-based reactive nanomaterials, Prog Energ Combust 35 (2009) 141-167.

[14] C. Rossi, K. Zhang, D. Esteve, P. Alphonse, P. Tailhades, C. Vahlas, Nanoenergetic materials for MEMS: A review, J Microelectromech S 16 (2007) 919-931.

[15] R.A. Yetter, G.A. Risha, S.F. Son, Metal particle combustion and nanotechnology, P Combust Inst 32 (2009) 1819-1838.

[16] N.H. Yen, L.Y. Wang, Reactive Metals in Explosives, Propell Explos Pyrot 37 (2012) 143-155.

[17] X.Z. Wang, T. Wu, M.R. Zachariah, Doped Perovskites To Evaluate the Relationship between Fuel-Oxidizer Thermite Ignition and Bond Energy, Electronegativity, and Oxygen Vacancy, J Phys Chem C 121 (2017) 147-152.

[18] G. Jian, N.W. Piekiel, M.R. Zachariah, Time-Resolved Mass Spectrometry of Nano-Al and Nano-Al/CuO Thermite under Rapid Heating: A Mechanistic Study, J Phys Chem C 116 (2012) 26881-26887.

[19] G.Q. Jian, S. Chowdhury, K. Sullivan, M.R. Zachariah, Nanothermite reactions: Is gas phase oxygen generation from the oxygen carrier an essential prerequisite to ignition?, Combust Flame 160 (2013) 432-437.

[20] K.S. Martirosyan, Nanoenergetic Gas-Generators: principles and applications, J Mater Chem 21 (2011) 9400-9405.

[21] H.Y. Wang, J.B. DeLisio, G.Q. Jian, W.B. Zhou, M.R. Zachariah, Electrospray formation and combustion characteristics of iodine-containing Al/CuO nanothermite microparticles, Combust Flame 162 (2015) 2823-2829.

[22] X.Z. Wang, W.B. Zhou, J.B. DeLisio, G.C. Egan, M.R. Zachariah, Doped delta-bismuth oxides to investigate oxygen ion transport as a metric for condensed phase thermite ignition, Phys Chem Chem Phys 19 (2017) 12749-12758.

[23] K. Zhang, C. Rossi, G.A.A. Rodriguez, C. Tenailleau, P. Alphonse, Development of a nano-Al/CuO based energetic material on silicon substrate, Appl Phys Lett 91 (2007).

[24] A. Prakash, A.V. McCormick, M.R. Zachariah, Tuning the reactivity of energetic nanoparticles by creation of a core-shell nanostructure, Nano Lett 5 (2005) 1357-1360.

[25] G.Q. Jian, L. Liu, M.R. Zachariah, Facile Aerosol Route to Hollow CuO Spheres and its Superior Performance as an Oxidizer in Nanoenergetic Gas Generators, Adv Funct Mater 23 (2013) 1341-1346.

[26] G. Jian, Chowdhury, S., Feng, J., Zachariah, M.R., The ignition and combustion study of nano-al and iodine pentoxide thermite, 8th U. S. National Combustion Meeting, Western States Section of the Combustion Institute, Utah, 2013, pp. 1-13.

[27] B.K. Little, E.J. Welle, S.B. Emery, M.B. Bogle, V.L. Ashley, A.M. Schrand, C.M. Lindsay, Chemical dynamics of nano-aluminum/iodine (V) oxide, J Phys Conf Ser 500 (2014).

[28] T. Wu, A. SyBing, X.Z. Wang, M.R. Zachariah, Aerosol synthesis of phase pure iodine/iodic biocide microparticles, J Mater Res 32 (2017) 890-896.

[29] T. Wu, X. Wang, J.B. DeLisio, H. Wang, M.R. Zachariah, Performance of iodine oxides/iodic acids as oxidizers in thermite systems, Combust Flame 191 (2017) 335-342.

[30] C. Farley, M. Pantoya, Reaction kinetics of nanometric aluminum and iodine pentoxide, J Therm Anal Calorim 102 (2010) 609-613.

[31] T. Wu, X.Z. Wang, J.B. DeLisio, S. Holdren, M.R. Zachariah, Carbon addition lowers initiation and iodine release temperatures from iodine oxide-based biocidal energetic materials, Carbon 130 (2018) 410-415.

[32] W.B. Zhou, J.B. DeLisio, X.Y. Li, L. Liu, M.R. Zachariah, Persulfate salt as an oxidizer for biocidal energetic nano-thermites, J Mater Chem A 3 (2015) 11838-11846.

[33] M. Comet, G. Vidick, F. Schnell, Y. Suma, B. Baps, D. Spitzer, Sulfates-Based Nanothermites: An Expanding Horizon for Metastable Interstitial Composites, Angew Chem Int Edit 54 (2015) 4458-4462.

[34] X.L. Hu, W.B. Zhou, X.Z. Wang, T. Wu, J.B. Delisio, M.R. Zachariah, On-the-fly green generation and dispersion of AgI nanoparticles for cloud seeding nuclei, J Nanopart Res 18 (2016).

[35] X.L. Hu, J.B. DeLisio, X.Y. Li, W.B. Zhou, M.R. Zachariah, Direct Deposit of Highly Reactive Bi(IO3)3- Polyvinylidene Fluoride Biocidal Energetic Composite and its Reactive Properties, Adv Eng Mater 19 (2017) 1500532.

[36] C.W. Wu, K. Sullivan, S. Chowdhury, G.Q. Jian, L. Zhou, M.R. Zachariah, Encapsulation of Perchlorate Salts within Metal Oxides for Application as Nanoenergetic Oxidizers, Adv Funct Mater 22 (2012) 78-85.

[37] W.B. Zhou, J.B. DeLisio, X.Z. Wang, M.R. Zachariah, Reaction mechanisms of potassium oxysalts based energetic composites, Combust Flame 177 (2017) 1-9.

[38] Y. Aly, S. Zhang, M. Schoenitz, V.K. Hoffmann, E.L. Dreizin, M. Yermakov, R. Indugula, S.A. Grinshpun, Iodine-containing aluminum-based fuels for inactivation of bioaerosols, Combust Flame 161 (2014) 303-310.

[39] C.L. He, J.H. Zhang, J.M. Shreeve, Dense Iodine-Rich Compounds with Low Detonation Pressures as Biocidal Agents, Chem-Eur J 19 (2013) 7503-7509.

[40] C.E. Johnson, K.T. Higa, Iodine-Rich Biocidal Reactive Materials, MRS Proceedings 1521 (2013).

[41] O. Mulamba, E.M. Hunt, M.L. Pantoya, Neutralizing bacterial spores using halogenated energetic reactions, Biotechnol Bioproc E 18 (2013) 918-925.

[42] J.B. DeLisio, X.L. Hu, T. Wu, G.C. Egan, G. Young, M.R. Zachariah, Probing the Reaction Mechanism of Aluminum/Poly(vinylidene fluoride) Composites, J Phys Chem B 120 (2016) 5534-5542.

[43] T. Wu, P.Y. Zavalij, M.R. Zachariah, Crystal structure of a new polymorph of iodic acid, delta-HIO3, from powder diffraction, Powder Diffr 32 (2017) 261-264.

[44] E. Rentz Do Comm Cnmo, Viral Pathogens and Severe Acute Respiratory Syndrome: Oligodynamic Ag+ for Direct Immune Intervention, Journal of Nutritional & Environmental Medicine 13 (2009) 109-118.

[45] J.R. Morones, J.L. Elechiguerra, A. Camacho, K. Holt, J.B. Kouri, J.T. Ramirez, M.J. Yacaman, The bactericidal effect of silver nanoparticles, Nanotechnology 16 (2005) 2346-2353.

[46] A.B. Smetana, K.J. Klabunde, G.R. Marchin, C.M. Sorensen, Biocidal activity of nanocrystalline silver powders and particles, Langmuir 24 (2008) 7457-7464.

[47] B.R. Clark, M.L. Pantoya, The aluminium and iodine pentoxide reaction for the destruction of spore forming bacteria, Phys Chem Chem Phys 12 (2010) 12653-12657.

[48] R. Russell, S. Bless, M. Pantoya, Impact-Driven Thermite Reactions with Iodine Pentoxide and Silver Oxide, J Energ Mater 29 (2011) 175-192.

[49] Y. Chen, W. Zhang, C. Yu, D. Ni, K. Ma, J. Ye, Controllable synthesis of NiCo2O4/Al core-shell nanowires thermite film with excellent heat release and short ignition time, Mater Design 155 (2018) 396-403.

[50] L.M. Shi, W.C. Zhang, J. Cheng, C.P. Yu, R.Q. Shen, J.H. Ye, Z.C. Qin, Y.M. Chao, A high energy output and low onset temperature nanothermite based on three-dimensional ordered macroporous nano-NiFe2O4, Rsc Adv 6 (2016) 93330-93334.

[51] K. Sullivan, M.R. Zachariah, Simultaneous Pressure and Optical Measurements of Nanoaluminum Thermites: Investigating the Reaction Mechanism, J Propul Power 26 (2010) 467-472.

[52] L. Zhou, N. Piekiel, S. Chowdhury, M.R. Zachariah, Time-Resolved Mass Spectrometry of the Exothermic Reaction between Nanoaluminum and Metal Oxides: The Role of Oxygen Release, J Phys Chem C 114 (2010) 14269-14275.

[53] S.H. Fischer, M.C. Grubelich, Theoretical energy release of thermites, intermetallics, and combustible metals, 24th International Pyrotechnics Seminar, The International Pyrotechnics Society, Monterey, California, USA, 1998.

[54] K.T. Sullivan, W.A. Chiou, R. Fiore, M.R. Zachariah, In situ microscopy of rapidly heated nano-Al and nano-Al/WO3 thermites, Appl Phys Lett 97 (2010).

[55] K.T. Sullivan, N.W. Piekiel, C. Wu, S. Chowdhury, S.T. Kelly, T.C. Hufnagel, K. Fezzaa, M.R. Zachariah, Reactive sintering: An important component in the combustion of nanocomposite thermites, Combust Flame 159 (2012) 2-15.

Chapter 9:

[1] C. Rossi, K. Zhang, D. Esteve, P. Alphonse, P. Tailhades, C. Vahlas, Nanoenergetic materials for MEMS: A review, J Microelectromech S 16 (2007) 919-931.

[2] R.A. Yetter, G.A. Risha, S.F. Son, Metal particle combustion and nanotechnology, P Combust Inst 32 (2009) 1819-1838.

[3] E.L. Dreizin, Metal-based reactive nanomaterials, Prog Energ Combust 35 (2009) 141-167.

[4] N.H. Yen, L.Y. Wang, Reactive Metals in Explosives, Propell Explos Pyrot 37 (2012) 143-155.

[5] F. S., A survey of combustible metals, thermites, and intermetallics for pyrotechnic applications, AIAA Meeting Papers on Disc, doi:https://arc.aiaa.org/doi/abs/10.2514/6.1996-3018(1996) 3018.

[6] J.L. Prentice, METAL PARTICLE COMBUSTION PROGRESS REPORT, (1967).

[7] A. MaČEic, J.M. Semple, Combustion of Boron Particles at Atmospheric Pressure, Combust Sci Technol 1 (1969) 181-191.

[8] A. MačekJ, J.M. Semple, Combustion of boron particles at elevated pressures, Symposium (International) on Combustion 13 (1971) 859-868.

[9] I. Glassman, F.A. Williams, P. Antaki, A physical and chemical interpretation of boron particle combustion, Symposium (International) on Combustion 20 (1985) 2057-2064.

[10] M.K. King, Boron Ignition and Combustion in Air-Augmented Rocket Afterburners, Combust Sci Technol 5 (1972) 155-164.

[11] M.K. King, Boron Particle Ignition in Hot Gas Streams, Combust Sci Technol 8 (1973) 255-273.

[12] C.L. Yeh, K.K. Kuo, Ignition and combustion of boron particles, Prog Energ Combust 22 (1996) 511-541.

[13] R.H. Knipe, Condensed phase effects in the combustion of boron particles, WSCI-70-9, Western States Section/The Combustion Institue, Berkeley, California, 1970.

[14] G. Mohan, F.A. Williams, Ignition and combustion of boron in O2/inert atmospheres, AIAA Journal 10 (1972) 776-783.

[15] W. Ao, Y. Wang, H.P. Li, J.F. Xi, J.Z. Liu, J.H. Zhou, Effect of Initial Oxide Layer on Ignition and Combustion of Boron Powder, Propell Explos Pyrot 39 (2014) 185-191.

[16] K. Sullivan, G. Young, M.R. Zachariah, Enhanced reactivity of nano-B/Al/CuO MIC's, Combust Flame 156 (2009) 302-309.

[17] T. Liu, X. Chen, A.J. Han, M.Q. Ye, S.T. Zhang, Preparation and Properties of Boron-Based Nano-B/CuO Thermite, KnE Materials Science | IV Sino-Russian ASRTU Symposium on Advanced Materials and Processing Technology (ASRTU), 2016, pp. 95-102.

[18] X.Z. Wang, T. Wu, H.Y. Wang, J.B. DeLisio, Y. Yang, M.R. Zachariah, Boron ignition and combustion with doped delta-Bi2O3: Bond energy/oxygen vacancy relationships, Combust Flame 197 (2018) 127-133.

[19] K.T. Sullivan, N.W. Piekiel, S. Chowdhury, C. Wu, M.R. Zachariah, C.E. Johnson, Ignition and Combustion Characteristics of Nanoscale Al/AgIO3: A Potential Energetic Biocidal System, Combust Sci Technol 183 (2011) 285-302.

[20] W.B. Zhou, J.B. DeLisio, X.Y. Li, L. Liu, M.R. Zachariah, Persulfate salt as an oxidizer for biocidal energetic nano-thermites, J Mater Chem A 3 (2015) 11838-11846.

[21] G.Q. Jian, S. Chowdhury, K. Sullivan, M.R. Zachariah, Nanothermite reactions: Is gas phase oxygen generation from the oxygen carrier an essential prerequisite to ignition?, Combust Flame 160 (2013) 432-437.

[22] W.B. Zhou, J.B. DeLisio, X.Z. Wang, G.C. Egan, M.R. Zachariah, Evaluating free vs bound oxygen on ignition of nano-aluminum based energetics leads to a critical reaction rate criterion, J Appl Phys 118 (2015).

[23] X. Wang, M.R. Zachariah, What atomic properties of metal oxide control the reaction threshold of solid elemental fuels?, Phys Chem Chem Phys 20 (2018) 26885-26891.

[24] X.Z. Wang, T. Wu, M.R. Zachariah, Doped Perovskites To Evaluate the Relationship between Fuel-Oxidizer Thermite Ignition and Bond Energy, Electronegativity, and Oxygen Vacancy, J Phys Chem C 121 (2017) 147-152.

[25] K.T. Sullivan, N.W. Piekiel, C. Wu, S. Chowdhury, S.T. Kelly, T.C. Hufnagel, K. Fezzaa, M.R. Zachariah, Reactive sintering: An important component in the combustion of nanocomposite thermites, Combust Flame 159 (2012) 2-15.

[26] T. Wu, X.Z. Wang, P.Y. Zavalij, J.B. Delisio, H.Y. Wang, M.R. Zachariah, Performance of iodine oxides/iodic acids as oxidizers in thermite systems, Combust Flame 191 (2018) 335-342.

[27] X.Z. Wang, R. Jayathilake, D.D. Taylor, E.E. Rodriguez, M.R. Zachariah, Study of C/Doped delta-Bi2O3 Redox Reactions by in Operando Synchrotron X-ray Diffraction: Bond Energy/Oxygen Vacancy and Reaction Kinetics Relationships, J Phys Chem C 122 (2018) 8796-8803.

[28] X.Z. Wang, W.B. Zhou, J.B. DeLisio, G.C. Egan, M.R. Zachariah, Doped delta-bismuth oxides to investigate oxygen ion transport as a metric for condensed phase thermite ignition, Phys Chem Chem Phys 19 (2017) 12749-12758.

[29] T. Wu, X.Z. Wang, J.B. DeLisio, S. Holdren, M.R. Zachariah, Carbon addition lowers initiation and iodine release temperatures from iodine oxide-based biocidal energetic materials, Carbon 130 (2018) 410-415.

[30] J.B. DeLisio, X.Z. Wang, T. Wu, G.C. Egan, M.R. Zachariah, Investigating the oxidation mechanism of tantalum nanoparticles at high heating rates. , J Appl Phys 122 (2017) 245901.

[31] K.T. Sullivan, W.A. Chiou, R. Fiore, M.R. Zachariah, In situ microscopy of rapidly heated nano-Al and nano-Al/WO3 thermites, Appl Phys Lett 97 (2010).

[32] N.W. Piekiel, G.C. Egan, K.T. Sullivan, M.R. Zachariah, Evidence for the Predominance of Condensed Phase Reaction in Chemical Looping Reactions between Carbon and Oxygen Carriers, J Phys Chem C 116 (2012) 24496-24502.

Chapter 10:

[1] Sullivan, K., Young, G., Zachariah, M.R., "Enhanced reactivity of nano-B/Al/CuO MIC's," *Combust. Flame,* Vol. 156, 2009, pp. 302-309.

[2] Yetter, R. A., Risha, G. A., Son, S. F., "Metal particle combustion and nanotechnology," *P. Combust. Inst.* Vol. 32, 2009, pp. 1819-1838.

[3] Meda, L., Marra, G., Galfetti, L., Severini, F., De Luca, L., "Nano-aluminum as energetic material for rocket propellants," *Mat. Sci. Eng. C.* Vol. 27, 2007, pp. 1393-1396.

[4] Jian, G., Feng, J., Jacob, R. J., Egan, G. C., Zachariah, M. R., "Super-reactive Nanoenergetic Gas Generators Based on Periodate Salts," *Angew. Chem. Int. Ed.* Vol. 52, 2013, pp. 9743-9746.

[5] Sadeghipour S., Ghaderian J., Wahid M., "Advances in aluminum powder usage as an energetic material and applications for rocket Propellant," presented at *The 4th International Meeting of Advances in Thermalfluids (IMAT 2011)*, 2012.

[6] Yan, S., Jian, G. Q., Zachariah, M. R., "Electrospun nanofiber-based thermite textiles and their reactive properties," *ACS Appl. Mater. Interf.* Vol. 12, 2012, pp. 6432-6435.

[7] Gromov, A. A., Teipel, U., *Metal Nanopowders: Production, Characterization, and Energetic Applications*, Wiley, 2014.

[8] Parthiban, S., Ragunandan, B., Jain, S. R., "Interpenetrating polymer networks as binders for solid composite propellants," *Defence Sci. J.* Vol. 42, 2013, pp. 147-156.

[9] Miller, H. A., Kusel, B. S., Danielson, S. T., Neat, J. W., Avjian, E. K., Pierson, S. N., Budy, S. M., Ball, D. W., Iacono, S. T., Kettwich, S. C., "Metastable nanostructured metallized fluoropolymer composites for energetics," *J. Mater. Chem. A* Vol. 1, 2013, pp. 7050-7058.

[10] Li, X., Liu, X., Cheng, Y., Li, Y., Mei, X., "Thermal decomposition properties of double-base propellant and ammonium perchlorate," *J. Therm. Anal. Calorim.* Vol. 115, 2014, pp. 887-894.

[11] Smith, D. W., Iacono, S. T., Boday, D. J., Kettwich, S. C., *Advances in Fluorine-Containing Polymers*, American Chemical Society, 2012.

[12] Koch, E. C., Metal-Fluorocarbon Based Energetic Materials, Wiley-VCH Verlag GmbH & Co. KGaA, Weinheim, Germany 2012.

[13] Lide, D. R., 77th CRC Handbook of Chemistry and Physics, CRC Press, Boca Raton, Florida 1996.

[14] Wang, Y., Travas, S. J., Steiner, R., "Polymer gel electrolyte supported with microporous polyolefin membranes for lithium ion polymer battery," *Solid State Ionics* Vol. 148, 2002, pp. 443-449.

[15] Jaworek, A., "Electrospray droplet sources for thin film deposition," *J. Mater. Sci.* Vol. 42, 2007, pp. 266-297.

[16] Bock, N., Dargaville, T. R., Woodruff, M. A., "Electrospraying of polymers with therapeutic molecules: State of the art," *Prog. Polym. Sci.* Vol. 37, 2012, pp. 1510-1551.

[17] Huang, G. Jian, J. B. Delisio, H. Wang, M. R. Zachariah, "Electrospray Deposition of Energetic Polymer Nanocomposites with High Mass Particle Loadings: A Prelude to 3D Printing of Rocket Motors," *Adv. Eng. Mater*. Vol. 17, 2015, pp. 95-101.

[18] Li, X., Guerieri, P., Zhou, W., Huang, C., Zachariah, M. R., "Direct Deposit Laminate Nanocomposites with Enhanced Propellant Properties," *ACS Appl. Mater. Interfaces*, Vol. 7, 2015, pp. 9103-9109.